EUROPEAN
COMMISSION

UNIVERSITÉ
DE PAU ET DES
PAYS DE L'ADOUR

SEVENTH FRAMEWORK
PROGRAMME

EBERHARD KARLS
UNIVERSITÄT
TÜBINGEN

---

# THESIS

submitted in fulfillment of the requirements for the degree of

***Doctor of Philosophy***

in Physical-Chemistry at

UNIVERSITÉ DE PAU ET DES PAYS DE L'ADOUR

and

EBERHARD KARLS UNIVERSITÄT TÜBINGEN

presented by

**Hugo SANTOS SILVA**

on

# Synthesis and Modelling of Polyfullerenes
## *Synthèse et Modélisation de Polyfullèrenes*

Advisors: **Dr Roger HIORNS, Pr Thomas CHASSÉ**

Co-advisors: **Pr Didier BÉGUÉ, Dr Heiko PEISERT**

defended on July 16th, 2015

for the commission composed by

## JURY

| | | |
|---|---|---|
| Dr Christophe RAYNAUD | Université de Montpellier, France | Rapporteur |
| Dr Johannes GIERSCHNER | IMDEA, Spain | Rapporteur |
| Dr Paul TOPHAM | Aston University, UK | Examinateur |
| Dr Brigitte PEPIN-DONAT | CNRS, France | Président |

# Acknowledgments

I would like to say a big "Thank you / Muito Obrigado / Merci beaucoup / Vielen Danke für alles" to the following people, whose help was of paramount importance during this thesis:

To my family, for the unconditional love. *Obrigado pai, obrigado mãe, pelo amor e dedicação mesmo em momentos difíceis.*

To Cédric, who showed me the need to fight for better days, and to smile then. *Merci pour tout, fofi!*

To all EPCP and ECP group members, for the help whenever needed.

To all ESTABLIS group members: the fellows for the friendship and the advisors for the good scientific discussions.

To Aurélien in particular, who helped unconditionally since the beginning.

To the Institut für Physikalische und Theoretische Chemie for their support in Tübingen and the group members, for their warm welcome and everyday life at the lab. *Vielen Danke für alles!*

To Mélanie, for her hard work making everybody's life easier.

To Abdel, whose advices in NMR technique were extremely helpful.

To Thomas and Heiko for their enormous help and patience as advisors in Germany.

To Roger, for the good pieces of advice and setting up everything that has been needed for this work.

To Didier, whose orientation came from all the possible sides during the PhD.

To European Union, Marie Curie Institute and the Marie Curie Actions for financing the ESTABLIS project.

*”Those who have read of everything, are thought to understand everything too; but it is not always so. Reading furnishes the mind only with materials of knowledge; it is thinking that makes what we read ours. We are of the ruminating kind, and it is not enough to cram ourselves with a great load of collections; unless we chew them over again, they will not give us strength and nourishment.”*

**John Locke**

*Science is a wonderful thing if one does not have to earn one’s living at it.*

***Einstein***

*Simplicity is the ultimate sophistication.*

***Da Vinci***

*To Adriana,*

*who has been the greatest*

*motivation to overcome self-imposed limitations.*

*À minha querida mãe,*

*que viveu com os olhos vendados*

*mas ainda assim não*

*foi poupada da Justiça.*

# Abstract

The work developed during this thesis include the design, modeling, synthesis and characterization of new polymeric materials based on fullerenes for application in organic photovoltaics as morphology stabilizers. In view of such use, these materials have to present particular properties, among which a good solubility in organic solvents, a good miscibility with the light-absorber polymer as well as a morphological stability superior to those currently used materials, such as (bis-)PC$_{60}$BM and the derivatives of indene-C$_{60}$.

Six different synthetic routes were studied and the electronic properties (LUMO orbital energy, electroaffinity, electrophilicity, reorganization energy, transfer integral and electron mobility) were determined by molecular modeling. Among these routes, the one called ”ATRAP”, not much studied in the literature yet, was finally retained.

The physicochemical properties of the so-synthesized materials, grafted with different lateral chains, were determined by different characterization techniques and their application in thin films for Organic Photovoltaic devices was performed. When used as additives, these materials display a potential of stabilizing the P3HT/PC$_{60}$BM layer, and this does not influence the performance of the device. After a thermal treatment, the observed behavior was the opposite of the expected, it means that a destabilization of the active layer was noted instead of a stabilization and the underlying mechanism was also studied by several experimental techniques.

Finally, a depolymerization mechanism induced by light and/or heat was proposed. Within this process, the cleavage of the monomer-fullerene bond is responsible for creating defects, such as the depolymerization, *cross-linkings* or irreversible rearrangement of the thin layer. This cleavage can be either thermally activated or induced by the triplet state

of the monomer, which also destabilizes this bond.

Beyond that, this work also interested in: i) the stabilization of the organic-inorganic interface within photovoltaic devices by tailoring organic groups able to bind to the inorganic surface, ii) the stabilization of the lateral chain of conjugated polymers by the insertion of alkoxy chains, as well as iii) the relation between the curvature of a carbon-based molecule and its reactivity to molecular oxygen.

These studies, performed in parallel, drove to the proposition of new donor-acceptor hybrid materials based on hexabenzocoronene, which are capable of stacking over itself to form supramolecular structures similar to discotic liquid crystals. From the conclusions of this document, two novel materials were proposed, which electronic properties reveal that it is possible to design new materials that may be stable and efficient at the same time for application in organic photovoltaics.

# Résumé

Les travaux développés au cours de cette thèse comprennent le design, la modélisation, la synthèse et la caractérisation de nouveaux matériaux polymérisés à base de fullerène. Dans l'optique d'une utilisation au sein de cellules photovoltaïques, ces matériaux doivent présenter des propriétés particulières, parmi lesquelles une bonne solubilité dans les solvants organiques, une bonne miscibilité avec le polymère absorbeur de lumière ainsi qu'une stabilité morphologique supérieure à celles rencontrées pour les matériaux actuellement utilisés, tels les (bis-)$PC_{60}BM$ et les dérivés d'indène-$C_{60}$.

Six voies de synthèse ont été étudiées et les propriétés électroniques (énergie de l'orbitale LUMO, électroaffinité, électrophilicité, énergie de réorganisation, intégrale de transfert et mobilité électronique) qui en résultent ont été déterminées au moyen de la modélisation numérique. Parmi ces voies de synthèse, le chemin dit «ATRAP», peu étudié dans la littérature, a été finalement retenu.

Les propriétés physico-chimiques de ces composés, greffés de différentes chaînes latérales, ont été déterminées au moyen de diverses techniques de caractérisation et leur application dans des couches minces au sein de dispositifs photovoltaïques a été mise en œuvre. Utilisés en tant qu'additifs, ces matériaux révèlent un potentiel de stabilisation de la couche de P3HT/$PC_{60}BM$, cette propriété n'affectant pas, pour autant, les performances de la cellule. Le comportement de ces couches après soumission à un traitement thermique a montré, à l'inverse, un phénomène de déstabilisation dont le mécanisme a été, lui aussi, étudié par diverses techniques expérimentales.

Finalement, un mécanisme de dépolymérisation, induit par la lumière et/ou par la chaleur, a été proposé. Dans ce processus, la rupture de la liaison chimique entre

le monomère et le fullerène est responsable de la création des défauts, comme de la dépolymérisation, des phénomènes de *cross-linking* ou du réarrangement irréversible de la couche mince. Cette rupture peut être soit thermiquement activée, soit induite par l'état triplet du monomère, qui déstabilise la liaison.

Outre l'étude de ces composés, le présent travail s'est également intéressé i) à la stabilisation de l'interface organique-inorganique au sein des dispositifs photovoltaïques, ii) à la stabilisation de la chaîne latérale des polymères conjugués, ainsi que iii) à la relation entre la géométrie de la molécule et sa réactivité avec l'oxygène moléculaire.Ces études, menées en parallèle, nous ont conduit à proposer de nouveaux matériaux hybrides du type donneur-accepteur, dérivés de l'hexabenzocoronène et capables de s'empiler pour former des structures similaires à des cristaux liquides discotiques. Partant de l'ensemble des conclusions tirées de ces travaux de thèse, deux composés ont été proposés, dont les propriétés électroniques révèlent qu'il est possible de dessiner des matériaux à la fois stables et efficaces pour une utilisation dans le domaine du photovoltaïque organique.

# Zusammenfassung

Die vorliegende Arbeit beinhaltet sowohl das Design und die Modellierung von neuartigen Fulleren-basierten Polymeren als auch deren Sythese und Charakterisierung. Für die Anwendung in photovoltaischen Zellen müssen diese Materialien spezielle Eigenschaften aufweisen, unter anderem eine gute Löslichkeit in organischen Lösungsmitteln, eine gute Mischbarkeit mit dem Licht-absorbienden Polymer sowie eineerhöhte morphologische Stabilität im Vergleich zu derzeit verwendeten Materialien, wie beispielsweise (bis-)PC$_{60}$BM oder Derivaten von indene-C$_{60}$.

Sechs verschiedene Syntheserouten wurden angewandt. Elektronische Eigenschaften (LUMO Energie, Elekronenaffinität, Elektrophilie, Reorganisationsenergie, Transferintergrale und Elektronbeweglichkeit) wurden durch "molecular modeling" bestimmt. Als Sytheseweg erwies sich ein bisher aus der Literatur bekannter Weg ("ATRAP") als erfolgreich.

Die physikalisch-chemischen Eigenschaften der synthetisierten Materialien, welche sich durch verschiedene Seitenketten unterscheiden, wurden durch verschiedene Methoden charakterisiert. Die Anwendung in dünnen Filmen für Organische Photovoltaik wurde getestet. Wenn diese Materialien als sogenannte Additive in P3HT/PC$_{60}$BM Schichten verwendet werden, stabilisieren sie die Morphologie während die Performance nahezu unverändert bleibt. Eine Wärmebehandlung führte überraschenderweise zu einer Destabilisierung der aktiven Schicht. Dieser Mechanismus wurde mit mehreren experimentellen Techniken studiert.

Es wurde ein Mechanismus für eine Depolymerisation Licht bzw. Hitze vorgeschlagen. In diesem Prozesses ist die Spaltung der Monomer-Fulleren Bindung für die Bildung

von Defekten durch Depolymerization, *cross-linking* oder irreversible Neuordnung der dünnen Schicht verantwortlich. Diese Spaltung kann thermisch entweder aktiviert werden oder aber durch Besetzung des Triplett-Zustandes des Monomers hervorgerufen werden, welcher auch diese Bindung destabilisieren kann.

Darüber hinaus beschäftigt sich diese Arbeit mit i) der Stabilisierung der organisch-anorganischen Grenzflächen inphotovolaischen Bauelementen ii) der Stabilisierung der Seitenketten von konjugierten Polymeren, sowie mit iii) dem Zusammenhang zwischen der Struktur von Kohlenstoff-basierten Molekülen und der Reaktivität gegenüber molekularem Sauerstoff.

Auf Grundlage dieser parallel durchgeführten Studienwerden neuartige, Hexabenzocoronene basierte Donor-Akzeptor Hybrid-Materialien vorgeschlagen, welche supramolekulare Strukturen (Stapel) bilden, ähnlich wie diskotische Flüssigkristalle. Als Ergebniswerden zwei Materialien vorgeschlagen, die sowohl eine erhöhte Stabilität zeigen als auch eine bessere Effizienz in organischen photovoltaischen Bauelementen.

# Table of Contents

**Preamble** **21**

**1 Introduction on Stability of Organic Photovoltaic Devices** **22**

1.1 Organic Photovoltaic Structures and Materials . . . . . . . . . . . . . . . . 24
1.2 Degradation of Photovoltaic Devices . . . . . . . . . . . . . . . . . . . . . 27
1.3 An overview on fullerene-containing polymers . . . . . . . . . . . . . . . . 30
1.4 Controlled radical copolymerization of fullerenes . . . . . . . . . . . . . . . 33
1.5 Fullerene polymer derivatives and their proposal as more stable acceptor materials . . . . . . . . . . . . . . . . . . . . . . 37
1.6 Final Remarks . . . . . . . . . . . . . . . . . . . . . . . . . . . . . . . . 39

**2 Design and Modeling of Target Structures** **40**

2.1 Which are the sought-after properties for fullerene derivatives? . . . . . . 40
2.2 How one can design polyfullerenes based on multi-scale molecular modeling? 44
2.3 Model polyfullerene systems and their general properties . . . . . . . . . 46
  2.3.1 Atom Transfer Radical Addition Polymerization . . . . . . . . . . 47
  2.3.2 Amino-fishing . . . . . . . . . . . . . . . . . . . . . . . . . . . 47
  2.3.3 Azide cycloaddition . . . . . . . . . . . . . . . . . . . . . . . . . 48
  2.3.4 Prato cycloaddition . . . . . . . . . . . . . . . . . . . . . . . . . 49
  2.3.5 Cyclopropanation . . . . . . . . . . . . . . . . . . . . . . . . . . 49
  2.3.6 Diels-Alder addition . . . . . . . . . . . . . . . . . . . . . . . . . 50
2.4 Revealing the position of bis-adduct formation . . . . . . . . . . . . . . . 52
  2.4.1 1,3-dipolar cycloaddition-based products . . . . . . . . . . . . . . 53

2.4.1.1 Prato-based products . . . . . . . . . . . . . . . . . . . . 53
2.4.1.2 Azide-based products . . . . . . . . . . . . . . . . . . . 59
2.4.1.3 Cyclopropanation-based products . . . . . . . . . . . . . 60
2.4.2 Diels-Alder . . . . . . . . . . . . . . . . . . . . . . . . . . . 60
2.4.3 Amino-fishing-based products . . . . . . . . . . . . . . . . . . . 61
2.5 Electronic acceptor properties and comparison with current benchmarks . 63
2.5.1 LUMO Orbital Analysis . . . . . . . . . . . . . . . . . . . . . 63
2.5.2 Electron Affinity (EA) . . . . . . . . . . . . . . . . . . . . . . 66
2.5.3 Electrophilicity . . . . . . . . . . . . . . . . . . . . . . . . . 68
2.5.4 Reorganization Energy . . . . . . . . . . . . . . . . . . . . . . 70
2.5.5 Transfer Integral . . . . . . . . . . . . . . . . . . . . . . . . 72
2.6 Final Remarks . . . . . . . . . . . . . . . . . . . . . . . . . . . . 77

**3 Syntheses of Polyfullerenes** **79**
3.1 Fullerene-containing polymers and photovoltaics . . . . . . . . . . . . . . 79
3.2 Synthesis of monomers derived from hydroquinone . . . . . . . . . . . . . 82
3.3 Synthesis and characterization of polymers derived from 1,4-dibromomethyl-2,5-dialkoxyphenylene . . . . . . . . . . . . . . . . . . . . . . . . . . . 87
3.3.1 UV-VIS Optical Absorption (UV-VIS) . . . . . . . . . . . . . . . 92
3.3.2 Size-Exclusion Chromatography (SEC) . . . . . . . . . . . . . . . 93
3.3.3 Nuclear Magnetic Ressonance (NMR) . . . . . . . . . . . . . . . . 97
3.3.4 Thermogravimetric Analysis (TGA) . . . . . . . . . . . . . . . . . 102
3.3.5 Differential Scanning Calorimetry (DSC) . . . . . . . . . . . . . . 104
3.3.6 Fourier-Transform Infrared Spectroscopy (FTIR) . . . . . . . . . 105
3.4 Final Remarks . . . . . . . . . . . . . . . . . . . . . . . . . . . . 108

**4 Photovoltaic Performance and Device Degradation** **109**
4.1 Photovoltaic devices and performance . . . . . . . . . . . . . . . . . . . 109
4.1.1 Interlayer Application . . . . . . . . . . . . . . . . . . . . . . 113
4.1.2 Blend Application . . . . . . . . . . . . . . . . . . . . . . . . . 115

4.1.3 Additive Application . . . 117
4.2 Morphological degradation of the blends using polyfullerenes as additives 119
4.3 Final Remarks . . . 124

**5 Degradation studies 125**

5.1 PolyC$_{60}$ degradation . . . 127
5.1.1 Thermal degradation . . . 127
5.1.1.1 UV-VIS . . . 127
5.1.1.2 Atomic Force Microscopy - AFM . . . 131
5.1.1.3 XPS . . . 138
5.1.2 Photochemical degradation . . . 140
5.1.2.1 UV-VIS . . . 140
5.1.2.2 XPS . . . 141
5.1.3 Photo-oxidation . . . 143
5.1.3.1 UV-VIS . . . 143
5.1.3.2 XPS . . . 145
5.1.3.3 Fourier-Transform Infrared Spectroscopy (FTIR) . . . 148
5.2 P3HT:PC$_{60}$BM:HSS46 blend degradation . . . 151
5.2.1 Thermal degradation . . . 151
5.2.1.1 UV-VIS . . . 151
5.2.1.2 Atomic Force Microscopy - AFM . . . 151
5.2.1.3 XPS . . . 152
5.2.2 Photochemical degradation . . . 156
5.2.2.1 UV-VIS . . . 156
5.2.2.2 Atomic Force Microscopy - AFM . . . 157
5.2.2.3 XPS . . . 158
5.2.3 Photo-oxidation . . . 159
5.2.3.1 UV-VIS . . . 159
5.2.4 Partial Remarks . . . 160
5.3 Revealing the degradation mechanism of ATRAP-based polyfullerenes . . 162

5.3.1 Thermally-induced depolymerization . . . . . . . . . . . . . . . . . 162

5.3.2 Light-induced depolymerization . . . . . . . . . . . . . . . . . . . . 170

5.4 Final Remarks . . . . . . . . . . . . . . . . . . . . . . . . . . . . . . 172

**6 Models for stabilization of OPV materials 173**

6.1 Interfacial stabilization . . . . . . . . . . . . . . . . . . . . . . . . . . 175

6.2 Side-chain stabilization . . . . . . . . . . . . . . . . . . . . . . . . . . 183

6.3 Correlating geometry of multidimensional carbon allotropes molecules and stability . . . . . . . . . . . . . . . . . . 189

6.4 Final Remarks . . . . . . . . . . . . . . . . . . . . . . . . . . . . . . 195

**7 Alternative Acceptor Materials 197**

7.1 Graphene-like systems and columnar H-bond-linked architecture . . . . . 198

7.2 HBC-P3AOT system . . . . . . . . . . . . . . . . . . . . . . . . . . . 201

7.3 HBC-ZP46 system . . . . . . . . . . . . . . . . . . . . . . . . . . . . 206

7.4 Final Remarks . . . . . . . . . . . . . . . . . . . . . . . . . . . . . . 211

**Conclusions 212**

**Appendices 215**

**A Synthetic Routes 216**

**B Experimental Conditions 221**

**C Molecular Modeling based on DFT calculations and the RIJCOSX approximation 223**

C.1 Description of electronic structure of molecules . . . . . . . . . . . . . . 223

C.1.1 Semi-empirical methods . . . . . . . . . . . . . . . . . . . . . . 225

C.2 Density Functional Theory (DFT) . . . . . . . . . . . . . . . . . . . . . 226

C.2.1 The exchange-correlation functionals . . . . . . . . . . . . . . . . . 228

C.3 The ”RIJCOSX” approximation . . . . . . . . . . . . . . . . . . . . . 230

D Résumé Général 231

E Zusammenfassung 235

# List of Figures

1.1 Molecular structure of $C_{60}$ molecule. . . . . . . . . . . . . . . . . . . . . . . . . 23

1.2 Level diagram of a photovoltaic $p-n$ junction. . . . . . . . . . . . . . . . . 25

1.3 Possible ways of assembling $p-n$ junctions in OPV devices. . . . . . . . 25

1.4 Degradation pathways of OPVs. . . . . . . . . . . . . . . . . . . . . . . . . . . . 27

1.5 $PC_{60}BM$ aggregation over time. . . . . . . . . . . . . . . . . . . . . . . . . . . 28

1.6 Family classification of the different polyfullerenes. . . . . . . . . . . . . . 30

1.7 Synthetic strategies for the synthesis of fullerene main-chain polymers. . 31

1.8 Synthetic strategies for the synthesis of fullerene side-chain polymers. . . 31

1.9 Synthesis of main-chain polymers with DNA-cleaving activity. . . . . . . 33

1.10 Synthetic strategies for the synthesis of fullerene star-shaped polymers. . 34

1.11 Synthesis of $(PS)_2C_{60}$ di-adducts using an NMP route. . . . . . . . . . . 34

1.12 Synthesis of $(PS)_2C_{60}$ di-adducts using an NMP route. . . . . . . . . . . 35

1.13 Formation of fullerene radical-attacked polymer chains. . . . . . . . . . . 35

1.14 Derivative of polyfullerene synthesized by the ATRAP route. . . . . . . . 36

1.15 Some examples of double-cable D-A polymers. . . . . . . . . . . . . . . . . 38

2.1 Molecular structures of (a) regio-regular Poly(3-hexylthiophene), (b) $C_{60}$, (c) $PC_{60}BM$, (d) bis-$PC_{60}BM$, (e) $IC_{60}MA$, and (f) $IC_{60}BA$. . . . . . . . 41

2.2 Possible structures of bis-attacked fullerene derivatives than could be polymerized. . . . . . . . . . . . . . . . . . . . . . . . . . . . . . . . . . . . . . 46

2.3 ATRAP synthetic route. . . . . . . . . . . . . . . . . . . . . . . . . . . . . . . 47

2.4 Amino-fishing synthetic route. . . . . . . . . . . . . . . . . . . . . . . . . . . . 48

2.5 $[3+2]$ cycloaddition of an azide. . . . . . . . . . . . . . . . . . . . . . . . . . 48

2.6 [3 + 2] cycloaddition of an azomethineylide. . . . . . . . . . . . . . . . . . 49
2.7 1,3-dipolar cyclopropation reaction. . . . . . . . . . . . . . . . . . . . . . . 50
2.8 [4 + 2] Diels-Alder cycloaddition reaction. . . . . . . . . . . . . . . . . . 51
2.9 Different sites for the second attack to take place during the formation of fullerene bis-adducts. . . . . . . . . . . . . . . . . . . . . . . . . . . 52
2.10 General structure for studying the bis-adduct formation in Prato reaction. 54
2.11 Theoretical-experimental UVVIS electronic transitions comparison for synthesized HHR23D material and Prato molecule model as proposed in Figure 2.10. . . . . . . . . . . . . . . . . . . . . . . . . . . . . . . . 55
2.12 Theoretical-experimental UVVIS electronic transitions comparison for synthesized Poly1HB material and Prato model molecule as proposed in Figure 2.10. . . . . . . . . . . . . . . . . . . . . . . . . . . . . . . . 56
2.13 General energy scheme for studying the bis-adduct formation in Prato reaction. . . . . . . . . . . . . . . . . . . . . . . . . . . . . . . . . 57
2.14 LUMO orbital of the Prato model molecule. . . . . . . . . . . . . . . . . . 57
2.15 LUMO orbital of the Azide-based model molecule. . . . . . . . . . . . . . 59
2.16 LUMO orbital of the cyclopropanation-based model molecule. . . . . . . 60
2.17 LUMO orbital of the Diels-Alder-based model molecule. . . . . . . . . . . 61
2.18 LUMO deviation compared to $C_{60}$ for the studied compounds. . . . . . . 65
2.19 Electron Affinity deviation compared to $C_{60}$ for the studied compounds. . 67
2.20 Electrophilicity deviation compared to $C_{60}$ for the studied compounds. . 70
2.21 Reaction coordinate space representation of the reorganization energy in function of the ionic and ground states. . . . . . . . . . . . . . . . . . . . 72
2.22 Reorganization energies of the anionic state and associated polaron energy for the proposed model compounds. . . . . . . . . . . . . . . . . . . . . 73
2.23 *cis* and *trans* conformers of ATRAP-based dimers. . . . . . . . . . . . . . 74
2.24 Intra-chain transfer integrals calculated for the series of dimers constructed in *cis* and *trans* configurations. . . . . . . . . . . . . . . . . . . . . . 75

2.25 Intra-chain electron mobility calculated for the series of dimers constructed in *cis* and *trans* configurations. . . . . . . . . . . . . . . . . . . . . . . . . 76

3.1 General scheme of the route used to synthesize multiblock copolymers based on ATRAP fullerene chemistry. . . . . . . . . . . . . . . . . . . . . . 81

3.2 Synthetic route used to obtain 1,4-dibromomethyl-2,5-dialkoxyphenylene monomers. . . . . . . . . . . . . . . . . . . . . . . . . . . . . . . . . . 82

3.3 Lateral branches R used for monomers synthesis. . . . . . . . . . . . . . 83

3.4 $^1$H NMR signal used to evaluate the conversion during bromomethylation reaction. . . . . . . . . . . . . . . . . . . . . . . . . . . . . . . . . . . 84

3.5 Mechanism for bromomethylation reaction. . . . . . . . . . . . . . . . . . . . 85

3.6 Proposed mechanism for ATRAP polymerization. . . . . . . . . . . . . . . 88

3.7 Fractionation of the crude polymerization reaction. . . . . . . . . . . . . 90

3.8 Measured UV-VIS optical absorption for the synthesized macromolecules. 92

3.9 General structure of the synthesized polymeric materials. . . . . . . . . . 94

3.10 SEC-THF traces. . . . . . . . . . . . . . . . . . . . . . . . . . . . . . . . 95

3.11 UV-VIS spectra comparing HSS14 and HSS46 *n*-hexane soluble and insoluble phases. . . . . . . . . . . . . . . . . . . . . . . . . . . . . . . . . . 96

3.12 $^1$H spectra of the 5 different polymeric materials. . . . . . . . . . . . . . 98

3.13 $^1$H spectra of the *n*-hexane soluble phases. . . . . . . . . . . . . . . . . 98

3.14 $^{13}$C spectra of the *n*-hexane soluble phases and their corresponding insoluble phase materials. . . . . . . . . . . . . . . . . . . . . . . . . . . . . 99

3.15 2D $^1$H-$^{13}$C HMBC spectra for the tetra-adducts. . . . . . . . . . . . . . . 101

3.16 TGA/DTG studies for the set of materials. . . . . . . . . . . . . . . . . . 103

3.17 TGA/DTG curves for the precursors of HSS46. . . . . . . . . . . . . . . 104

3.18 DSC cycles for HSS46 showing no evidence of any thermal-activated transition in the 40-200 °C temperature range. . . . . . . . . . . . . . . . . . . 105

3.19 Simplified chemical structures studied as models for vibrations calculations. 106

3.20 Experimental and Calculated infrared spectra/transitions for HSS42, HSS45, HSS46 and $C_{60}$ model compounds. . . . . . . . . . . . . . . . . . . . . . . . 107

4.1 General structure of the synthesized polymeric materials. . . . . . . . . . 111

4.2 $JxV$ curvse for the OPV cells using different deposition methods. . . . . 113

4.3 OPV properties of cells using HSS46 as interlayer. . . . . . . . . . . . . . 114

4.4 $JxV$ curves for the OPV cells using different loads of HSS46 in the blend. 115

4.5 OPV properties of cells using HSS46 as acceptor material. . . . . . . . . 116

4.6 $JxV$ curves for the OPV cells using different loads of HSS46 in the blend. 117

4.7 OPV properties of cells using HSS46 as an additive to the blend. . . . . . 118

4.8 OPV properties of cells using different polyfullerenes as additives to the blend. . . . . . . . . . . . . . . . . . . . . . . . . . . . . . . . . . . . . 120

4.9 Evolution in time of $J_{SC}$ for the different synthesized polyfullerenes used as additives under thermal annealing. . . . . . . . . . . . . . . . . . . . . 121

4.10 Evolution in time of $V_{OC}$ for the different synthesized polyfullerenes used as additives under thermal annealing. . . . . . . . . . . . . . . . . . . . . 121

4.11 Evolution in time of FF for the different synthesized polyfullerenes used as additives under thermal annealing. . . . . . . . . . . . . . . . . . . . . 122

4.12 Evolution in time of PCE for the different synthesized polyfullerenes used as additives under thermal annealing. . . . . . . . . . . . . . . . . . . . . 122

4.13 Normalization of the Evolution in time of $J_{SC}$ for the different synthesized polyfullerenes used as additives under thermal annealing. . . . . . . . . . 123

4.14 Normalization of the Evolution in time of PCE for the different synthesized polyfullerenes used as additives under thermal annealing. . . . . . . . . . 123

5.1 UV-VIS spectra of THF and Toluene HSS46 solutions and film deposited over ITO by Doctor-blade technique. . . . . . . . . . . . . . . . . . . . . 128

5.2 Temporal evolution of UV-VIS spectra of HSS46 deposited on ITO/glass annealed at different temperatures. . . . . . . . . . . . . . . . . . . . . . 129

5.3 Gaussian fit of UV-VIS spectrum of pristine HSS46 in solid state. . . . . 131

5.4 Time evolution of $RR$ and $\Phi$ for films annealed at (a) 85 °C, (b) 140 °C and, (c) 200 °C. . . . . . . . . . . . . . . . . . . . . . . . . . . . . . . 132

5.5 AFM (a,c) height and (b,d) amplitude images of HSS46 on ITO/glass at $t = 0$. . . . 133
5.6 AFM (a) height, (b) amplitude and (c) 3D reconstruction images of HSS46 on ITO/glass annealed at 85 °C for 240 min. . . . 134
5.7 AFM (a,c) height, (b,d) amplitude and (e,f) 3D reconstruction images of HSS46 on ITO/glass annealed at 140 °C for 60 min. . . . 135
5.8 AFM (a) height, (b) amplitude and (c,d) 3D reconstruction images of HSS46 on ITO/glass annealed at 140 °C for 300 min. . . . 136
5.9 AFM (a) height, (b) amplitude and (c) 3D reconstruction images of HSS46 on ITO/glass annealed at 200 °C for 60 min. . . . 137
5.10 Time evolution of RMS for different annealing temperatures. . . . 137
5.11 Overview XPS spectrum of HSS46 deposited on ITO/glass. . . . 138
5.12 Carbon 1$s$ XPS peak for HSS46 polymer submitted under different annealing times. . . . 139
5.13 Temporal evolution of UV-VIS spectra of HSS46 deposited on ITO/glass illuminated under AM1.5 conditions in inert atmosphere. . . . 141
5.14 Carbon 1$s$ XPS peak for HSS46 polymer submitted under different irradiation times. . . . 142
5.15 Temporal evolution of the gaussian broadening of the core level transition, the first shake-up position and total contribution to the $C1s$ peak for increasing exposition times. . . . 142
5.16 Evolution of the UV-VIS spectra under photo-oxidation conditions. . . . 143
5.17 Evolution of the UV-VIS spectra under photo-oxidation conditions compared to the pristine sample. . . . 144
5.18 Carbon 1$s$ XPS peak for HSS46 polymer submitted under different irradiation times in SA atmosphere. . . . 145
5.19 Oxygen 1$s$ XPS peak for HSS46 polymer submitted under different irradiation times in SA atmosphere. . . . 145
5.20 Rate of photo-oxidation products formation analyzed by XPS. . . . 146

5.21 Temporal evolution of relative area and energy of the first carbon shake-up. 147
5.22 Time evolution of HSS46 FTIR spectra during photo-oxidation. . . . . . 148
5.23 Evolution in time of HSS46 FTIR spectra during photo-oxidation. . . . . 149
5.24 Decay and increasing rates for vanishing (a) and photo-oxidation products formation (b). . . . . . . . . . . . . . . . . . . . . . . . . . . . . . 149
5.25 Temporal evolution of the UV-VIS spectra for (a) BE1 and (b) BE2 with increasing annealing times. . . . . . . . . . . . . . . . . . . . . . . . . 152
5.26 3D reconstruction of the BE1 and BE2 nanomorphologies. . . . . . . . . 153
5.27 3D reconstruction of the BE1 and BE2 nanomorphologies annealed at 140 °C for increasing times. . . . . . . . . . . . . . . . . . . . . . . . . 154
5.28 Temporal evolution of roughness for BE1 and BE2 samples annealed at 140 °C under nitrogen atmosphere. . . . . . . . . . . . . . . . . . . . . . 155
5.29 Overview XPS spectra for BE1 and BE2 samples at $t = 0$. . . . . . . . . 155
5.30 Evolution in time of (a) BE1 and (b) BE2 UV-VIS spectra during photochemical degradation. . . . . . . . . . . . . . . . . . . . . . . . . . . 156
5.31 Evolution in time of BE1 and BE2 UV-VIS spectra during photochemical degradation. . . . . . . . . . . . . . . . . . . . . . . . . . . . . . . . 157
5.32 3D reconstruction of the BE1 and BE2 nanomorphologies illuminated in AM1.5 conditions under nitrogen atmosphere. . . . . . . . . . . . . . . . 157
5.33 Evolution in time of (a) BE1 and (b) BE2 UV-VIS spectra during photo-oxidation. . . . . . . . . . . . . . . . . . . . . . . . . . . . . . . . . 159
5.34 Evolution in time of BE1 and BE2 UV-VIS spectra during photo-oxidation. 160
5.35 Proposed depolymerization mechanism of ATRAP polymeric materials. . 162
5.36 Bond-dissociation reaction coordinate scan for the ATRAP proposed model material calculated by different level of theories. . . . . . . . . . . . . . 163
5.37 Modified ATRAP structures used to study the influence on stability of the -$CH_2$-link. . . . . . . . . . . . . . . . . . . . . . . . . . . . . . . . . 164
5.38 Chain propagation of the depolymerization reaction. . . . . . . . . . . . . 165

5.39 $^{1}$H-NMR spectra of HSS46 $d_8$-toluene solution heated to 100 °C for a 16h period time. . . . . . . . . . . . . . . . . . . . . . . . . . . . . . . 166
5.40 $^{1}$H-NMR spectra of HSS46 $d_8$-toluene solution heated to 100 °C for a 16h period time - zoom in the 3.5-5.0 ppm regions. . . . . . . . . . . . . . . . 167
5.41 $^{1}$H-NMR spectra of HSS46 $d_8$-toluene solution heated to 100 °C for a 16h period time - zoom in the aromatic regions. . . . . . . . . . . . . . . . . . 168
5.42 Two possible products of degradation being formed during thermal treatment. . . . . . . . . . . . . . . . . . . . . . . . . . . . . . . . . . . . 169
5.43 Molecular orbital diagram for the first photo-excitation of the comonomer depicted in the inset. . . . . . . . . . . . . . . . . . . . . . . . . . . . 170

6.1 General structure of polystyrene-based ligands. . . . . . . . . . . . . . . . . 176
6.2 Several proposed ligands based on polystyrene. . . . . . . . . . . . . . . . . 176
6.3 Optimized structure of $(ZnO)_{12}$ cluster. . . . . . . . . . . . . . . . . . . . . 177
6.4 Ligand 1 - $(ZnO)_{12}$ complex. . . . . . . . . . . . . . . . . . . . . . . . . 178
6.5 Ligand 2 - $(ZnO)_{12}$ complex. . . . . . . . . . . . . . . . . . . . . . . . . 179
6.6 Ligand 3 - $(ZnO)_{12}$ complex. . . . . . . . . . . . . . . . . . . . . . . . . 179
6.7 Ligand 4 - $(ZnO)_{12}$ complex. . . . . . . . . . . . . . . . . . . . . . . . . 180
6.8 Ligand 5 - $(ZnO)_{12}$ complex. . . . . . . . . . . . . . . . . . . . . . . . . 180
6.9 Ligand 6 - $(ZnO)_{12}$ complex. . . . . . . . . . . . . . . . . . . . . . . . . 180
6.10 Ligand 7 - $(ZnO)_{12}$ complex. . . . . . . . . . . . . . . . . . . . . . . . . 181
6.11 Ligand 8 - $(ZnO)_{12}$ complex. . . . . . . . . . . . . . . . . . . . . . . . . 181
6.12 Ligand 9 - $(ZnO)_{12}$ complex. . . . . . . . . . . . . . . . . . . . . . . . . 181
6.13 Ligand 10 - $(ZnO)_{12}$ complex. . . . . . . . . . . . . . . . . . . . . . . . 182
6.14 Ligand 11 - $(ZnO)_{12}$ complex. . . . . . . . . . . . . . . . . . . . . . . . 182
6.15 Chemical groups used in the discussion: aromatic-alkyl; aromatic-oxy-alkyl; and aromatic-alkyl-oxy-alkyl. . . . . . . . . . . . . . . . . . . . . . . . 184
6.16 Proposed chain-radical oxidation of the side-chain of MDMO-PPV . . . . 184

6.17 Comparison of the rates of photo-oxidation of polyethylene (PE) and poly(ethylene oxide) (PEO) as indicated by infra-red measurements of the concentration of carbonylated oxidation products. . . . . . . . . . . . . . . . . . . . . . . 185
6.18 Basic molecular structures used in this study. . . . . . . . . . . . . . . . . 186
6.19 Additional chemical structures used in this study. . . . . . . . . . . . . . . 186
6.20 Definition of the chord caused by the lateral strain. . . . . . . . . . . . . . 191
6.21 Relation between Pyramidalization angle and Inverse Radii. . . . . . . . 192
6.22 Relation between Pyramidalization angle and binding energy in epoxy formation. . . . . . . . . . . . . . . . . . . . . . . . . . . . . . . . . . . . . 193
6.23 Relation between Pyramidalization angle and binding energy of a singlet oxygen molecule. . . . . . . . . . . . . . . . . . . . . . . . . . . . . . . . . 194
6.24 Relation between Pyramidalization angle and binding energy of a hydroxyl radical. . . . . . . . . . . . . . . . . . . . . . . . . . . . . . . . . . . . . 195

7.1 General structure of circular hexabenzocoronenes. . . . . . . . . . . . . . . 198
7.2 Functionalized structure of circular hexabenzocoronenes. . . . . . . . . . 199
7.3 Supramolecular columnar organization of HBC-COOH-based molecules with a discotic liquid crystal behavior. . . . . . . . . . . . . . . . . . . . . 200
7.4 Oligo-3-propyloxy-thiophene with $n$ ranging from 1 to 10 units grafted to the HBC core. . . . . . . . . . . . . . . . . . . . . . . . . . . . . . . . . . 201
7.5 Evolution of the HOMO and LUMO energies of P3AOT with the increase of the chain length. . . . . . . . . . . . . . . . . . . . . . . . . . . . . . . 202
7.6 Evolution of the calculated UV-VIS absorption spectra of P3AOT with increasing chain length of P3AOT. . . . . . . . . . . . . . . . . . . . . . . 203
7.7 Evolution of the HOMO and LUMO energies of P3AOT with the increase of the chain length. . . . . . . . . . . . . . . . . . . . . . . . . . . . . . . 203
7.8 Evolution of the calculated UV-VIS absorption spectra with increasing chain length of HBC-COOH-P3AOT . . . . . . . . . . . . . . . . . . . . . 204
7.9 Molecular orbitals traces of the HBC-COOH-P3AOT ($n = 10$) molecule. 205
7.10 ZP46's molecular structure. . . . . . . . . . . . . . . . . . . . . . . . . . 206

7.11 Evolution of the HOMO and LUMO energies with the increase of the chain length for ZP46. . . . . . . . . . . . . . . . . . . . . . . . . . . . . . . . . 207
7.12 Evolution of the calculated UV-VIS absorption spectra with increasing chain length of ZP46. . . . . . . . . . . . . . . . . . . . . . . . . . . . . . . . 207
7.13 Evolution of the HOMO and LUMO energies with the increase of the chain length for HBC-COOH-ZP46. . . . . . . . . . . . . . . . . . . . . . . . . . 208
7.14 Evolution of the calculated UV-VIS absorption spectra with increasing chain length of HBC-COOH-ZP46. . . . . . . . . . . . . . . . . . . . . . . . 208
7.15 Molecular orbitals traces of the HBC-COOH-ZP46 ($n = 5$) molecule. . . 209

D.1 Structures moléculaires du (a) Poly(3-hexylthiophène) régio-régulaire, (b) $C_{60}$, (c) $PC_{60}BM$, (d) bis-$PC_{60}BM$, (e) $IC_{60}MA$ et (f) $IC_{60}BA$. . . . . . . 232
D.2 Structure générale des molécules synthétisées par la voie ATRAP. . . . . 233
D.3 Réaction de dépolymérisation avec propagation en chaîne. . . . . . . . . 233
D.4 Proposition de composés dérivés d'hexabenzocoronène. . . . . . . . . . . 234

E.1 Molekülstrukturen von (a) Poly (3-hexylthiophen), (b) $C_{60}$, (c) $PC_{60}BM$, (d) bis-$PC_{60}BM$, (e) $IC_{60}MA$ und (f) $IC_{60}BA$. . . . . . . . . . . . . . . . 236
E.2 Allgemeine Struktur der Moleküle, die durch die ATRAP Route synthetisiert 237
E.3 Depolymerisation Mechanismus durch Licht und / oder Wärme induzierter vorgeschlagen. . . . . . . . . . . . . . . . . . . . . . . . . . . . . . . . . 237
E.4 Neuer Donor-Akzeptor-Hybridmaterialien auf Basis von Hexabenzocoronen vorgeschlagen. . . . . . . . . . . . . . . . . . . . . . . . . . . . . . . 238

# List of Tables

3.1 Stoichiometry of the synthesized polymers. . . . . . . . . . . . . . . . . . . . 91
3.2 SEC-CB parameters against polystyrene standards. . . . . . . . . . . . . . 93

5.1 Relative elementary concentration from XPS spectra analyzed for increasing annealing times in BE1 and BE2 films. . . . . . . . . . . . . . . . . . . . 153
5.2 Relative elementary concentration analyzed for increasing irradiation times in BE1 and BE2 films. . . . . . . . . . . . . . . . . . . . . . . . . . . . 158

6.1 Calculated Binding Energy (kcal/mol) of the ligand-$(ZnO)_{12}$ complex. . . 177
6.2 Calculated values for EBD for models 1-6 within B3LYP/6-31G** level of theory. . . . . . . . . . . . . . . . . . . . . . . . . . . . . . . . . . . . . 187
6.3 Calculated thermodynamic stabilities of the macroradicals 2-6 formed following the hydrogen abstraction within B3LYP/6-31G** level of theory. . 188
6.4 Calculated bond dissociation energies ($E_{BD}$) within the B3LYP/6-31G** level of theory. . . . . . . . . . . . . . . . . . . . . . . . . . . . . . . . 189

# List of Abbreviations

$C_{60}$ - *buckminster* fullerene

$C_{70}$ - Higher fullerene molecule with 70 carbon atoms

P$C_{60}$BM - Phenyl-$C_{61}$-butyric acid methyl ester

bis-P$C_{60}$BM - Phenyl-$C_{61}$-butyric acid methyl ester attacked twice

I$C_{60}$MA - $[1', 4']$-dihydro-naphtho$[2', 3' : 1, 2][5, 6]$fullerene-$C_{60}$

I$C_{60}$BA - $1', 1'', 4', 4''-$tetrahydro-di$[1, 4]$methanonaphthaleno$[1, 2 : 2', 3', 56, 60 : 2'', 3''][5, 6]$-fullerene-$C_{60}$

AFM - Atomic Force Microscopy

ATRAP - Atom Transfer Radical Addition Polymerization

ATRP - Atom Transfer Radical Polymerization

BHJ - Bulk-heterojunction

B3LYP - 3-parameters exchange (Becke) and correlation (Lee, Yang and Parr) functional

def2-TZVPP - Karlshuhe's triple-$\zeta$ gaussian basis set with polarization functions for all atoms and hydrogen

DFT - Density Functional Theory

EA - Electronic Affinity

ECP - Equipe de Chimie-Physique

EKUT - Eberhard-Karls Tübingen Universität

EPCP - Equipe de Physique et Chimie des Polymères

ESTABLIS - Ensuring Stability in Organic Solar Cells

FTIR - Fourier-Transform Infrared Spectroscopy

FWHM - Full-width at the half-maximum

HF - Hartree-Fock method

HF-3C - Stefan Grimme's corrected Hartree-Fock method with three parameters (basis superposition, geometry distortions and van der Waals interactions)

HOMO - Highest Occupied Molecular Orbital

IP - Ionization Potential

IPREM - Institut des Sciences Analytiques et de Physico-Chimie pour l'Environnement et les Matériaux

LUMO - Lowest Unoccupied Molecular Orbital

MO - Molecular Orbital

MP2 - 2nd order Møller-Plesset Perturbation Theory

NMP - Nitroxi-mediated Polymerization

NMR - Nuclear Magnetic Ressonance

OM - Optical Microscopy

OPV - Organic Photovoltaics

PL - Photoluminescence

PM7 - Parametric Method 7

P3HT - poly(3-hexylthiophene)

RI - Resolution of the Identity method

RIJCOSX - method

$RR$ - Resonant Ratio

$TiO_x$ - Titanium Oxide

UPPA - Université de Pau et des Pays de l'Adour

UPS - Ultraviolet Photoelectron Spectroscopy

UV-VIS - Ultraviolet-visible optical absorption

XPS - X-ray Photoelectron Spectroscopy

ZnO - Zinc Oxide

$\eta$ - hardness

$\lambda$ - reorganization energy

$\mu$ - electrophilicity

$\Phi$ - Differential total flux of absorption spectra

$\xi$ - electron mobility

6-31G - Pople's double-$\zeta$ gaussian basis set

6-311G - Pople's triple-$\zeta$ gaussian basis set

6-31G* - Pople's double-$\zeta$ gaussian basis set with polarization functions for all atoms except hydrogen

6-311G* - Pople's triple-$\zeta$ gaussian basis set with polarization functions for all atoms except hydrogen

6-31G* - Pople's double-$\zeta$ gaussian basis set with polarization functions for all atoms and hydrogen

6-311G* - Pople's triple-$\zeta$ gaussian basis set with polarization functions for all atoms and hydrogen

# Preamble

This thesis is a part of the European Project ESTABLIS. This project has been created with the aim to provide different approaches to avoid organic solar cells performance loss caused by degradation over an extended period of time, see 10 to 15 years. This might only be accessible by a very general approach in which experimental and theoretical power is used to tune synthesis of new materials, morphological properties, device architecture, and the comprehension of how these factors contribute to the degradation kinetics of materials and devices.

This thesis is a cotutelle between the Université de Pau et des Pays de l'Adour, in France, and Eberhard Karls Universität Tübingen, in Germany. The time division of this thesis followed a division consisted of 33% of Molecular Modeling, 33% of Synthetic work and 33% of Spectroscopic and Degradation studies.

This thesis has received funding from European Union Seventh Framework Program (FP7/2011) under grant agreement no. 290022.

Some parts of this thesis have already been published. This is the case of sections 6.2 and 7.2. Other parts are being considered for publication. This is the case of subsection 2.4.1, chapters 3, 4 and 5, and sections 6.3 and 7.3. The reference of what has already been published is given in the appropriate section.

# Chapter 1

# Introduction on Stability of Organic Photovoltaic Devices

*This thesis is dedicated to the problematic of stability of the electron acceptor materials in Organic Photovoltaic Devices (OPVs). This is treated by a theoretical approach comparing some of the most potential polymerization routes for* $C_{60}$*-based molecules (depicted in Figure 1.1), thus creating what is called Polyfullerenes. The relevant properties that arise from these routes are studied and one of them is chosen to an experimental study on these materials, namely the atom transfer radical addition polymerization route (ATRAP). Thus, this document is divided in the following chapters: 1 - Introduction on the stability of OPVs and how polymeric structures of fullerene might help; 2 - Design and modeling of functional structures; 3 - Synthetic work, mechanisms and physical-chemical characterization; 4 - Photovoltaic performance; 5 - Materials' degradation studies; 6 - Stabilization models and routes; 7 - Alternative acceptor materials; 8 - Conclusions and future work.*

The hypotheses that motivated this thesis are the following:

A - Polymerization of $C_{60}$ molecules might prevent aggregation, phase segregation and morphological performance loss in organic photovoltaic devices;

B - Polymerized $C_{60}$s might be more stable against photo-oxidation than isolated fullerene molecules based on the steric protection over the sphere;

C - Comonomer engineering might allow one to protect $C_{60}$ in bulk and to increase performance by light-induced electronic sensitization;

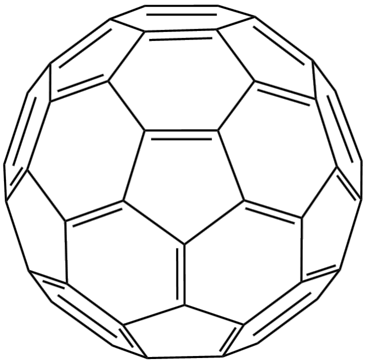

**Figure 1.1:** Molecular structure of $C_{60}$ molecule. Although pentagons are not aromatic in fullerene, we highlight that this is a simple 2D-representation.

D - Side-chain engineering might allow one to increase stability based on the theoretical analysis of the mechanism of degradation;

E - Stability might also be increased by different approaches, such as interlayer engineering and analysis of conformational properties of the blends in devices.

The critical advantage of either organic small molecules or polymers which display photovoltaic properties over their inorganic counterparts are their low-temperature processing, for the former, and processing from solution for the latter. This allows one either to deposit these organic materials on substrates over which the inorganic cannot cover, based on the incompatibility of the required temperature. Moreover, the fact that OPV can be semi-transparent gives them another advantage over the inorganic counterparts. Thus, flexible, light and/or portable solar modules could be envisaged and potential applications can already be found in the market. Not only these modules can be used in such *gadget* concept, but also they can be employed in *built-in* concepts, such as for buildings and smart windows.[1]

The Organic Photovoltaics (OPV) industry relies on the ”magic triangle”,[1] in which vertices one can find the **efficiency**, **cost** and **lifetime** of a module. The meaning of these concepts will be explored in the following pages.

## 1.1 Organic Photovoltaic Structures and Materials

The photovoltaic effect is based on a junction of two major types of semiconductors: $p$ and $n$ types. The former consists of an electron-poor and the latter an electron-rich layer. They are obtained by extrinsic or intrinsic doping for the case of inorganic materials. For organic ones, these differences are obtained by means of the electronic structure of the arrangement of carbon and heteroatoms on the molecular level, which leads to different acceptor ($n$-type - A) or donor ($p$-type - D) characteristics for each molecule. Hence, this is achieved without any doping and the species are locally and globally neutral, most of the time.[2]

The desired semiconductor character of these materials is assured by the Peierls distortion mechanism, which creates the energy gaps necessary for UV-VIS light absorption.[3] Then, under illumination, following a $\pi \rightarrow \pi^*$ transition, neutral excitons can be formed either in one or both materials. If one has a large enough energy offset between the lowest unoccupied molecular orbital (LUMO) of the $p$-type material and the LUMO of the $n$-type one, the exciton will dissociate via an *ultrafast electron transfer*[4, 5][1] into long-lived charged species called polarons (namely, an electron on the $n$-type molecule and a hole on the $p$-type one). The same process can happen when the HOMO (highest occupied molecular orbital) offsets are large enough as well. These photoactive heterojunctions can lead to a diode-like behavior in current-voltage characteristics and to the photovoltaic effect. Efficiencies of energy conversion up to 10% have been reported for such structures.[7, 8, 9, 10][2][3] The Figure 1.2 shows schematically how this process can take place.

The level diagram depicted in this figure stands for a so-called "normal" device architecture, for which the $p$-type material (donor) is in direct contact with the cathode, generally an Aluminum/Calcium layer, whereas the anode is a transparent conductive oxide, such as indium-tin oxide (ITO) or fluor-tin oxide (FTO). A photon is absorbed by HOMO electrons of the donor material. A electron is then promoted to the LUMO level and then can be transfered to the same level of the acceptor molecule.

The most currently used OPV architectures are based on a layout called "inverse", in which this oxide becomes the anode and it allows the use of lower work functions ($\Phi$) materials, which are more resistant against oxidation, such as silver or gold. A very good and in-deep review on this approach can be found in ref. [11] by Bernard Kippelen and Jean-Luc Brédas. In this case, $\epsilon_{DA}$ stands for the energy offset need for the dissociation

---

[1] The ultrafast electron transfer was the basis of the development of BHJ field of research.[6] This was first discovered after the observations that the luminescence of a conjugated polymer is heavily quenched by the addition of fullerenes, which suggests that the electron transfer must occur on a time scale significantly faster than the decay time of the photoluminescence (on the order of ps).

[2] And the references therein.

[3] The barrier of 10% represents the minimum efficiency with which OPVs can be scaled up in industry.

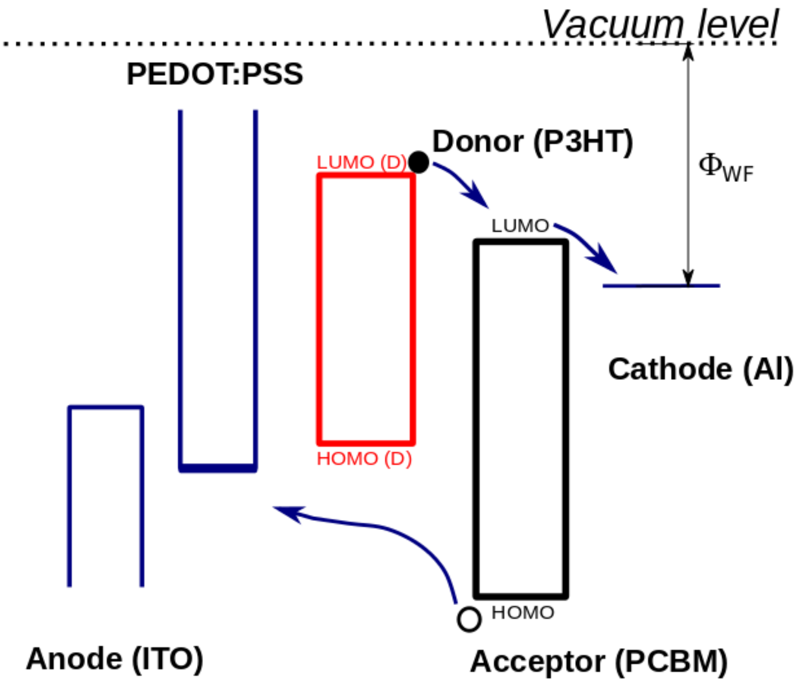

**Figure 1.2:** Level diagram of a photovoltaic $p - n$ junction.

of the exciton, whereas V$_{OC}$ stands for the Open-circuit voltage. Filled spheres depict electrons and hollow ones depict holes.

In practice, this effect can be achieved by using thin films of blended conjugated polymers and fullerene derivatives as electron donor and acceptor, respectively.[6, 11] This is known as D-A bulk heterojunction (BHJ) and it is of paramount importance to control the surface contact area between the two types of molecules in order to have the maximum of excitons efficiently dissociated into electrons and holes.[6] Figure 1.3 shows how one can achieve the heterojunctions needed for the photovoltaic effect.

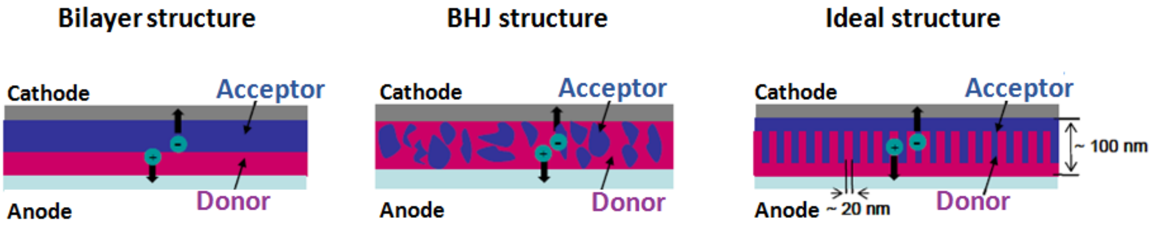

**Figure 1.3:** Possible general ways of making the donor-acceptor junction in a photovoltaic cell, regardless of its architecture.

The first assembling methodology is a bilayer based on classical inorganic $p - n$ junctions and offers the lowest contact surface between the materials but it has been mostly used for materials deposited by evaporation of small molecules. Moreover, this assembling presents the problem of thickness of the layers: for a sufficient light absorption, one needs a thick layer, but it leads to a small exciton diffusion. This motivated the appearance of the second type, the BHJ structure itself, in which the junction is created by the physical mixture between the two semiconductors. The acceptor should display a contact surface with the donor molecule as high as possible, keeping a structure called percolation path, through which the electrons should travel to the electrode.[6, 11]

It is known from literature that the exciton diffusion radius is about 10 nm. It means that the exciton can diffuse within the BHJ and it should find a donor-acceptor interface in a radius of $\sim$ 10-20 nm, before recombination occurs.[6, 12, 13, 14] The most efficient way of maximizing both the interface between these materials and obeying this constraint is tailoring structures such as the third one, termed ideal.[15] This structure is based on the interdigitation of both semiconductor materials.

The electron acceptor is one of the most important constituents of an OPV responsible for driving up the obtained yields. It must display properties such as poor electron density, high mobility and appreciable solubility in the *p*-type material matrix, besides not displaying charge-trap behavior as cations would have, for instance. Fullerenes have been the first choice in this class and this is mostly due to the fact that they can easily accept up to 6 electrons under mild conditions.[16] These strong electron acceptor properties can be explained from the three-dimensional generalization of the Hückel's rule.[17, 18] It states that a fullerene is completely aromatic when there are $2(N+1)^2$ $\pi$-electrons, where $N$ is the number of atoms in the conjugated network. This is a result from the fact that an aromatic fullerene must have an icosahedral (or other appropriate) symmetry in order to be a closed-shell configuration. So, fullerene would need 72 electrons to have a closed-shell configuration, from where its acceptor properties can be deducted.[19]

An in-deep and very clear review on the characterization of OPVs and the parameters used to quantification can be found in ref. [6]. This will be not be treated here since this is not exactly the scope of this thesis. Whenever we refer to such parameters, we refer the reader to this paper.

## 1.2 Degradation of Photovoltaic Devices: Intrinsic and Extrinsic Mechanisms (Photochemical and Morphological)

It is a rational sense that the OPV's future as a widespread and not only a niche technology will depend on their economic potential, which depends on the efficiency, manufacturing cost, weight, scalability, sustainability and, mainly, lifetime.[1, 20]

When speaking about lifetime, one first thinks about photo-oxidation and how the materials are encapsulated.[21] An encapsulating barrier is needed in order to protect the active layer materials against photo-oxidative reactions induced by molecular oxygen and/or moisture.[22] Such molecules, by action of light, can induce extrinsic doping, hydrogen abstraction, lose of conjugation, etc., hindering the photovoltaic effect of the bulk. Of course, with appropriate packaging, the materials can operate for longer, although enormously increasing manufacturing prices.[21] However, even in a situation without such oxidizer molecules, light can induce photolysis and reorganization reactions, which can also hinder performance. Moreover, the temperature to which modules are exposed during production of operation can also induce conformational changes within the active layer, which are responsible for photovoltaic performance loss. Before explaining further this effect, Figure 1.4 schematically illustrates the possible OPV failure mechanisms.

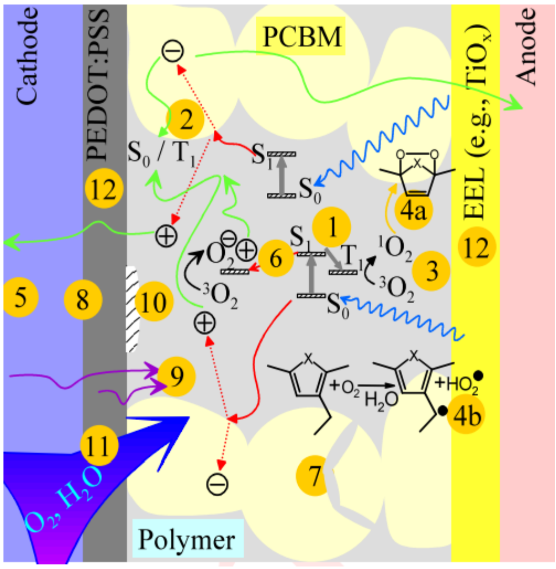

**Figure 1.4:** OPV cross section view with some of the possible degradation processes. Specially, we highlight the photo-chemical reactions induced by the presence of oxygen and moisture under irradiation. The processes taking place are: 1 - triplet formation; 2 - triplet formation from charge-transfer complex; 3 - singlet oxygen production; 4 - oxidation of polymer; 5 - oxidation of electrodes; 6 - light assisted doping by $O_2$; 7 - morphological changes; 8 - inter-layer reaction; 9 - diffusion of metal ions; 10 - delamination; 11 - diffusion of $H_2O$ and $O_2$; and 12 - poor conductivity. Adapted from Hans-Joachim Egelhaaf.

The photo-oxidation or photochemical reactions are not the sole factor able to hinder OPV performance: morphological failure concerning the interface between the donor and the acceptor must also be focus of attention. This is normally the case when the fullerene derivative, for instance, migrates through the *p*-type matrix, aggregating in clusters and causing a phase segregation.[23, 14, 24] This is most of the time accompanied by a crystallization of the *p*-type material as well. Even if this crystallization phenomenon may be beneficial for the charge mobility, the extracted current decreases considerably in the device, due to the reduced contact interface. One has also to keep in mind that some extent of aggregation is needed to guarantee percolation. Figure 1.5 presents an example for this type of degradation based on SEM[4] measurements of P3HT/PC$_{60}$BM[5] polymer blends[6] for different temperatures.

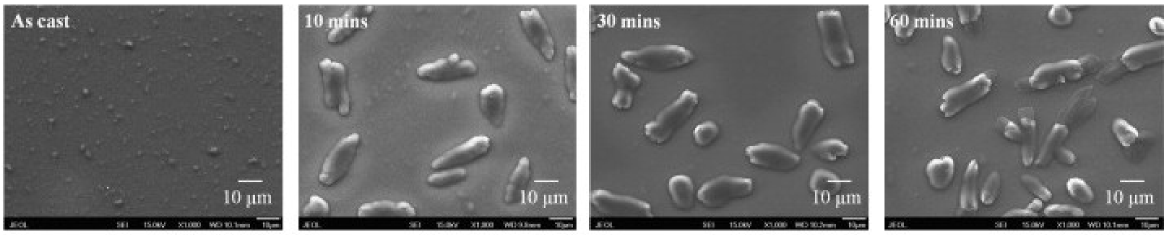

**Figure 1.5:** SEM images (1000x) of a P3HT:PC$_{60}$BM spun-cast over silicon substrates using ODCB as solvent, with variation of the time of annealing at T=150 °C. It becomes evident that the PC$_{60}$BM domains rapidly grow in size for these films. Reproduced from ref. [25]

In these images, one can clearly see the formation of micrometer-sized fullerene clusters. This is an evidence of the phase segregation undergone by the active matrix. Although the molecules are chemically unchanged, the optimal morphology needed for the photovoltaic effect is lost.[26] This concerns a stage in the crystallization of both the components where the charge transfer at interfaces are reduced. To circumvent this, fine tuning of the morphology has been achieved by using process additives[27, 28] which do have a preference in solubilizing more (or less) a component than the other. Despite of encouraging results obtained so far, no one has demonstrated an actual method to control the nanomorphology over time.[6]

Afterwards, the degradation can also start in several other parts of the cell: at the electrodes (metal oxidation, diffusion into the bulk, ...),[29] at the hole-extraction layer (delamination between the PEDOT:PSS[7] and active layers),[30] at the electron-extraction layer (delamination between oxide and active layers, loss of conductivity, local electron traps, ...).[31, 32]

---

[4] Scanning Electron Microscopy

[5] This stands for Poly(3-hexylthiophene) and Phenyl-C$_{61}$-butyric acid methyl ester. More details can be found in Chapter 2.

[6] Although literature treat this mixture of materials as a blend this is not strictly the case. Blends are mixtures of polymers whereas here one has what is called a *composite*, since PC$_{60}$BM is not a polymer. We use the terminology *blend* for the sake of simplicity.

[7] PEDOT stands for Poly(3,4-ethylenedioxythiophene) and PSS stands for Polystyrene sulfonate.

Alan J. Heeger, in his last review on the field, [6] identified, concisely, that to be economically efficient, OPV cells should overcome these limitations and demonstrate lifetimes of several years and yields around 20%.[8] Even more, to reach this goal of economic efficiency, other features should also be present, such as: 1 - band gap of *p*-type material accordingly to an optical absorption up to 1000 nm with a broad absorption spectrum to capture the maximum quantity of solar photons; and 2 - Increased mobility of the BHJ nanomorphology, ideally based on a column-like structure as presented in Figure 1.3, to enable collection of charges prior to recombination.

Such scenario describes a complex problem with several variables to be optimized at the same time. This thesis tries to contribute on this problem taking two general approaches:

1 - Investigate and design *n*-type materials that are more stable against photo-oxidative stress;

2 - Design materials which are stable against thermal stress.

For approach 1, both *p*- and *n*-type materials are concerned, since both of them are victims of the performance loss induced by photochemical reactions. Once it is done, one can try to generalize the results to apply them to the *p*-type materials as well. On the other hand, approach 2 is much more dependent on the *n*-type materials and on its solubility in the donor matrix, keeping at the same time a supramolecular structure with a percolation path for the electrons towards the cathode.

Throughout the chapters, the specific actions needed to accomplish each approach are further explained and detailed. Particularly, in Chapter 5, some of these degradation mechanisms are studied with more details. We should first start discussing the fullerene-containing polymers as an option for both approaches.

---

[8] This value is very debatable. Some authors[33, 34] state that a value around 10% would be enough. What should settle this value down is the life-time and production costs of the cell.

## 1.3 An overview on fullerene-containing polymers

Since their discovery in 1985[35] and their multigram availability from 1990s,[36, 37, 38] fullerenes became a source of new potential materials for innumerous applications and which chemistry, although tricky, may allow chemists to imagine new functionalities. These derivatives showed outstanding properties such as structural,[39] magnetic,[40] superconducting,[41] electrochemical,[42] and photophysical.[43, 44]

Fullerene-containing polymers have also been synthesized promptly after their discovery. Indeed, the first reported polyfullerene compound has been done by Olah *et al.*[45], who reacted a $C_{60}$/ $C_{70}$ mixture with polystyrene (PS) in a Friedels-Crafts reaction using $AlCl_3$ as catalyst. Several polyfullerenes have been employed since, having their place in electroluminescent, non-volatile flash memories and photovoltaic devices, which is one of their most realist applications.

They can be classified according to their chemical structure and how fullerenes are incorporated into the polymeric chain. Figure 1.6 presents a schematic family classification for these materials as it can be found in the book by Martín and Giacalone.[46]

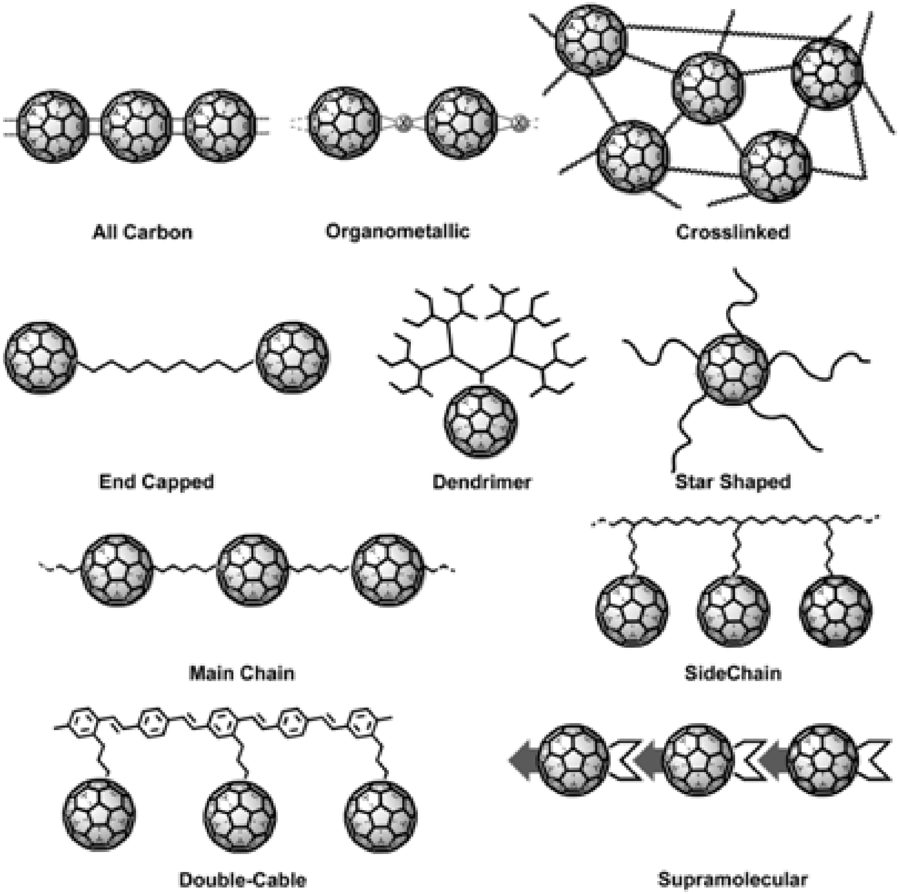

**Figure 1.6:** Family classification of the different polyfullerenes. Reproduced from ref. [46]

All-carbon, organometallic and cross-linked polyfullerenes are the easiest materials to produce. They are issued from straightforward chemical reactions and the degree of control over the structure is almost non-existing. End-capped, dendrimer and star-shaped materials request a slightly higher degree of control and this is generally obtained by steric hindrance instead of chemical selectiveness. Main-chain, side-chain, double-cable and supramolecular ones are those who needs the highest control on the synthetic steps in order to obtain materials that can have successfully fullerenes incorporated, not only sparse molecules distributed on the chain. It is a consensus that the most challenging routes are those of main and side chain polymers, which the synthetic control needed slowed their development down over the last years. The synthetic strategies normally used to achieve these materials are displayed in Figure 1.7 and Figure 1.8.

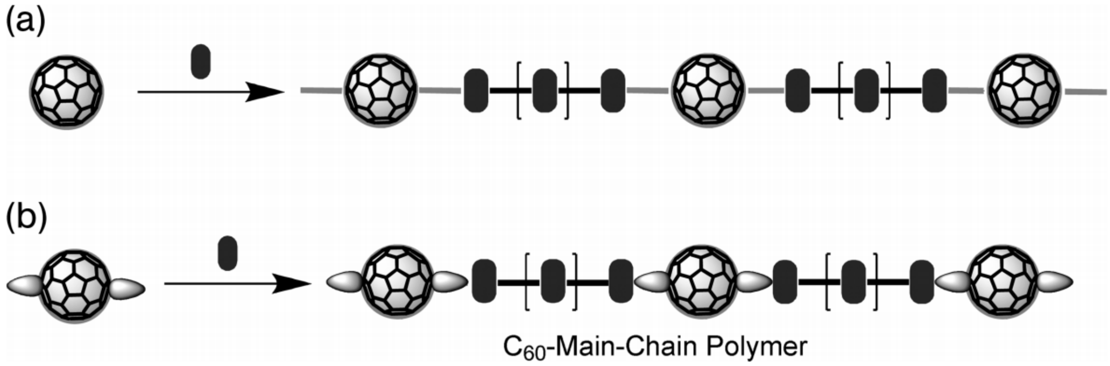

**Figure 1.7:** Synthetic strategies for the synthesis of fullerene main-chain polymers. In (a), a direct reaction between fullerene and a symmetrically difunctionalized monomer takes place whereas in (b) the reaction follows a polycondensation between a bisadduct of fullerene and a difunctionalized monomer. Reproduced from ref. [46]

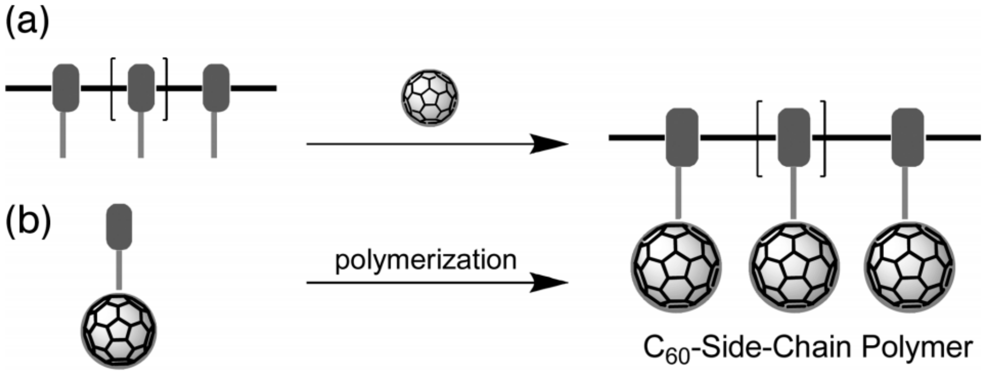

**Figure 1.8:** Synthetic strategies for the synthesis of fullerene side-chain polymers. In (a), a direct reaction between a polymer bearing functional groups that attach to fullerenes and in (b), a monomer-functionalized fullerene is polymerized to yield fullerene side-chain polymers. Reproduced from ref. [46]

In this thesis, we will concentrate on the development of main-chain polyfullerenes and a proper description of the other classes can be found in ref [46]. In this family of $C_{60}$[9]

---

[9] Polymers of higher fullerenes can also be synthesized, but two major impediments oppose to this:

materials, the fullerenes are located in the backbone of the polymer. Their synthesis has been achieved by direct reaction between $C_{60}$ and a symmetrically bisfunctional monomer or a polycondensation between a $C_{60}$ bis-adduct and a bisfunctional monomer. Although the latter has been the most employed in the literature, we will treat in this thesis, mainly the materials issued from the former. This is due since it can be a done as an one-pot reaction and be more easily scalable to industrial scale.

Due to the low control of the double-addition over the sphere, up to 8 stereoisomer multi-adducts are obtained as mixture,[47] which can be hardly separated. This fact is not particularly a drawback in material chemistry, but any addition on the fullerene opens at least one of the thirty 6,6 double bonds, inducing a considerable change in the electronic properties, mainly on its electron acceptor performance. $C_{60}$-polymers which electronic properties are well-defined must contain an identical number of attacks for all the fullerenes, and for the case of multi-adducts, they must be identically distributed over the sphere. Moreover, the formation of crosslinking products is also possible and probable and avoiding this has showed to be a considerable chemical effort, as described in [46].

From the first strategy of polyfullerenes synthesis, very few examples can be found in literature. The most remarkable are the production of water soluble poly(fullerocyclodextrin)s, prepared by Geckeler *et al.*[48] by reacting $\beta$-clyclodextrin-bis-amino complexes directly with $C_{60}$, as it is depicted in Figure 1.9. These materials showed good solubility in water, over 10 mg/mL, and an excellent DNA-cleaving activity. The other interesting example is the thermoreversible main-chain polyfullerene obtained from the reaction between $C_{60}$ and with a bis-anthracene derivative in a Diels-Alder cycloaddition strategy. Upon temperatures comprising 60-75 °C, the polymer converts back to the reagents and this process can be repeated several times without any decomposition.

Radical copolymerizations of fullerenes are also issued from this approach of direct reaction of monomers and $C_{60}$ and they are going to be studied in more details in the next section.

---

1 - the fact that the carbon atoms do not have the same chemical environmental, *i.e.* they are not equivalent, as it is the case of $C_{60}$ and; 2 - the non-availability of multigram quantities in affordable price.

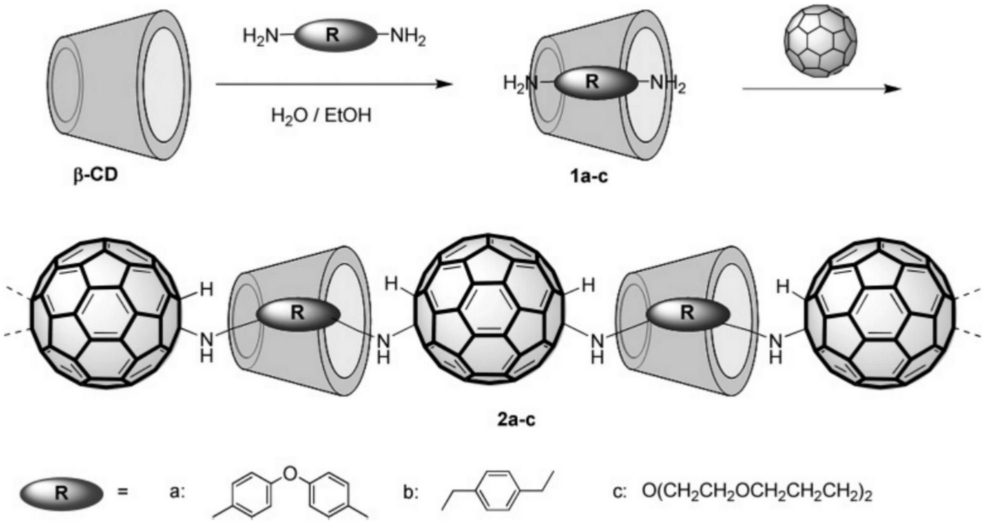

**Figure 1.9:** Synthesis of main-chain polymers with DNA-cleaving activity, as reported by Geckeler*et al.*[48] Reproduced from ref. [46]

## 1.4 Controlled radical copolymerization of fullerenes

Not only controlling the number of stereoisomers and the degree of crosslinking of the so-obtained polymer, in order to have materials with well-defined electronic properties, it is essential to control the molar mass of the polymer and keep its dispersity as low as possible. The polymerization routes able to do so are namely the anionic and "controlled" radical polymerizations, which give the best control over the chain length and produce polymers with the lowest dispersities. The most representative class of materials using this type of radical additions is the star-shaped polyfullerenes obtained by grafting of linear polystyrene chains onto $C_{60}$.[49, 50, 51, 52] The same can be obtained with nucleophilic additions under different conditions though. The general scheme of this strategy is depicted in Figure 1.10.

This type of chemistry was only possible thanks to the progress in the last decade in radical polymerizations. In fact, the various "controlled radical polymerizations" such as nitroxide-mediated polymerization (NMP)[53] and atom transfer radical polymerization (ATRP)[54] allow one to synthesize high-length chains and with low dispersity. The first reports in literature on this chemistry using NMP route confirms that an even number of polymer chains are added to fullerene and these materials displayed interesting micellization behavior in THF solutions, where $C_{60}$ is insoluble.[55, 56] These di-adducts aggregate even in dilute solution to form micelles containing up to 20 molecules.[57] Figure 1.11 displays a synthetic protocol to achieve di-adduct $(PS)_2C_{60}$ using NMP route.

Another alternative is using atom transfer radical addition (ATRA) to graft macroradicals on $C_{60}$ and two polymer materials outstand in literature: ATRP-prepared PMMA[10]

---

[10] Poly(methylmetacrilate)

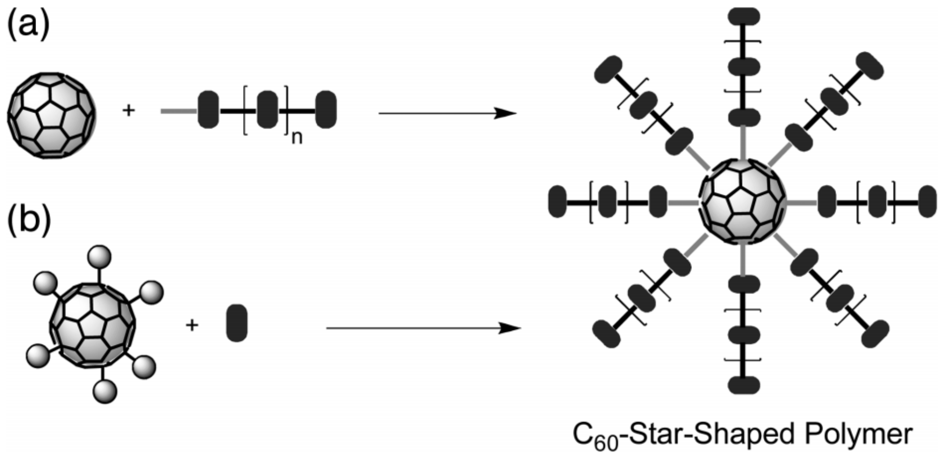

**Figure 1.10:** Synthetic strategies for the synthesis of fullerene star-shaped polymers. In (a), a direct reaction between a polymer bearing end-chain functional groups that attach to fullerenes and in (b), a functionalized fullerene is reacted with difunctional monomers in a polymerization reaction to yield fullerene star-shaped polymers. Reproduced from ref. [46]

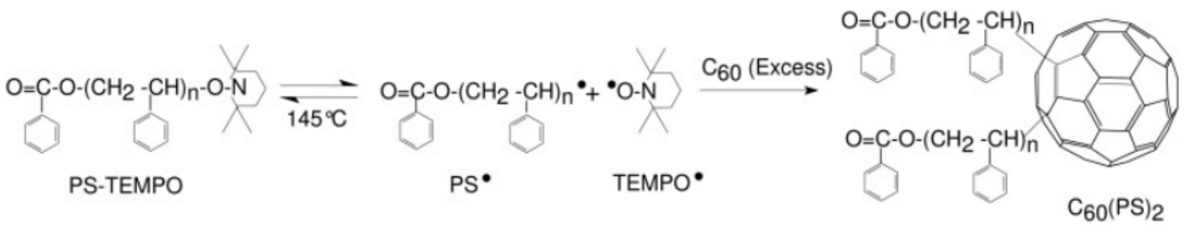

**Figure 1.11:** Synthesis of $(PS)_2C_{60}$ di-adducts using an NMP route. TEMPO stands for 2,2,6,6-tetramethylpiperidine-N-oxyl intermediate. Reproduced from ref. [46]

and PS, which were further reacted with $C_{60}$ under the presence of Cu(I)Br and 2,2'-bipyridine in chlorobenzene at 100 °C.[58] Under these conditions, the covalent C-Br chain-end bond of the polymer is in equilibrium with the free radical form (see Figure 1.13). This macroradical adds to the sphere and a Br is located on the same hexagon over the fullerene. Size-exclusion chromatography in THF confirms an increase of molar mass of around 1000 g/mol. However, under these experimental conditions, $C_{60}$ normally displays lower molar mass than toluene, as one can see in Figure 1.12.[59]

This fact led some authors to reject the fact that this mass increase could be due to the grafting of a fullerene molecule to the polymeric chain. Nevertheless, we believe that fullerene can indeed be incorporated and its derivatives should have a detected mass closer to the real rather than what happens to the pristine molecule itself. This must be due to the completely different THF-solubility behavior of fullerene when it is in its pristine phase or incorporated/reacted with anything else.[60, 51]

One year later, using monodisperse PS samples,[50] it has been proved that there is no bromine atom bonded to fullerene on the final material and only an even number of polymeric chains are added to $C_{60}$ even if it is in a concentration 10-fold related to the polymeric reagent. This is easily explained since a fullerene-Br bond should be much

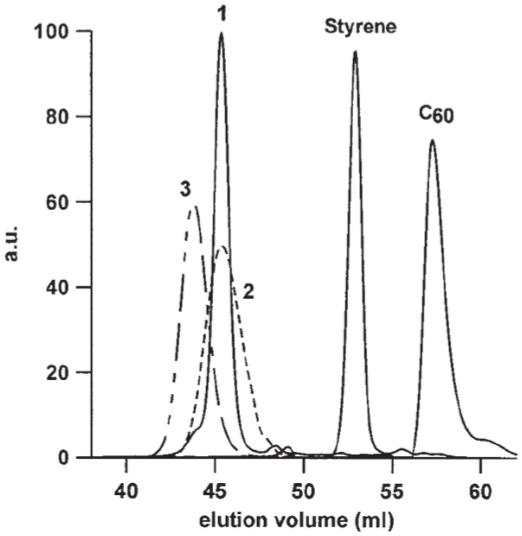

**Figure 1.12:** Comparison between the elution volumes of $C_{60}$; styrene; (1-phenylethyl)$_x C_{60}$ ($x \geq 6$) (1); polystyrene ($M_w = 600D$) (2); and polystyrene ($M_w = 1300D$) (3). Reproduced from ref. [59]

less stable than a C-Br one in the polymeric chain. Then, the former is easily converted into the radical form (PS-Br).[51] This mechanism is perturbed if the solvent system is halogenated, indicated by a non-negligible number of mono-adducts in chlorobenzene compared to toluene. This route is schematically depicted in Figure 1.13.

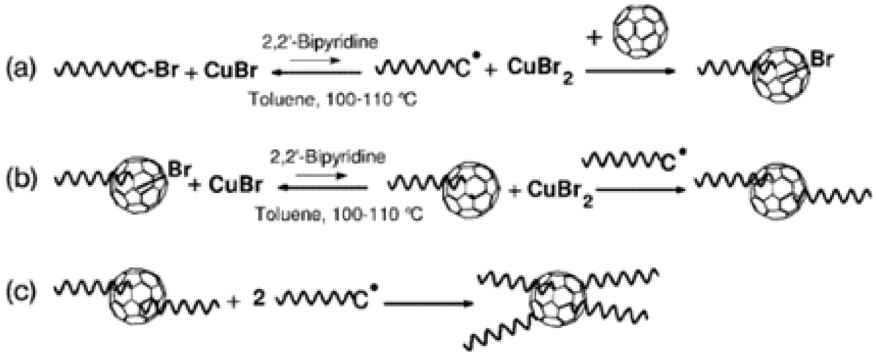

**Figure 1.13:** Formation of fullerene radical-attacked polymer chains. Reproduced from ref. [46]

It is important to stress that these experiments allowed one to define that, for each pair, the chains are attached at 1,4 positions on the same hexagon. Moreover, only one double bond is opened on the $C_{60}$ core of a di-adduct $(PS)_2C_{60}$, for example, thereby keeping the electronic structure minimally perturbed.

If one takes the size of the macroradical to a simple molecule and assures that it is bis-functional, main-chain polyfullerenes can be obtained driven by the same mechanism. This approach can also produce theoretically only one type of structure, without an isomeric mixture, favoring the synthesis of materials with well-defined electronic properties. This is only true since it is consisted of only two attacks on the fullerene sphere and both attacks happen on the same hexagon, instead of taking place in different sites on the molecule. This strategy was adapted and explored by Hiorns *et al.*[61, 62] and they proposed structures of the type poly(1,4-$C_{60}$-*alt*-1,4-bismethylene-2,5-dialkoxyphenylene), as the one depicted in Figure 1.14. This class of molecules will be explored in further details in Chapter 3 of this thesis.

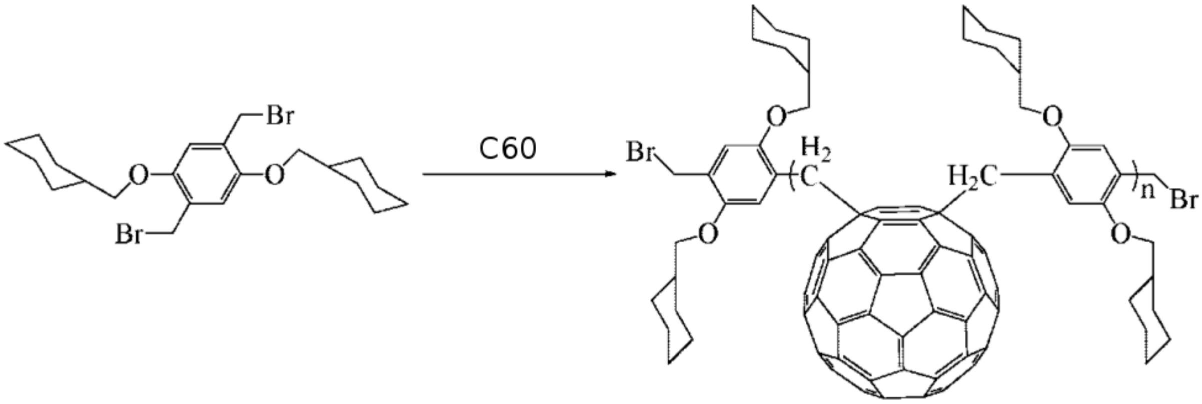

**Figure 1.14:** Poly(1,4-$C_{60}$-*alt*-1,4-bismethylene-2,5-dialkoxyphenylene) derivative synthesized by Hiorns *et al.*[61, 62]. Reproduced from ref. [61]

## 1.5 Fullerene polymer derivatives and their proposal as more stable acceptor materials

As we have seen, the BHJ is a solid mixture and its nanostructure morphology is formed by spontaneous phase separation: the donor and acceptor components self-assemble to form bi-continuous inter-penetrating networks (Figure 1.3). This process is correlated to the fact that high polymers tend to phase separate because of the "like likes like" behavior, besides the small entropy of mixing. Still, one knows that crystallinity drives strongly the phase separation.[33]

Annealing at high temperatures is responsible for improving the crystallinity within the donor and acceptor networks. This makes the charge transport to the electrodes easier and hence the power conversion efficiency can be increased. Other parameters known to control the BHJ morphology are: i) the solvent from which the BHJ is cast, ii) the ratio between the *p*- and *n*-type materials, iii) chemical additives, iv) concentration of the solution, v) solvent annealing and, vi) molecular structure of the materials, which is the driving force of the solubility in organic solvents and the miscibilities of the components of the blend.

We also know that the crystallization should be **optimal** in order to not decrease the contact interface between the donor and the acceptor. Normally, under operational conditions, the OPV cells should be exposed to heating and this can drive the phase segregation of these materials over the optimal point. Controlling this feature of thermal stability is then a key-parameter to control the OPV efficiencies and lifetimes.

One way of inducing crystallization and avoiding the phase segregation phenomenon is consisted on grafting fullerenes directly on the donor polymer backbone. This strategy, where both D and A moieties can be found in the same molecular structure is known under the name of double-cable polymers and they were the first type of polyfullerenes synthesized for OPV applications, aiming directly the solution of this morphological failure.[63] Some examples of such structures can be found in Figure 1.15, based on the work of Yassar *et al.*[64] et Ferraris *et al.*[65].

Although elegant as solution, an overly homogeneous D-A distribution is counterproductive for the operation of OPVs: in a 3D scenario, they suffer from recombination and reduced $V_{OC}$, leading to an electronic failure.[66] This is due to the fact that, in an OPV, illumination, alongside with D-A phase separation, establishes a gradient of chemical potential (since electrons and holes are not created in the same phase) that drifts the carriers in addition to the external electric field due to the asymmetry of the electrodes. Then, this gradient is beneficial for the BHJ architecture, being extremely dependent on the phase separation.[67, 68]

A middle-way between using small-molecule fullerene-derivatives and grafting it to

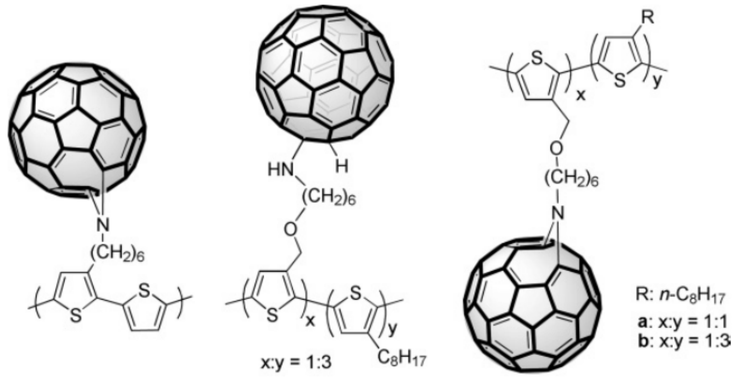

**Figure 1.15:** Some examples of double-cable D-A polymers. The left polymer was electrochemically obtained by Yassar *et al.*,[64] whereas Ferraris *et al.*[65] obtained both on the right by reacting head-to-tail copolythiophenes functionalized with azido- or primary amino-groups and $C_{60}$. Reproduced from ref. [46]

the conjugated polymer, is the polymerization of $C_{60}$ so that it can be more soluble besides promoting a plasticizing effect on the BHJ domains. Two major approaches are then possible: 1) using new polymeric fullerene derivatives as the sole *n*-type material or 2) using it as an additive responsible for avoiding the fullerene-derivative aggregation. One has to keep in mind that these new polyfullerenes should also be stable against photo-chemical process in order to be efficiently proposed as stabilizer agents of the BHJ.

Therefore this is the driving force of this thesis: design of new polyfullerenes that could efficiently be employed as a morphological stabilizer in BHJ OPVs being stable against photo-chemical degradation as well. This is followed by a molecular modeling approach and the ATRAP route is explored in this path. Then, the photo-chemical and morphological degradation of these materials will be studied by an experimental approach. The modeling technique will be of great help to the understanding of photo-chemical degradation mechanisms and how to avoid them.

## 1.6 Final Remarks

In this chapter, the stability of the active layer morphology was briefly discussed and its dramatic influence on the operational lifetime of a solar cell device has been discussed. Others mechanisms of degradation include: electrodes interface, photo-oxidation of active layer, electrodes, charge transport layers, etc.

Considering most of OPV designs, thermal annealing can improve the performance of the cell due to the crystallization of both $p-$ and $n-$type materials domains. This results in enhanced hole and electron mobilities, respectively, besides the optimal phase segregation that optimizes charge separation and collection.[69, 70, 71, 72] However, as the materials further crystallize, the phases can be coarsened and this leads to reduced $p-n$ interfaces, hindering the efficiency. The equilibrium in-between is subtle and can be easily dislocated towards the aggregation of fullerenes, particularly.

Several approaches have been taken to circumvent this: solvent annealing, grafting of fullerene molecules onto $p-$type polymer, use of (self-)assembled structures, and fullerene polymerization strategies, for instance. The latter showed to be a challenging approach and in this thesis the hypothesis that these materials can avoid morphological failure is pursued.

# Chapter 2

# Design and Modeling of Target Structures

*In this chapter the design of new polymeric acceptor materials based on $C_{60}$ for photovoltaic devices is explored using modeling techniques, which are as well explored as far as it is relevant for this thesis. The new materials as-designed should obey some parameters thought to be able to accomplish more stable and efficient layers in the face of intrinsic and extrinsic degradation mechanisms.*

## 2.1 Which are the sought-after properties for fullerene derivatives?

The major impediment to the wide implementation of OPVs is the lower efficiency and shorter lifetime of the cells when compared to the inorganic ones. The majority of the research groups who has worked on the subject focused in BHJ devices efforts to increase the performance of P3HT/$PC_{60}BM$ matrix (see Figure 2.1). Then, literature turned towards the design of new *p*-type materials still using $PC_{60}BM$ as the acceptor molecule. And, finally, new combinations of novel *p*-type and innovative $C_{60}$-derivatives have been designed accomplishing devices which yields are over 10%.[7, 8, 9]

Knowing that the best set of properties of a material and/or device is the one which maximizes both yield and stability against time, we should as well at least predict how efficient the new materials could be compared to the already well known small-molecule fullerene derivatives. The so-far success of fullerenes arises from their properties as electron acceptors, which include:

1. high electron mobility;
2. delocalized LUMO over the whole molecule surface. This allows the 3D electron transfer and transport;
3. LUMO energy level compared to the *p*-type material, allowing an efficient electron transfer;
4. reversible electrochemical reduction that allows the formation of stable reduced charged species;
5. formation of domains from solution deposition, allowing charge separation when an appropriate length-scale is obtained.

Among the most successful materials that have passed over this ensemble of requirements, one can find the small-molecule-based fullerene molecules, mainly those derived of $C_{60}$. The molecules that have been extensively studied in the literature include $PC_{60}BM$,[73, 74] bis-$PC_{60}BM$,[29, 75, 76, 77] and indene-$C_{60}$ mono-($IC_{60}MA$) and bisadduct ($IC_{60}BA$).[78, 77, 79] The molecular structures of these molecules can be found in Figure 2.1, where one can also found the structure of regio-regular P3HT, the most used *p*-type polymer material.[80]

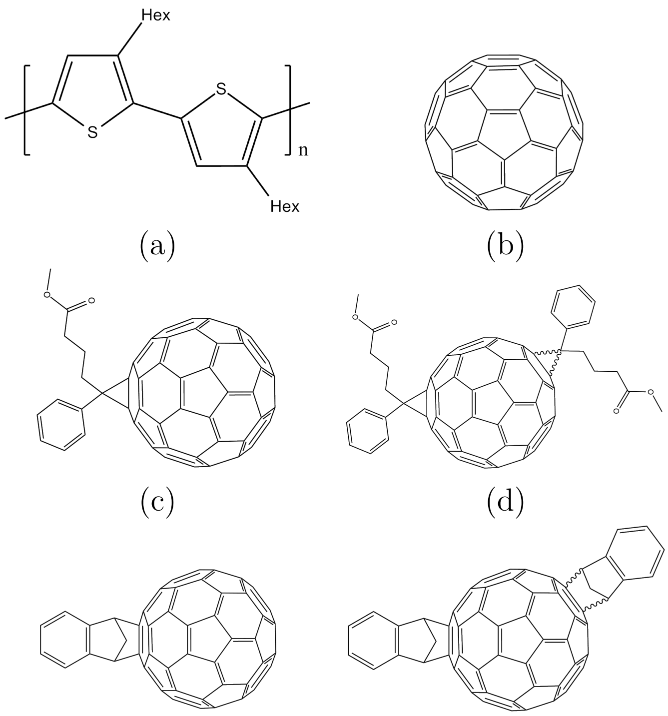

(a) (b)

(c) (d)

(e) (f)

**Figure 2.1:** Molecular structures of (a) regio-regular Poly(3-hexylthiophene), (b) $C_{60}$, (c) $PC_{60}BM$, (d) bis-$PC_{60}BM$, (e) $IC_{60}MA$, and (f) $IC_{60}BA$.

$PC_{60}BM$, for instance, has been such a successful acceptor molecule since it has an appropriate LUMO level and electron affinity and it is capable of forming semi-crystalline domains in the bulk which act as percolation channels for the photo-generated electrons.[74] Moreover, its solubility is increased compared to its precursor, which makes it more easily processable.[75] As $PC_{60}BM$ and P3HT have very different surface energies, the mixture with these two materials, at the initial time $t = 0$, is homogeneous and, with the annealing process, $PC_{60}BM$ segregates out and aggregates, forming semi-crystalline domains within the domains of P3HT, also formed with the annealing temperature. The efficiency of this system lies on the maximization of both contact surface between both materials and the size of their crystal domains. In this way, both charge dissociation and mobility is maximized, reducing charge recombination within P3HT.

Varying the lateral chain in $PC_{60}BM$ structure, several authors have found that the photovoltaic performance is tightly correlated to the solubility of the resultant material.[77, 81] Motivated by this, but not solely, bis-adduct $PC_{60}BM$ derivatives, namely bis-$PC_{60}BM$, could be developed, allowing one to increase the optical absorption in the visible region (it can contribute to the photo-current in the OPV) and to increase the LUMO level (leading to an increase of the $V_{OC}$).[82][1] In this way, higher photovoltaic efficiency could be obtained.

For improving even more the photovoltaic properties of cells based on P3HT, Li *et al.*[78, 79] have developed $C_{60}$-indene[2] derivatives, as presented above. These molecules, be it the mono- or the bis-adduct, present an up-shifted LUMO compared to $PC_{60}BM$ and best solubility, which is even better than that of $PC_{60}BM$. These properties, without further device optimization, were able to provide devices with a 40% gain in efficiency compared to $PC_{60}BM$.[77] All that said, $PC_{60}BM$ is still the most used and understood system in OPVs and remains, since many years, the reference on the topic and that explains why it is in vogue despite the presence of many other acceptors.

Despite these advantageous properties, fullerene-based acceptors have some limitations, which the bottleneck concerns the development of long-life stable cells. Generally, thin film blends are morphologically unstable over time, leading to macroscopic crystallite formation (aggregation) and consequent device failure. Moreover, the synthetic procedures needed for producing them demands expensive purification to separate out higher-order adducts. Finally, there is a limited scope for synthetic control over electronic and structural properties.[83, 84] This concept will be further explored in the next sections.

On the point of view of stability, two major processes can be associated to them:

---

[1] The $V_{OC}$ stands for the open circuit voltage. This is the voltage obtained when the contacts are isolated and the potential difference has its maximum value. In Figure 1.2, the $V_{OC}$ is associated to the difference between the LUMO energy level of the electron acceptor and the HOMO energy level of the donor material.

[2] Indene are polycyclic hydrocarbons composed of a benzene ring fused with a cyclopentene ring.

the first one is linked to the morphological evolution on time of the P3HT:$PC_{60}BM$ domains, *i.e.*, each component aggregates out of the mixture and the contact surface is drastically reduced, mitigating the electron dissociation and electron transfer (see Section 1.2); and the second one is linked to the chemical degradation of each component with environmental dopants, such as $H_2O$ and $O_2$[85] in the presence of energetic stresses such as light and heat (or the combination of both).[86, 87, 88, 89, 90]

For the $p$-type molecules, the latter degradation is illustrated by the absorption cross-section reduction caused by the destruction of the $\pi$-conjugated system; and for the $n$-type material this is illustrated by the creation of charge traps caused by the lowering of the LUMO level of the fullerene derivative when attacked if compared to the pristine molecule.

In a very general way, we can state the sought-after parameters for an acceptor molecule in photovoltaics:

1. Concerning the electronic structure:
    - Good electron-acceptor properties (increased electron affinity)
    - Well-defined LUMO (absence of trap levels inside the gap)
    - Increased mobility (assured by morphological properties, mainly)
2. Concerning the morphological structure:
    - Good solubility (assured by lateral chain engineering, mainly)
    - Reduced phase segregation (good solubility in $p$-type matrix)
    - Reaction selectivity should somehow depend on the available fullerene surface; controlling this parameter should avoid uncontrolled multi-adducts formation and consequent LUMO broadening
    - Formation of percolation paths needed for electron transport

With all this in mind, treating the issue of stability turns into a multi-parameter maximization (or minimization, depending on the frame of reference) problem which variables are somehow interconnected. Moreover, the stability variables are connected to the efficiency ones and one should take somehow both of them into account when designing new acceptor molecules. In the same way, a cheap synthesis is also a parameter to be considered in designing new materials.

In this way, the next sections are intended to explore these possibilities of assuring, at the same time, both optimal electronic properties and morphological structure through the insertion of fullerene into polymeric backbones, using six different chemical routes. This chapter will treat in more details the electronic properties of the resultant molecules whereas their stability is treated in parts in Chapter 6.

## 2.2 How one can design polyfullerenes based on multi-scale molecular modeling?

Molecular modeling techniques should be chosen considering the type of system being studied and the properties that are required to be described/calculated/understood. Several approaches exist to treat either small or big molecules, ranging from *ab initio* methods to molecular mechanics ones.

In the context of this thesis, one is interested in describing structural, electronic and morphological properties of fullerene derivatives. These calculations are done either to comfort experimental data, to make previsions on molecules that do not exist yet or to study trends for a property within a class of materials.

Being a multi-electron system, their electronic properties should clearly be treated within a *many-body* approach, in which exchange and correlation are treated. This treatment may be either explicit or not, and for the case of *Density Functional Theory* (DFT), for instance, it is rather approximative and taken into account by the choice of the appropriate *exchange-correlation* functional.[3]

The theory behind DFT is briefly described in Annex C and the eager reader is redirected to the recent review by A. Becke.[91] DFT, coupled with the Hellmann-Feynman theorem,[92] is capable of calculating equilibrium geometries of molecules and the agreement between theory and experiment is generally improved with larger basis sets. Thus, the computational time scales with the number of basis set functions of the molecules, which also scales with the number of atoms and this is really more cumbersome during a geometry optimization run. A compromise between accuracy and machine time needs then to be done.

The possible ways to treat molecules with increased number of atoms having this constraint are listed below:

1. Explore physical-mathematical approximation within the DFT methodology, such as the RIJCOSX method described in Annex C;
2. Use smaller basis sets, although it can compromise the electronic analysis;
3. Use semi-empirical methodologies which were minutiously parametrized, such as PM7 hamiltonian;
4. Use of molecular mechanics hybrid parameters, which are taken from similar molecules and experimental data.

---

[3] It is worthy noting that this methodology is the most appropriate to describe the electronic structure of systems which dimensions are comprised between 100 and 300 atoms.

These approaches are enumerated following the order of the number of atoms. When having more and more atoms to treat and to study the electronic/structural properties arising, one should go down on this list when choosing the molecular modeling method.

The application of each aforementioned approach is described whenever they are used and it is then justified the reasons for the choice.

These methods are implemented in several suites of molecular modeling software packages. In this thesis, the use of ORCA package[93] is used for approach 1 and 2, and MOPAC2012 for approach 3. All these softwares are free of charge and can be used freely within the academia.

## 2.3 Model polyfullerene systems and their general properties

Initially, $C_{60}$ was thought to be unreactive and to have an aromatic-like structure.[4] But, the particular delocalization of the $\pi$-electrons allows them to take part in a wide variety of reactions characteristic of alkenes. Besides that, they also have an electron deficient alkyne characteristic that permits reactions with electron rich species. This opens a range of possibilities of incorporating them into polymers.[94]

The formation of polymeric $C_{60}$-based materials should, first of all, answer to synthetic constraints related to the cost and difficulty of the chosen route. Here we present six routes that are able of forming at least bis-attacks on fullerene and are capable of reacting further to form polymers. One can find in literature variation of these and others that are not explored herein since their synthesis may not be that straightforward.[95, 96, 97]

These routes were chosen based, mainly, on their relative easiness of synthesis, since the most part of the needed functional groups can be achieved starting from a bromomethyl or an aldehyde group. If $M$ is our comonomer, the structures depicted in Figure 2.2 show how bis-adducts could be then obtained. *In these images, $M$ is assumed to be mono- or bis-functional forming, in this way, bis-adducts or polymers, respectively.*

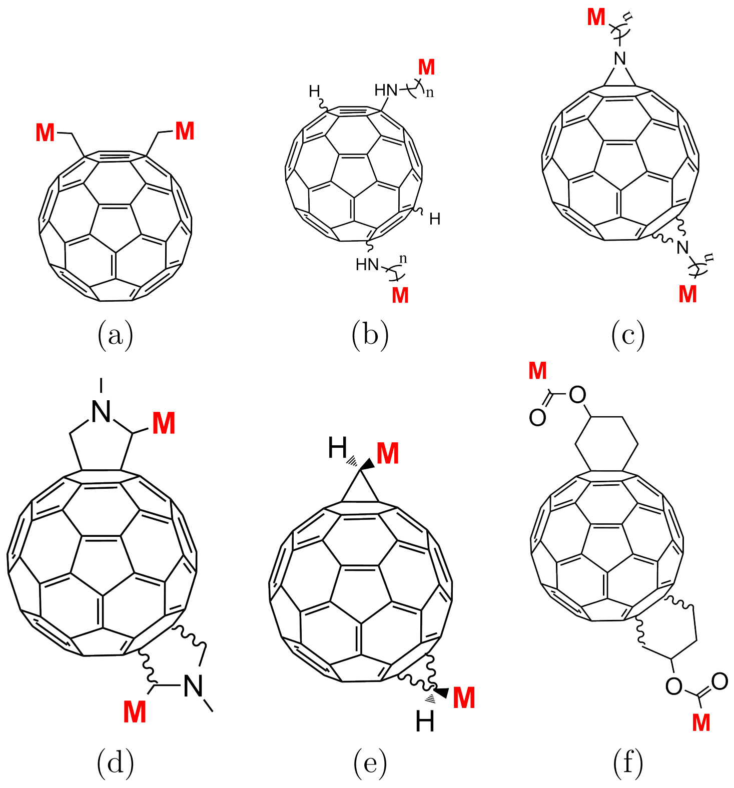

(a) (b) (c)

(d) (e) (f)

**Figure 2.2:** Possible structures of bis-attacked fullerene derivatives than could be polymerized.

---

[4] The reader is invited to keep this affirmation in mind when reading Chapter 6 of this document.

### 2.3.1 Atom Transfer Radical Addition Polymerization

The first route is the one called ATRAP, developed by Hiorns *et al.*[61, 62] However, the first reports on radical attacks on fullerenes were reported a decade ago by Mathis and others,[49, 51, 52] when PMMA and PS were covalently attached to such spheres. This will be discussed with more details in the next chapter. The route is based on a halogen, mainly bromine, abstraction by a copper(I) salt from an organohalide. The copper salt is suspended in solution by using a ligand such as 2,2'-bipyridine. The reaction reaches its maximum of conversion around 24h and the purification can be easily done as it will also be discussed in the next chapter.

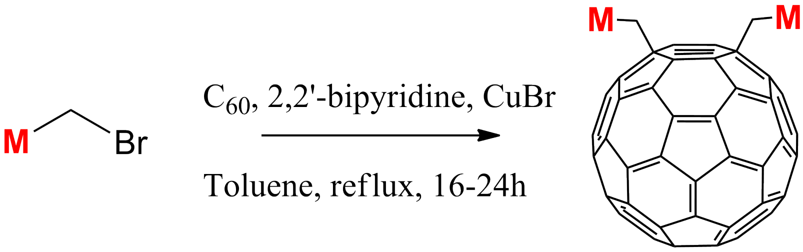

**Figure 2.3:** ATRAP synthetic route.

One of the most interesting properties of the materials obtained by this route is the fact that the fullerene system has 58$\pi$-electrons after bis-adducts are formed. This represents the minimum of modification on the electronic structure of the sphere.

### 2.3.2 Amino-fishing

This route, depicted in Figure 2.4, is based on the addition of amines to $C_{60}$ and it was one of the first reactions to be investigated in fullerene chemistry.[98, 99, 100] With respect to the mechanism behind the formation of these compounds, both nucleophilic and radical addition of amines to the $C_{60}$ are possible and closely related and in some cases it is difficult to determine which mechanism is actually taking place.[101]

For this so-called "amino-fishing" route, both nucleophilic and radical attacks should be studied as possible mechanisms in the next steps of analysis. The quantity of molecules attached to the fullerene that can be obtained from this reaction depends on the steric hindrance, the polarity of the solvent and the presence or not of oxygen, light or temperature, as described in the review by Tzirakis *et al.*[102]

This synthesis will form 56-$\pi$-electron structures and the position over a hexagon where the H atom will be bonded may be variable over the 2 or 4 position respectively to where the amine attaches. This should not be the case for the molecules based on the ATRAP route, since the steric hindrance in this case should avoid this position of the second attack, whereas for H, since it is a very small radical, it can be attached on both positions. The advantage of this synthetic route is the absence of metal catalysts. More details on this route can be found in the thesis of B. Bregadiolli[5] and in the ref. [102].

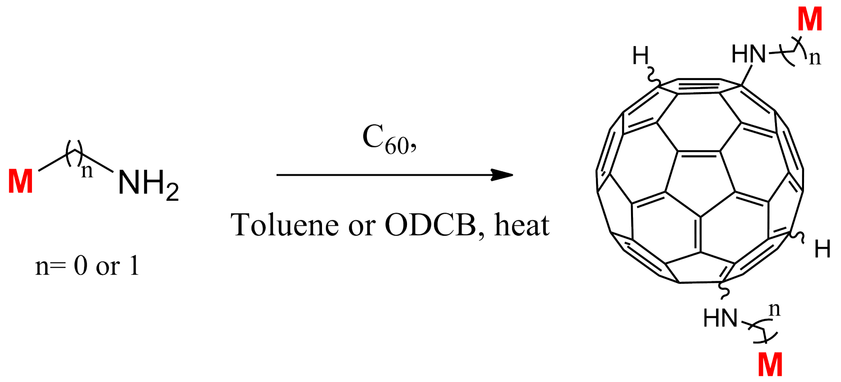

**Figure 2.4:** Amino-fishing synthetic route.

### 2.3.3 Azide cycloaddition

Molecule 2.5 is obtained from a [3+2] cycloaddition based on a 1,3-dipolar addition of azides. At temperatures below 80 °C, this addition occurs preferentially to a 6,6 double bond affording the corresponding thermally labile triazolines. Another advantage of this route is the absence of chemical catalyst, issuing a purer product at the final step. Although the use of azides can be considered dangerous, the C/N ratio of the monomer can be increased in order to work in safe conditions. Moreover, the fact that no radical reaction is involved, chlorinated solvents may be used, leading to smaller reaction pots, based on the increased solubility of $C_{60}$ in solvents as *o*-dichlorobenzene. More information on this route can also be found in thesis of Bregadiolli as well as in the references [103, 104].

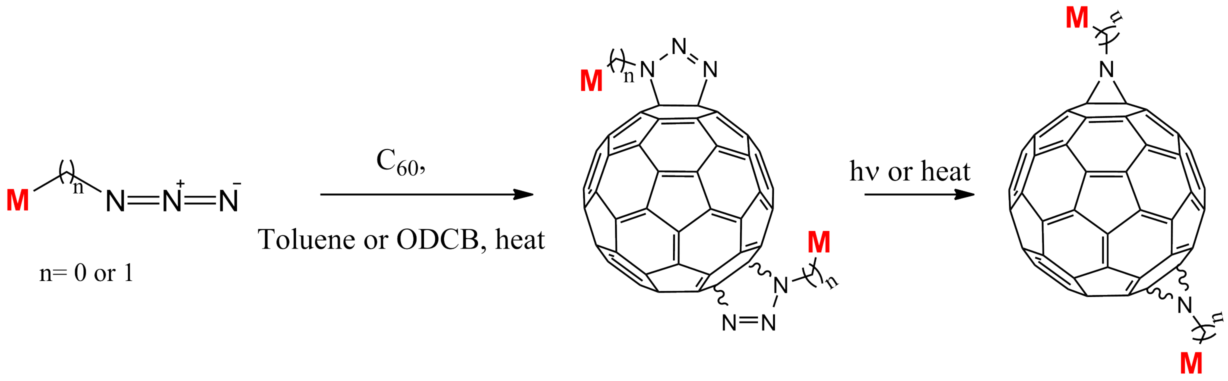

**Figure 2.5:** [3 + 2] cycloaddition of an azide.

---

[5] Ph.D. student in our group.

### 2.3.4 Prato cycloaddition

Structure of Figure 2.6 is obtained from a [3+2] cycloaddition based on a 1,3-dipolar addition of azomethine ylides what leads to the formation of the well-known fullereno-pyrrolidines. This synthetic route has been extensively explored on the chemistry of olefins, and can be found under the name of Prato synthesis. Maybe this is one of the routes that can provide the most important yield based on literature and another advantage is the absence of chemical catalyst as well. Only water and carbon dioxide are released during the synthesis, issuing purer metal-free materials at the end. More details on this route can be found on the thesis of H. H. Ramanitra[6], who extensively explores this route. The details of this route are not presented because of confidentiality issues and patents that are not yet deposited.

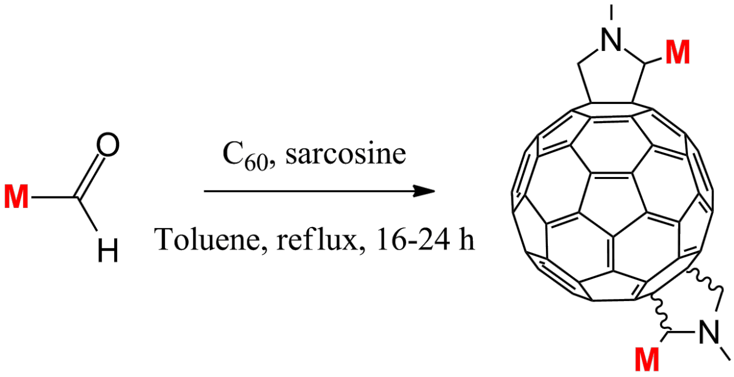

**Figure 2.6:** $[3+2]$ cycloaddition of an azomethineylide.

### 2.3.5 Cyclopropanation

Another interesting route to explore is based on the formation of a cyclopropane bridge group onto the fullerene sphere. Originally, to obtain such molecules, as the ones depicted in Figure 2.7, one would use the so-called Bingel reaction,[105] which is based on a nucleophilic attack. This is not the first choice to achieve such compounds based on the difficulties found during the preparation of the bromomalonates needed for this nucleophilic attack.[106]

Another way to achieve these compounds is using a route intermediated by a diazoalkane generated by the base-induced decomposition of tosylhidrizines.[73, 107] The diazo compound is then generated *in situ* and trapped by $C_{60}$ to undergo a 1,3-dipolar addition in an one-pot reaction. Finally, it is worthy noting that this is the route used to synthesize $PC_{60}BM$ molecule and its derivatives.

---

[6] Ph.D. student in our group.

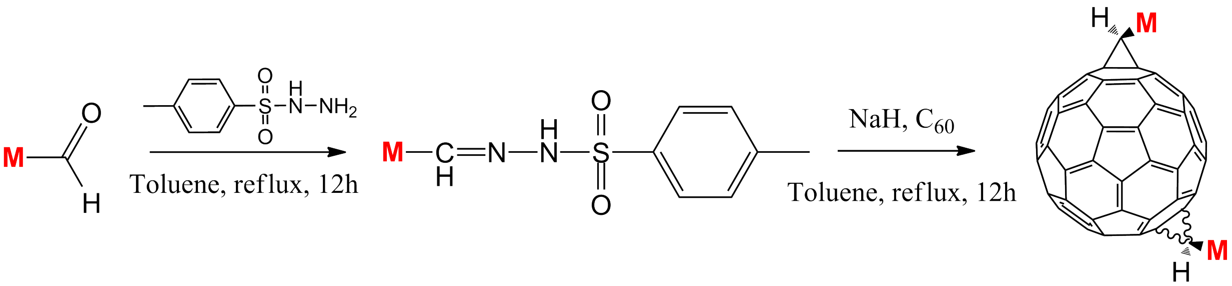

**Figure 2.7:** 1,3-dipolar cyclopropation reaction.

### 2.3.6 Diels-Alder addition

Finally, a multiple-step bis-adducts preparation can be achieved affording molecules as depicted in Figure 2.8, consisting of a classical Diels-Alder cycloaddition where an oxygenated diene[7] adds to fullerene to form cyclohexene rings fused to $[6,6]$ junctions.[109] This type of cycloaddition has the advantage of controlling the degree as well as the site of the addition and a fullerene monomer is formed before being polymerized with the other comonomer $M$, in two different steps. This route seems interesting from the practical point of view since the solubility of the intermediary fullerenes-comonomers is higher in toluene than $C_{60}$ itself, reducing considerably the volume of reaction pot. The comonomer $M$ used is a di-carboxylic acid and this can be straightforwardly obtained from the bromomethyl groups, in the same way the previous needed functional groups can also be so done. This chemistry has been explored by A. Isakova[8] and more details can be found in her thesis and as well in references [103, 104].

---

[7] Also called Danishefsky's dienes.[108]

[8] Ph.D. student at Aston University.

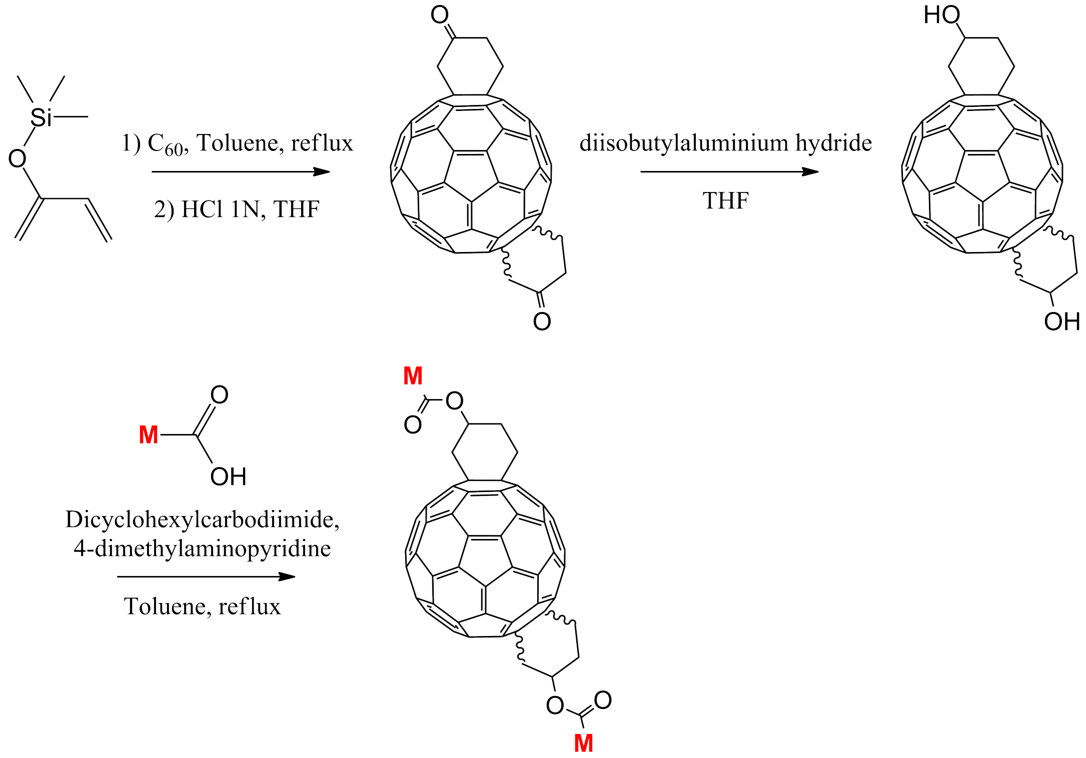

**Figure 2.8:** [4 + 2] Diels-Alder cycloaddition reaction.

## 2.4 Revealing the position of bis-adduct formation

Once the first attack on the fullerene sphere happens, the second can take place in eight different positions and this is valid for all the molecules studied up to now, exception made for the ATRAP-based ones.

Hirsch *et al.*[110] identified these eight positions and called them *cis-1*, *cis-2*, *cis-3*, *equatorial*, *trans-1*, *trans-2*, *trans-3*, and *trans-4*, taking into account their distribution around the planes of symmetry of $C_{60}$, as it can be seen in Figure 2.9.

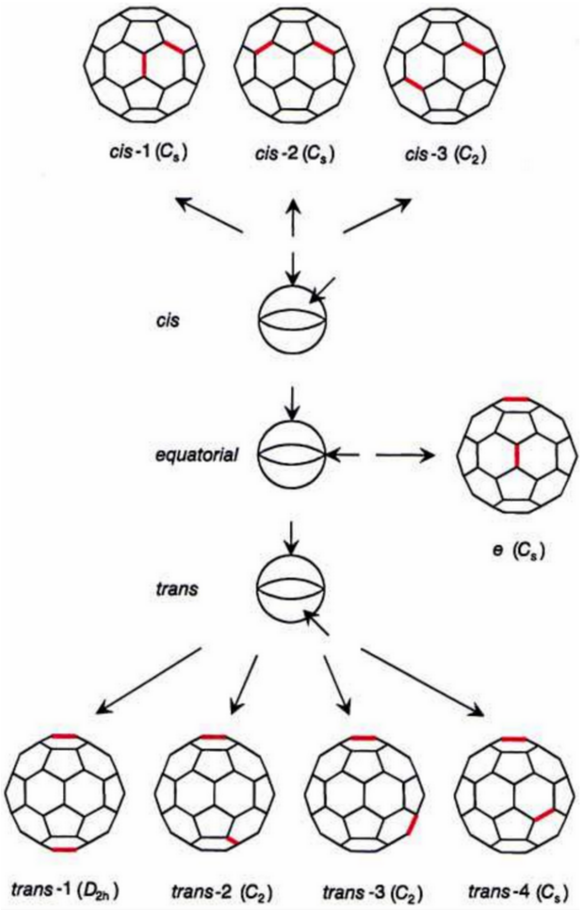

**Figure 2.9:** Different sites for the second attack to take place during the formation of fullerene bis-adducts with indication of the symmetry group of each molecule. Reproduced from ref. [110].

Controlling the position of the second attack is not simple and depends on the electronic structure and mainly on the steric hindrance sensed around the fullerene sphere, as it was noted by Cheng *et al.*[107] These same authors have demonstrated the use of tethering groups as an efficient way to control sterically the formation of bis-adducts.

Moreover, the position of the second attack should be somehow dependent on the type of reaction used to produce it. For ATRAP reaction, this is not an issue since the formation of the second attack is definitely in position *o* or *p* related to the first attack, being the latter the most likely to happen because of steric hindrance.

To study the position of the second attack for the molecules herein presented, we should separate them by the type of reactions employed: cycloadditions, radical or nucleophilic attacks. Among the cycloadditions, one should count the 1,3-dipolar additions on the fullerene (Azide, Cyclopropanation and Prato reactions) and the Diels-Alder based on oxygenated dienes. The Amino-fishing reaction, as already mentioned, can be described by a nucleophilic or a radical attack and thus, both mechanism are presented.

## 2.4.1 1,3-dipolar cycloaddition-based products

The Prato, Azide and Cyclopropanation based products are herein studied since they are all based on 1,3-dipolar cycloaddition reactions. The prevision of the position of the second attack is done here by a coupled experimental-theoretical approach where model compounds based on Prato reaction were synthesized by H. H. Ramanitra[9] and the experimental UV-VIS spectra were compared to the TD-DFT/6-31G** calculated ones.[10]

Determining the same for the other proposed molecules relies on the analysis of the molecular orbitals considering that this type of cycloaddition depends on the LUMO of $C_{60}$s (this is explained *vide infra*).

### 2.4.1.1 Prato-based products

The eight known attack positions for bis-adducts formation in Prato synthesis were studied by Time Dependent Density Functional Theory (TDDFT). The geometries were fully optimized within the B3LYP/6-31G** level of theory in ground state. 20 UV-VIS electronic transitions were calculated using the same formalism. For all the calculations the RIJCOSX[11] approximation was used and run in Orca 3.0.2 software. The studied structures follow the general scheme depicted in Figure 2.10 (herein presented for a generic geometry).

The calculated electronic transitions were enveloped with Gaussian functions having 0.125 eV at FWHM. The experimental spectra were treated to remove the non-resonant backgrounds due to Rayleigh scattering.[12] Theoretical spectra were shifted in order to have their highest-intensity maximum coincident with the one of the experimental spectrum. In this way, we eliminate any energy discrepancy parameter and we avoid discussions on the method-induced error on the energies.[13]

---

[9] Ph.D. fellow in the same laboratory.

[10] TD stands for Time Dependent.

[11] see Appendix 1

[12] The suppression of the elastic scattering was done by subtraction of a $\sim \lambda^4$ function. Although enough as a first approximation, the scattering functions are more complex in the region of absorption.

[13] The applied shifts are equal to: *cis-1* 1.42, *cis-2* 0.92, *cis-3* 0.95, *equatorial* 0.99, *trans-1* and *trans-2* 1.03, *trans-3* 1.11, and *trans-4* 0.92 eV.

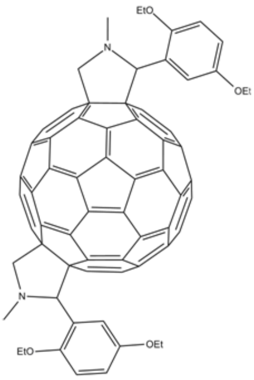

**Figure 2.10:** General structure for studying the bis-adduct formation in Prato reaction (HHR23D). Here the *trans-2* bis-adduct is presented. The product named Poly1HB has the same structure however no lateral chain is grafted on the comonomer.

The proposed model to determine the position of attack is based not only on the spectral recovering, but also on the interband spacing and band ratios. Below one can find these results considering HHR23D (polymerization of 1,4-bisformyl-2,5-bisoctyloxybenzene) and Poly1HB (polymerization of terephthaldehyde)[14].

For both compounds, *cis-2*, *trans-2* and *trans-3* show very good qualitative agreement between theoretical and the experimental spectra. Namely for *trans-3*, the interband distance between the first maximum and the second lower energy band is remarkable. One should keep in mind that the applied shift took into consideration the maximum intensity among the high energy transitions, explaining the shoulder found for *trans-3* simulated spectrum. Moreover, it is judicious to think that experimentally, the highest energy band is not mono-composed but there is not enough resolution to resolve them, like one can do theoretically. Also, the subtraction of the non-resonant background cannot be assured as final and, in this way, the features around 2.0-2.7 eV should not be treated as absorption bands. Finally, one can also have a mixture of different bis-adducts in the analyzed sample. Being this the case, the major contribution must be due to product with the best agreement between the calculated and measure spectra.

Experimentally, the several bis-adducts could be distinguished by high-performance liquid chromatography (HPLC). However, for the case where this becomes a polymer, this technique is no longer appropriate to separate the fractions. One may then considerer that the polymer should be consisted of a dispersion of different bis-adducts for which the most present type of adduct is the one with the best agreement in this study.

In order to further investigate this, one should take a look on the frontier molecular orbitals-based mechanism of the Prato reaction to corroborate or not the results indicated above. The Prato reaction is a 1,3-dipolar cycloaddition and thus, a pericyclic reaction, which obey the Woodward-Hoffmann rules, where an orbital overlap between the dipole

---

[14] whose details on the synthesis are not on the scope of this thesis and should be consulted in Hamanitra's PhD thesis.

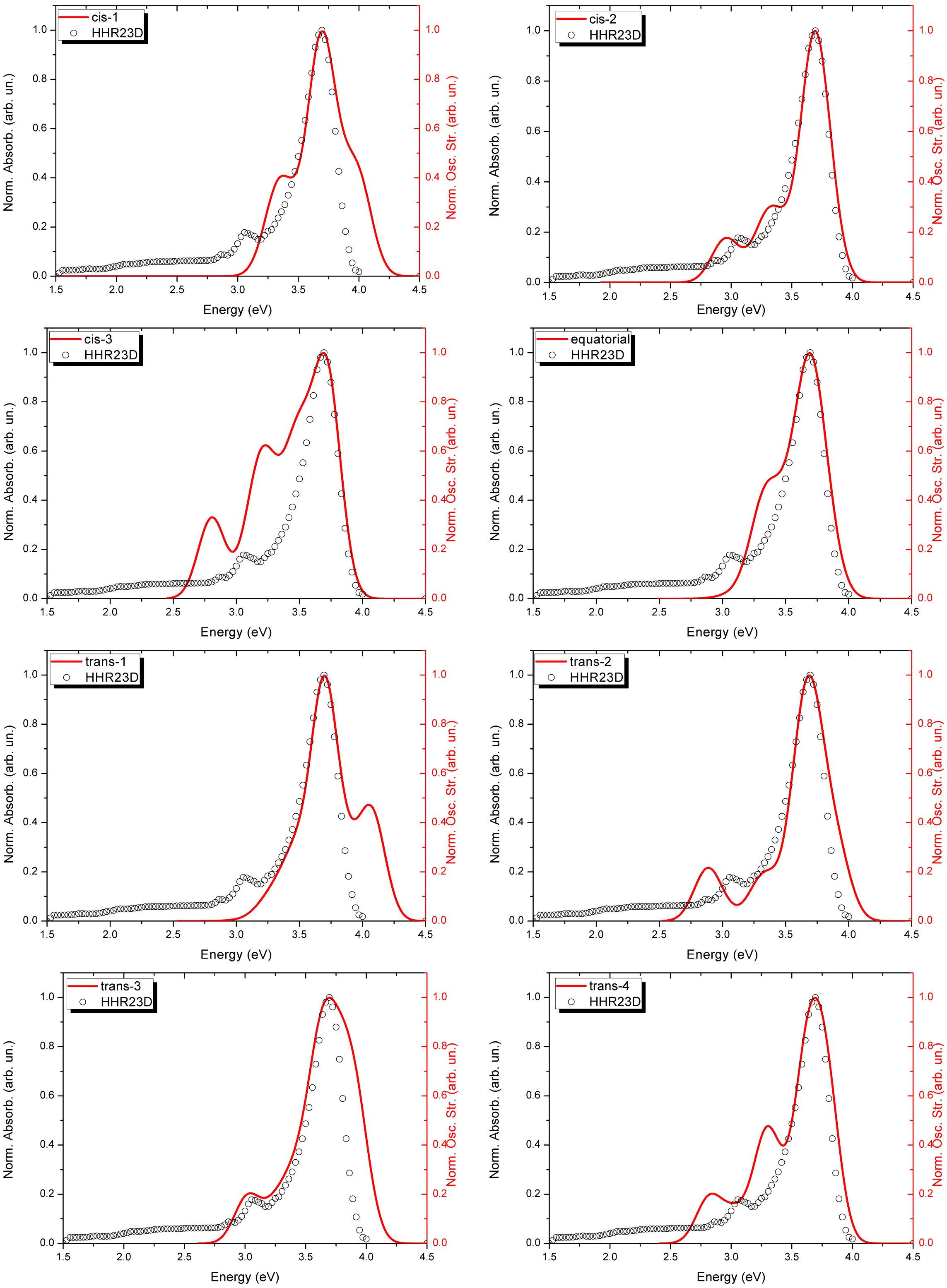

**Figure 2.11:** Theoretical-experimental UVVIS electronic transitions comparison for synthesized HHR23D material and Prato molecule model as proposed in Figure 2.10.

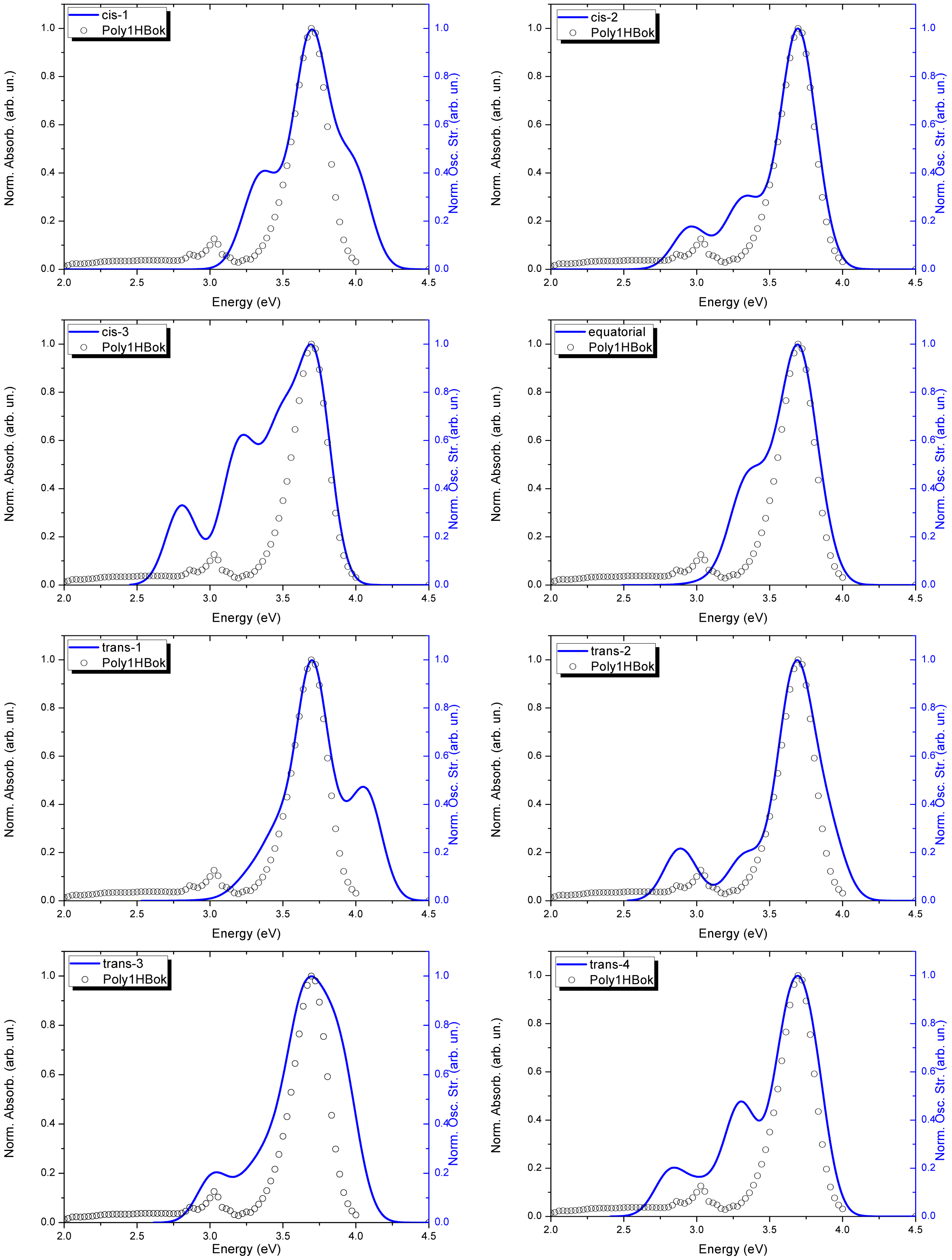

**Figure 2.12:** Theoretical-experimental UVVIS electronic transitions comparison for synthesized Poly1HB material and Prato model molecule as proposed in Figure 2.10.

and the dipolarophile is needed. The dominant overlap is the one which possesses the smallest HOMO-LUMO energy gap.[111]

For fullerenes as dipolarophiles, as it has a deep LUMO, the orbital overlap happens between the HOMO of the 1,3-dipole and the LUMO of the already firstly-attacked fullerene. The energy diagram is depicted in Figure 2.13.

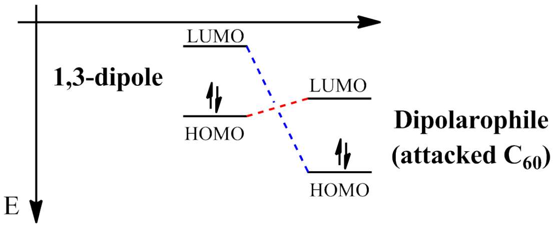

**Figure 2.13:** General energy scheme for studying the bis-adduct formation in Prato reaction.

The HOMO-LUMO gap for the blue configuration is 4.54 eV while it is only 0.43 eV for the red one. In this way, the reaction is ruled not by the HOMO of $C_{60}$, but by its LUMO. Then, taking a closer look at this orbital for the first attacked fullerene, one has what is depicted in Figure 2.14.

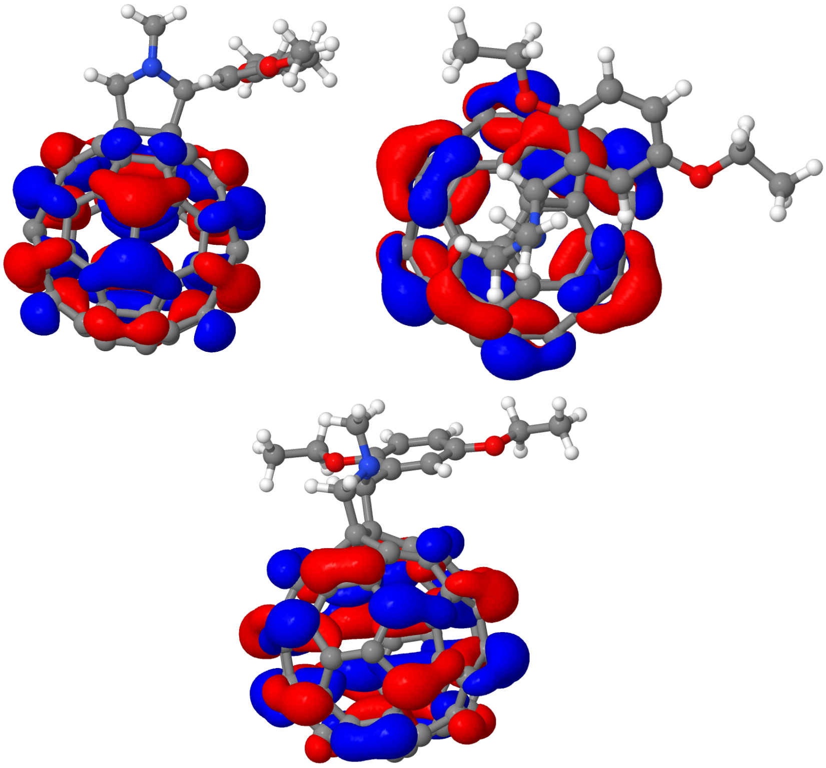

**Figure 2.14:** LUMO orbital of the Prato model molecule from different perspectives.

One can note that the LUMO density is zero for the region where a fully linear polymer would be expected (based on *trans-1* attacks). However, these densities indicate that the center of the sphere is much more electronically active. Considering this, one should expect that the polymers are formed in such a way that the monomer of each side should be at 90 °C to each other.

Moreover, one can also see, as it is presented in Figure 2.14 that the lobe is very intense in the region where an equatorial attack would be formed. In fact, the density of the LUMO orbital is this region is more important than the one for *trans-3* (which has the best agreement in TDDFT calculations). Very probably the attack is not favored because of steric hindrance caused by the long alkyl chains of the monomer.

Based on this analysis, we could say that:

1. *trans-1* is not favorable based on the distribution of the LUMO;
2. *cis-1* is not favorable based on steric hindrance;
3. *cis-2* may occur, but the density of LUMO in this region is lower than in others, moreover there is the steric hindrance taking place as well;
4. *cis-3* may occur based on the distribution of the LUMO but it is not consistent with the TDDFT calculations;
5. *equatorial* is not favorable based on the distribution of the LUMO;
6. *trans-4* is the same case as *cis-3*;
7. *trans-2* and *trans-3* are favorable based on the distribution of the LUMO and on the steric hindrance;
8. *trans-3* matches the best when one compares the TDDFT spectra with the experimental ones.

Thus, based only on this analysis, we would state that the most probable position of the second attack follows the order:

$$\textit{trans-3} > \textit{trans-2} > \textit{cis-2} \;/\; \textit{trans-4} \;/\; \textit{cis-3} > \textit{equatorial} \;/\; \textit{trans-1} >> \textit{cis-1}$$

This is in good agreement with the results obtained by Lu *et al.*[112] and Hirsch *et al.*[110]. This analysis is purely based on kinetic arguments. The thermodynamic considerations of the total energies of different isomers are not treated because we believe that steric hindrance combined to electronic factors should play a major role than the thermodynamical stability of the formed compounds.

Ideally, the synthesis of bisadducts should be performed alongside their $^{13}C$ NMR spectrum. In this way, one could compare it with the simulated one and we should find a very precise agreement capable of defining the geometry of the second attack.

It is worth keeping in mind that these calculations were performed in vacuum and the experiment is done in the presence of factors such as temperature and solvent. Finally, 1,3-cycloadditions experience very weak solvent dependency since the transition state is apolar.

#### 2.4.1.2 Azide-based products

Using the energy diagram depicted in Figure 2.13, the formation of the bis-adducts by the Azide attack faces a HOMO-LUMO gap dependent on the stage that the first adduct is found: before or after the $N_2$ release of the intermediary. In the first scenario, this gap between the dipole and the dipolarophile is 2.39 eV for $C_{60}$'s LUMO-Monomer's HOMO interaction and 4.68 eV for the other way round.

If the second attack happens after the release of the $N_2$ molecule, these orbitals interactions face gaps of 2.48 and 4.61 eV, respectively. This indicates that the LUMO orbital of $C_{60}$ rules the formation of the cycloaddiction products and it is the dominant pathway.

Within the same level of theory, we can then propose the positions of bis-adduct formation based on the knowledge that the reaction is ruled by the LUMO of $C_{60}$ and the HOMO of the monomer. In this way, one can find the spatial distribution of this molecular orbital in Figure 2.15.

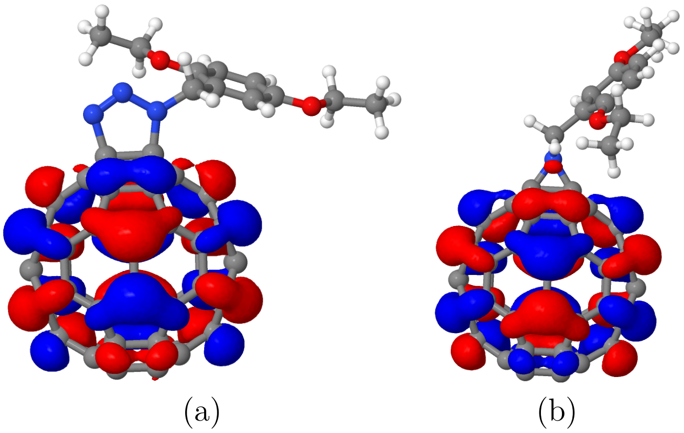
(a) (b)

**Figure 2.15:** LUMO orbital of the Azide-based model molecule. In (a) one can find the LUMO distribution before the release of the $N_2$ molecule and in (b), after it.

In this figure, for the azide reaction, we present two possible mono-adducts: the first is based on the first step of the cycloaddition, when $N_2$ molecule has not been released yet and, the second is when it has already been done.

As for the case of Prato reaction, the spatial distribution of the LUMO orbital is not drastically changed and the selectivity must be towards an attack on the positions forming *trans-3* and *trans-2* isomers.

#### 2.4.1.3 Cyclopropanation-based products

Similarly, the same is here presented for the cyclopropanation-based products. Again, two scenarios can be found: in Figure 2.16.a, the second attack may take place before the release of the $N_2$ molecule from the intermediate species and in Figure 2.16.b, this will happen after the $N_2$ release already took place. The HOMO-LUMO energy gaps found for the first configuration equals 4.31 eV when $C_{60}$'s HOMO - monomer's LUMO interact and equals 1.68 eV in the other way round. For the second case, these gaps equal 4.20 and 1.80 eV, respectively. This indicates that the mono-adducts' LUMO orbital rules the second attack.

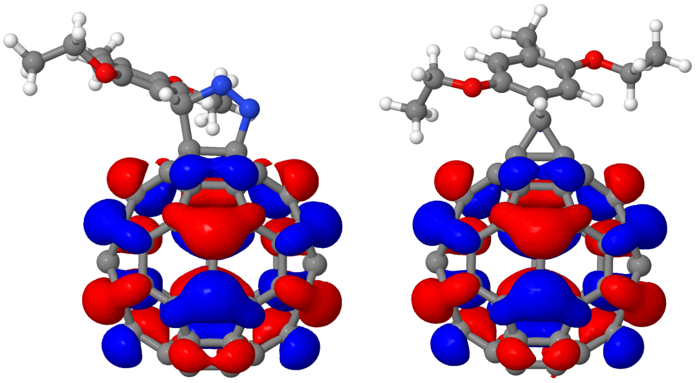
(a) (b)

**Figure 2.16:** LUMO orbital of the cyclopropanation-based model molecule. In (a) one can find the LUMO distribution before the release of the $N_2$ molecule and in (b), after it.

Clearly, no difference in the LUMO orbitals of these two species is sensed, as it is the case of the Azide-based compounds.

In this way, one could say that Azide- and Cyclopropanation-based compounds should form bisadducts in the same positions as the Prato reaction, forming preferably *trans-3* and *trans-2* isomers.

### 2.4.2 Diels-Alder

The products formed by a Diels-Alder reaction are not based on a 1,3-dipolar cycloaddition but as they are still pericyclic reactions, the dominant pathway is still the one with the smallest HOMO-LUMO gap between the diene and the dienophile.

Considering this, a value of 2.75 is found when the $C_{60}$'s LUMO - diene's HOMO interact. The other way round faces a gap equals to 5.21 eV. In this way, the pathway is still ruled by $C_{60}$'s LUMO and its spatial distribution can be found in Figure 2.17.

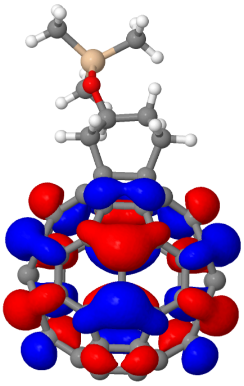

**Figure 2.17:** LUMO orbital of the Diels-Alder-based model molecule.

### 2.4.3 Amino-fishing-based products

This attack route can follow two distinct mechanisms: a single electron transfer from the amine to the $C_{60}$ or a complex sequence of radical recombinations, deprotonations, and redox reactions.[102]. To determine the position of the formation of the bis-adduct, both mechanism are herein explored.

To determine the most probable positions for the second attack to take place in both mechanisms, one can analyze the Fukui Condensed Functions (FCF) of the mono-adduct. The analysis of these functions provides helpful hints on the propensity of an atomic site to suffer an electrophilic, nucleophilic or radical attack based on the vertical charge distribution of the ground, cationic and anionic states.

Considering the electronic density $\rho$ at a certain point of the space $\vec{r}$, $\rho(\vec{r})$, the FCFs $f(r)$ are mathematically defined as:

$$f(r) = \left(\frac{\partial \rho(\vec{r})}{\partial N}\right)_{\nu(\vec{r})} \tag{2.1}$$

Where $N$ stands for the number of electrons on the ground state and the derivative is calculated for a given external potential.[15]

The discretization of the electron density function leads to the local site-dependent analysis at $\alpha$ and gives rise to three different functions based on the addition or removing of an electron charge defined as follows:[113, 114, 115, 116]

$$f_\alpha^+ = q_{N_e} - q_{N_e+\Delta N_e} \tag{2.2}$$

$$f_\alpha^- = q_{N_e-\Delta N_e} - q_{N_e} \tag{2.3}$$

$$f_\alpha^0 = \frac{1}{2}(f_\alpha^+ + f_\alpha^-) \tag{2.4}$$

---

[15] Practically, this is obtained by imposing vertical transitions.

Where $q_{N_e}$ stands for the partial charge on the site $\alpha$ on the ground state ($N_e$) electrons, and $\Delta N_e$ stands for the increase or decrease of an electron on the same site. So, $f_\alpha^+$ and $f_\alpha^-$ describe the ability of the atom $\alpha$ to accommodate an extra electron (nucleophilic attack) or to lose one (electrophilic attack). The function $f_\alpha^0$ is then associated to a radical attack.

Maximizing these functions, one can maximize the probability of the attack in consideration taking place on the specific atomic site. It is worth saying that this definition is intrinsic from the formalism of density functional theory based on the electron density and, moreover, these functions are calculated for a constant chemical potential, that is why the need of vertical cationic and anionic states to be chosen.

One should keep in mind that, the analysis of the FCF must be careful, since one cannot compare FCFs for different molecules. Moreover, for such systems submitted to environmental conditions, the FCF might not assure that this selectivity will be respected.

For the Amino-fishing-based mono-adduct, the $f_\alpha^+$ and $f_\alpha^0$ were calculated and their distribution around the sphere indicate that for a nucleophilic attack, the bis-adducts should be formed following a propensity like:

$$\textit{cis-2} > \textit{equatorial} > \textit{cis-3} > \textit{cis-1}$$

whereas for a radical attack, this order should be more like:

$$\textit{cis-3} > \textit{cis-1} > \textit{cis-2} > \textit{equatorial}$$

The *trans* positions are not probable to be attacked by both mechanisms. Whatever the predominant mechanism is, it seems that this type of route to synthesize bis-adducts should probably produce *cis* isomers in higher proportions, whereas the routes based on cycloadditions tend to produce *trans* ones.

## 2.5 Electronic acceptor properties and comparison with current benchmarks

As already described, the OPV properties of fullerene-based electron acceptor depend on different factors concerning their electronic structure and solid-state morphology. Hereafter, we will study in more details these properties calculated for the molecules proposed with different routes as well as the current benchmarks: $C_{60}$, $PC_{60}BM$, bis-$PC_{60}BM$, $IC_{60}MA$ and $IC_{60}BA$.

Considering the different possibilities for the formation of the bis-adduct around the fullerene sphere, they were here constructed using a *trans-1* position (symmetrically opposed to the first attack on the $C_{60}$ sphere), regardless this is or not the most probable structure to be formed during synthesis and across all the routes being studied. This was done so in order to homogenize the properties being studied here and to reduce the quantity of species modeled and reducing the scattering of the properties' values.

These molecules had their molecular geometries in gas phase fully optimized within the B3LYP/6-31G**[16] level of theory, using Orca 3.0.3 package, as already discussed before. The electronic properties that were analyzed comprise LUMO energy level, vertical and adiabatic electron affinity, electrophilicity, reorganization energy, and transfer integrals[17]. $C_{60}$'s values were used in each case as internal reference, in order to avoid using these values as absolute and eliminating the experimental method dependence on the determination of these quantities and the discrepancy between experiment and theory. One should keep in mind that these properties indicate general trends and solid-state effects are not (or roughly) taken into account, what can inverse the observed experimental behavior of these compounds. Therefore, the approach used herein should be thought as a guide in the design of new-molecules, not as absolute rock-solid truth.

### 2.5.1 LUMO Orbital Analysis

It is known that the yield of an OPV is directly proportional to the short-circuit current ($J_{SC}$) and the open-circuit voltage ($V_{OC}$) and, for a polymer-fullerene photovoltaic cell, only a little improvement on the $J_{SC}$ can be achieved since it is very close to the maximum feasible value. Thus, improving $V_{OC}$ may considerably result in improved OPVs.

Originally, the $V_{OC}$ parameter is proportional to the difference between the energy of the HOMO of the *p*-type material and the LUMO of the *n*-type one. On the other hand, in order to have an efficient charge transfer in place, a threshold value of about 0.2-0.5 eV in

---

[16] The reader is refereed to the List of Abbreviations in the beginning of the thesis. This stands for the use of the Becke three parameters exchange and Lee, Yang and Parr correlation functional with double-$\zeta$ Pople's basis set with polarization functions on $d$ and $p$ orbitals.

[17] A different geometry optimization was needed to calculate this property. Details are given in the appropriate subsection.

energy gap of the *p*-type LUMO and *n*-type LUMO should be respected.[117] So, $V_{OC}$ can be tailored by preserving this double LUMO gap and raising the LUMO of the *n*-type material, revealing, among others, that a universal *n*-type material is not a realistic concept.

Hence, for a given *p*-type polymer, the lower the LUMO level energy, the higher the $V_{OC}$. We analyze then the LUMO levels of the proposed bis-adducts beforehand presented as well as with other efficient fullerene derivatives, like the $IC_{60}BA$ family.

Controlling how deep or shallow the LUMO energy level will be is a task which demands taking into account several parameters that are concomitant. High-symmetry, presence of electron-poor groups, increased electronic resonance and open-shell configurations are some of the factors that induces a deeper LUMO in a system, for instance.[118, 119, 120] In this way, one can estimate that, in zeroth order, any disruption of the electronic structure and/or molecular geometry of $C_{60}$ will lead to molecules with a shallower LUMO level, as a matter of fact.

Within the Density Functional Theory (DFT) approach, defining LUMO (or whichever other orbital) is not straightforward. This is due to the fact that DFT is not a wavefunction method and, hence, does not lead to explicit orbitals, but to Kohm-Sham ones, $\phi_i$, with associate eigenvalues $\epsilon_i$. However, the fundamental variable within this context, which determines all the observables, is the total electron density at the point $\vec{r}$, $\rho(\vec{r})$, given by:

$$\rho(\vec{r}) = \sum_{i}^{N} |\phi_i(\vec{r})|^2 \tag{2.5}$$

Calculated over the N-particle system.[18]

These Kohm-Sham orbitals have been, for a long time, viewed as an auxiliary concept, not necessarily meaningful and just a way to build the total density. This is so based on the fact that, in the process of construction of these orbitals, an approximative exchange-correlation potential has to be used, and it may keep reality away of their definition. A complete and extensive discussion on the evolution of this concept is done by Stowasser and Hoffmann,[121] but we can jump to the general conclusion achieved by Baerends and co-workers,[122] who argue that these orbitals are very suitable for qualitative, chemical applications. That is why care must be taken if one wants absolute LUMO energy values when designing new molecules. Furthermore, identifying the $V_{OC}$ via the LUMO energies relies on a one-electron picture (orbital relaxation is not taken into account) and on the validity of the Koopman's theorem.

On the other hand, the determination of the LUMO energies is done experimentally by Cyclic Voltammetry (CV) and the values so-obtained are mistaken as good approximations to the energies of this orbital. The usual procedure consists of measuring the reduction potential of the molecule which LUMO energy one wants to determine and

---

[18] More details can be found in Annex C

correlate it with the electron affinity of a standard molecule (usually Ferrocene). Then, assuming the validity of Koopman's theorem, the obtained value is correlated with the LUMO energy. We believe that this leads to a hollow definition and interpretation of the physical-chemical phenomena underlying. We believe that using molecules of different nature in reference and analyte (as it is the case of using Ferrocene as standard) may not take into account the solvent stabilization and reorganization energy, to cite two among these phenomena. In such situations, we believe that the approach taken by Nardes *et al.*[123] is a good compromise between theoretical DFT LUMO estimation and experimental CV LUMO energy measurement. Last, but not least, ideally CV experiments should be compared to Electron Affinities estimations instead of evoking the concept of LUMO energy. The reasons behind this are better described in the following section and we can anticipate that doing so, the multi-electron scenario is then taken into account.

In Figure 2.18, these values related to $C_{60}$'s one can be found. The terms $0C$ and $1C$ for Amine- and Azide-based compounds refer to the number of carbon atoms between the monomer and the functional group: for the former, the functional group is directly attached to the monomer and for the latter, there is a $-CH_2-$ group in-between, as depicted in Figure 2.4 and 2.5.

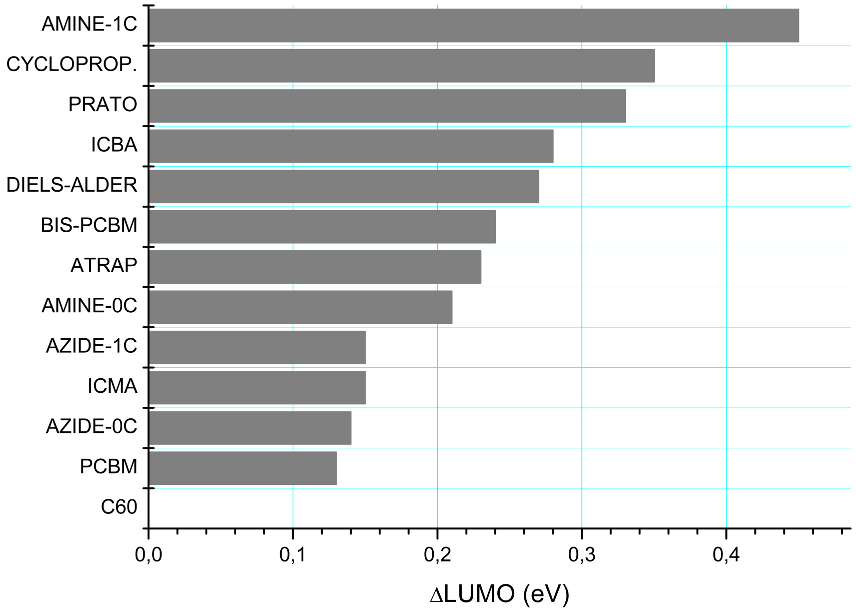

**Figure 2.18:** LUMO deviation compared to $C_{60}$ for the studied compounds altogether the common fullerene-derivatives currently used ($PC_{60}BM$, bis-$PC_{60}BM$, $IC_{60}MA$ and $IC_{60}BA$).

One can then deduct that whichever further modification undergone by $C_{60}$ rises the LUMO energy level, and this may increase the $V_{OC}$ of a resultant OPV device for any given polymer.

### 2.5.2 Electron Affinity (EA)

Brabec *et al.*[117] showed that the $V_{OC}$ of the plastic OPVs are independent of the device geometry and thickness of the film, but it is strongly correlated to the reduction potential of the fullerene derivative. Lenes *et al.* [124] showed that the $V_{OC}$ of a polymer-fullerene cell has a negative linear relation with the first reduction potential of the $n$-type molecule used only for device with ohmic contacts. Others then confirmed a similar relationship but with the first oxidation potential of the $p$-type material.

The electron affinity of these fullerene bis-adducts were also analyzed since there is a direct relation between the $V_{OC}$ and accepting potential of the fullerenes. The first EA values for these compounds are calculated in the same level of theory[19] [20]. This can be calculated in two scenarios: vertical or adiabatic. For the former, one electron of the neutral molecule is removed without letting the geometry to relax (vertical electron affinity) whereas for the latter, the relaxation of the molecular coordinates is allowed. The difference between the ground state total energy of the neutral molecule and the total energy of the reduced state gives the EA value.

Within Janak's definition of electron affinity (EA), one has:

$$EA = E(N_0) - E(N+1) \tag{2.6}$$

Where $N_0$ states for the number of electrons in the ground state and $N+1$ stands for the number of electrons of the ground state with another electron added to it (negatively charged specie).

It is interesting to note that this definition is the one that should be used within DFT method, where Koopmans' theory cannot hold. In a Hartree-Fock (or whatsoever other wavefunction-based method - where the correlation energy is not explicitly treated) scenario, EA would be defined as the negative of the LUMO energy, and this assumes no orbital relaxation during reduction. Within DFT, Janak's definition of EA takes into account this specific orbital relaxation although the molecule may or not be allowed to relax within the internal coordinate system (see next section on Reorganization Energies).

Figure 2.19 presents these results.

---

[19] Based on the structures just beforehand obtained, using an unrestricted Kohn-Sham scheme (UKS) applied to the self-consistent field.

[20] Diffuse functions were not used here, although their use is recommend and almost mandatory for the calculation of anion-like species. There are huge electron density convergence problems for fullerene-based materials in the anionic state using these functions. Morever, besides the common sense, Treitel *et al.* indicate that molecules with extended conjugation do not need these functions for calculating electron affinity, whereas they are highly needed in the calculation of NMR shifts, for example. In this way, we believe that the extended conjugation found in the molecules herein proposed makes that the non-use of diffuse functions has a very little effect on the final electron affinity of the molecule and this difference is on the order of 1 meV.[125] Also, the absence of of polarizability effects (no solvent) imposes quite a large error in the calculation of charged species that should be taken into consideration if absolute values are required, what is not the case here.

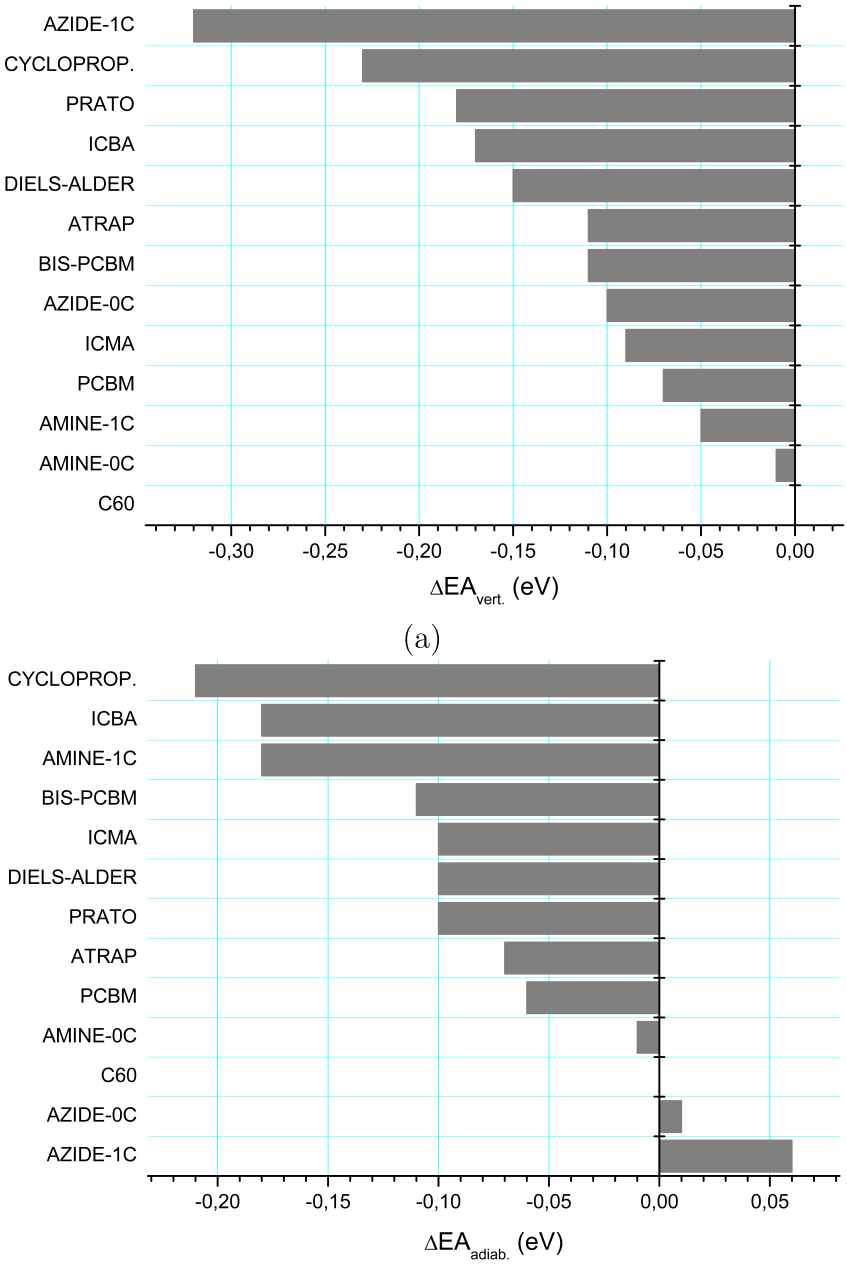

(a)

(b)

**Figure 2.19:** Electron Affinity deviation compared to $C_{60}$ for the studied compounds altogether the common fullerene-derivatives used nowadays ($PC_{60}BM$, bis-$PC_{60}BM$, $IC_{60}MA$ and $IC_{60}BA$). In (a), the vertical electron affinity is presented and in (b), the adiabatic one is presented.

Within the vertical scenario, one can note that whichever attack happens to the fullerene sphere causes a decrease on the electron affinity, what is, in theory, associated to a lower electron acceptor character. However, in an adiabatic scenario, Azide-based molecules present positive deviations, meaning that these molecules seem to be *as good as* $C_{60}$ as an electron acceptor, or at least it does not prejudice this property. In a general way, Cyclopropanation-based molecules seem to be the most sensible on this property.

### 2.5.3 Electrophilicity

All that said, common sense tells us that the efficiency of an acceptor in solar cells depends not only on its electron affinity so that a surrounding electron can be absorbed, but also on its resistance against electron back transfer to a donor molecule. So, two parameters come to mind in order to quantify and predict the efficiency of the OPV made using such $n$-type materials for a given $p$-type polymer by looking on their LUMO energies and on their first electron affinities (EA) calculated within the Janak's scheme. Anafcheh *et al.*[126] showed that, generally, there is a linear correlation between experimental $V_{OC}$s and theoretically-calculated LUMOs and EAs. Within Density Functional Theory standard calculations, one can define as well a global index for the electrophilicity strength of a system as it was defined by Parr *et al.*[127] This index correlates the quantitative chemical concepts of the electronic chemical potential ($\mu$) and hardness ($\eta$). Such quantity can then be assigned as a basis for evaluating how electrophilic a system is by using $\mu$ to measure the propensity of the system to acquire an additional electron from adjacent electron-rich species, and by means of $\eta$ to describe the resistance of the system to exchange this electron with the environment.

Finally, the electrophilicity index, as described before, seems also to be a good indicative on the acceptor properties of fullerene-derivative materials, since it also measures their resistance to electron back transfer, and it is indeed determinant for OPV efficiency. The chemical quantities $\mu$ and $\eta$ have been interpreted by Parr *et al.*[127] as the first and second partial derivatives, respectively, of the electronic energy with respect to the number of electrons at a constant external potential $\nu(r)$. This means that the geometry is unchanged between the two states and represents then a vertical regime. Mathematically, we have:

$$\mu = \left(\frac{\partial E}{\partial N}\right)_{\nu(\vec{r})} \tag{2.7}$$

$$\eta = \left(\frac{\partial^2 E}{\partial N^2}\right)_{\nu(\vec{r})} \tag{2.8}$$

Assuming that $E(N)$ can be differentiated (it is a continuous function on the number of electrons), it can be expanded as a Taylor function around $N_0$ (the number of electrons of the neutral system) using the definitions of $\mu$ and $\eta$ given just before:

$$E(N) = E(N_0) + (N - N_0)\mu + (N - N_0)^2\frac{\eta}{2!} + (N - N_0)^3\frac{\gamma}{3!} + ... \tag{2.9}$$

Where $\gamma$ has no physical meaning. If a finite difference approximation is employed considering a quadratic $E = E(N)$ curve, $\mu$ and $\eta$ could be given by:

$$\mu = \frac{E(N+1) - E(N-1)}{2} \tag{2.10}$$

$$\eta = E(N-1) + E(N+1) - 2E(N_0) \tag{2.11}$$

Using Janak's definition of ionization potential (IP) and electron affinity (EA):

$$IP = E(N-1) - E(N_0) \tag{2.12}$$

$$EA = E(N_0) - E(N+1) \tag{2.13}$$

We can then rewrite $\mu$ and $\eta$:

$$\mu = \frac{-(IP + EA)}{2} \tag{2.14}$$

$$\eta = IP - EA \tag{2.15}$$

Finally, the electrophilicity ($\omega$) can be defined as:

$$\omega \equiv \frac{\mu^2}{2\eta} \tag{2.16}$$

This index is proposed like this in analogy to the power equation of classical electricity ($Power \equiv W = V^2/R$, where $V$ stands for the voltage on the terminal of any given resistor with resistance $R$). In this way, one can think of $\omega$ as a sort of "electrophilic power", as described originally by Parr *et al.*[127]

Figure 2.20 shows these results.

From this, we can deduct that the disruption of equivalent double bonds on the fullerene sphere does not interfere in the same way for the studied compounds. For example, taking bis-PC$_{60}$BM and cyclopropanation-obtained molecule, which have the same type of attack on the same position over the sphere, they present very different electronic behaviors to their acceptor properties. This means that the presence of a

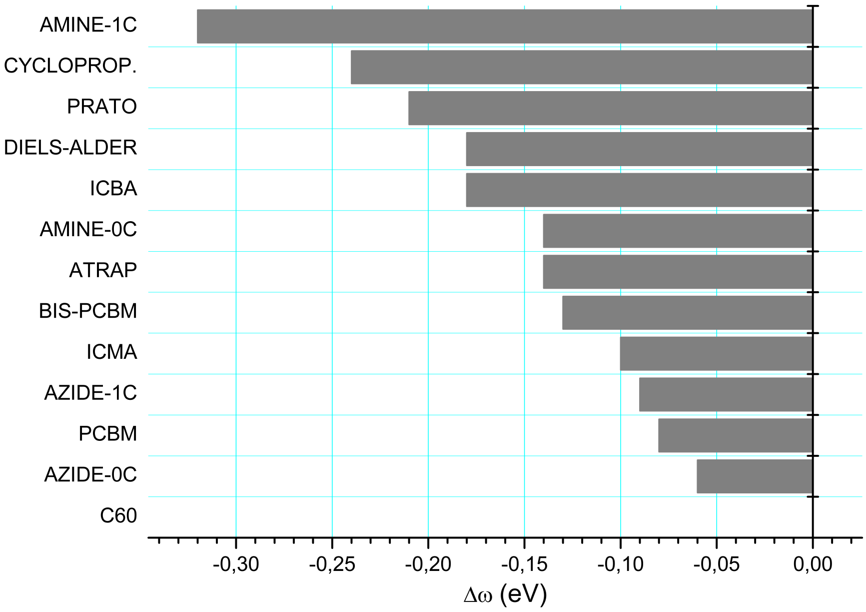

**Figure 2.20:** Electrophilicity deviation compared to $C_{60}$ for the studied compounds altogether the common fullerene-derivatives used nowadays ($PC_{60}BM$, bis-$PC_{60}BM$, $IC_{60}MA$ and $IC_{60}BA$).

lateral comonomer is sensed by the conjugation of the fullerene and may hinder the $n$-type character of the designed material.

Moreover, it is remarkable the fact that, again, Azide-based compounds seems to preserve (or at least disrupt as minimum as possible) the electron acceptor properties of $C_{60}$, whereas the others significantly hinders it.

## 2.5.4 Reorganization Energy

The aforementioned properties are calculated from vertical transitions for isolated molecules. They do not take into account the contribution of the environmental molecules and any geometrical reorganization induced by the charge acceptance.

In order to account for these effects in the estimation of the electron acceptor character of new molecules, the semi-classical Marcus theory proposes a well-documented model to estimate these effects on the charge transfer.

Rudolph A. Marcus [128] originally proposed a model to explain the rates of electron-transfer reactions induced by a hopping mechanism based on the evaluation of the mobility $\xi$[21], which is defined in function of the charge-transfer rate (hopping probability per unit time) $k_{CT}$ as:

$$\xi = \frac{ea^2}{2k_BT}k_{CT} \tag{2.17}$$

Where $k_B$, $T$, $a$, and $e$ are the Boltzmann constant, temperature, transport dis-

---

[21] Normally, the mobility is also denoted by the Greek letter $\mu$, but here we are already using it to represent the electrochemical potential. Then, to describe mobility, we use the Greek letter $\xi$.

tance and electronic charge, respectively. The transport distance can be obtained from a quantum-chemistry geometry optimization. The function $k_{CT}$ can be expressed as follows:

$$k_{CT} = \frac{2\pi}{\hbar^2} t^2 \sqrt{\frac{1}{4\lambda\pi k_B T}} \exp\left[\frac{-(\Delta G^0 + \lambda)^2}{4\lambda k_B T}\right] \tag{2.18}$$

Where $t$, $\hbar$ and $\lambda$ strand for the transfer integral, the reduced Planck's constant and the inner reorganization energy, respectively. The $\Delta G^0$ term stands for the difference in the Gibbs free energy of the system before and after the charge-hopping process and is equal to zero if the molecular segments are equal.

Finally, the reorganization energy $\lambda$ comes from the vibrational structure change due to the electron gain/loss process of the segment.[129, 130] It is defined as:

$$\lambda = \lambda_1 + \lambda_2 \tag{2.19}$$

$\lambda_1$ and $\lambda_2$ are, respectively, the energy difference due to the structural relaxation of gaining one electron by the molecular structure and the energy difference of losing one electron. In other words, $\lambda_1$ is the difference between the neutral state energy of the ionic state geometry and the ground state energy of the native state. $\lambda_2$ is then the difference of the ionic state energy in the ground state geometry and the ionic state energy in the ionic state geometry as well. Schematically, for the reaction coordinate system $Q$, it can be depicted as found in Figure 2.21, where the two quadratic potential energy curves are depicted, for both ground and ionic state. The vertical transitions are represented by full-trace arrows and the relaxation on the coordinate system are illustrated by curved-dotted arrows.

Based on this model, in order to maximize the mobility of a given material, one must decrease the reorganization energy, for a given temperature and interatomic distance. This is direct from the concept of energy payback. Overall, the transport mechanism in organic semiconductors results from a balance between the energy gained by the electron delocalization in the electronic state and the energy gained by the geometry optimization of an individual chain around the charge to form a polaron. This term, in specific, is denominated the polaron binding energy ($E_{pol}$), which measures efficiently the stabilization energy of the charged stated by the molecular deformation. In this way, the lower this energy, the higher the polaron is stable and localized, and the lower is the charge-transfer rate, lowering as well the mobility of the material.[131] Mathematically:

$$E_{pol} = \frac{1}{2}\lambda \tag{2.20}$$

These quantities were calculated for the proposed model materials using an unrestricted open-shell wave function scheme for the Kohn-Sham orbitals (UKS). Although the spin contamination is not a pathologic effect in DFT calculations, we monitored the

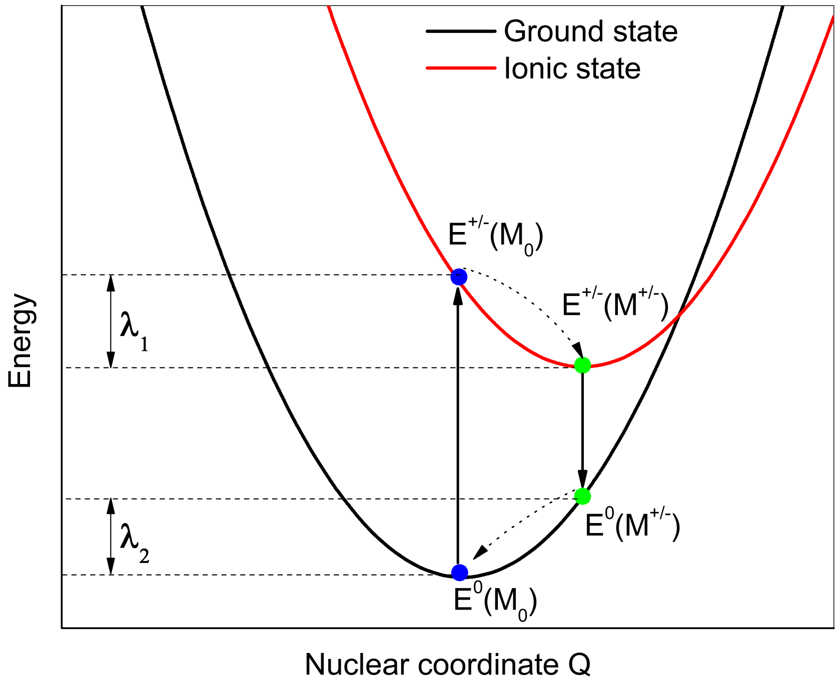

**Figure 2.21:** Reaction coordinates space representation of the reorganization energy in function of the ionic and ground states.

mean value of $< S^2 >$ in order to have it deviated at maximum 10% of the expected value of a $\frac{1}{2}$ spin system. The ground state, however, was calculated in a restricted open-shell scheme (RKS), not allowing any spin polarization. As we are interested in an electron-gain process, only the significant anionic species have their reorganization energies herein presented.

In Figure 2.22, we can find the anionic reorganization energy for the model compounds compared to the reference $n$-acceptor materials.

If one takes a closer look on the total anionic reorganization energy, one can note that Azide-, Prato- and Cyclopropanation-based molecules have a comparable lower energy payback under reduction if compared to the other molecules. On the other hand, indene-based molecules disrupt as minimum as possible this property of the fullerene, being very close to the original value.

### 2.5.5 Transfer Integral

The transfer integral $t$ of a given system is related to the energetic splitting of electronic levels, attributed to the interaction between adjacent segments. For an electron-hopping process, this can be given by:

$$t = \frac{1}{2}\sqrt{(E_{L+1} - E_L)^2 - (\epsilon_1 - \epsilon_2)^2} \tag{2.21}$$

$E_{L+1}$ and $E_L$ are the energies of the LUMO+1 and LUMO molecular orbitals of the

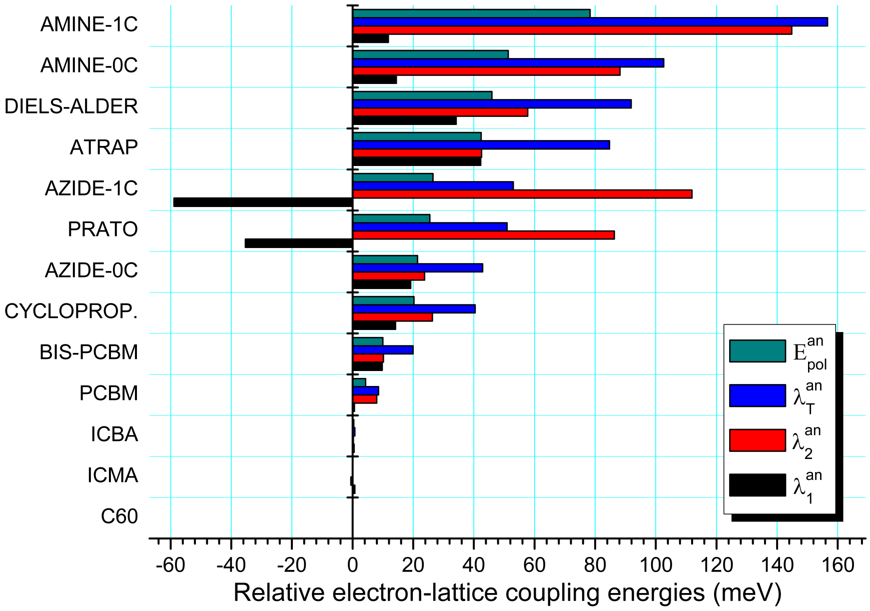

**Figure 2.22:** Reorganization energies of the anionic state and associated polaron energy for the proposed model compounds.

interacting segments (representing the splitting of the individuals LUMOs due to the interaction) and $\epsilon_{1,2}$ are the total energies of the molecular segments. As they are equal, $\epsilon_1 = \epsilon_2$. A final form of the equations is:

$$t = \frac{1}{2}|E_{L+1} - E_L| \tag{2.22}$$

In order to estimate the **intra-chain** transfer integrals, one needs to construct dimer molecules from the proposed polymerization routes. These dimers, besides the possibility of multi-isomer bis-adduct formation, can adopt two different spatial conformations, as described by Gügel *et al.*[132]. For the ATRAP dimers, Figure 2.23 depicts these two possible spatial conformations. For these ones, the *cis* configuration is energitically more stable than the *trans* by 6.2 kcal/mol (HF-3C) (9.2 kcal/mol - B3LYP/6-31G** with dispersion corrections). This is due to the fact that the dispersion energy between the two adjacent fullerenes overwhelms the nuclear repulsion of the pair.

Visibly the transfer integral depends on the *cis* or *trans* spatial conformation of the dimers. The closer proximity of the *cis* conformers is not a constant across all the proposed polymeric molecules. For some of them, these two conformations are almost unchanged and this is based on the geometrical arrangement of the functional group attached to the fullerene sphere.

Hence, dimer structures of the six presented polymerization routes were constructed based on the *trans-1* bis-adducts and fully optimized in both *cis* and *trans* configurations using the HF-3C method.[22] This use of this lower-level-of-theory method was motivated

---

[22] This method is based on the Hartree-Fock method using a minimal Gaussian basis set and to which, corrections on the long-range interactions and the energy are applied. More details can be obtained in

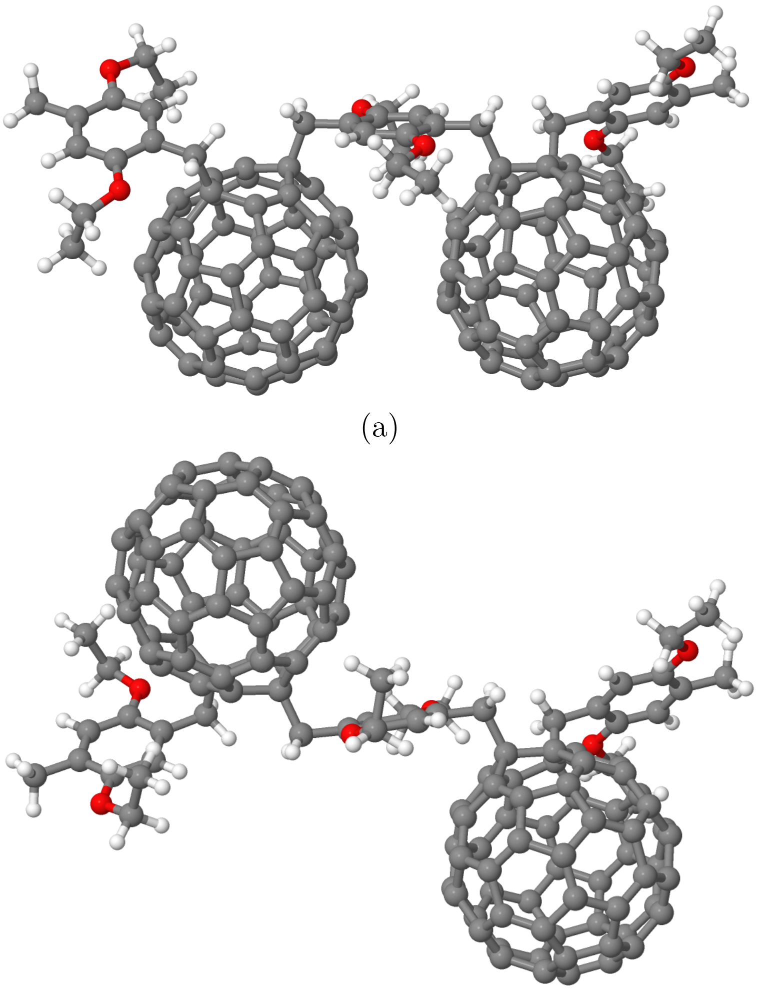

(a)

(b)

**Figure 2.23:** (a) *cis* and (b) *trans* conformers of ATRAP-based dimers.

by the high number of atoms of the dimer molecules (∼ 300). Even though one can increase the number of cores to speed up the calculation, it is not feasible based on the memory storage needed. Decreasing the number of cores, the amount of computational memory is also reduced but the time of calculation is not practical. The use of this method for geometry optimization followed by B3LYP/6-31G** single-points was a good compromise to estimate the splitting of the LUMO(+1) orbitals.

Figure 2.24 depicts the calculated intra-chain transfer integrals across the series of molecules for the two different spatial conformers.

One can note that in a general manner, the *cis* configurations present higher values of transfer integrals, what is expected seen the fact that the two fullerenes of the dimer are closer, and hence their LUMO's are more split. The values obtained by the Cyclopropanation- and Azide(no intermediary carbon)-based compounds are remarkable since this configuration of the functional group forces the fullerenes to assume spatial

---

ref. [133].

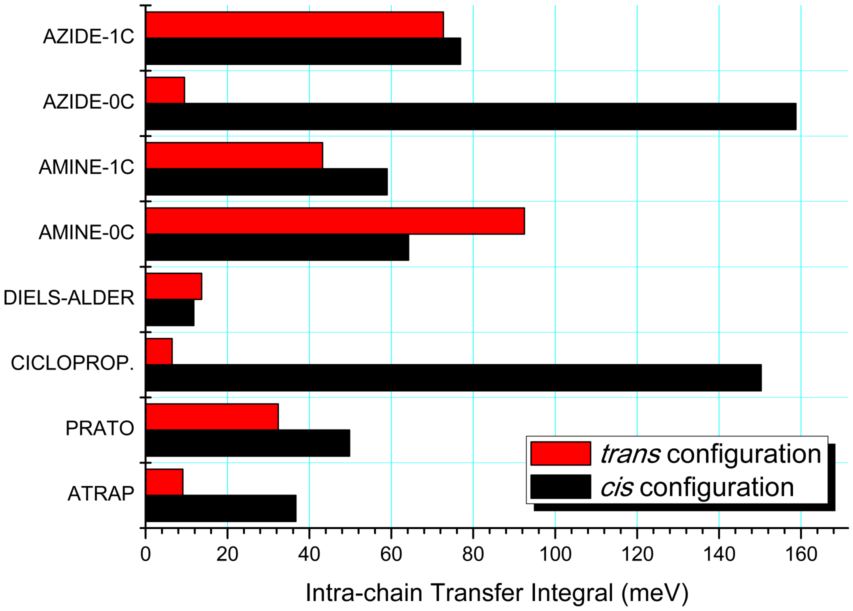

**Figure 2.24:** Intra-chain transfer integrals calculated for the series of dimers constructed in *cis* and *trans* configurations.

configurations minimizing their intermolecular distance. In contrast, molecules based on Diels-Alder present low transfer integrals and this is based on the fact that regardless the configuration, both fullerenes are at least $\sim 20\text{Å}$ apart.

With this in hands, we have estimated the electron mobility using the reorganization energy values obtained for the monomers (bis-adduct fullerenes). This is not the most indicated methodology because there are two different methods being used at the same time to solve the Marcus equation and also because the fact that the reorganization energy is not calculated for the dimers. Even so, these results are presented in Figure 2.25.

It is clear that the electron mobility is generally lower in *trans* configurations. Moreover, it can vary at least one order of magnitude across the different molecules for a same configuration, as it is the case of of Diels-Alder- and Azide-based compounds. This is true because the former has an increased separation of the fullerene molecules within the dimer caused by the functional group.

In the real system, both configurations are assumed to coexist, what will induce a spreading of the electron mobility of the system across one chain. The average of these values indicate that polymerizing fullerenes using one of these six routes would produce materials with intra-chain mobilities between $1.10^{-7}$ and $1.10^{-6}$ $cm^2.V^{-1}.s^{-1}$.

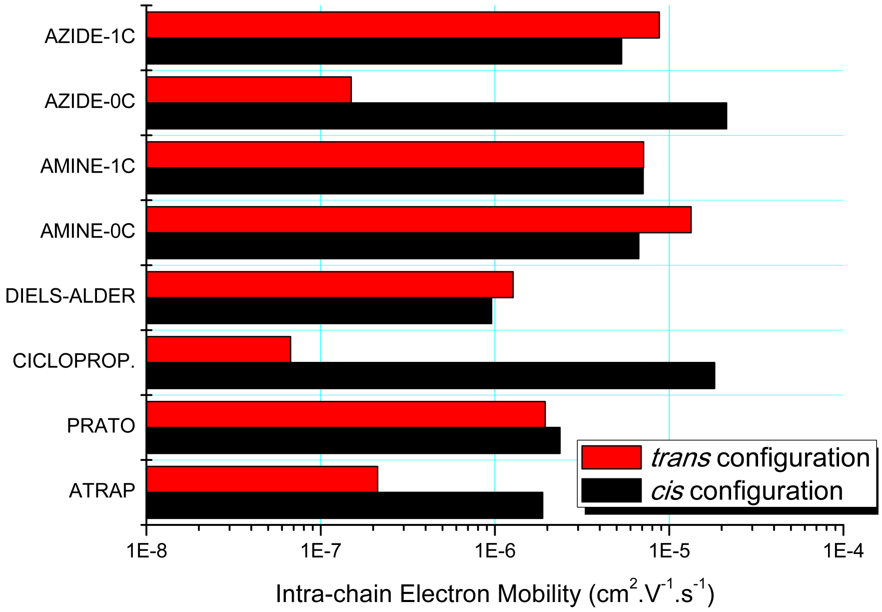

**Figure 2.25:** Intra-chain electron mobility calculated for the series of dimers constructed in *cis* and *trans* configurations.

## 2.6 Final Remarks

In this chapter, six chemical routes able to form at least bis-adducts of fullerenes were investigated on the electronic point of view. These routes are able to theoretically produce polymers and electronic parameters such as LUMO energy, electron affinity, electrophilicity, reorganization energy, intra-chain transfer integrals and electron mobilities were calculated. Some of these properties were compared to the currently used $n$-type materials such as (bis-)PC$_{60}$ and the indene-derivatives such as IC$_{60}$MA and IC$_{60}$BA.

The position of the formation of the bis-adduct was also studied and the compounds with routes based on a pericyclic reaction (Azide, Cyclopropanation, Diels-Alder and Prato) tend to form *trans-3* and *trans-2* isomers. The Amine-based compounds, regardless of the mechanism behind its formation, may preferably induce the formation in the *cis-1,2,3* and *equatorial* positions.

Using artificially constructed *trans-1* isomers, the electronic properties of these compounds were studied and compared to the benchmarks. One can then state:

- No matter the modification of C$_{60}$ that is done, the LUMO energy level is always going to be shifted. It means that, theoretically, the V$_{OC}$ of OPVs can be increased by using bis-functionalized fullerenes.
- This is the same for the vertical electron affinity, but the adiabatic value can beat C$_{60}$'s values, as is the case of the Azide-based compounds.
- The electrophilicity index follows the same trend and states Azide-based compounds as the ones that are interesting to be used as $n$-type materials, competing in the same class as the already currently used materials.
- Considering the anionic reorganization energy, the fact of adding a comonomer to the structure of the fullerene increases the energy payback during reduction, but Azide- and Cyclopropanation-based materials, for example, are remarkable for keeping this value as low as possible and comparable with (bis-)PC$_{60}$BM molecules.
- The dimers of bis-adducts can assume *cis* and *trans* spatial conformations and the transfer integrals of the former are generally superior to the ones of the latter. Again, Azide- and Cyclopropanation-based molecules in the *cis* configurations are remarkable.
- Finally, the estimation of the electron mobility indicates that these two compounds are the ones with the highest intra-chain electron mobility based also on the fact that the functional groups in place force fullerenes to stay closer. Moreover, one can find at least one order of magnitude of difference between the two configurations.

In this way, it seems that Azide- and Cyclopropanation-based molecules are interesting as electron acceptor molecules only if one can have an increased control on the spatial configuration of the chains. Maybe it would be interesting to achieve these products using multi-steps routes such as the Diels-Alder one, so that this control may be thinkable.

So, the final argument that should state a route interesting to study is the stability of the resultant materials. Retro-Diels-Alders reactions are known, and in this way, the link between the monomer and the fullerene can be broken. Similarly, radical based reactions can also suffer the same degradation pathway thermally or light induced, and this is going to be studied throughout this thesis. The routes with formation of 5-membered rings with consequent expulsion of $N_2$ molecule (Azide and Cyclopropanation) may be again worth trying in the future because once the 3-membered ring is formed, it is very difficult to break it apart based on the double-bond characteristics of it (compared to the single bond of all the others).

# Chapter 3

# Syntheses of Polyfullerenes

*This chapter is dedicated to the synthetic routes used to achieve polymers by ATRAP route. It is divided in the following way: section 1 - an overview on fullerene-containing polymers and their application to photovoltaics; 2 - synthesis of monomers derived from hydroquinone; section 3 - synthesis and characterization of polymers derived from 1,4-dibromomethyl-2,5-dialkoxyphenylene. It will cover the basics of each reaction and procedure used and one can found a discussion on the mechanism for the polymerization reaction herein used.*

## 3.1 Fullerene-containing polymers and photovoltaics

In Chapter 1, the general characteristics of fullerene-containing polymers and their application on organic photovoltaics have been described. Moreover, some general desired design parameters that these materials should follow were described in Chapter 2. Here we take over some of the important concepts that are believed to play a role on the synthesis and development of morphologically stable materials.

These materials are classified accordingly to their chemical structure and how fullerenes are incorporated into the polymeric chain, as presented in Chapter 1, Figure 5. It is a consensus that the most challenging routes are those of main and side chain polymers, for those the synthetic control needed slowed their development down over the last years.

On the other hand, the mechanisms involved in the photovoltaic effect in organic structures demand, on the same time, an optimal crystallization of the donor and acceptor materials and a good miscibility among them. In this way, both light can be appropriately absorbed and charges can be dissociated and transfered to the electrodes. Nevertheless, the two materials' phases self-assemble to form bi-continuous inter-penetrating networks that tends to be a bottleneck under annealing and operational conditions. This is so because of the "like likes like" behavior that takes place in the bulk and creating strategies to make these structures compatible are highly desired in order to obtain longer lifetimes OPVs.

The possibility of designing and synthesizing new main-chain polyfullerenes that could efficiently be employed as an electron acceptor and/or a morphological stabilizer in BHJ-OPVs is a promising way to contribute. In this field, the work performed by Hiorns *et al.*[61] presents easily-accessed fullerene-based polymeric materials and their application in devices. The chemical route used by this group consists on the use of a so-called ATRAP route.

In this procedure, chain ends created during a polymerization reaction are reacted with $C_{60}$ using atom transfer radical addition (ATRA). This chemistry was chosen by its easiness, the fact that the paired additions on the fullerenes only disrupts one double bond for each attack, perturbing the minimum the electronic structure of the sphere. The materials synthesized in this way have been used by these authors as pure electron acceptors blended with P3HT donor polymers in OPV devices, as well as to the development of donor-acceptor multiblock copolymers in which fullerene backbone was incorporated as repeating unit.[62] These materials present controllable solid-state domains that can be finely tuned for application in OPVs. Figure 3.1 represents the intended structures synthesized back then.

Another advantage of this chemistry is the theoretical non-formation of the 8 stereoisomer multi-adducts that are obtained using other reactions. In this way, linear main-chain fullerene molecules can be obtained with a high control of the double-addition. Using these very same arguments, this radical copolymerization reaction can decrease cross-linkings through the polymeric matrix. Ahead one can find the detailed description for the synthesis of the polyfullerene materials.

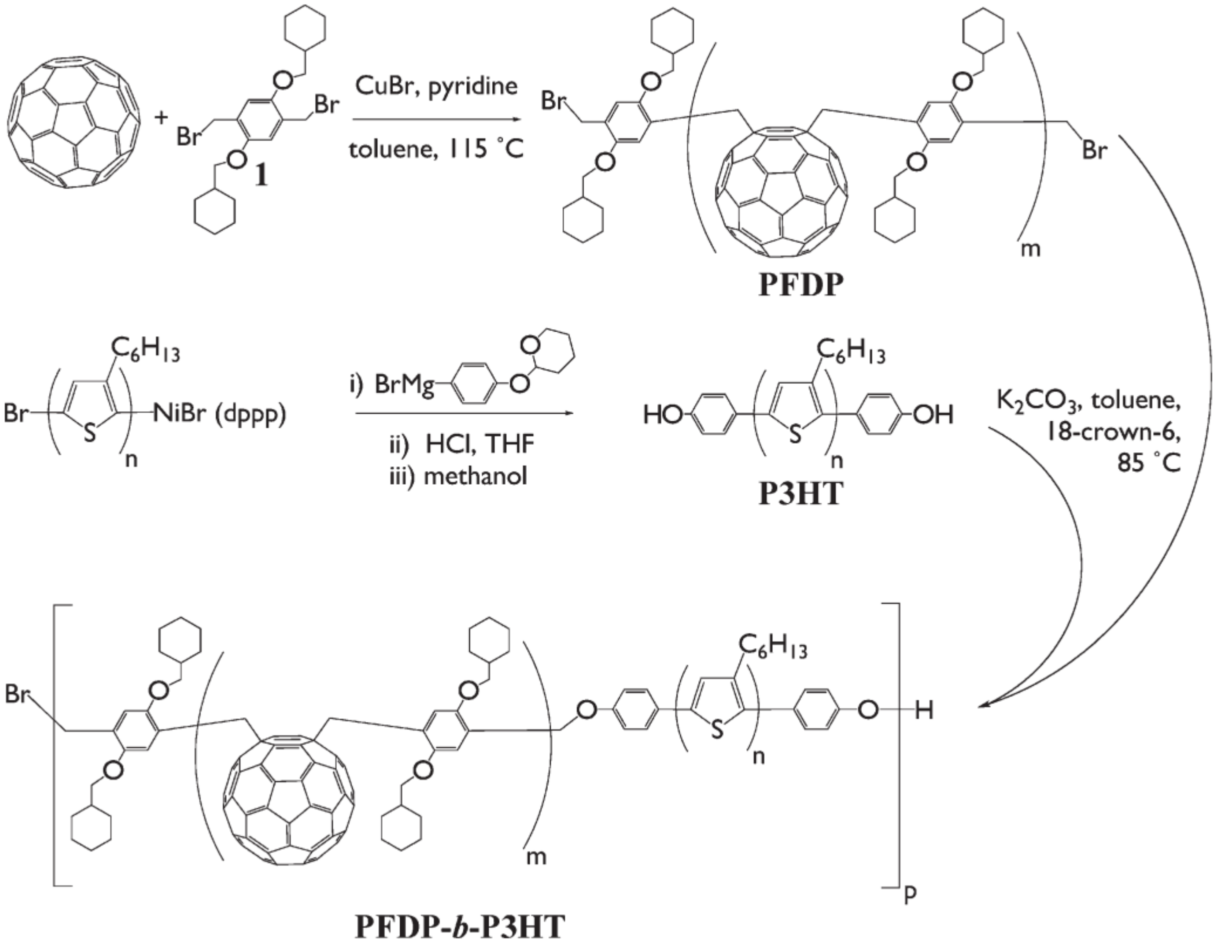

**Figure 3.1:** General scheme of the route used by Hiorns *et al.* to synthesize multiblock copolymers based on ATRAP fullerene chemistry.

## 3.2 Synthesis of monomers derived from hydroquinone

Molecules of the type 1,4-dibromomethyl-2,5-dialkoxyphenylene have been the first ones studied with this new type of polymerization able to successfully insert fullerene into the main-chain of ATRAP polymers. Prior work demonstrated the efficiency of polymerizing such very simple molecules and their ability to form polymeric structures in appreciable quantities.[62] Due to its simple synthesis and handling, these comonomers display as well an excellent ambient stability due to its elevated ionization potential and oxygen-protected lateral branches, as it will be described in the next chapter. One can find in Figure 3.2 the general chemical route to achieve to the monomers.

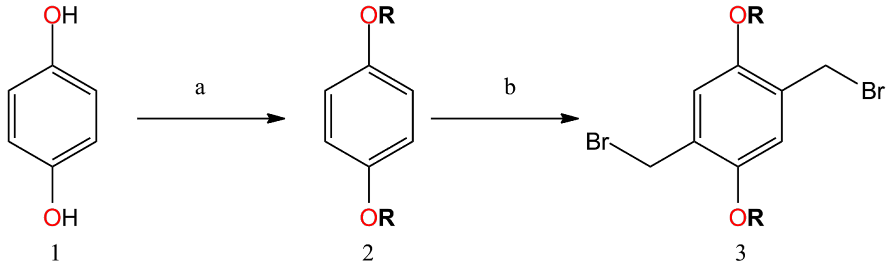

**Figure 3.2:** Synthetic route used to obtain 1,4-dibromomethyl-2,5-dialkoxyphenylene monomers.

The lateral chains **R** used can be found in Figure 3.3. The choice of these lateral chains was driven by the hypothesis that bulky[134] or long lateral chains can ensure insertion of solvent between fullerenes and thus controlled additions to $C_{60}$ can be obtained, besides materials with a better solubility.[135] Longer alkyl chains can also produce materials with low chain-mobility in bulk and with some extent of phase segregation, which may be optimal for the required photovoltaic standards.[136] Moreover, based on the stereo-electronic behavior of $C_{60}$, the steric nature of the incoming group may influence strongly the point of addition around the sphere. Finally, it is believed that the use of long linear alkyl chains may induce a liquid-crystal behavior on the molecule, which may also present lamellar structure.[137, 138, 139, 140, 141] In order to explore the most these sought-after properties, one can propose these lateral branches as representatives of bulky/non-bulky behavior (keeping constant the number of carbons - *n*-octyl, 2-ethyl-hexyl and (cyclohexane)ethyl) and of the long linear chains (*n*-octyl, *n*-dodecyl and *n*-hexadecyl). Last but not least, bulky or long-chain substituents prevent close contact among fullerene spheres, thus improving solubility.

The reaction conditions for each step are the following: a - $K_2CO_3$, *RBr* and Acetone ($CH_3CN$, DMF or DMSO can also be used, being Acetone safer and easier to evaporate), reflux, 48 h, in air; b - paraformaldehyde, HBr (33% in $CH_3COOH$), $CHCl_3/CH_3COOH$ (1:1 vol.), 50-80 °C, 2-48 h. These conditions needed to be modified upon the lateral branch since the kinetics of the bromomethylation step is highly dependent on the solu-

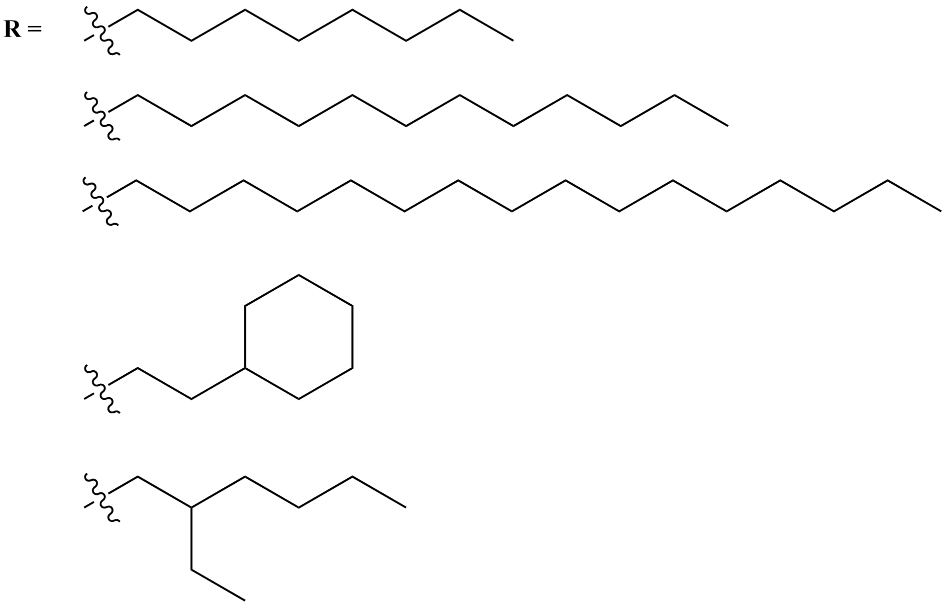

**Figure 3.3:** Lateral branches R used for monomers synthesis, from top to bottom: *n*-octyl, *n*-dodecyl, *n*-hexadecaloxy, (cyclohexane)ethyl, and 2-ethyl-hexyl.

bility of **2** and on the polar character of the reaction medium[142]. In this way, while for the shorter lateral chains as *n*-octyl, 2-ethyl-hexyl and, (cyclohexane)ethyl $CH_3COOH$ only can be used as solvent for the reaction, [143] the same is not true for the ones with *n*-dodecyl and *n*-hexadecaloxy lateral chains: these are not completely soluble in such polar conditions and need to have the polarity of the reaction medium controlled by using a co-solvent as $CHCl_3$, $CH_2Cl_2$ or $CH_2Br_2$. However, one must consider that in this way the electrophilic species are weakened (less supported) and the acid concentration should then be increased.

While step **a** is characterized by a $S_N1$ (monomolecular nucleophilic substitution) reaction, step **b** is a typical $S_EA$ (aromatic electrophilic substitution) followed by a $S_N2$ (bimolecular nucleophilic substitution). This implies that the choice of solvent, the concentration of electrophilic species for the first step and the pH of the medium are extremely important to control the completeness of the reaction as well as its rate of conversion. Once the traditional conditions used for the longer alkyl-chained molecules, one can find, by NMR analysis, that the conversion is not total and one has then a complex mixture of bisbromomethylated, monobromomethylated and non-reacted substrates which can be separated neither by precipitation/crystallization nor by Flash Chromatography, for instance. The same is also valid for more complex molecules that have been tested but are not reported in this document. Figure 3.4 presents the $^1$H NMR peak of the bromomethylated *n*-hexadecaloxy-derivative molecule with partial and total conversion accompanied by both the $-CH_2Br$ protons (around 4.4 ppm) and the aromatic ones (around 6.8 ppm).

Because of such importance to have pure bisbromomethylated substrates in order to

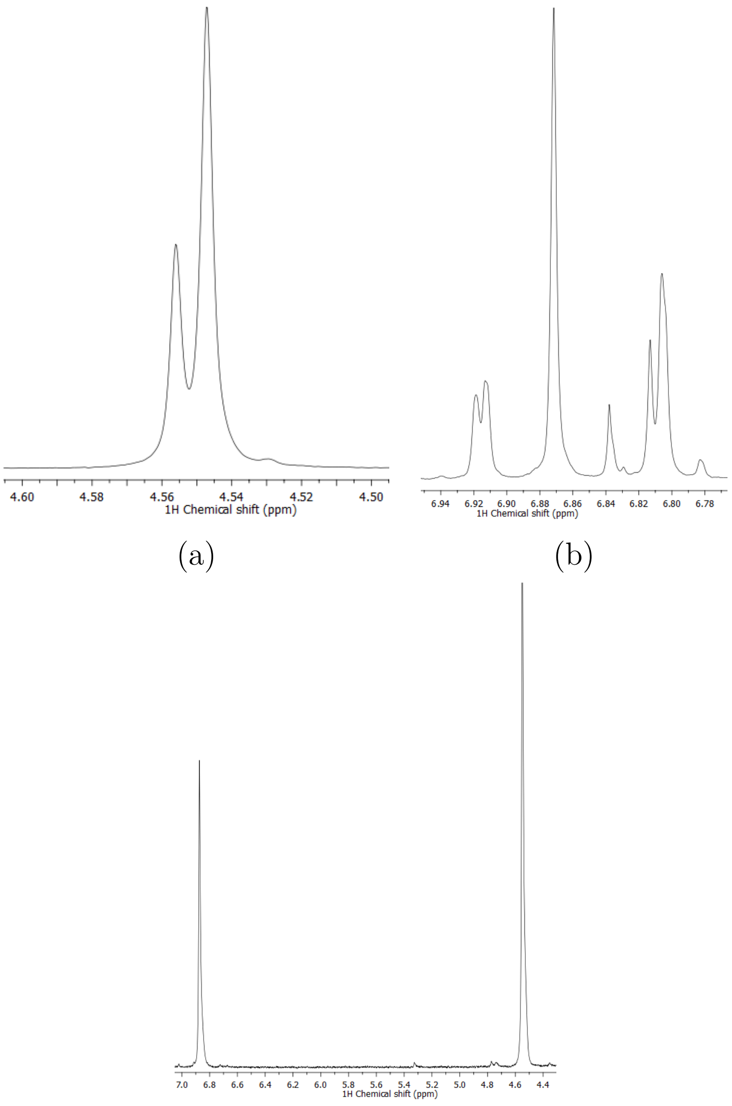

(a) (b)

(c)

**Figure 3.4:** $^1$H NMR signal used to evaluate the conversion during bromomethylation reaction. In (a), the -$CH_2Br$ protons signal of a partially-converted molecule are presented, where one can note the split when one should expect a single peak; in (b), the aromatic protons of the same molecule are split as well and may be interpreted as the pristine, the target and mono-bromethylated molecules, which are responsible for the diversity of signals. The peak centered in 6.87 ppm is the one one should expect in the case of a bis-bromomethylated aromatic core. Finally, in (c), one can find these peaks for the case of a total conversion, following the procedures described in Appendix A accordingly to the conditions explained above.

avoid the occurrence of early dead-chains during the polymerization, this reaction was fully explored so that one can drive it to completeness. Moreover, based on its easiness, it was preferred to study how to push it further instead of changing the reaction scheme passing through other intermediates. It is then worthy to analyze its mechanism in details since it is an important piece of synthetic work during this thesis: without this direct functionalization by a bromomethyl group, a more time-consuming and indirect route should be used. This mechanism was first described by Blanc in 1923 [144] using hydrochloric acid [145] instead of hydrobromic acid and it can be found in Figure 3.5.

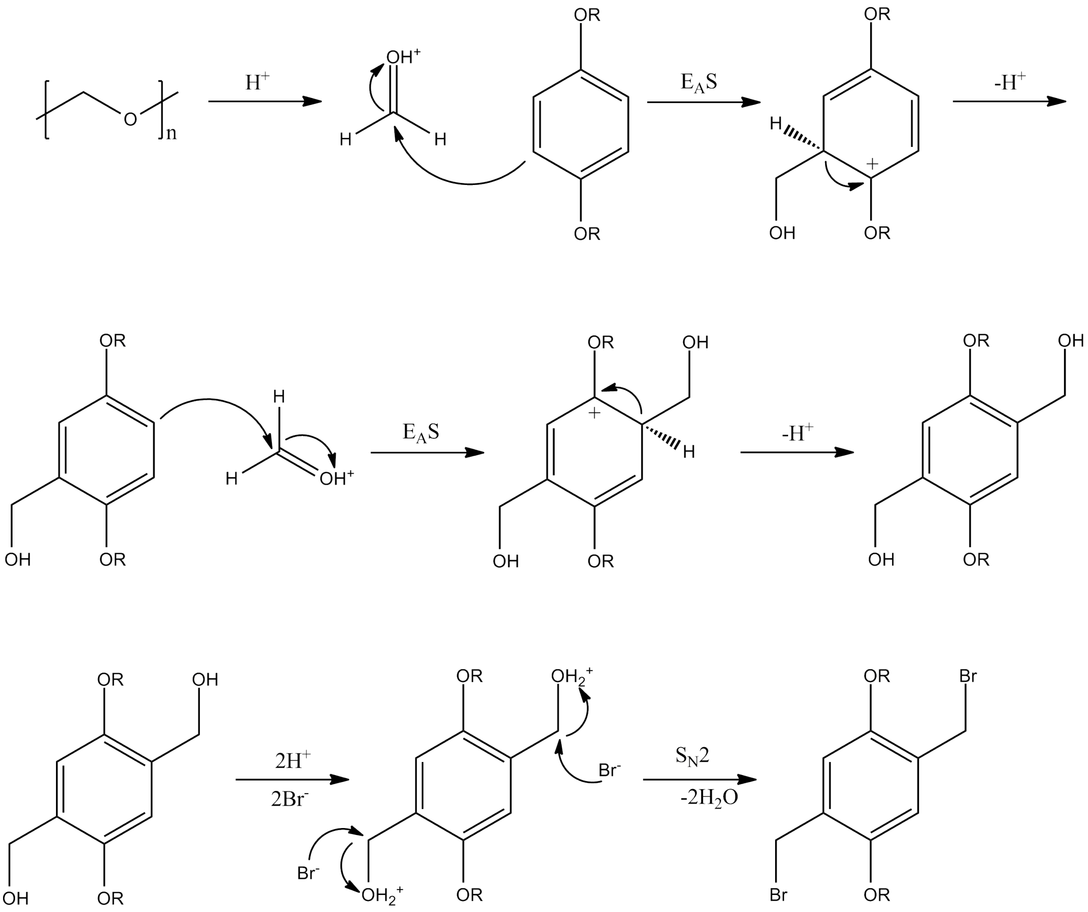

**Figure 3.5:** Mechanism for bromomethylation reaction on the studied substrates.

The very first step of the reaction [146] is consisted of the depolymerization of paraformaldehyde induced by the acid conditions and the formation of the electrophilic species by the protonation of the resultant formaldehyde. Theoretically, the same can be performed using 1,3,5-trioxane,[147] but we were not capable of having the same results. This species is stabilized by the polar conditions of the reaction and, if this character is decreased by the introduction of an apolar solvent,[148] as chloroform, which increases the solubilization of the substrate, such stability of the electrophilic agent should be regained by increasing pH; *i.e.*, the molar equivalence of hydrobromic acid should over-exceed the one of the substrate. In this way, one can assure that the electrophilic agent will not dissociate back to the neutral form of formaldehyde.

Once the electrophilic agent attacks the aromatic group, an arenium ion is formed with a hydroxymethyl group then covalently linked to it. After proton elimination, the system regains its neutrality and can be attacked once again in the *para* position to the first attack. Now, the alcohol group is protonated by the very acidic medium forming the good leaving group -$OH_2^+$. This allows the $S_N2$ reaction to take place, when bromine anion back-attacks the -$CH_2$ group, forming finally the desired bromomethyl group with elimination of water.

Some details should then be highlighted:

A - So that this reaction takes place, the solvent system should be compatible with the used substrate, *i.e.*, molecules with longer apolar chains are not completely soluble in highly polar solvents, as acetic acid or DMSO; thus, an apolar solvent should be used in order to drive reaction to completeness;

B - The medium must be polar enough to stabilize the electrophilic agent;

C - If condition A is satisfied with an apolar solvent, then the acid concentration should be increased in order to satisfy as well condition B;

D - A consequence of conditions B and C is the lowering of the rate of the formation of bis-substituted substrates. The reaction can then need up to 48 h and 80 °C to be driven to completeness, instead of 2 h at 60 °C;

E - If the substrate concentration goes high enough, the formation of side products due to a second addition are observed in a way of coupling two molecules together, as it is described by Blanc;

F - The workup of the reaction with such acid conditions needs some quenching of HBr after the bis-attack is accomplished. For this, methanol is used to extinguish HBr by forming bromomethane and water;

G - Driving the reaction to completeness, it can be purified by normal workup with sodium chloride and extraction in diethyl ether or dichloromethane.

The specific reaction protocols are given in Appendix A.

## 3.3 Synthesis and characterization of polymers derived from 1,4-dibromomethyl-2,5-dialkoxyphenylene

The monomers for those the syntheses were described in the last section were used as comonomers for the polymerization of $C_{60}$ fullerene molecules. This was achieved by **A**tom **T**ransfer **R**adical **A**ddition **P**olymerization (ATRAP).

The polymerization is based on the radical scavenger properties of fullerene $C_{60}$. Due to its thirty available double bonds and the high electron affinity (*ca.* 2.7-2.8 eV), it can trap instantly radicals created in the reaction medium. This property of fullerenes has been used to the development of anti-oxidants in polymeric bulks, as it is the case of the work reported by Fang *et al.*[149] and Pozdnyakovet al.[150] Moreover, radical reactions of fullerenes are also being used in fullerene chemistry in order to create several interesting molecules, as one can find in the review by Tzirakis *et al.*[102] Pharmaceutical industry is one of the targets interested in this chemistry so that fullerene can be incorporated in controlling many diseases that result from radical damage. The general reaction route is then described in Figure 3.6.

The mechanism involves the chain initiation of free radical polymerization by a brominated organic species in the presence of a transition metal halide (copper(I) bromide, in this case). The metal has a number of different oxidation states that allows it to abstract a bromine radical from the organobromine, creating a macroradical that starts the free radical polymerization, depicted in (1), which adds to the fullerene (2). The radical introduced onto the $C_{60}$ is converted into a fullerene-bromine bond by reacting with the catalyst in its higher oxidation state. Thus, the redox process gives rise to equilibrium between dormant (polymer-bromine) and active (polymer-radical) chains.[151] This fullerene-bromine bond is easily broken (3) and it is converted again to the radical form, coupling with another comonomer macroradical, what leads to the polyaddition (4). The equilibrium is designed to heavily favor the dormant state, which effectively reduces the radical concentration to a sufficiently low level to limit bimolecular coupling. That is why one can consider that reactions (5) and (6) are not major. Reaction (5) may indeed take place but with a probability at least 60 times lower than (2) or (4) (based on the number of available sites for the radical attack). The products so formed should be easily eliminated by the purification process. Finally, reaction (6) may also take place but as the formed bond between fullerenes is very easily broken, it should not be present in the crude material, even more if one considers the high temperature used for the synthesis.

This reaction is most likely a polyaddition (which is a step polymerization - in opposition to a chain polymerization) with fast formation of low molecular weight material and consumption of monomers, with a slow and steadily decreasing rate of consumption

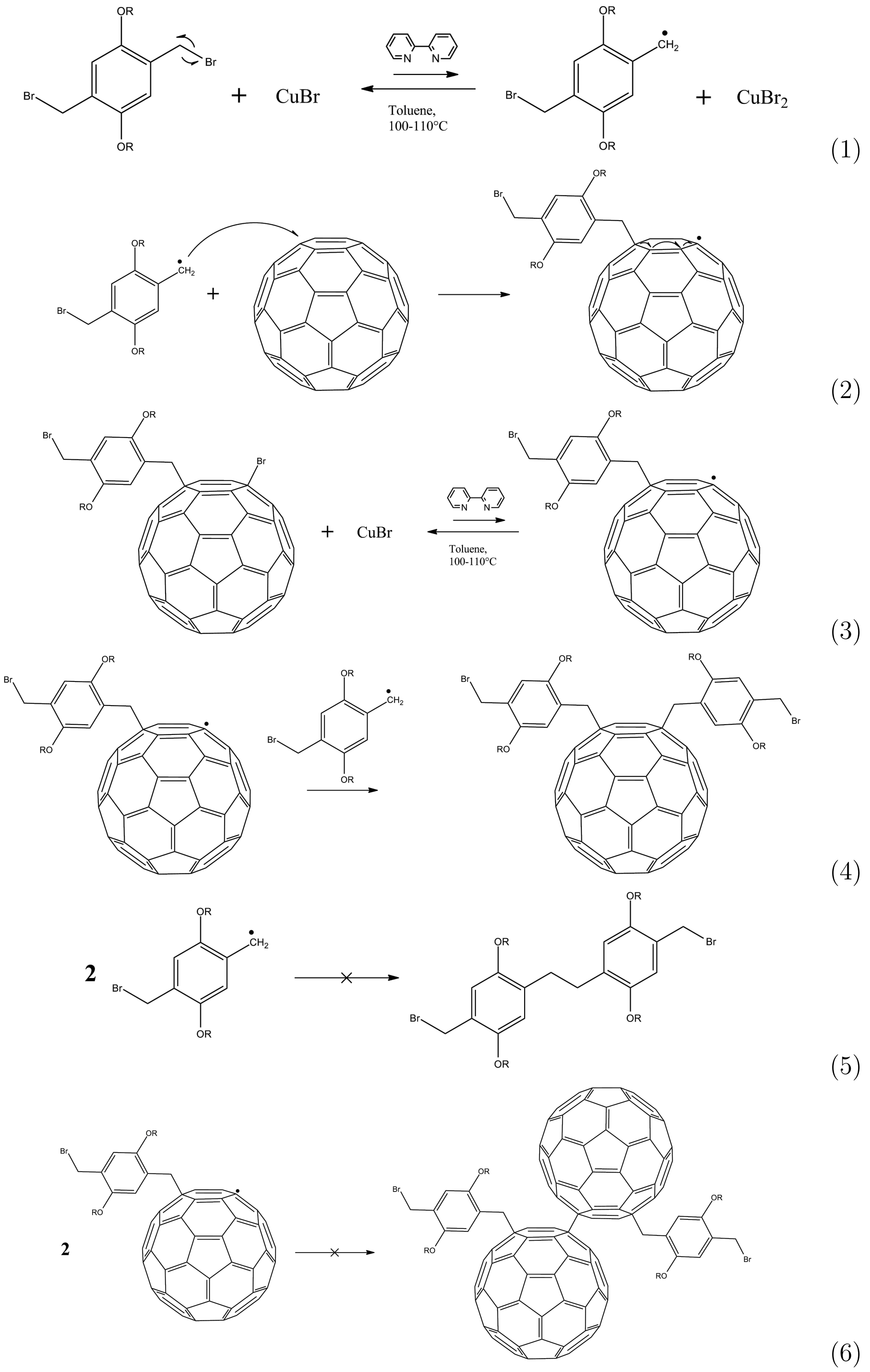

**Figure 3.6:** Proposed mechanism for ATRAP polymerization.

of $C_{60}$ as time goes on. The difference resides on the fact that in a chain polymerization, the polymer chain proceeds exclusively by the reaction(s) between (a) monomer(s) and (a) reactive site(s) on the polymer chain with regeneration of the reactive site(s) at the end of each growth step; whereas a polyaddition is a polymerization in which the growth of polymer chains proceeds by addition reactions between molecules of all degrees of polymerization, which may also lead to a broader distribution of molecular weights.[152]

It is worth noting that the underline mechanism is an ATRAP one in contrast to the ATRP (Atom Transfer Radical Polymerization) one. As stated above, ATRAP is believed to be a polyaddition whereas ATRP is a chain polymerization.[153]

Besides that, the formation of the $C_{60}$-monomer bond follows an equilibrium which can be easily shifted to the direction of the reagents, which competes with the formation of longer chains. Finally, in a general manner, radical reactions used to incorporate fullerenes into a polymer structure are self-inhibited by the fullerene's inherent antioxidative properties, as it was reported by Zeynalov *et al.*[154]

The obstacles associated with this reaction is the low solubility of the copper(I) bromide, which limits its availability and catalyst activity. Thus, adding a ligand reduces considerably this drawback. However, this makes it difficult to remove the catalyst out of the polymeric product and we had to face this while trying to maintain a reasonable yield.

The general synthetic and purification route of the polymerization is described below. Afterwards, in Table 1, one can find the specific parameters of each polymeric material synthesized with the different comonomers.

***Poly[1,4-bismethyl-2,5-alkoxybenzene-co-1,4-fullene]:*** *In a flame-dried $N_2$-filled double-necked flask, some volume of freshly sodium-distilled toluene [155] is added. The solvent is then heated up in an oil bath to reflux. After the solvent is already refluxing, one molar equivalent of the comonomer (**2**, **4**, **6**, **8** or **10**) is added with four molar equivalents quantity of 2,2'-bipyridine. Then, one molar equivalent $C_{60}$ is added and the system is left to solubilize for some minutes. Once the solution is deep purple, two molar equivalents of copper(I) bromide is added and system is left to react under $N_2$ flux, dark and reflux conditions for 24 h. After this time, the solution is transferred under anaerobic conditions to an evaporation flask and all the toluene is moved away. The solid deposited on the flask is solubilized by a minimal quantity of 1,2-dichlorobenzene and methanol is added on it, forcing the material to precipitate out. Then, this is filtered directly in a cellulose tube and solvent purified in Soxhlet for 96 h: from which, 48 h of it under acetone and the rest under n-hexane. The solid extracted after this process is vacuum-dried and characterized. Recovery yields are around 40-60% (compared to the quantity of starting $C_{60}$).*

Beyond the fact that the polymerization takes place under anaerobic and anhydrous conditions, no further challenge is proposed for the purification. The purification is based on the fact that copper(II) bromide is soluble in acetone as well as 2,2'-bipyridine, when hot, and pristine fullerene is moderately soluble in *n*-hexane, although the polymerized material is not.

The Soxhlet extraction appeared to be the easiest way to recover the synthesized product.[156] We have tried other techniques such as: 1) precipitation of the reaction product in methanol and *n*-hexane followed by filtration[62, 155]; and 2) silica column extraction with *n*-hexane, toluene and chlorobenzene phases (an adaptation of the method used in ref. [61]). The former technique yields non-reacted-$C_{60}$ rich samples, also contaminated with residual copper(II) bromide and; the latter is able of efficiently separate non-reacted fullerene, polymerized material, insoluble highly cross-linked phase and, copper salts, exposing the crude material to light and air, though. Figure 3.7 shows the products that can be so-extracted.

Furthermore, during the purification step of $C_{60}$-based materials, one can have to deal with crosslinking of $C_{60}$s either by oxidation[143] or reaction with UV light.[157] Considering this, the Soxhlet extraction really seems to be the most appropriate purification technique for this type of materials, since it can be performed at the same time in dark and under inert atmosphere.

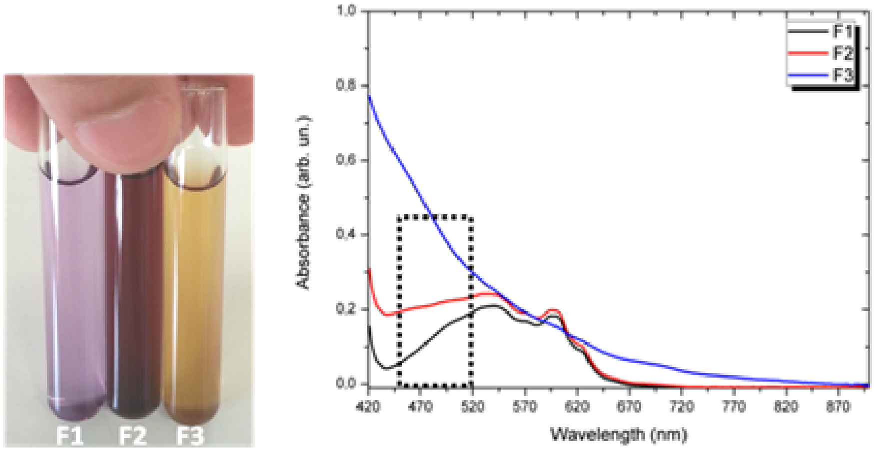

(a) (b)

**Figure 3.7:** (a) extracted fractions using the silica column separation technique (in this case, the lateral chain is a *n*-octyl) - F1 is the phase soluble in *n*-hexane, F2 soluble in toluene and, F3 soluble in chlorobenzene; (b) the UV-VIS optical absorption of the extracted phases in toluene, where one can identify the region characteristic of attacked fullerenes (inside the square - see discussion in following pages) and the non-resonant region characteristic of a material that has lost its ordered electronic structure, i.e., amorphous carbon, overreacted fullerene, etc.

In Table 3.1, all the synthesized polymeric materials can have their stoichiometry found.

| Entry | # of moles comonomer (mmol) | # of moles $C_{60}$ (mmol) | Concentration of $C_{60}$ (g/mol) | Isolated yield(%) † | Product Label |
|---|---|---|---|---|---|
| **2** | 1.67 | 1.67 | 1.66 | 60.5 | HSS11 |
| **4** | 1.39 | 1.39 | 1.66 | 52.5 | HSS46 |
| **6** | 1.20 | 1.20 | 1.66 | 41.9 | HSS14 |
| **8** | 1.39 | 1.39 | 1.66 | 73.3 | HSS49 |
| **10** | 1.39 | 1.39 | 1.66 | 66.9 | HSS48 |

**Table 3.1:** Stoichiometry of the synthesized polymers. †The presented isolated yields refer to the *n*-hexane insoluble phase and were calculated based on the fullerene content of a theoretical infinite polymer chain.

For the products HSS11, HSS49 and HSS48, the *n*-hexane extraction is basically consisted of non-reacted $C_{60}$, whilst HSS14 and HSS46 present another fraction that was also characterized and seemed to be shorter oligomers bis or tetra-attacked, as it will be readily presented.

In order to characterize such set of materials, we have performed $^{1}H$ and $^{13}C$ NMR measurements, size-exclusion chromatography in tetrahydrofuran (SEC-THF) and in chlorobenzene (SEC-CB), thermogravimetric analysis (TGA), differential scanning calorimetry (DSC) and, UV-VIS optical absorption in solution (UV-VIS).

### 3.3.1 UV-VIS Optical Absorption (UV-VIS)

UV-VIS has been used as a first tool to characterize fullerene multi-adducts. Back in 1997, Okamura *et al.*[60] based on the work of Murata *et al.*[158, 159] presented enough evidence to state that the UV-VIS properties of attacked fullerenes are dependent on the relative positions of substitution. They were then able to show that 1,4-bisadducts exhibit a broad absorption at around 440 nm, while 1,2-bisadducts has a sharp absorption around 400 nm. It is worth noting that 1,2-bisadducts cannot be entirely avoided, except, perhaps, for samples prepared by anionic polymerization, using, notably, PMMA.

In this way, very dilute solutions concentrated up to 0.5 mg/mL of the synthesized $C_{60}$ derivatives in THF were prepared and had their UV-VIS spectra recorded. Zooming in the specific region of around 445 nm, one can found the very same characteristics described by Okamura *et al.*[60] and by Kadish *et al.*[160, 161, 162, 163], and they are very strong arguments towards the confirmation of the synthesis of 1,4-bisattacked fullerene moieties, as one can see on Figure 3.8, but 1,2-bisattacked moieties can also be noted.

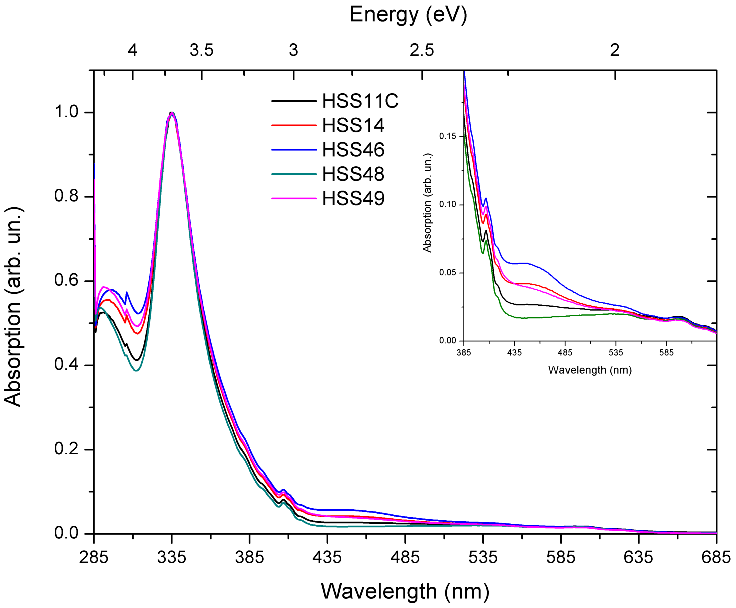

**Figure 3.8:** Measured UV-VIS optical absorption for the synthesized macromolecules.

### 3.3.2 Size-Exclusion Chromatography (SEC)

SEC is undoubtedly the most used technique to characterize polymeric materials. The calibration of the elution time is done based on the screening of polystyrene range of different molecular weight samples and all the measurements are related to this calibration. These experiments were performed by eluting at 1 mL/min of a chlorobenzene (CB) solutions at 50 °C through 10 micrometer SEC column. The polymers were analyzed with a refractive index detector calibrated with narrow polystyrene standards.

These quite robust conditions for a SEC experiment were chosen since the solubility of these materials are extremely different in THF when compared among them, whilst in a heavier solvent, as CB, their solubilities are more comparable. This should reduce the error bar of the extracted parameters considerably and has been used as a way to evaluate their relative molecular weight. Another problematic point is the very different hydrodynamic volume between the polystyrene standards and molecules derived from fullerenes. As an example, $C_{60}$ comes out in a SEC-THF experiment after toluene,[59] what indicates that, even though it is a big molecule, it is much slower in the gel column than other smaller compounds.[1][60] In this way, the molecular weight extracted from SEC experiments should be considerably lower than they really are (by a factor of 2 to 4).[132]

Table 3.2 presents the extracted masses and dispersity from a SEC-CB experiment at 50 °C. Products labeled ($f_2$) are issued from the *n*-hexane soluble phase and should consist of a mixture of attacked and pristine fullerene, *c.f.* discussed previously. After it, for the sake of simplicity, one can find the general structure of these materials based on the labeling system used.

| Product Label | $M_n$ (g/mol) | $M_w$ (g/mol) | $M_z$ (g/mol) | $M_v$ (g/mol) | Đ |
|---|---|---|---|---|---|
| HSS11 | 920 | 1290 | 1820 | 1730 | 1.40 |
| HSS46 | 2990 | 4900 | 8240 | 7630 | 1.64 |
| HSS14 | 3110 | 4610 | 6670 | 6330 | 1.48 |
| HSS49 | 970 | 1750 | 3160 | 2910 | 1.81 |
| HSS48 | 560 | 810 | 1180 | 1120 | 1.45 |
| HSS46($f_2$) | 1860 | 3110 | 6150 | 5530 | 1.68 |
| HSS14($f_2$) | 2500 | 3740 | 5790 | 5440 | 1.50 |

**Table 3.2:** SEC-CB parameters against polystyrene standards.

Although the molecular weight distribution so-acquired is large, the macromolecules can yet be considered *quasi*-monodisperse oligomers or polymers. One can note that the

---

[1] This has to do with the pore size of the gel in the column, which traps fullerene molecules, releasing them lately. Moreover, THF is not a good solvent to $C_{60}$s, what also contributes to slow it down during elution.

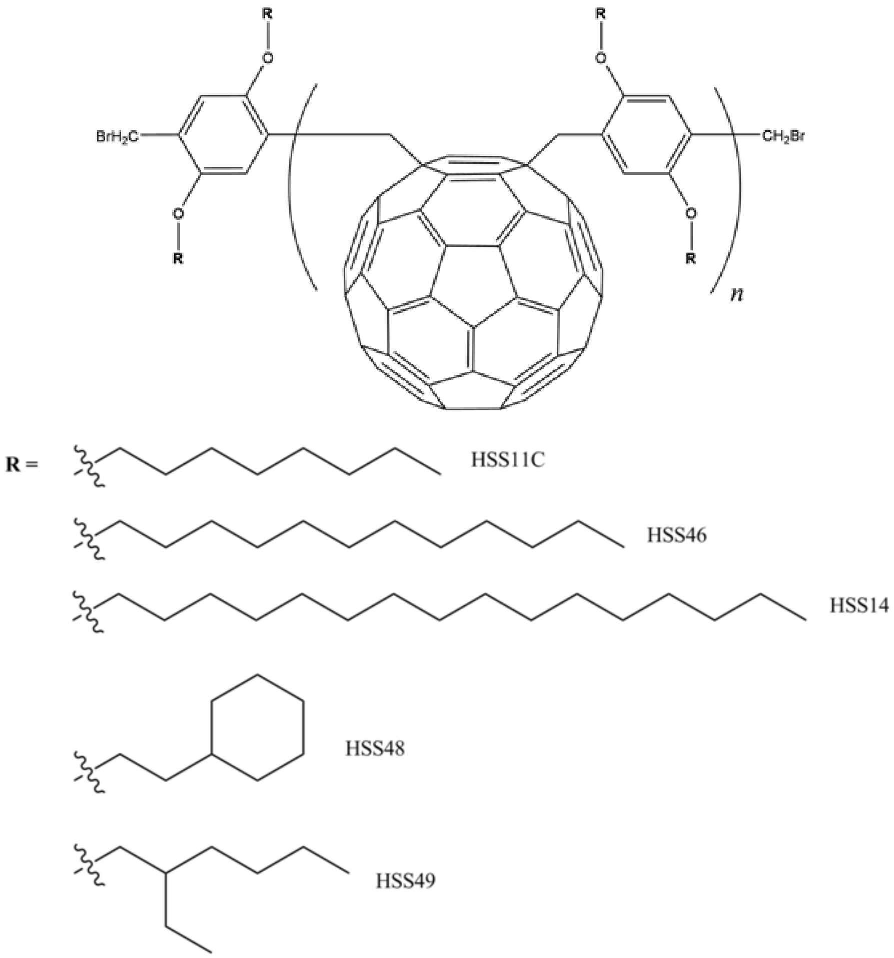

**Figure 3.9:** General structure of the synthesized polymeric materials which the labeling system herein used.

longer the lateral chain of the comonomer, the longer tend to be the synthesized polymers. This can be issued from three different factors: 1 - the steric hindrance caused by the lateral chain avoids fullerenes to form multi-adducts (*i.e.*, undergo crosslinking through more than two additions) and allows them to form longer chains; 2 - the molecular volume of the lateral group is vital to the solubility of the as-formed molecules, helping them to keep in solution available to further addition reactions, while those which are just formed but are not soluble enough, precipitate out in the reaction medium, lowering molecular weight; 3 - they have bigger volume within the SEC column.

It is also interesting to note the surprising high molecular weights of the materials issued from the n-hexane soluble phase during polymers' purification. While one should expect that only $C_{60}$ comes out, for the longer alkyl chains, we observed a fullerene-derivative material coming out altogether. Based on the SEC and UV-VIS results, these structures seem to be consisted of overreacted fullerenes which are still poor-defined, *i.e.*, several attacks on the fullerene sphere did not rendered it an insoluble material, as the one evidenced in Figure 3.8.

We also performed SEC-THF (30 °C) experiments and the most relevant results are the ones obtained for the most THF-soluble materials. The elution diagrams of these materials show specific peaks that can be attributed to an integral increasing of the chain. This can be illustrated by Figure 3.10.

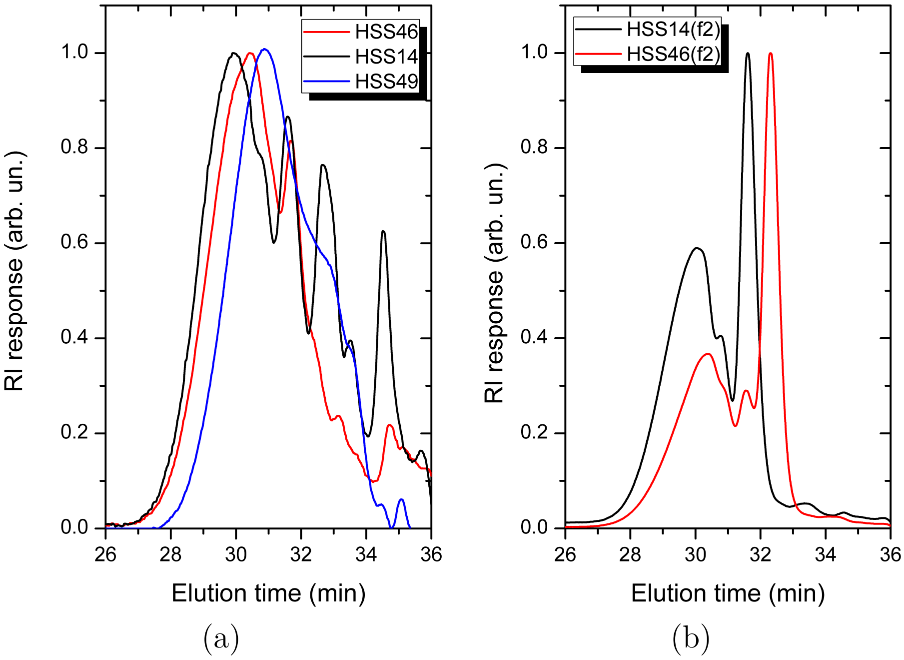

(a) (b)

**Figure 3.10:** SEC-THF traces for the most THF soluble materials (a) and for the *n*-hexane soluble phases extracted (b) from HwhatSS14 and HSS46 purifications.

In (a), one can see that HSS14 should have a slightly higher molecular weight than HSS46, going against what have been deduct up to now from SEC-CB measurements. Moreover, from the SEC traces of HSS46, distinguishing increasing number of $C_{60}$ molecule on the linear chain is not as easy as it is for HSS14. Empirically, if we consider that the peak that elutes the last represents one bis-adduct, then one would have a chain with 4-6 $C_{60}$ units, what would give theoretically a molecular weight ranging from 5152 to 7728 g/mol (considering HSS14), agreeing with the molecular weights extracted from SEC-CB. In this way, one should not expect that, in average, the synthesized molecules have more than **5** (HSS14) or **7** (HSS46) $C_{60}$s incorporated in the main-chain.

In (b), the SEC traces of the *n*-hexane soluble phases issued from the purification of HSS14 and 46 are presented. These samples have an increased solubility in THF and present different UV-VIS properties (see Figure 3.11) if compared to the *n*-hexane insoluble phases. From the SEC traces, the elution order is consistent with the fact that HSS14($f_2$) has a bigger lateral chain than HSS46($f_2$). For both traces, one can also identify the non-reacted comonomers as single sharp peaks whose elution time is also consistent with their molecular weight. This may indicate that this fraction should be consisted of non-polymeric materials, probably double- or tetra-additions to the fullerene core. This is corroborated by non-powder solid-state characteristic, as the one described by Michinobu *et al.*[164]

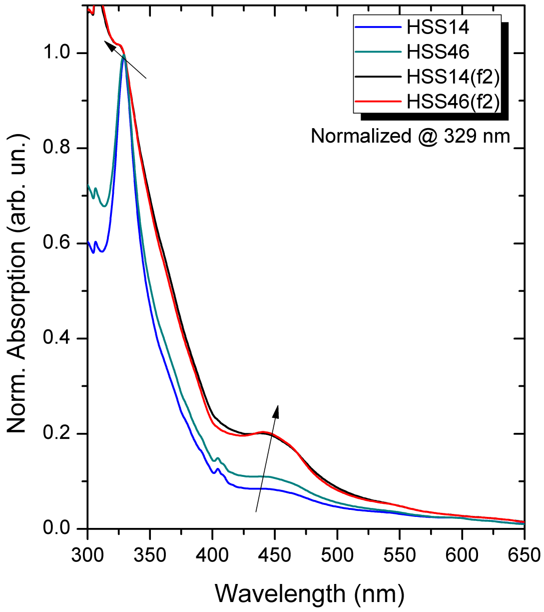

**Figure 3.11:** UV-VIS spectra comparing HSS14 and HSS46 phases that are soluble ($f_2$) or not in *n*-hexane during Soxhlet extraction.

### 3.3.3 Nuclear Magnetic Ressonance (NMR)

Although NMR is a common-place characterization technique in polymer chemistry, it is known that it may not be very useful to determine the structure of $C_{60}$ multiadducts, as it is reported by Troshin *et al.*[81]

In our case, the UV-VIS/SEC-CB combination showed to be very useful in determining how many attacks there are around the fullerene sphere by combining both the electronic structure and the more accurate molecular weight measure, if compared to a traditional SEC-THF apparatus. NMR technique was applied to the synthesized polymeric materials, nevertheless.

Several difficulties appear for these materials, specially: 1 - the low solubility of some of the polymeric materials does not propitiate the acquisition of a good spectrum; 2 - the quaternary carbons in fullerene have very long relaxation times and; 3 - since these molecules tend to aggregate, increasing the quantity of material in the sample do not mean that a more net signal will be acquired, being possible even the opposite. Based on this, samples were prepared by dissolving them over the limit of solubility in $C_6D_6$, with low-power sonication and then they were filtered through a 45 $\mu$m PTFE membrane. Long acquisition times and extended number of cycles were required for both proton and carbon signals (over 10 s of relaxation, and over 3k cycles for carbon, particularly). In Figure 3.12 one can find the superposition of the $^1$H spectra for the polymeric materials.

In agreement with the pioneering work done by Kadish *et al.* on model systems,[163, 162, 165] Hiorns *et al.*[62] reported peaks due to $-CH_2-$ group as a double doublet, one located at 4.0 and the other at 4.4 ppm. For the series of reported materials, these peaks can be localized but it happens that they are much broader and less resolved than the ones beforehand reported. Moreover, peaks due to $\alpha$-protons in alkoxy groups can be found in the region comprised between 3.5-4.0 ppm. Still, in the 4.5 region, one can find final $-CH_2-$ groups' peaks. The two intense peaks around benzene's one, centered in 7.16 ppm are due to the two protons attached to the aromatic ring, copolymerized with fullerene. Peak in 3.0 ppm is attributed to methanol, 2.0 to toluene and the other small peaks in the aromatic region due to toluene and 1,2-dichlorobenzene.

The same analysis was performed for the *n*-hexane soluble phases of HSS14 and HSS46, as discussed before. The resonant signals in this region between 3-5 ppm are much more resolved and also look like to the signature published by Hiorns *et al.*[62] In Figure 3.13, one can find the comparison between the $^1$H NMR spectra of the *n*-hexane soluble and insoluble phases of HSS14 and HSS46 in the 3-5.5 ppm region. One can see that the peaks are structured in the same way, although more resolved.

The $^{13}$C spectra could not be resolved for all the materials even using long times of relaxation and extremely large number of scans. What can be seen however for all the polymeric materials is the presence of unreacted $C_{60}$ even after the long Soxhlet

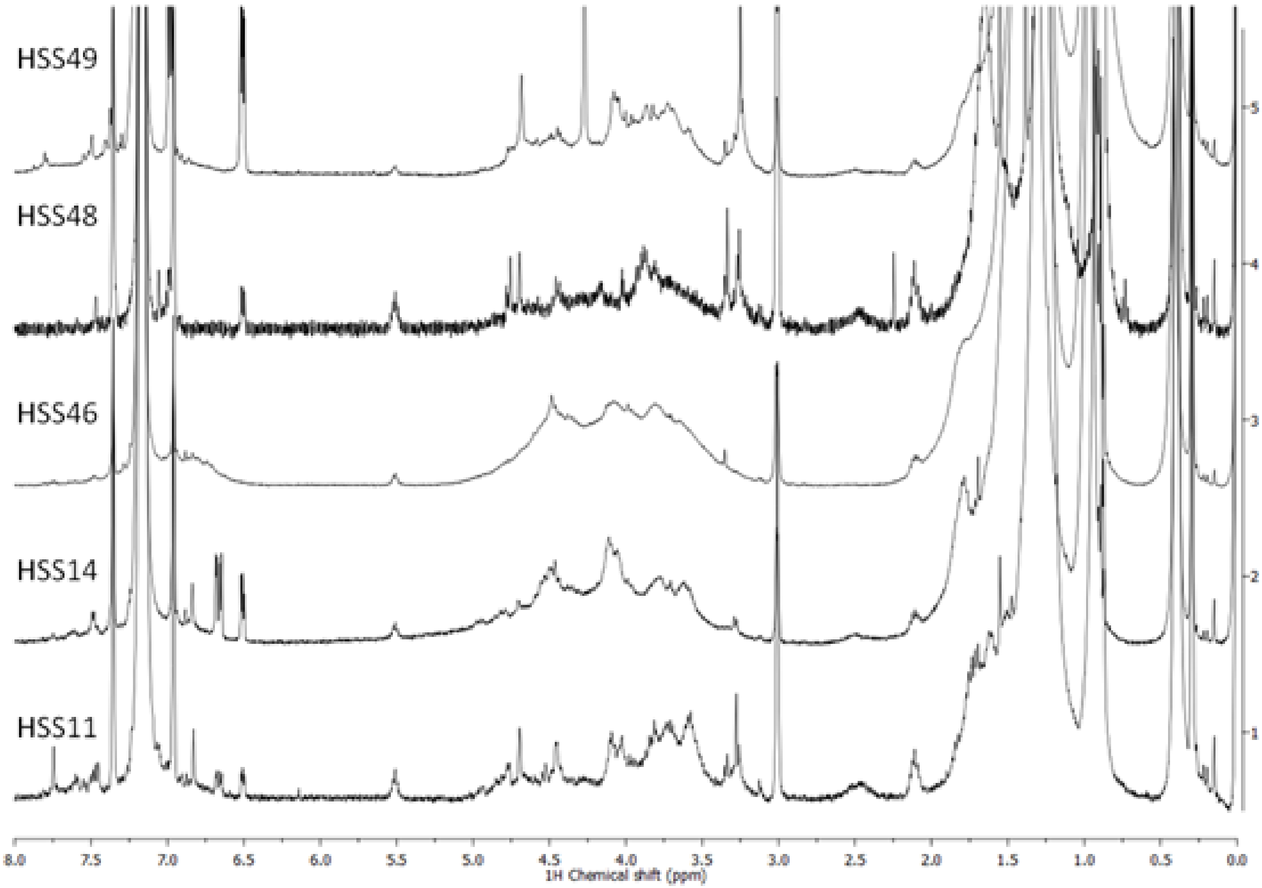

**Figure 3.12:** $^1$H spectra of the 5 different polymeric materials. The region of interest concerning the attacks over the fullerene sphere is comprised between 3.25-4.75 ppm.

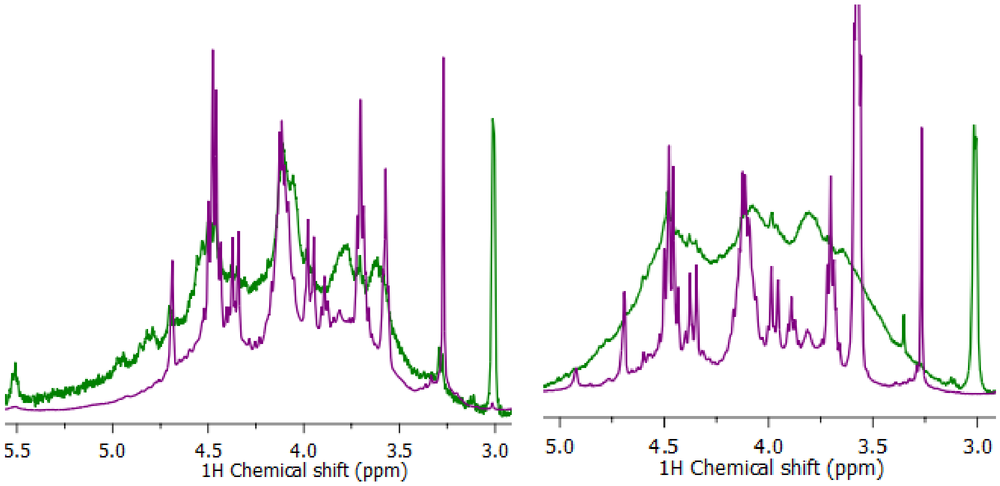

HSS14 HSS46

**Figure 3.13:** $^1$H spectra of the *n*-hexane soluble phases. The region of interest concerning the attacks over the fullerene sphere is comprised between 3.25-4.75 ppm.[163, 162, 165] In purple, the signals of these particular phases and in green the signal of the *n*-hexane insoluble phases of the same material, separated during Soxhlet extraction.

purification step. One should keep in mind though, that the intensity of this signal should be divided by 60 if one wants to estimate the concentration of unreacted fullerene. But, for the same $n-$hexane soluble phases, compared to their counterparts, a very distinct scenario is shown: now the region centered in 145 ppm becomes resolved and one can identify individual peaks due to attacks over the fullerene in a comparable intensity with the peak of the unreacted fullerene itself. This may indicate that, alongside the proton spectra and SEC-CB results, these are not polymeric materials and should be somehow consisted of double- or tetra-attacks on the fullerene.

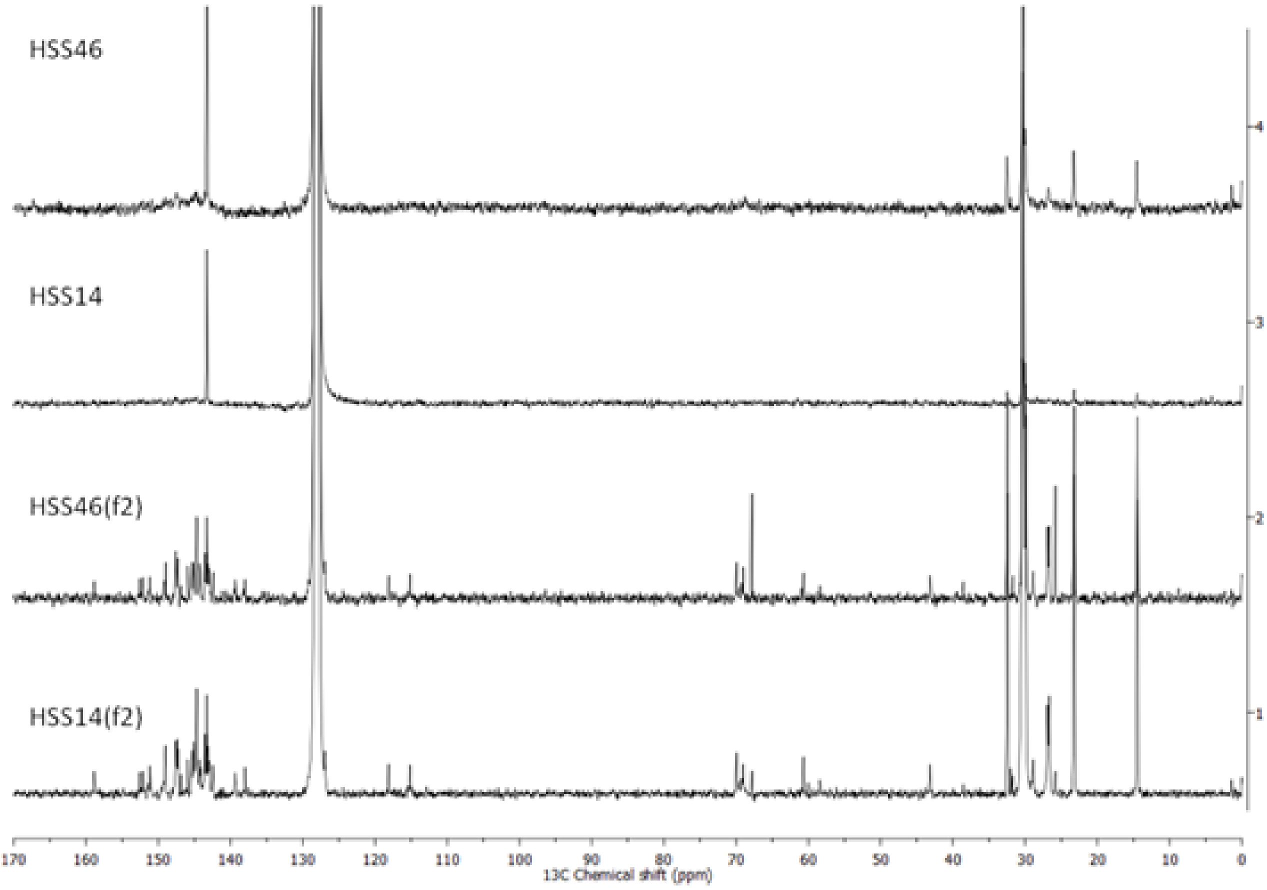

**Figure 3.14:** $^{13}$C spectra of the $n$-hexane soluble phases and their corresponding insoluble phase materials.

Finally, the 2D $^1$H-$^{13}$C HMBC spectra of the synthesized materials were obtained under the same measurements conditions, and again it was not resolved for all of them. The most remarkable spectra are the ones obtained for the $n$-hexane soluble phases, where one can clearly define the correlation of the peaks, as one can see in Figure 3.15. The correlation pair (4.46;28.77) corresponds to the $-CH_2Br$ groups pointing outside the fullerene; the two distinct correlation pairs at (4.35;43.29) and (3.98;42.96) indicates two different proton chemical environment with the same carbon chemical environment and corresponds to the two protons in the $-CH_2-$ group which links the comonomer and the $C_{60}$; the extended correlation pairs for the carbons at around 68 ppm with proton from 3.5 up to 3.7 corresponds to the triplets found for the protons in $\alpha$ position to the alkoxy group and; the protons of the aromatic group are found for the (6.88;114.92) and (7.25;117.76) correlation pairs.

Thus, even though the NMR spectra cannot be fully resolved for all the materials, a main piece of information can be extracted: the NMR is capable of identifying low and high molecular weight molecules based on the resolution of the signal, as it would be expected.

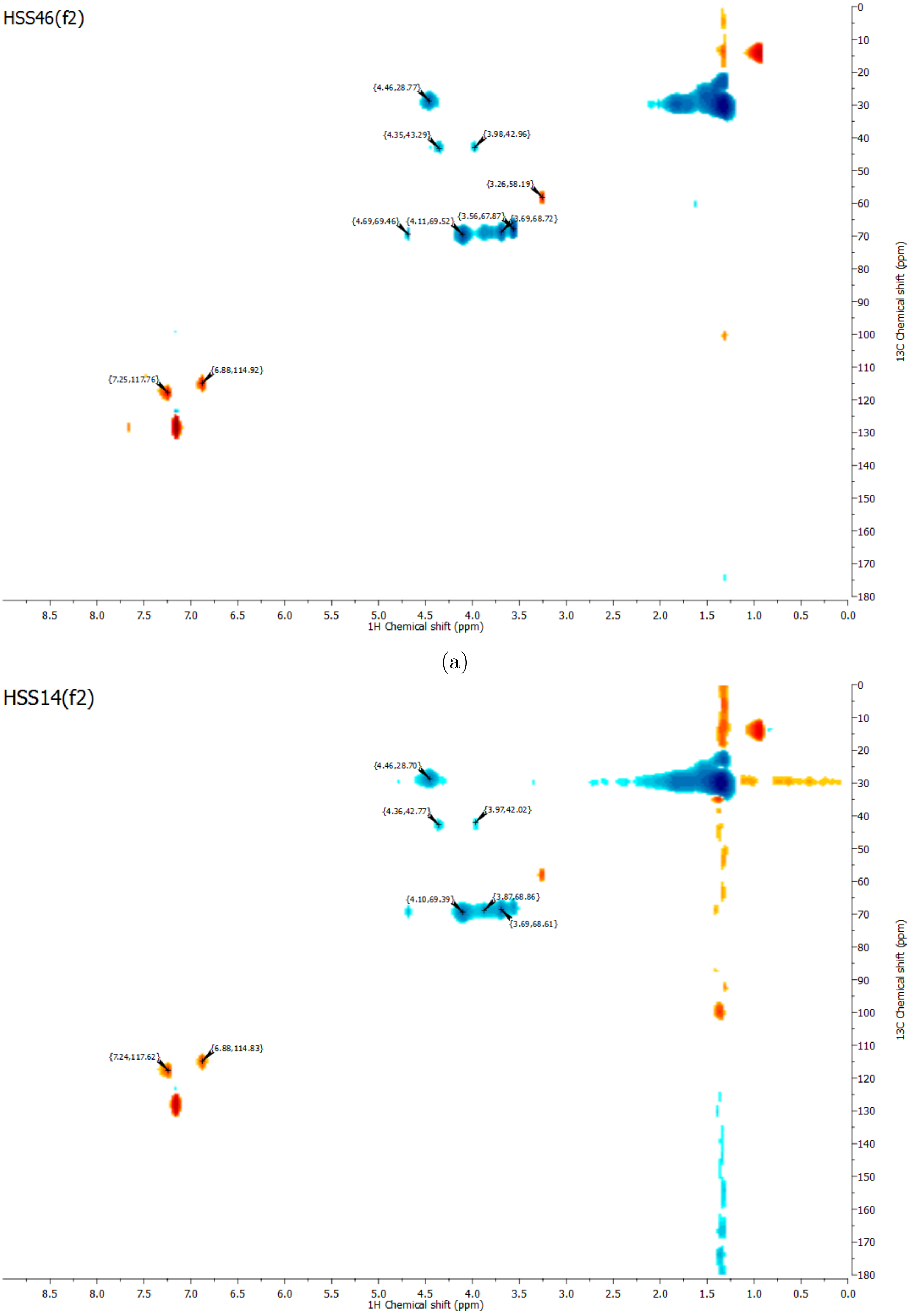

(a)

(b)

**Figure 3.15:** 2D $^1$H-$^{13}$C HMBC spectra for the tetra-adducts.

### 3.3.4 Thermogravimetric Analysis (TGA)

TGA can then be employed to characterize the thermal degradation profile of the polymers, besides their fractional composition for the case of copolymers.

To study this, the set of materials were heated in a $N_2$ atmosphere with a temperate ramp of 10 °C/min up to 500 °C. All of them present similar thermal degradation profiles consisted of around 4 peaks between the room temperature - 500 °C temperature range. Figure 3.16 presents their thermal degradation profiles. The structures associated with each label are presented in Figure 3.9.

Beyond the degradation profiles of the polymeric materials themselves, we also ran, for HSS46, the same experiments (see Figure 3.17) for its comonomer 1,4-bis(bromomethyl)-2,5-bis(dodecyloxy)benzene (4) and for the material before the bromomethylation step 1,4-bis(dodecyloxy)benzene (3).

Based on this joint analysis, one can make the peaks attribution for the whole set of materials. The first peak around 80 °C is associated to residual solvent evaporation.[166] The second peak, centered at 290 °C is associated to the loss of the lateral chains of the monomers, as one can deduct from the TGA analysis of 1,4-bis(bromomethyl)-2,5-bis(dodecyloxy)benzene. For this curve (blue one in Fig. 3.17.a.), there is a sudden bump at this temperature representing around 50% of weight loss. This is consistent with the molecular ratio of the alkyl lateral chains. The third peak, around 380 °C is consistent with the $C_{60}$ release reported by Pozdnyakov *et al.*[166] They studied the degradation of polystyrene stars with a $C_{60}$ core and observed this low-temperature degradation of radical-attacked fullerenes. Then, the last peak at 440 °C is consisted, again considering the degradation profile of HSS46 precursor - a weight loss of 30%, with the departure of $-CH_2Br$ groups.

These degradation profiles are consistent with the ones found by Pozdnyakov *et al.*[166] for polystyrene stars with $C_{60}$ cores. They found that 2-arm stars have an average activation energy for the release of $C_{60}$ of 45.45 kcal/mol. This is also consistent with the results found by Mathis *et al.*[49, 52] and Audouin *et al.*[51], who attest that the link between $C_{60}$ and the polystyrene chain is weaker than the carbon-carbon bond in the PS chain, for their case. This fact is going to be discussed in more details in the chapters 4 and 5 of this thesis.

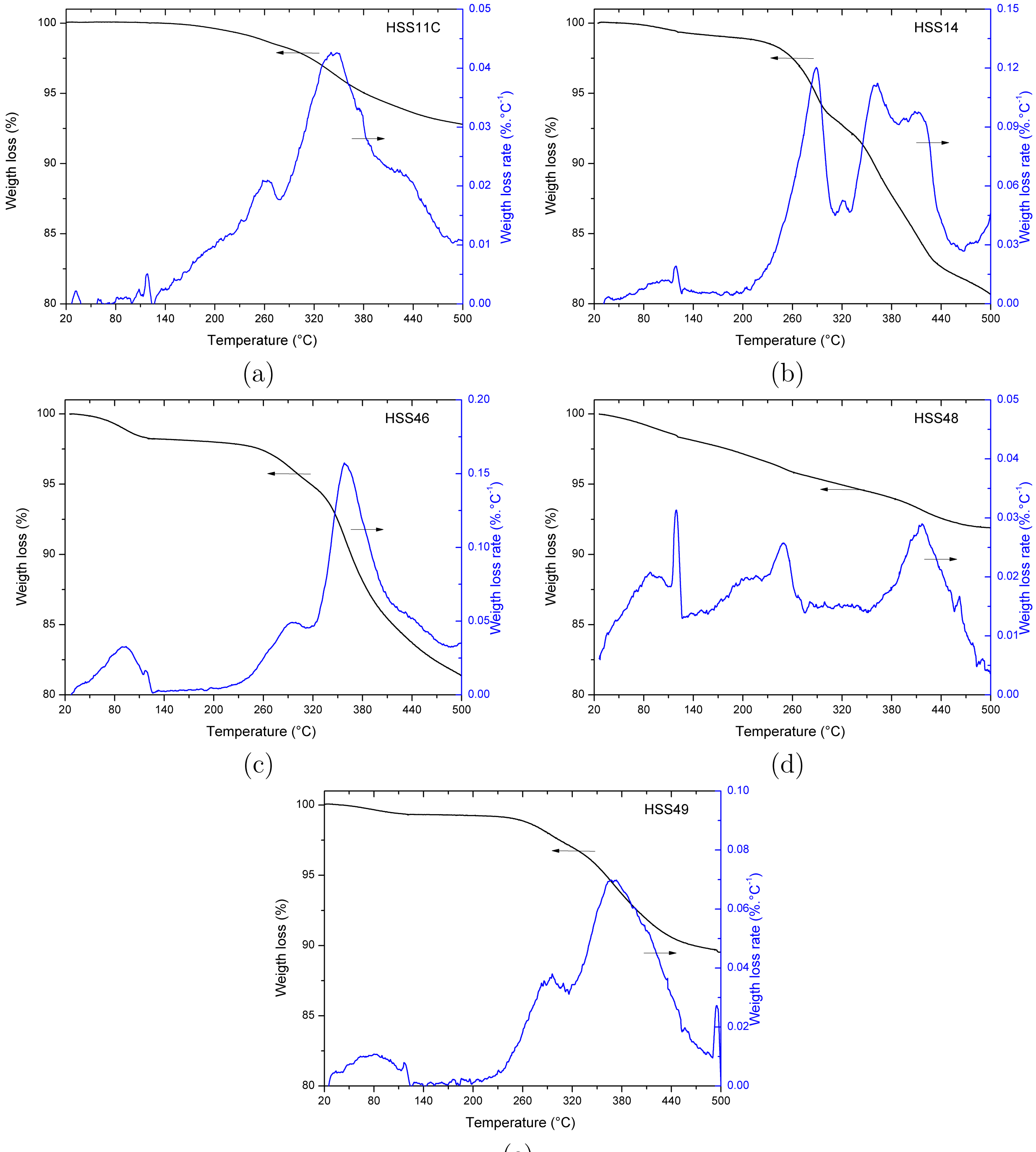

(a) (b)

(c) (d)

(e)

**Figure 3.16:** TGA/DTG studies for the set of materials.

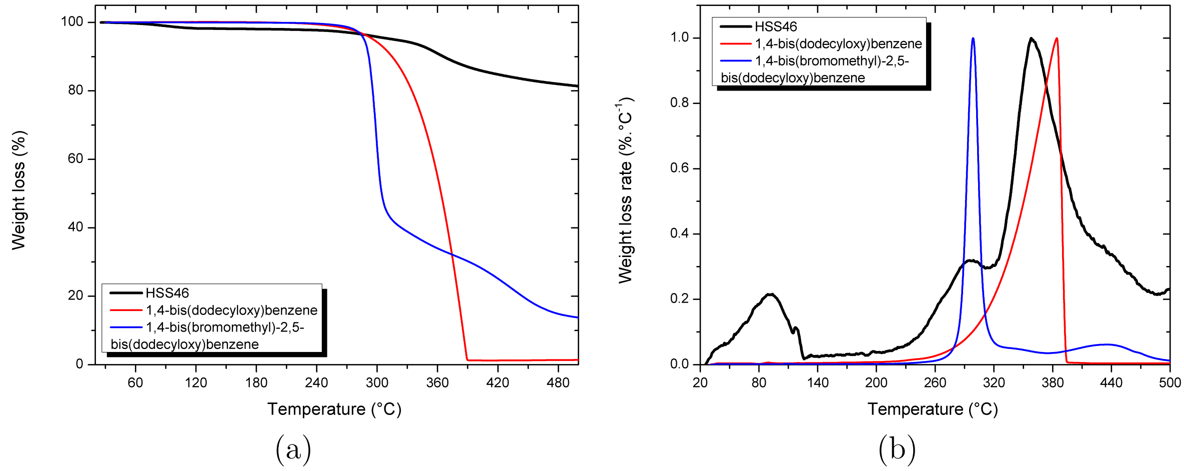

(a) (b)

**Figure 3.17:** (a) TGA and (b) DTG curves for the precursors of HSS46.

### 3.3.5 Differential Scanning Calorimetry (DSC)

Finally, DSC is a useful tool to characterize polymeric materials and to identify thermal transitions whenever they can take place. This is not always the case for the majority of amorphous polymers materials and it is even rare that we could identify these transitions even though they exist. For the set of synthesized materials, respecting the limit imposed by TGA measurements, the DSC data do not show any particular transition in both senses (heating or cooling).

For all the cases, a scanning procedure consisted of equilibrating at 40 °C, do a temperature ramp at 10 °C/min up to 200 °C, equilibrating at 200 °C, ramp down to 40 °C with the same rate and equilibrating at this temperature was repeated three times. Normally, one would scan up to higher temperatures, but it was limited by the degradation temperature presented in TGA measurements. These scans do not present any thermal-activated defined transitions for the whole set of materials and, for the sake of instance, the results for HSS46 are presented below.

Not only amorphous polymers materials present no transition in the DSC thermogram, but also the ones which are somehow cross-linked. This could be the case for the materials which are the least soluble (a good indication of cross-linking), but it can rarely be the case of HSS46, which presents very good solubilities in common organic solvents and has a very monodisperse SEC elution diagram. In this way, we believe that the fact that no transitions can be observed is due to the fact that these materials are completely amorphous in this state.

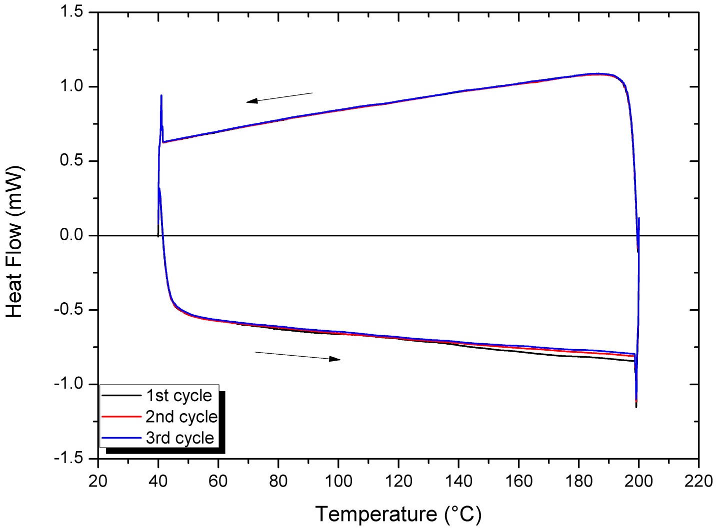

**Figure 3.18:** DSC cycles for HSS46 showing no evidence of any thermal-activated transition in the 40-200 °C temperature range.

### 3.3.6 Fourier-Transform Infrared Spectroscopy (FTIR)

For FTIR measurements, a tiny amount of material was pressed in KCl pellets. For the sake of comparison, for HSS46 material, the starting materials also had their spectra acquired. More details on the interpretation of the bands are found in Chapter 5. We also performed DFT calculations of the infrared spectra to help assigning the bands.

The vibrations of these molecules were calculated within the B3LYP/6-311G** level of theory using the RIJCOSX approximation (for this, consult Annex C). The geometries were fully optimized with tight convergence criteria and the resulting vibrational transitions were empirically shifted accordingly to their intrinsic characteristics. This means that, vibrations associated to angular deformations were not shifted in the same way as vibrations associated to a bond stretching, for example. One can find in Figure 3.20 these transitions superimposed to their experimental counterparts. But before this, in Figure 3.19, the models studied for those vibrations were compared to their experimental counterparts, are presented.

The intention of doing such approximations is to reduce the computational cost associated to the long alkyl chains. Furthermore, treating only a double-attacked fullerene instead of the whole molecule may be an oversimplification. The effects of cutting off the lateral chains must be clearly sensed on the $-CH_2-CH_2-$ vibrations intensity, found $\sim$ 1425 cm$^{-1}$ ($C-H$ bending). For the case of HSS46 polymeric material, the comparison between experiment and calculated vibrations is herein shown for the region comprised between 900-1200 cm$^{-1}$. It is in this region that differences between the comonomer's and $C_{60}$'s individual spectra arise.

Generally, the calculation of these vibrations can provide reasonable agreement in the spectrum shape, although their positions should be corrected systematically with

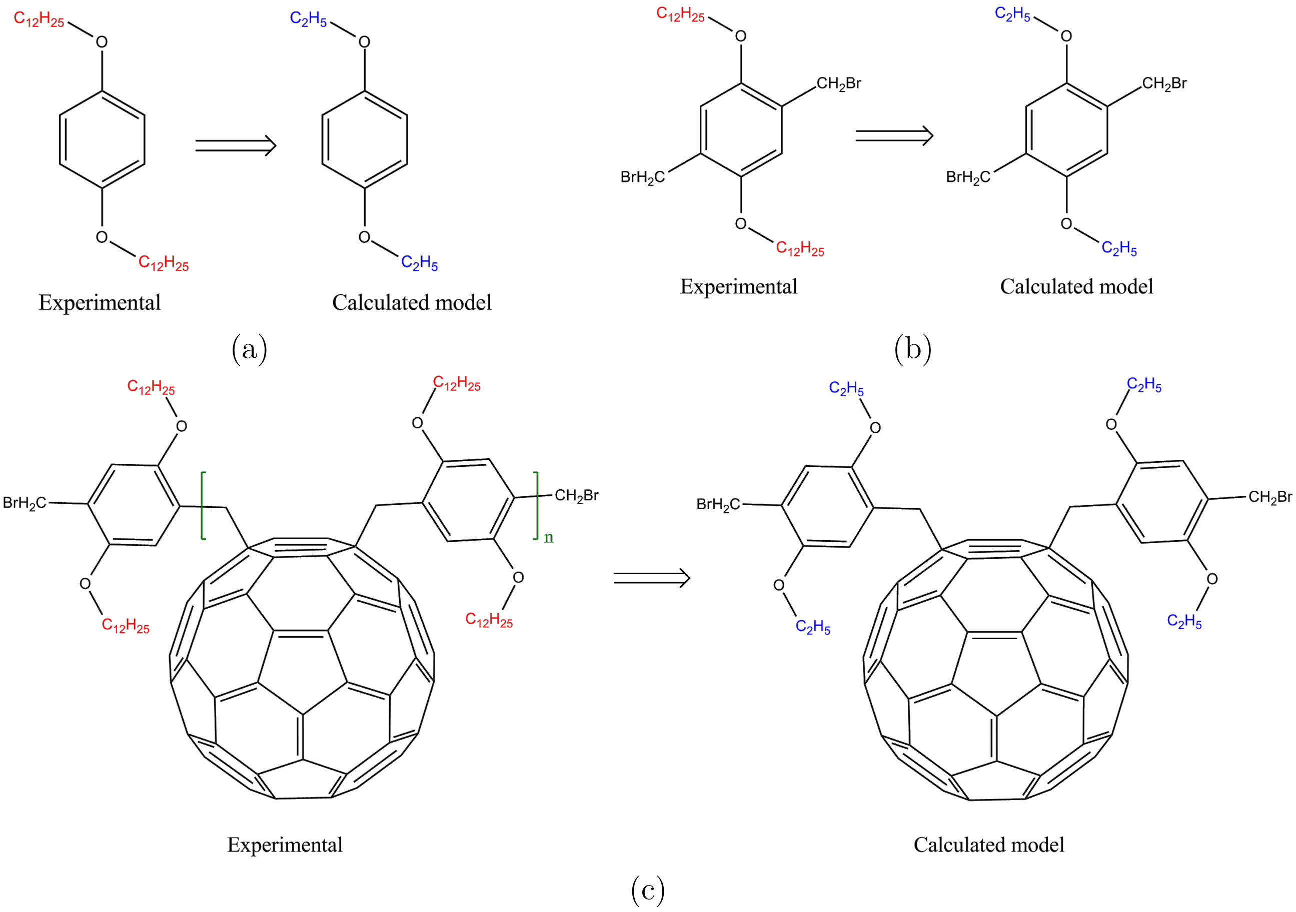

**Figure 3.19:** Simplified chemical structures studied as models for vibrations calculations. In (a), one can find the comonomer before being functionalized (label HSS42), after the bromomethylation reaction (b, label HSS45), and the final polymer (c, HSS46).

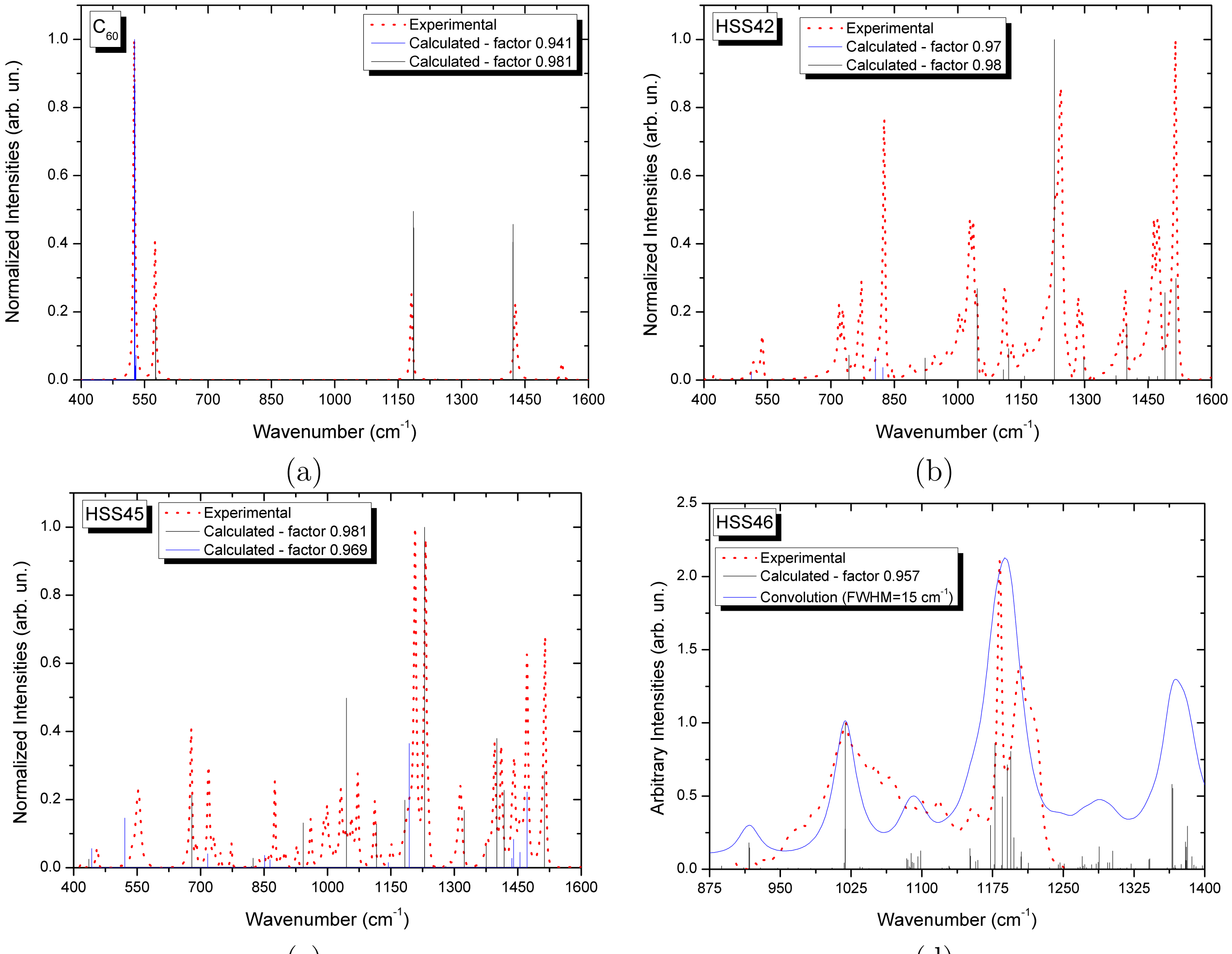

(a) (b)

(c) (d)

**Figure 3.20:** Experimental and Calculated infrared spectra/transitions for HSS42, HSS45, HSS46 and $C_{60}$ model compounds.

correction parameters depending on the nature of the vibration. For HSS46 material, the band that appears for the compound that is not present neither in the comonomer or $C_{60}$ spectra is centered at 1064 cm$^{-1}$ and the theoretical attribution of this band is the one appearing at 1018 cm$^{-1}$. The mode associated is the symmetric twisting of the $C_{60}$-comonomer groups *via* the $-CH_2-$ groups.

## 3.4 Final Remarks

In this chapter, the design and synthesis of polyfullerenes by the ATRAP route have been performed and fully described.

The choice of this route of synthesis was done based on the easiness to double attack fullerenes, the fact that a double-attack only disrupts one double bond, the lack of stereoisomeric mixing due to the definition of the mechanism, the lack of data concerning this new type of synthesis only recently described. In this way, easily-synthesized materials for application as electron acceptor and/or morphology stabilizers in BHJ-OPVs cells can be envisaged.

In this document we present the use of a simple comonomer based on 1,4-dialkoxy-2,5-dimethylene-phenylene, with five different lateral chains. These chains were chosen in order to screen the effect of bulk and long-linear groups on the molecular weight, control of attacks during the polymerization, and, mainly, solubility.

The so-synthesized materials were characterized by UV-VIS, NMR, GPC, TGA, DSC and FTIR. These techniques allowed one to make considerations on their polymeric character, degree of control on the attacks, opto-electronic, structural and morphological properties. Other techniques such as XPS and AFM were also used but they are presented in Chapter 5, where they are relevant for the discussion therein.

Finally, the results presented in this Chapter may indicate that ATRAP-based polyfullerenes may not be the most appropriate for OPVs which aim is to be more stable. This is based on the fact that the comonomer-fullerene link seems to be weak which leads to:

1. low molecular weight based on a competitive degradation mechanism during the synthesis;
2. low thermal energy is needed to cleave the comonomer-fullerene bond, yielding free $C_{60}$ and a likely stable vinylene compounds (this is going to be further explored in Chapter 5);
3. possible UV-VIS visible homolytic cleavage of this bond;
4. loss of molecular ordering on the chain;

For future works, other more stable routes may be envisaged as it was described in Chapter 2. Among them, azide route seems to be, on the electronic and stability point of view, one that should be further explored.

# Chapter 4

# Photovoltaic Performance and Device Degradation

*The photovoltaic performance of the synthesized polymeric materials applied in devices are herein studied. Three major applications have been proposed for polyC*$_{60}$*s: a - as interlayer between the active matrix and the electron extraction layer; b - as the sole electron acceptor material within the blend and; c - as an additive used to stabilize the morphology of the blend under thermal stress. From this, one can have the first outlook of the photovoltaic performance of these polymeric materials. The devices and experiments presented here were performed by Dr S. A. Downland, from Belectric OPV GmbH.*

## 4.1 Photovoltaic devices and performance

In Chapter 1, the basics of the photovoltaic effect has been shown and here we should, before presenting the results obtained from the cells, present in more details the key parameters for the characterization of these devices.

The solar cell can be considered as a two terminal device with a diode-like conductor behavior in dark and generates a photocurrent (photovoltage) when illuminated by the sun. In a circuit, the cell can take the place of a battery but they differ intrinsically on the fact that the battery is better described as a voltage generator and the cell as a current generator. In dark, the cell delivers no current and when light is switched on, a voltage appears. When the terminals are isolated (or infinite resistance is placed among them), the voltage developed is called *open circuit voltage* $\mathrm{V}_{OC}$ and it is dependent on the intrinsic electronic structure of the matrix materials. On the other hand, the current draw when the terminals are connected is called *short circuit current* $\mathrm{J}_{SC}$. The current-voltage curve of the cell ($JxV$) describes then the behavior between these extremes, obeying, for a series resistance, the Ohm's law.

This photocurrent at short circuit depends on the incident light by the *cell's quantum efficiency* (QE). This parameter represents the probability that an incident photon of a given energy will deliver one electron to the external circuit. Then, it depends upon the absorption coefficient of the solar cell material, the efficiency of charge separation and the efficiency of charge collection in the device, even though it does not depend on the incident spectrum.

When illuminated, the light causes a temporary change in the electrochemical potential, and then, a potential difference develops between the terminals. This potential generates a current which acts in the opposite direction of the photocurrent, and the net current is reduced from the short circuit one. This reverse current is called *dark current* and flows across the device under a bias in the dark. When both dark and short circuit currents cancel each other, one achieves the maximum potential difference, the $\mathrm{V}_{OC}$ (what is equivalent to separate the terminals).

Further on, the operating regime of the cell is in the range comprised between 0 and $\mathrm{V}_{OC}$, where the cell delivers power, the *power density*. This entity reaches a maximum at the cell's operating point (*maximum power point*). In this point, one can define the *fill factor* parameter ($FF$) as:

$$FF = \frac{J_m V_m}{J_{SC} V_{OC}} \tag{4.1}$$

Where $J_m$ and $V_m$ stand for the current and the voltage at the maximum point, respectively. The efficiency $\eta$[1] of the cell is the power density delivered at operating point reported to the incident light power $P_S$.

$$\eta = \frac{J_m V_m}{P_S} \tag{4.2}$$

And it can be related to $FF$ as:

$$\eta = \frac{J_{SC} V_{OC} FF}{P_S} \tag{4.3}$$

The quantities $J_{SC}$, $V_{OC}$, $FF$ and $\eta$ are the key performance parameters for the OPV cell. They should always be reported for any given particular illumination condition. The most common is to use Air Mass 1.5 (AM1.5) spectrum as a light source, which has an incident power density of 1000 $W/m^2$, at 25 °C.

Last but not least, the ohmic behavior of the cells may not always be preserved and *parasitic resistances* can appear. This is due to the fact that in real cells power is dissipated through the resistance of the contacts and through leakage currents in this region. These resistances can be in series ($R_s$) or in parallel ($R_{sh}$) and the former arises from the resistance of the cell materials to the current flow and from resistive contacts;

---

[1] To not be mistaken by the hardness $\eta$, presented in Chapter 2.

whereas the latter (also called shunt resistance) arises from leakage of current through the cell and between contacts of different polarity.

Based on these concepts, the photovoltaic performance of the synthesized materials have been tested in devices. From the series of materials presented in Chapter 3, see Figure 4.1, HSS46 (*n*-dodecyl lateral chain) was chosen to be tested first. The choice of this material was based on the chromatography results that indicates as the one with higher molecular weights. To this, we should add the fact that it is the most soluble material in non-halogenated solvents (toluene, in evidence).

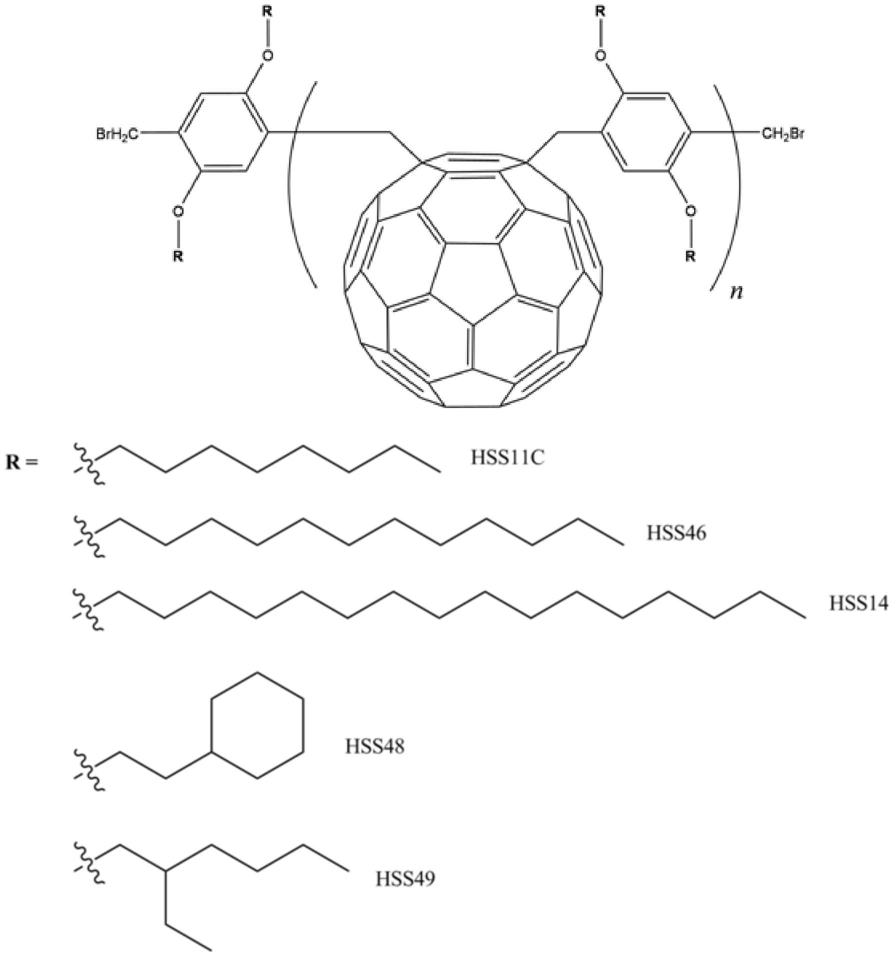

**Figure 4.1:** General structure of the synthesized polymeric materials with the labeling system herein used.

Concerning their application in the devices, three options have been tested for this material:

A - as an interlayer between the active layer and the electron selective layer;

B - as a replacement for $PC_{60}BM$ in the active layer;

C - as an additive in the active layer.

Option A is justified by the need to solve delamination problems that arise from the incompatibilities between the ZnO/TiO$_x$ layer and the BHJ layer. Inserting an intermediate layer based on polyfullerenes could make the transition smoother between the two layers and increase the charge collection. Furthermore, as will be discussed in Chapter 6, this can be an indication of the viability of synthesizing block polymers of polyfullerenes and inorganic-ligands-based polymers.

Then, B is the straightaway application when one thinks about fullerenes: using it as the only acceptor material. As one could see in Chapter 2, this is justified based on the almost unchanged electronic properties of ATRAP-based molecules, as is the case of HSS46. Ideally, this would also induce a morphological stabilization of the BHJ, avoiding the aggregation of PC$_{60}$BM.

Finally, option C, alongside with what was justified for the one before, would ideally avoid the scenario of morphological failure of PC$_{60}$BM molecules by aggregation. The additive application of the polyfullerene might them have a plasticizing effect of the BHJ.

Devices with 27 mm$^2$ ($\sim$ 9x3 mm) of active area were then produced in Belectric GbmH by Dr S. A. Downland employing the following general architecture:

- ITO / ZnO / P3HT:PC$_{60}$BM / PEDOT:PSS / Ag (this is the control)
- Interlayer positioned at electron selective side of the active layer: ZnO / *Interlayer HSS46* / P3HT:PC$_{60}$BM
- Additive and Blend solutions of P3HT:HSS46 replace P3HT:PC$_{60}$BM as the active layer.

The properties arising from these applications are explored and presented in the following sections.

### 4.1.1 Interlayer Application

Deposited films of HSS46 from 7.8 mg/ml *o*-xylene solution at different coating speeds (5, 20 and 80 mm/s - in order to produce different thicknesses) were exposed to different annealing temperatures (room temperature - rT, 70 or 140 °C - all in air) for 20 mins. Over this layer, P3HT:PC$_{60}$BM blend is deposited. In Figure 4.2 one can find the $JxV$ for the OPV cells so-made using different deposition methods.

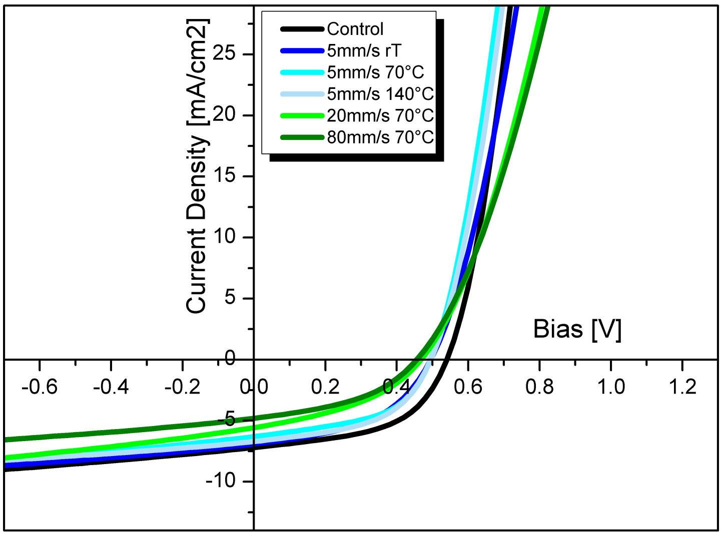

**Figure 4.2:** $JxV$ curves for the OPV cells using different deposition methods. The control device is the one where no polyC$_{60}$ has been added.

From this, one can deduct that, although the sensibility of the $JxV$ curves to the deposition technique (5, 20 or 80 mm/s), the cells are operational and no S-shape[2] can be noted, even if compared with the control device. Moreover, the higher the temperature of annealing (room temperature, 70 or 140 °C for the films deposited at 5 mm/s), the lower are the photovoltaic properties obtained from these curves. In Figure 4.3, the extracted parameters quantify the obtained yields.

As can be noted from these parameters, the current density, open circuit voltage, fill factor and power conversion efficiency are strongly influenced by the presence of the HSS46 material if compared with the control device and it has a stronger dependence on the thickness of the layer rather than the annealing temperature. More precisely, it is the current density the parameter the most affected by the presence of the interlayer. This means that the presence of a thicker interlayer worsens the charge extraction of the cell. This is true for even very thin layers (5 mm/s blade speed).

These results lead to the evidence that, used as an interlayer, the HSS46 polymer worsens the devices in all cases. This effect is exacerbated by an increase in the interlayer thickness (for the Doctor-blade coating, this is determined by the blade speed).

---

[2] The S-shape of the $JxV$ curve is attributed to the appearance of parasitic resistances, mainly the shunt resistance and it is a straightforward indicative of the existence of leakage current.

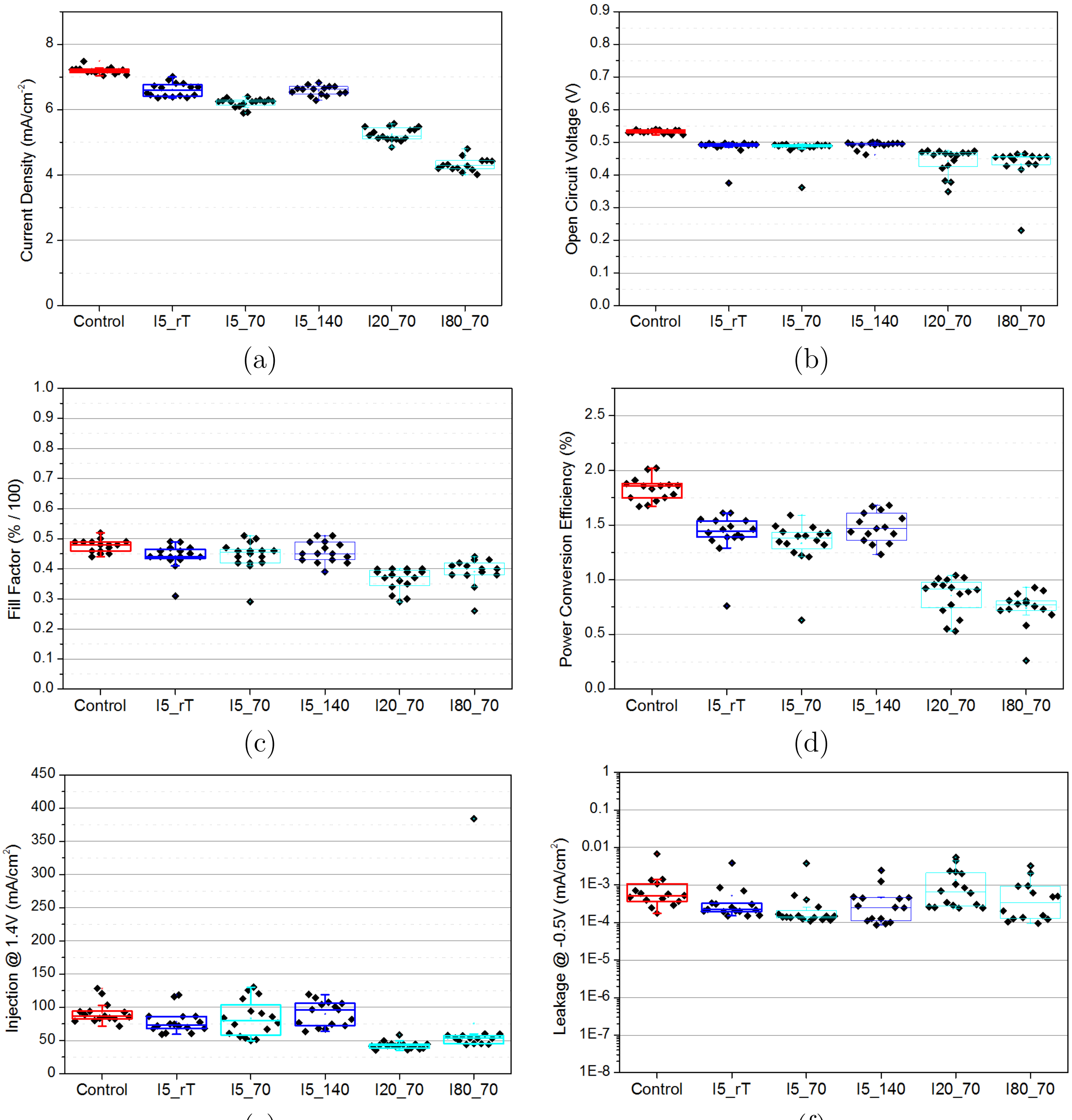

(a) (b)

(c) (d)

(e) (f)

**Figure 4.3:** OPV properties of cells using HSS46 as interlayer for different annealing temperatures and film thicknesses. These figures present: (a) the current density; (b) the open circuit voltage; (c) the fill factor; (d) the power conversion efficiency; (e) the injection current; and (f) the leakage current. The indexes indicate the coating speed (5, 20 or 80 mm/s) and the annealing temperature (room temperature, 70 or 140 °C).

### 4.1.2 Blend Application

For this application, several solutions with varying amounts of HSS46 and $PC_{60}BM$ were prepared. The total fullerene content was kept constant across all solutions by adapting the ratio of the two fullerene sources. So, one can have blends with 100%, 80%, 60%, 40%, 20% and 0%(control) of fullerene from HSS46 material.

As for the former application, the $JxV$ curves for the varying loads of HSS46 in the blend is presented in Figure 4.4

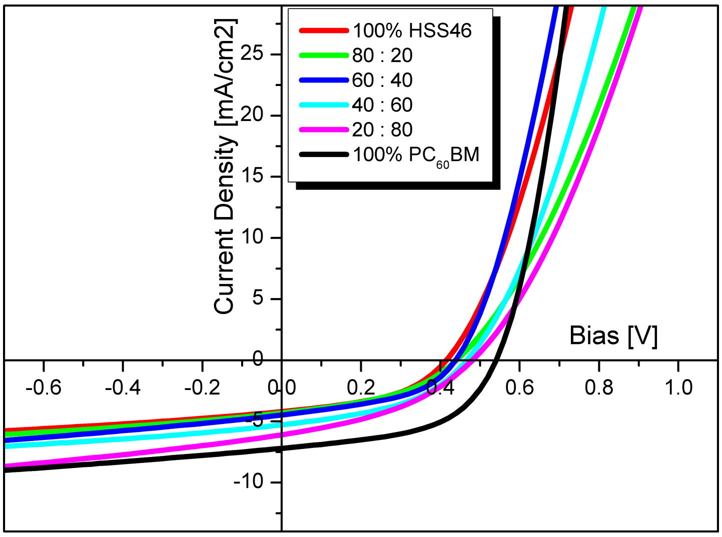

**Figure 4.4:** $JxV$ curves for the OPV cells using different loads of HSS46 in the blend.

As previously, the cells are operational with the use of the polyfullerene and they do not present any S-shape. However, one can clearly identify that such use worsens the cell performance and the more fullerene from HSS46 is added, the worse it becomes. The quantification of the photovoltaic parameters can be found in Figure 4.5

The application of the polymerized fullerene do not contribute positively as well to the OPV cell performance when used as the acceptor. This is primarily due to a loss in the current extracted (as shown by the changes in $J_{SC}$). However there are also some reduction in $V_{OC}$ and FF. This drop in performance is caused by a reduction in all device parameters, which may be simply a result of the absence of $PC_{60}BM$ and the failure of the fullerene polymer to act as an effective substitute.

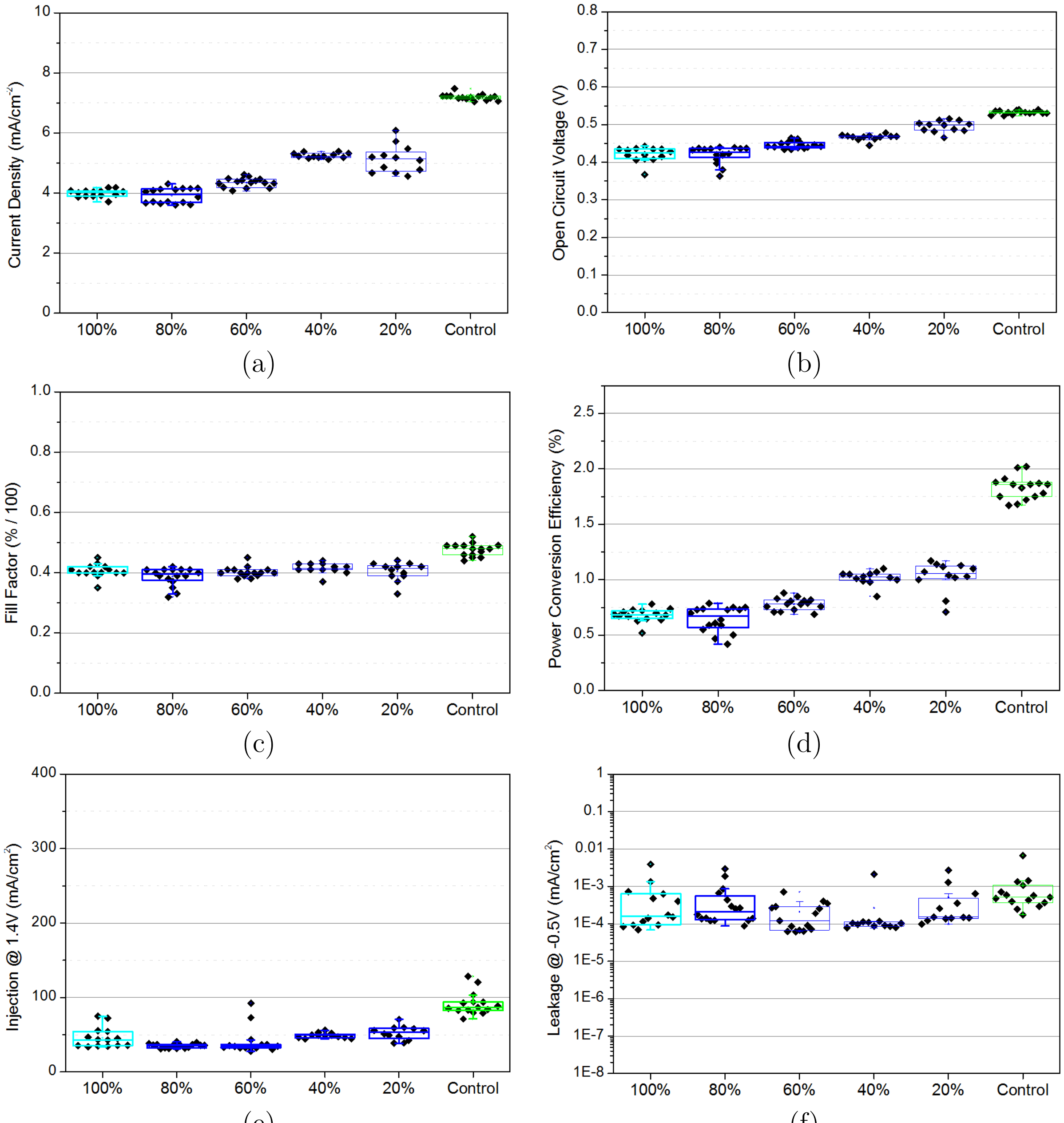

(a) (b) (c) (d) (e) (f)

**Figure 4.5:** OPV properties of cells using HSS46 as acceptor material with different loads of HSS46 compared to PC$_{60}$BM. These figures present: (a) the current density; (b) the open circuit voltage; (c) the fill factor; (d) the power conversion efficiency; (e) the injection current; and (f) the leakage current. The indexes indicate the load of HSS46.

### 4.1.3 Additive Application

Additional fullerene content in the form of HSS46 was added to typical P3HT:PC$_{60}$BM blend solution (+ 1, 2, 5 or 10 % additional fullerenes introduced by HSS46 relative to those in the control solution - provided by the PC$_{60}$BM). These load values were stipulated based on the results coming from the application of the polyfullerene in the blend, where loads of 20% were already prejudicial.

Figure 4.6 presents the $JxV$ curves for such use.

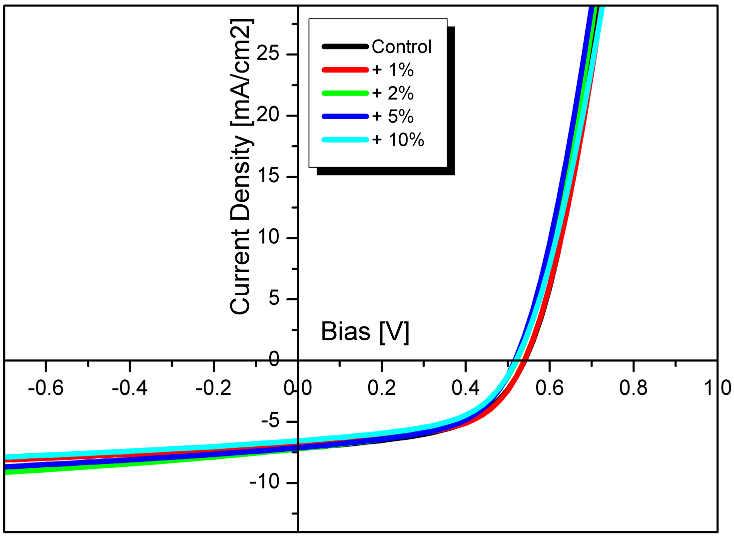

**Figure 4.6:** $JxV$ curves for the OPV cells using different loads of HSS46 in the blend.

Clearly, introduction of the HSS46 as an additive does not appear to have a strong influence except at a loading of +10%. The drop in performance here correlates with a drop in the short circuit current, and it can be noted from the extracted parameters, in Figure 4.7.

Considering these results, one can note that the difference in cell efficiencies is negligible with loads up to 10%. This result clearly defines the application of the synthesized polyfullerenes as an additive to the BHJ with loads up to 10%, since the devices are not heavily affected except when more of HSS46 is added. Using this argument, we can then study the morphological stability of these blends under annealing conditions, using the five different polymeric materials with the lateral-chain variation. This is the topic of the next section.

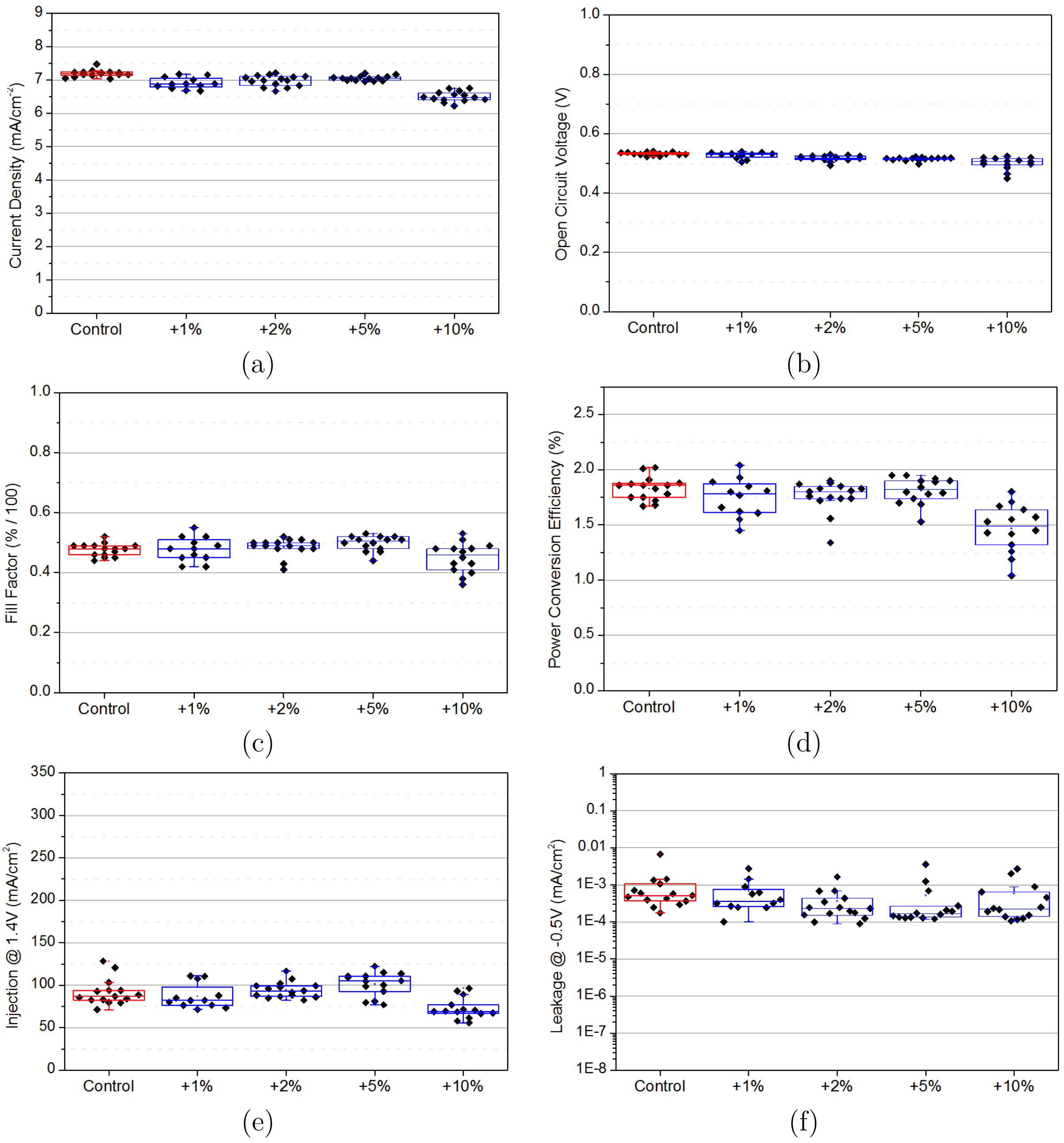

**Figure 4.7:** OPV properties of cells using HSS46 as an additive to the blend with different loads of HSS46 compared to PC$_{60}$BM. These figures present: (a) the current density; (b) the open circuit voltage; (c) the fill factor; (d) the power conversion efficiency; (e) the injection current; and (f) the leakage current. The indexes indicate the load of HSS46.

## 4.2 Morphological degradation of the blends using polyfullerenes as additives

Having the results just presented in hands, one can study the morphological degradation of the BHJ using the polyfullerenes synthesized in Chapter 3 as additives. For this study, all the five polymeric materials were employed with 10% load and annealed under nitrogen atmosphere for different times. This load is the maximum one can have without prejudicing the photovoltaic properties of the devices.

The aim is to check if these materials can be used as morphology stabilizers and if there is an influence of the lateral chain on these results. The lateral chains should modify the solubility of the polyfullerene within the blend, inducing different plasticizing effects. The devices architecture was kept unchanged from the one used in the previous section. A pre-annealing step was employed, during which the devices were heated at 140 °C for 5 minutes. Then, they were intentionally annealed longer and their photovoltaic properties were studied for the increasing time.

Figure 4.8 presents the photovoltaic properties of the devices for the different prepared materials at initial time of annealing.

As one can see, the control devices were working correctly and the cell without any polyfullerene has a performance slightly better than the other containing polyfullerenes.

Then, these blends have been submitted to thermal annealing and their photovoltaic properties were accompanied during time. Figures 4.9, 4.10, 4.11 and 4.12 present the evolution of $J_{SC}$, $V_{OC}$, $FF$ and $PCE$, respectively.

From this, one can note that the control cell (without polyfullerenes) degrades slower in the beginning but catches up the other cells' performance by 5 h mark time. Moreover, the degradation in control is caused by a drop in $J_{SC}$ and $FF$ but offset by steep rise in $V_{OC}$. However, the degradation of the polyfullerene-containing cells are due to a fast drop in $J_{SC}$ which is quickly stabilized.

However, if one normalizes the results obtained in Figures 4.9 and 4.12, one can verify that the proportional loss in performance is greater in control cell due to significant loss in current density. From this point of view, one could say that polyfullerenes retard the rate of degradation devices however this is only true because they start worse and end at the same point in what concerns the photovoltaic properties.

These results should then be better understood with the analysis of the morphological behavior of the polyfullerene itself under thermal stress. In this way, the next chapter is consecrated to the degradation studies of the synthesized polyfullerenes and their role in the degradation of the blend when used as additive.

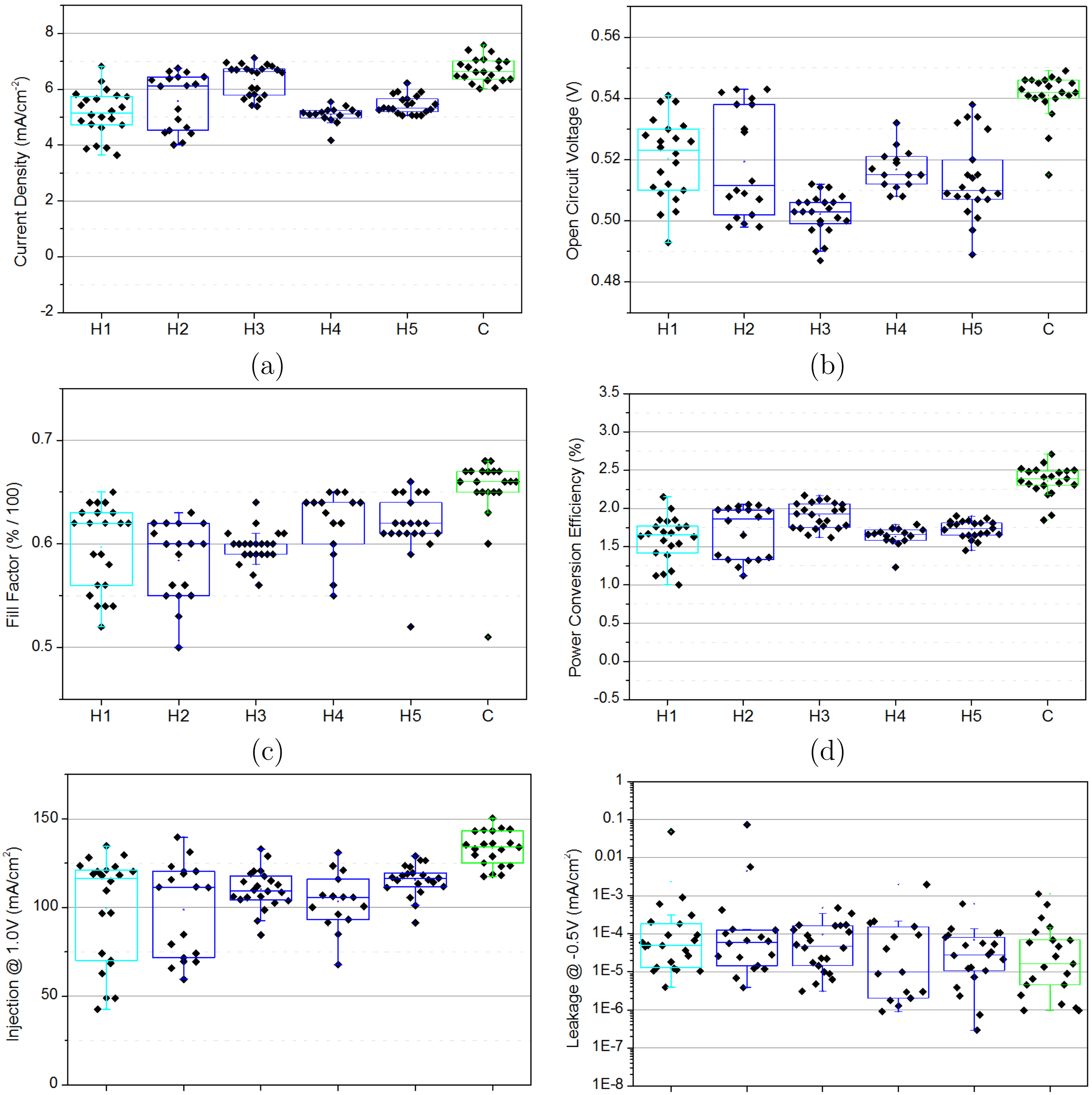

(a) (b)

(c) (d)

(e) (f)

**Figure 4.8:** OPV properties of cells using different polyfullerenes as additives to the blend with loads of 10%. These figures present: (a) the current density; (b) the open circuit voltage; (c) the fill factor; (d) the power conversion efficiency; (e) the injection current; and (f) the leakage current. The indexes stand for the different polyfullerenes employed. The correspondence is: H1 - HSS11; H2 - HSS14; H3 - HSS46; H4 - HSS48; H5 - HSS49; and C - control cell without any polyfullerene. The reader is reported to Figure 4.1 for identification of the structures being treated here.

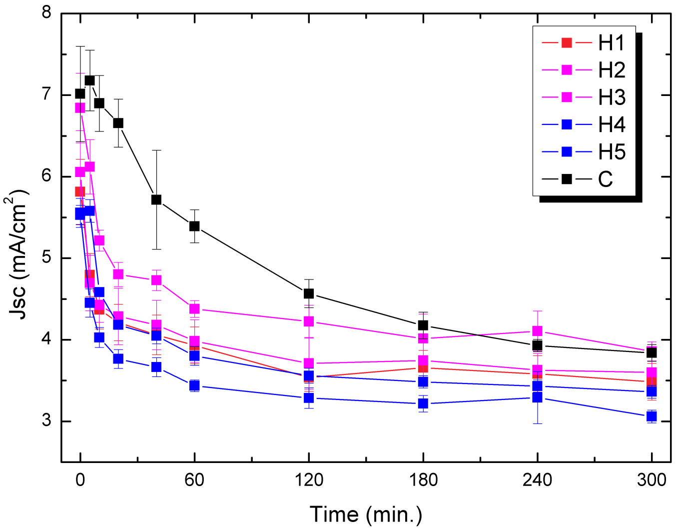

**Figure 4.9:** Evolution in time of $J_{SC}$ for the different synthesized polyfullerenes used as additives under thermal annealing.

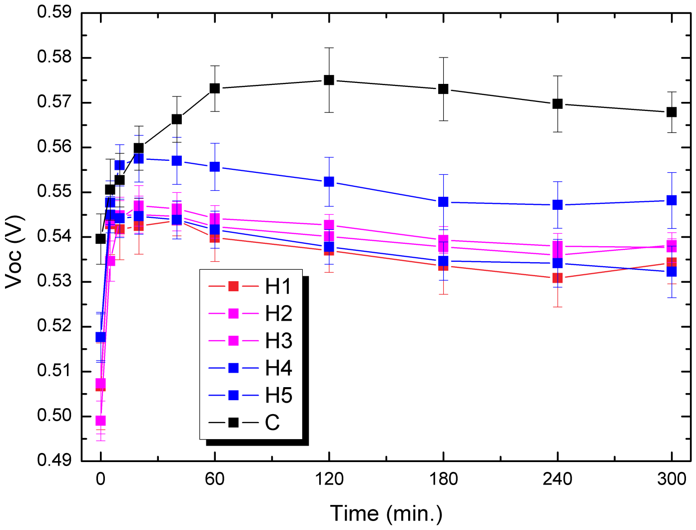

**Figure 4.10:** Evolution in time of $V_{OC}$ for the different synthesized polyfullerenes used as additives under thermal annealing.

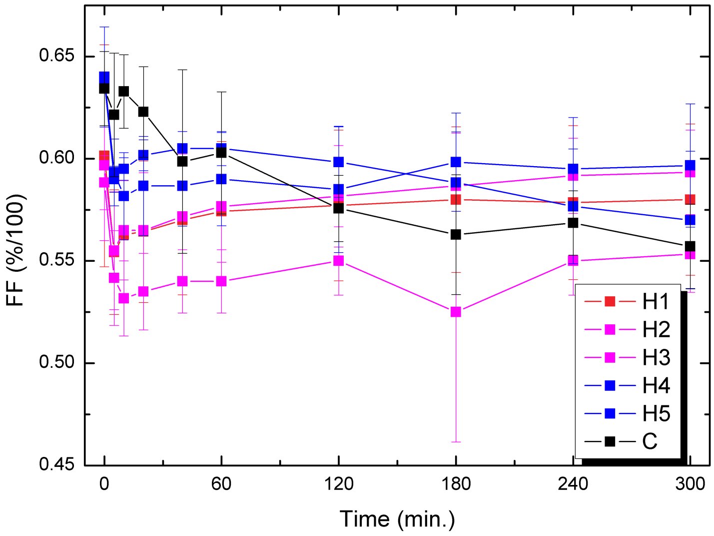

**Figure 4.11:** Evolution in time of FF for the different synthesized polyfullerenes used as additives under thermal annealing.

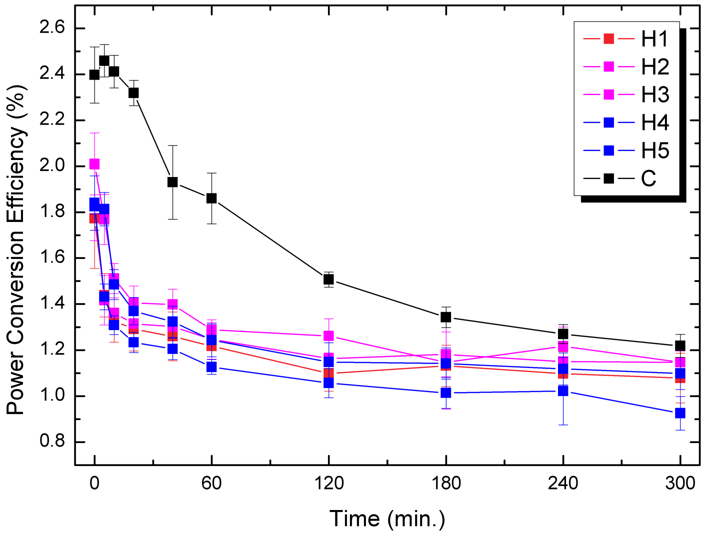

**Figure 4.12:** Evolution in time of PCE for the different synthesized polyfullerenes used as additives under thermal annealing.

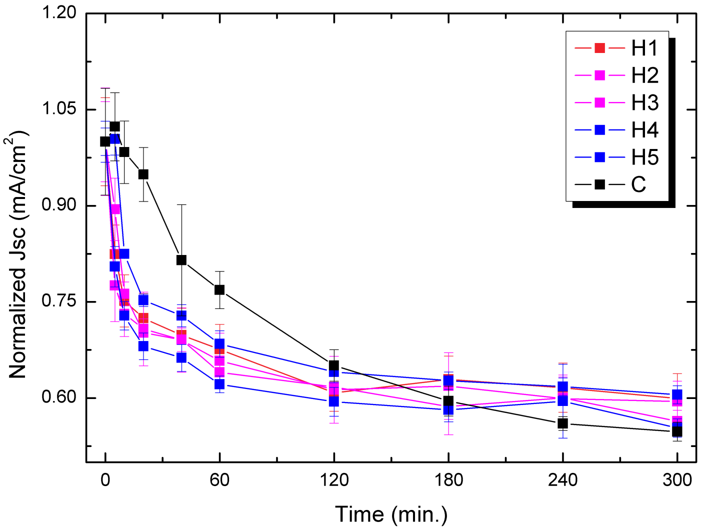

**Figure 4.13:** Normalization of the Evolution in time of $J_{SC}$ for the different synthesized polyfullerenes used as additives under thermal annealing.

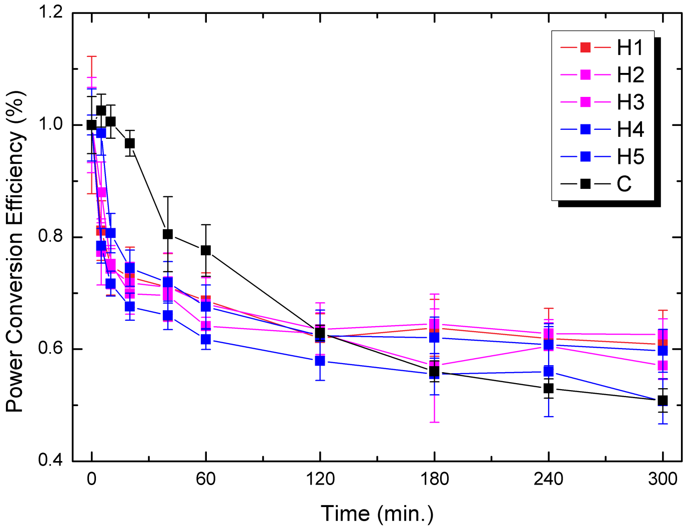

**Figure 4.14:** Normalization of the Evolution in time of PCE for the different synthesized polyfullerenes used as additives under thermal annealing.

## 4.3 Final Remarks

The results presented in this Chapter comprise the use of polyfullerenes in three different applications within OPV devices: as an interlayer, as the sole electron acceptor material and as an additive to the blend.

Considering the interlayer application, the thicker this layer gets, the lower is the photo-current extracted from the cell. This is true even for the very thin layers of the polymeric material (blade speed of 5 mm/s). This depends stronger on the thickness rather than on the temperature of annealing of the cell.

For the blend application, where the polyfullerene is used as the sole electron acceptor (or in collaboration with $PC_{60}BM$), the cells' performance are heavily impacted by the presence of the polyfullerene material, being the extracted current the factor most sensible to it. From 0% of HSS46 up to 100%, one can loose 25% of the current density of the cell. The open circuit voltage is also impacted by the same proportion.

Using HSS46 material as an additive turned to be a much more likely application. With loads up to 10% of HSS46 compared to $PC_{60}BM$, the cells' parameters are very little impacted. This application is then pursued further to study if the presence of the additive can help improving cells' morphology stability under thermal stress.

For a 10% load of polyfullerene material, the total ensemble of materials was tested under thermal annealing. Initially, the cells made with all the materials are operational similarly to the control. With annealing at 140 °C, cells loose quickly performance over time and this is due to the loss in extracted current density. Normalizing the results of the cells made with the several polymers to the one without any, one can note that the polyfullerenes retard the rate of degradation due to a quick drop on the current density but they stabilize at the same point as the control cell after 5 h of annealing.

With all these considerations, the next chapter will be dedicated to understand in more details the processes behind this non-stabilization of the bulk by the polyfullerenes. Moreover, photochemical and photo-oxidation degradations are also going to be studied.

# Chapter 5

# Degradation studies

*In this chapter, the materials' stabilities are studied against photo- and thermal stresses, either in a pure bulk or in a blend with P3HT. These studied are conducted under accelerated degradation experiments and evaluated by several characterization techniques. The motivation behind these studies are the results from the application of polyfullerenes in OPV cells, as reported in Chapter 4. Moreover, not only the morphological degradation is herein addressed, but also the photochemical and photo-oxidation mechanisms are explored. The work developed in this Chapter was accomplished during the cotutelle period, in Eberhard Karls Universität Tübingen.*

Lately, the power conversion efficiency (PCE) of OPVs has been driven above 10%[7, 8, 9] and this value continues to increase. Even though this is promising, this represents the initial performance and it surely decays over time during degradation of the cell.[167]

As already explained, the cell can degrade in several ways, and the ones to which we pay attention in this document are related to the degradation of the *n*-type material. So, fullerenes (or their derivatives) can degrade by action of either temperature or light, and the effect of these agents can be further declined considering the presence or not of oxidants (oxygen and/or water). Thus, the following discrimination is used in this thesis.

- Temperature-induced degradation

  Presence of oxidants - thermo-oxidation

  Absence of oxidants - thermal degradation[14]

- Light-induced degradation

  Presence of oxidants - photo-oxidation

  Absence of oxidants - photochemical degradation

Thermal annealing induces migration of molecules and phase segregation within the BHJ, what is characterized by a type of thermal degradation. This can also lead to aggregation of fullerene-molecules (like-likes-like behavior), hindering the photovoltaic performance.

Photochemical degradation can be characterized by induced light-activated chemical reactions capable of changing morphology and chemical structure of both *p*- and *n*-type materials, as shown by Tournebize *et al.*[168] Particularly, it is known that fullerene-derivatives are light-sensitive under inert atmospheres. It has already been shown that these materials can undergo dimerization (polymerization for pristine $C_{60}$) when irradiated with UV-VIS light.[169] This process is the first step of the aggregation mechanism of fullerenes.

On the other hand, thermo- and photo-oxidation induce performance losses by the alteration of the electronic structure of the materials. Chambon *et al.*[86] showed that the products issued from the thermo-oxidation are similar to those issued from photo-oxidation, for the case of fullerene-derivatives. Based on this, only photo-oxidation studies are performed in this thesis. The chemical products formed during the photo-oxidation of the materials are known under the name of photo-oxidation products and their determination plays a key-role on the understanding of the underlying mechanism.

It is interesting to note that, while encapsulation of OPV cells can slow down the effects of thermo- and photo-oxidation mechanism by excluding oxidants of the bulk, it has almost no effect on the intrinsic degradation mechanisms of the materials, either induced by light or by temperature.

Herein the thermal-, photochemical and photo-oxidation degradation studies will be presented for both a Poly$C_{60}$ material and for a P3HT:P$C_{60}$BM blend in which the polyfullerene has been used as an additive. These studies should allow one to identify the weak points of the synthesized material and to understand the results obtained in device's applications.

## 5.1 PolyC$_{60}$ degradation

The polyfullerene chosen for these studies was the one labeled as HSS46 ($n$-dodecyl lateral chain). This choice was motivated by the SEC-CB results, solubility and yield, as already presented in Chapters 3 and 4.

Thin films were prepared by the doctor-blade deposition of the material on ITO/glass substrates from an *o*-xylene solution of 10.6 mg/mL.[1] ITO/glass substrates were previously cleaned by Acetone/iso-propanol ultrasound bath (15 minutes each) followed by an ozone treatment (15 minutes). This procedure was employed in order to minimize the carbon contaminants on the surface.

During deposition, the blade speed was set to 80 mm/s so that one could obtain thicker films and they were annealed at 70 °C for 5 minutes to allow solvent evaporation. The films so-obtained are 150-200 nm thick (measured by AFM). Each type of degradation is studied separately by different techniques.

### 5.1.1 Thermal degradation

As seen in Chapter 4, polyfullerenes have shown very low morphological stability in blends under annealing conditions when used as additives. Although the annealing times were longer than usually performed in industry, the OPV devices should be able to resist to some level of heating when operational. The consequent annealing times up to 5 h is a way of evaluating the stability of the bulk under accelerated conditions.

In order to understand the underlying processes, HSS46 films were annealed under Nitrogen atmosphere at 85, 140 and 200 °C. The morphology time evolution was studied by UV-VIS optical absorption, Atomic Force Microscopy (AFM), Fourier-transform Infrared Spectroscopy (FTIR) and X-ray Photoelectron Spectroscopy (XPS).

#### 5.1.1.1 UV-VIS

The UV-VIS spectrum of HSS46 in solid state is composed of the same bands as the one in solution, as one can see in Figure 5.1.

The band associated with the polymerization attack is found at $\lambda \sim 450$ nm for both solution and solid state spectra in the former.[160, 161, 162, 163] One can also see that the bands associated with the internal transitions of the C$_{60}$ molecule are preserved unchanged if toluene solution and solid state spectra are compared, although broadened in the latter. Based on the absence of bathochromic shift, one can state that fullerene molecules may behave in solid state not differently than they behave in solution. Moreover, no band

---

[1] Degradation determined by the optimization performed by Belectric GmbH on the blend solutions. See Chapter 4.

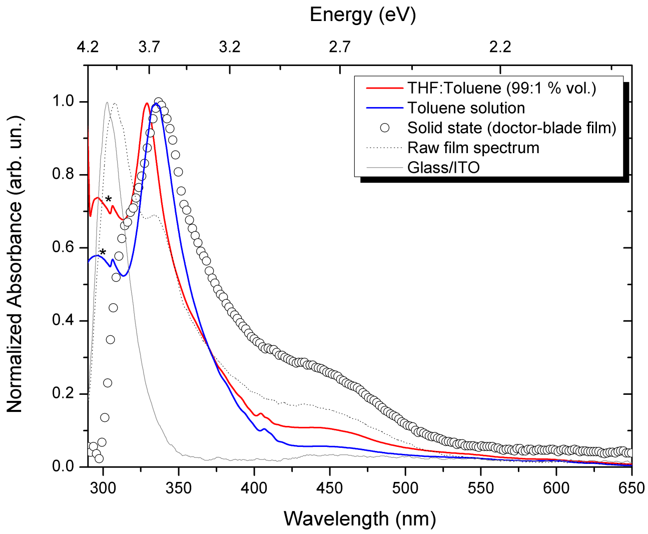

**Figure 5.1:** UV-VIS spectra of THF and Toluene HSS46 solutions and film deposited over ITO/glass by Doctor-blade technique. The solid state spectrum has been subtracted from the ITO/glass transitions. Stars indicate lamp change in diffraction grade device used for measuring solution spectra. Solid state spectrum was measured using a prism-based device.

over 600 nm can be detected neither for solutions' nor for solid state's spectra. This is an indicative of the absence of aggregation taking place.

The films deposited on ITO glass were annealed at temperatures of 85, 140 and 200 °C for different times. One can find the evolution of the UV-VIS spectra for these three treatments in Figure 5.2. As the films were not the same during the time evolution at any given temperature, the presented spectra were all normalized to the C$_{60}$ band in 311 nm, so that any difference in film thickness could be swept out.

With the annealing process, clearly no shift in main absorption band wavelength of the spectra can be seen, although a significant increase in the background can be straightforwardly noted, as it can be indicated by the arrows.

Although aggregates can be identified in solution with wide and low-intensity bands around 700-900 nm, in most of times, this effect can induce scattering of light when the size of the particles increases. It means that, when they are small, aggregates can absorb light resonantly, although at lower energies. However, when they increase in size, the absorption intensity is overwhelmed by the light scattering intensity, which now has a $\lambda^{-4}$ dependence. Thus, when no distinct band can be identified in the lower energy part of the spectrum but even so the background is increasing, one can associate this effect to the light scattering process.

Moreover, for the annealing temperature of 200 °C, one can see that changes occur in the structure of the spectra: even though C$_{60}$'s electronic structure is kept unchanged (no shift for its band), the band associated to the polymerizing attack (around 450 nm)[160, 161, 162, 163] is heavily changed: it increases quick in intensity and broadness and the effect seems to be much stronger than the one observed for the lower temperatures.

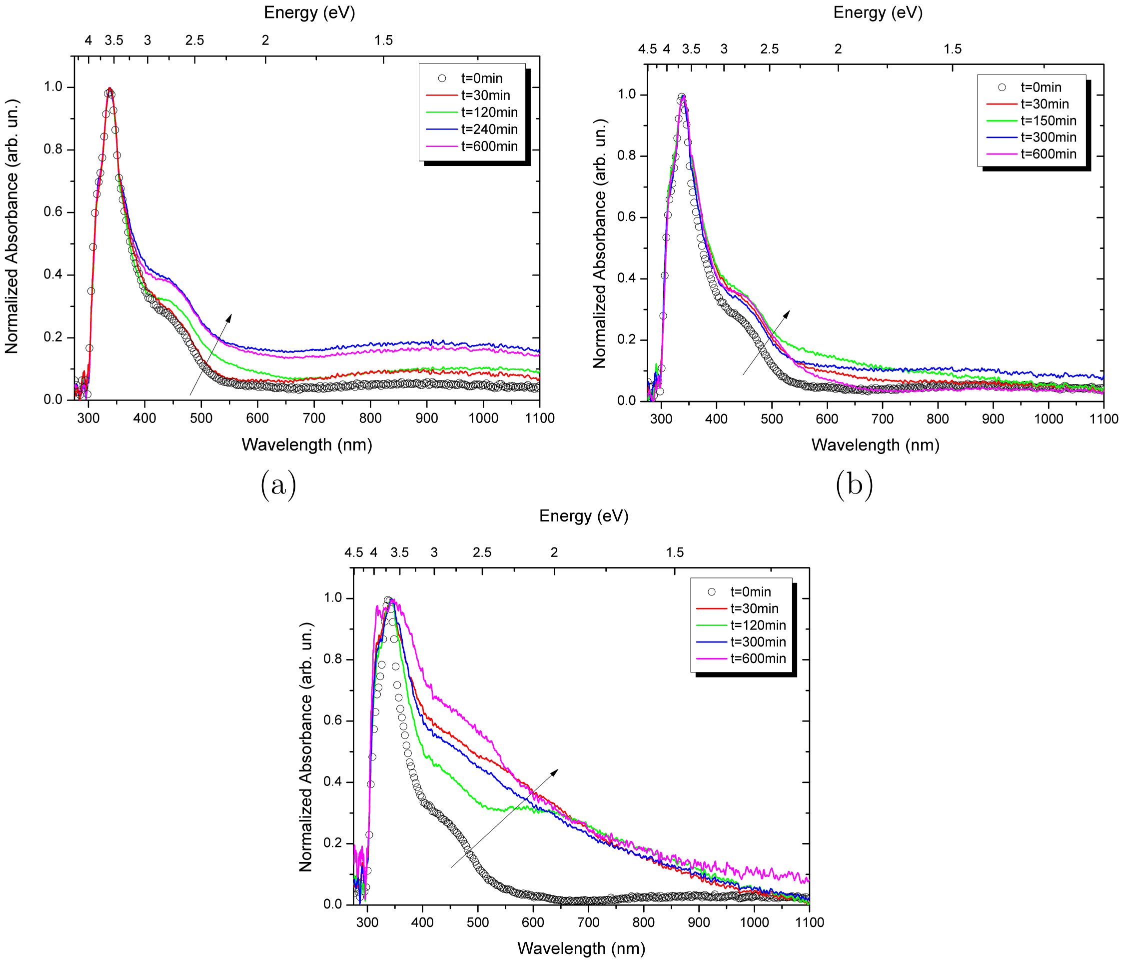

(a) (b)

(c)

**Figure 5.2:** Temporal evolution of UV-VIS spectra of HSS46 deposited on ITO/glass annealed at (a) 85 °C, (b) 140 °C and, (c) 200 °C.

Whereas for the lower ones, the non-background increases steeply, for this temperature one can associate a complete destruction of the structure of the polymer for a period under 30 min. Interestingly, this does not remain unchanged even further: the band continues to evolve and this might be associated to a dynamic cross-linking mechanism taking place, where comonomer-fullerene bonds are constantly broken and reformed with nearby fullerenes. This could also explain why fluctuations like that are also seen for the lower temperatures, although in a more moderate way.

The effect of absorption in the lower energy part of the spectrum is a non-resonant effect and has been already used to quantify the quality of carbon nanotubes dispersions, as it has been shown by Tan *et al.*[170] The authors attest that the quality of a carbon nanotubes' dispersion is dependent on how disaggregate they are in the surfactant solution and this has a direct impact over the non-resonant background and on the band width of the molecular resonant transitions. We propose here an adaptation of their method to analyze the aggregation of fullerenes. Considering the ratio:

$$RR = \frac{\displaystyle\int_{spectrum} A(\lambda,t)d\lambda}{\displaystyle\int_{spectrum} NRB(\lambda,t)d\lambda} \tag{5.1}$$

Where $RR$ is called Resonance Ratio, $A(\lambda,t)$ is the temporal dependence of the resonant bands of the absorption spectra and $NRB(\lambda,t)$ is the temporal dependence of the non-resonant background of the absorption spectra.

For this specific case, the spectrum can be fitted using six Gaussian functions, three of which are used to fit the C$_{60}$'s internal transitions (the ones with higher energy, centered at 312, 334 and 360 nm), the forth, centered at 418 nm, is used to fit the band associated to the polymerizing attack over the sphere and the last two are used to fit the non-resonant background. $RR$ then becomes:

$$RR = \left.\frac{\displaystyle\sum_{n=1}^{n=4}\int_{275}^{1100} A_n^{RB}(\lambda)}{\displaystyle\sum_{n=5}^{n=6}\int_{275}^{1100} A_n^{NRB}(\lambda)}\right|_t \tag{5.2}$$

The need of four Gaussian functions to fit the resonant bands can be determined by the derivatives analysis of the spectrum. The second- and fourth-order derivatives indicate the need of four functions.

One can readily identify the difference between these two classes of Gaussian functions based on their FWHM[2]. While for the four first ones, it is an acceptable parameter in the order of 10-25 nm, for the latter it becomes as large as the spectrum can be (over 100 nm). In Figure 5.3 one can find the application of this concept for the pristine HSS46 (t=0).

Besides this $RR$ parameter, one can quantify the increase of the background by simply comparing the integral density of absorbed photons $\Phi$, *i.e.*:

$$\Phi = \int_{spectrum} A(\lambda,t) - \int_{spectrum} A(\lambda,t=0) \tag{5.3}$$

This is based on the assumption that the resonant bands are not influenced by any aggregation process that may take place and the only difference in the time evolution of the spectrum is the increase of scattered light interpreted by the detector as an absorption process. One has to pay close attention to the fact that $RR$ and $\Phi$ will behave in the same way only if the observed changes are not electronically (shifts, decrease/increase of absorption coefficient) but solely based on the aggregation. For the case of $RR$, this

---

[2] Full-Width at the Half-Maximum

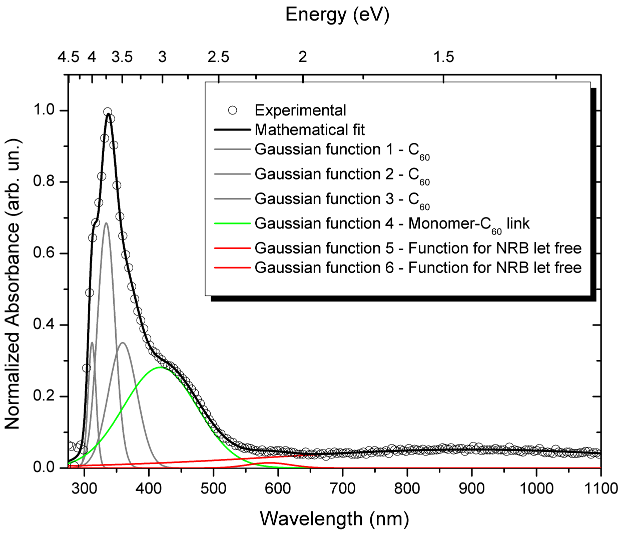

**Figure 5.3:** Gaussian fit of UV-VIS spectrum of pristine HSS46 in solid state.

is assured by using the Gaussian curves parameters of the four first bands (resonant) as a constraint in the fit of the spectra of time evolution. Then, only the two Gaussian functions responsible for fitting the non-resonant background are let free.

One can find in Figure 5.4 the evolution of these parameters for the temperatures in study.

The interpretation of these curves is as follows: the increase of the $\Phi$ value indicates that the integrated number of photons increases compared to $t = 0$ and this increase is related to the increase of the non-resonant background, associated to aggregation. On the other side, the decrease of the $RR$ parameter also indicate the decay in the "quality" of the fullerene dispersion within the sample. But, as here the inverse of $RR$ is presented ($RR^{-1}$), the increase of this parameter indicates an increased absorption, in the same way as $\Phi$.

### 5.1.1.2 Atomic Force Microscopy - AFM

Atomic Force Microscopy was used to follow the morphological changes induced by thermal annealing on the samples. Figure 5.5 presents the height and amplitude images of the HSS46 film at $t = 0$ using 10 and 5 $\mu$m scales.

These images have a RMS of 1.8 ± 0.2 nm for the 10 $\mu$m scale and 0.8 ± 0.1 nm for the 5 $\mu$m one. The films are 150 nm thick. Such variation in the RMS for different scales indicate that there are indeed at least two roughnesses: one local and other non-local, which should envelope the first one. By these values, one can say that the films appear homogeneous, although the presence of small clusters of $\sim 0.1$ $\mu$m large may be indicated by the pictures, which may be due to pristine/unreacted fullerene which aggregated from solution deposition.

In Figure 5.6, one can find the AFM pictures of films following an annealing process

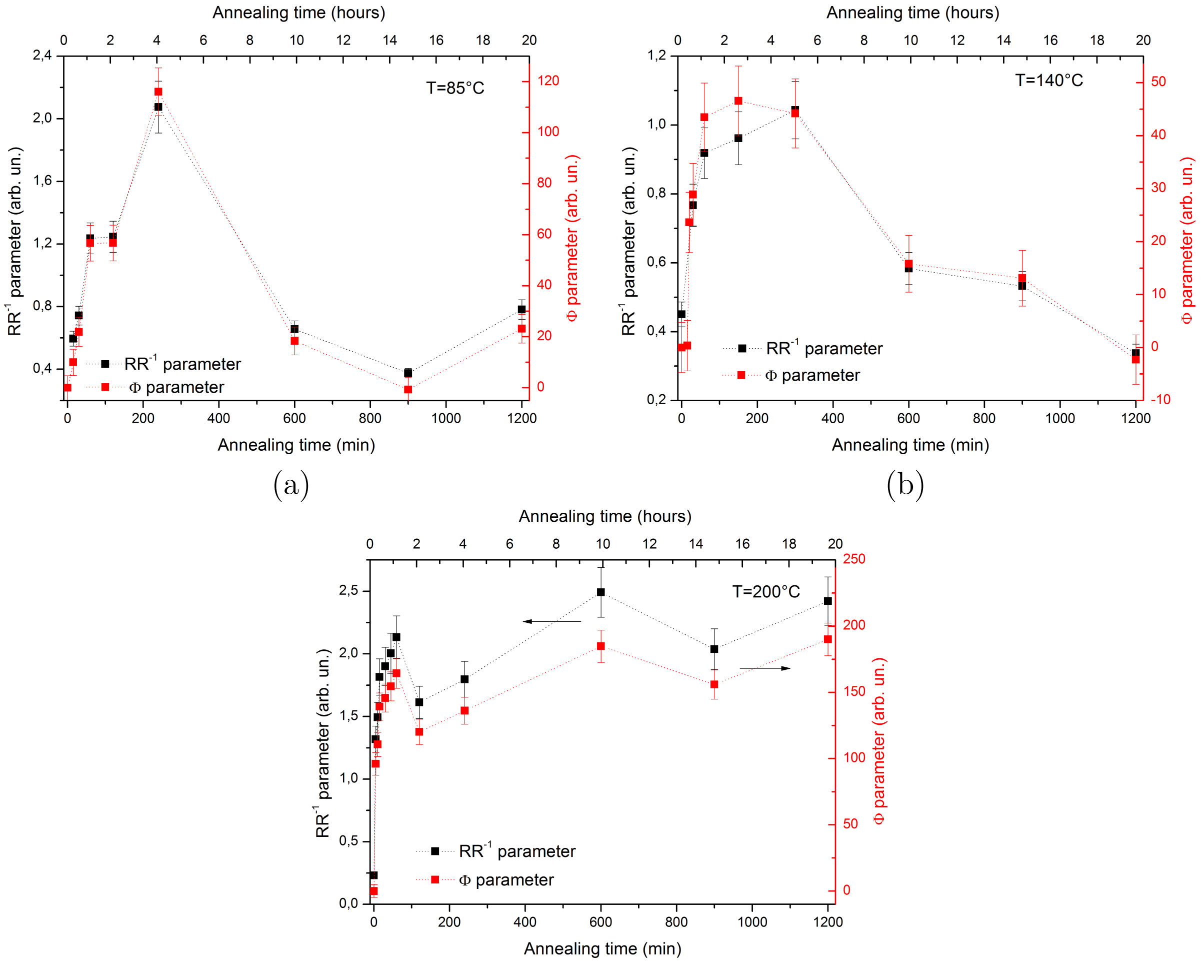

(a) (b) (c)

**Figure 5.4:** Time evolution of *RR* and Φ for films annealed at (a) 85 °C, (b) 140 °C and, (c) 200 °C. Here we present, for the sake of comparison with Φ, the inverse of *RR*. In this way, the bigger it is, the lower is the aggregation undergone by the bulk.

at 85 °C.

One can note bright spots that may indicate the formation of islands within the film, very probably constituted of fullerene molecules, increasing the RMS to ∼ 17 nm. Figures 5.7, 5.8 and 5.9 present the same results for annealing at 140 and 200 °C, respectively.

From these images, one can see that annealing at 140 °C induces the same type of aggregation as formerly observed for the 85 °C experiment. But, very well resolved fullerene islands can be noted this time, mainly for the short annealing times (60 min. - Figure 5.7). These images have a RMS of ∼ 95 and 72 nm for the 20 and 10 $\mu$m scales, respectively.

Still, for longer annealing times (300 min. - Figure 5.8), one can also identify in this time the underlying ITO/glass layer. Some parts of the film are spared from the appearance of ITO/glass, as one can see in Figure 5.8.c. The RMS of this image is closer to the one found for a shorter annealing time (∼ 62 nm), although one has to consider that this is not realistic based on the appearance of the underlying ITO/glass surface.

Finally, annealing at 200 °C for 60 min. only is already enough to achieve a serious

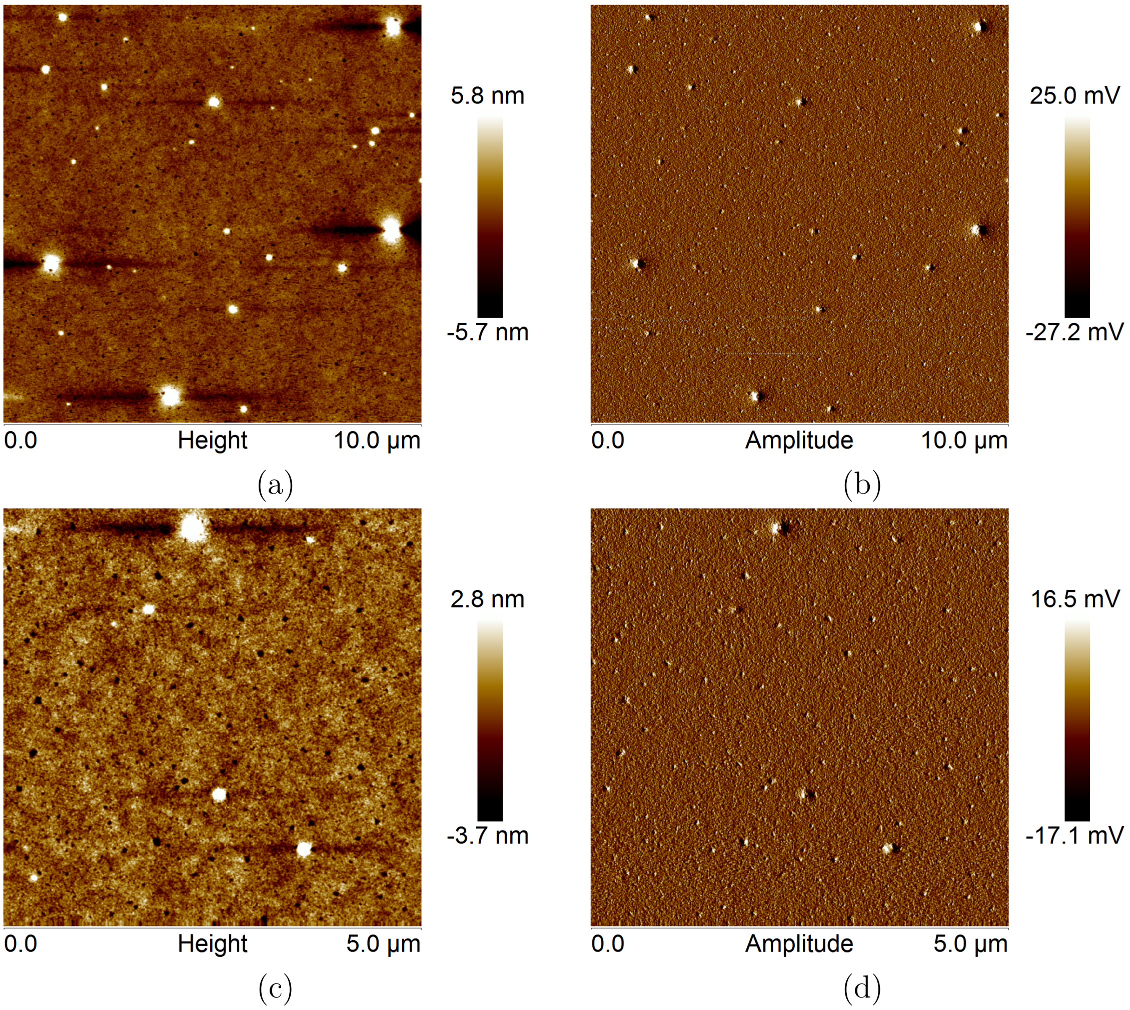

(a) (b) (c) (d)

**Figure 5.5:** AFM (a,c) height and (b,d) amplitude images of HSS46 on ITO/glass at $t = 0$.

level of island formation (and aggregation, consequently), corroborating the results found by UV-VIS analysis. One can note that the film is fully structured by these islands and lateral homogeneity is lost.

Last, but not least, the time evolution of RMS for the different annealing temperatures can be plotted and summarized in Figure 5.10. It can be noted that the evolution of RMS somehow decreases for 85 and 140 °C temperatures, as it is demonstrated by UV-VIS analysis, whereas it is not the case for the 200 °C one. The reason why this is so is still unclear and the blend degradation studies may be useful in this direction.

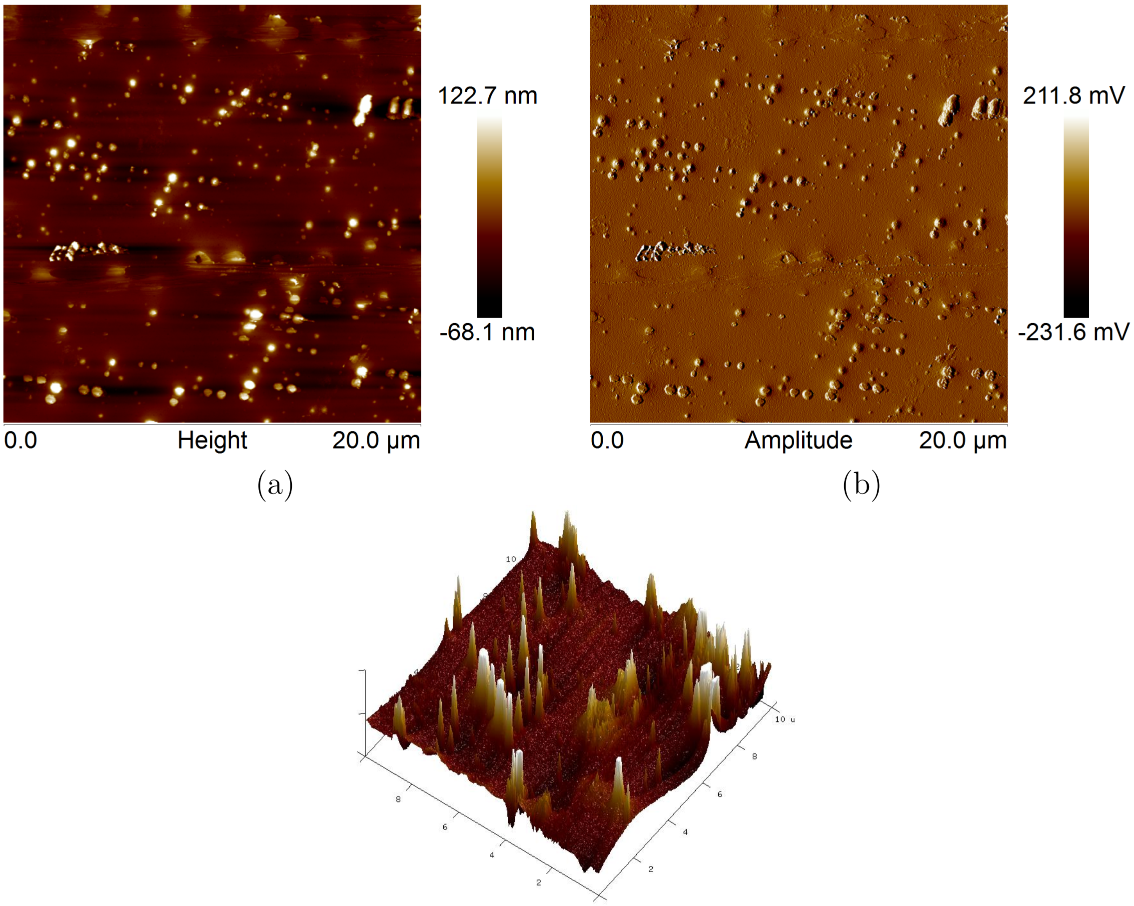

(a) (b)

(c)

**Figure 5.6:** AFM (a) height, (b) amplitude and (c) 3D reconstruction images of HSS46 on ITO/glass annealed at 85 °C for 240 min.

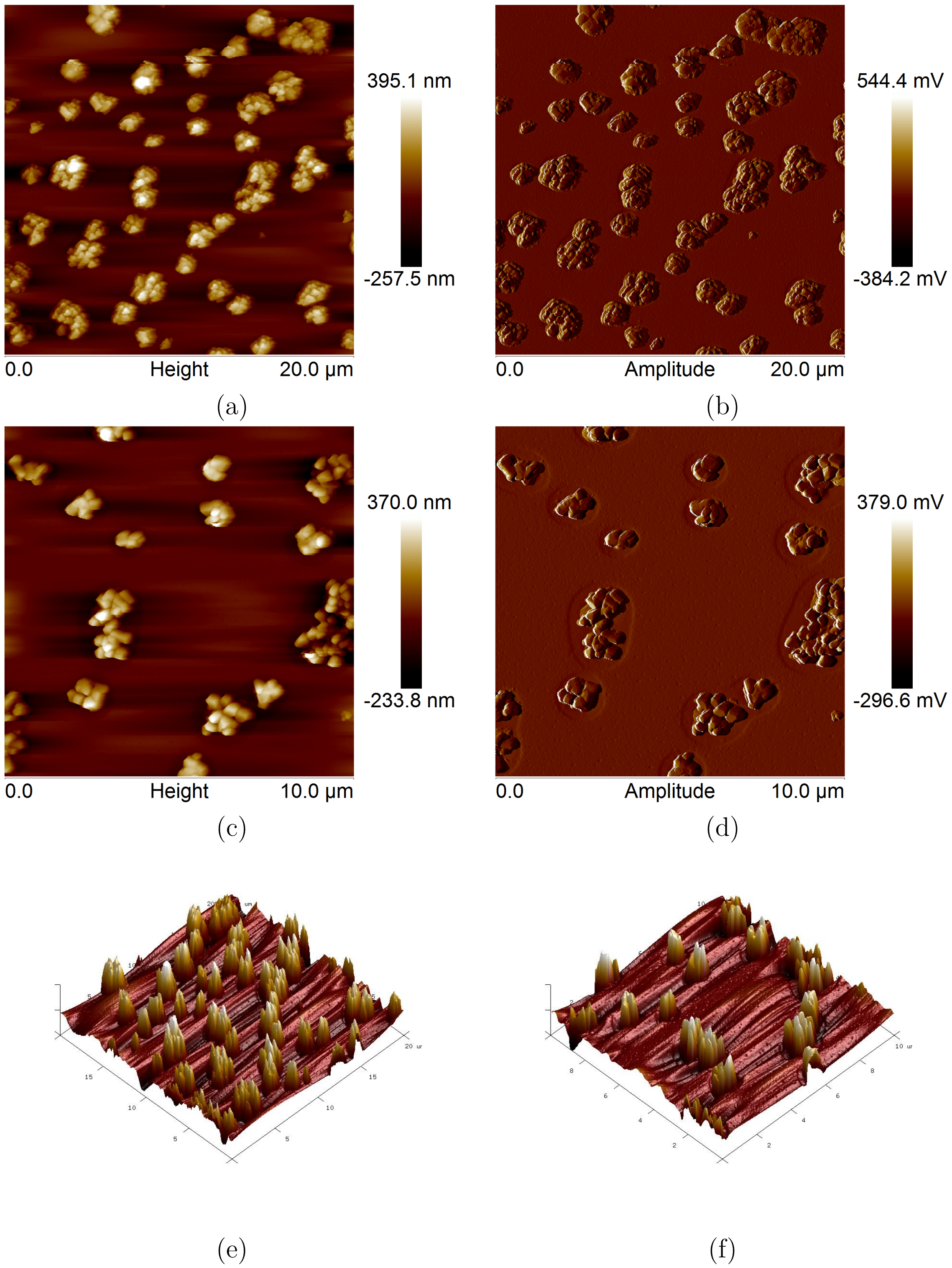

(a) (b) (c) (d) (e) (f)

**Figure 5.7:** AFM (a,c) height, (b,d) amplitude and (e,f) 3D reconstruction images of HSS46 on ITO/glass annealed at 140 °C for 60 min.

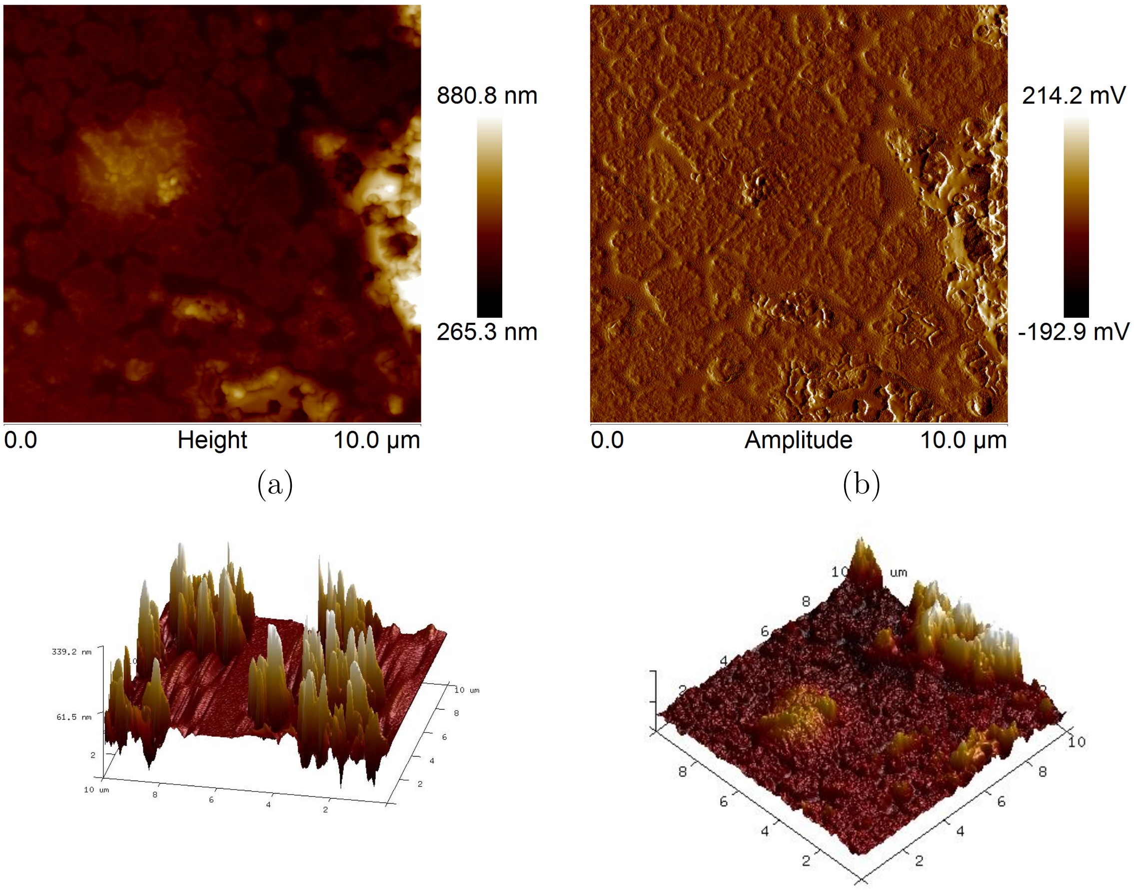

(a) (b)

(c) (d)

**Figure 5.8:** AFM (a) height, (b) amplitude and (c,d) 3D reconstruction images of HSS46 on ITO/glass annealed at 140 °C for 300 min.

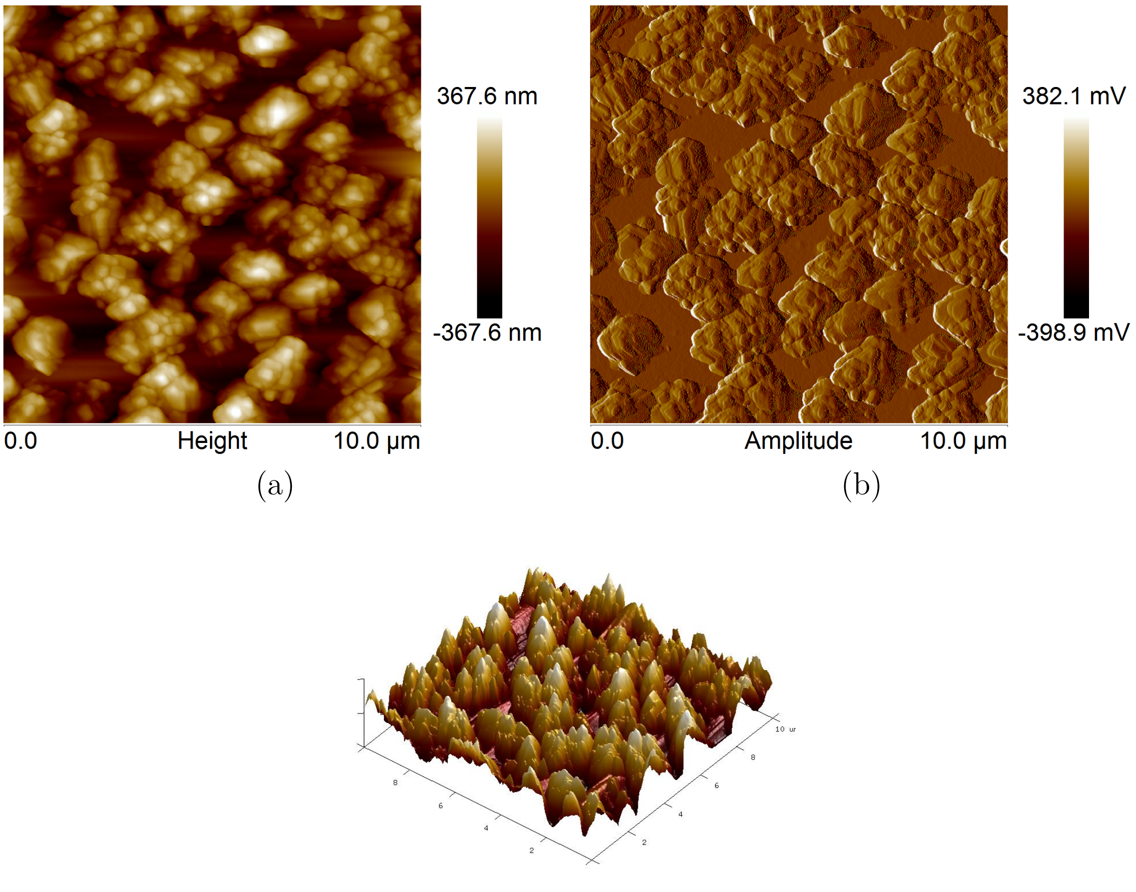

(a)

(b)

(c)

**Figure 5.9:** AFM (a) height, (b) amplitude and (c) 3D reconstruction images of HSS46 on ITO/glass annealed at 200 °C for 60 min.

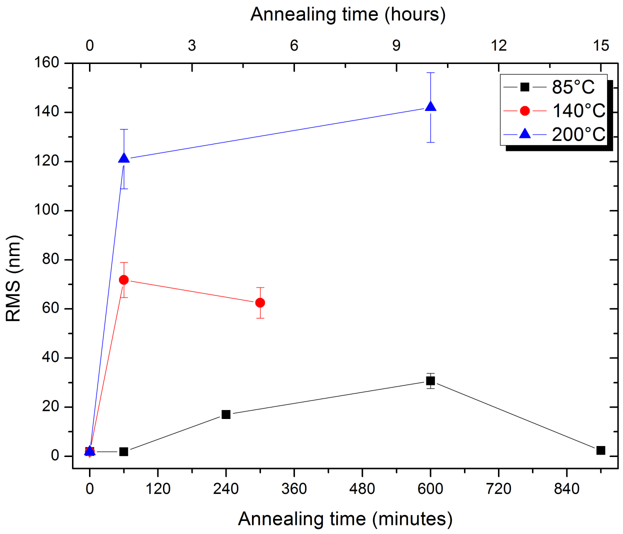

**Figure 5.10:** Time evolution of RMS for different annealing temperatures. Not all the points used for UV-VIS analysis have an AFM image, what explains the few points found in this image.

#### 5.1.1.3 XPS

X-ray Photoelectron spectroscopy was used to infer on the chemical structure changes induced by temperature treatment by means of the chemical shift description of XPS signals.[3]

The same batch of HSS46 films submitted to previous analysis had their XPS spectra for Carbon 1$s$ and Oxygen 1$s$ photoelectrons recorded. In Figure 5.11, one can find the overview spectra for $t = 0$ h and in Figure 5.12, the individual $C1s$ signals are presented, for the sample annealed under different conditions.

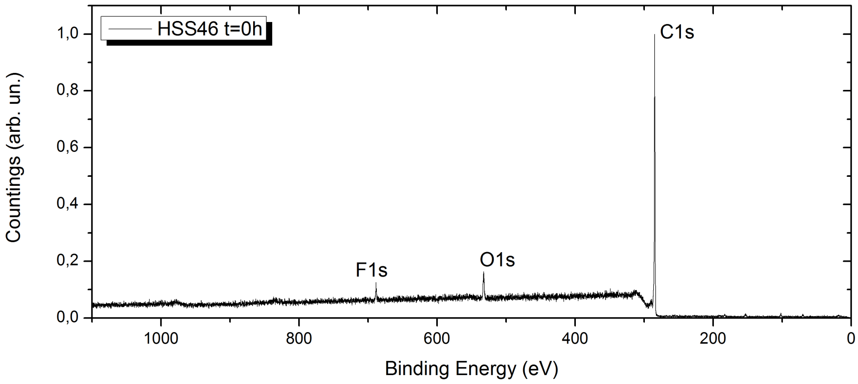

**Figure 5.11:** Overview XPS spectrum of HSS46 deposited on ITO/glass. Note the absence of Indium and Tin peaks, what indicates that the film is, at least, 10 nm thick.

One can note that, besides $C1s$ and $O1s$ signals, one can also find a $F1s$ peak.[4] The atomic concentration of the film is calculated to be 91.97% Carbon, 5.79% Oxygen and 2.24% Fluorine.[5] The stoichiometry derived from it indicates the presence of three times more oxygen than the theoretical value. This can be due either by the presence of unreacted comonomer or atmospheric oxygen that might have been physically or chemically absorbed by the film and were not removed by the ultra-high vacuum conditions. The first hypothesis is corroborated by the results issued from SEC-THF (*c.f* Chapter 3), which indicate that even Soxhlet purification times can not fully eliminate unreacted comonomers.

It is important to highlight that no major change is noticed in the $C1s$ peak besides a broadening for increasing annealing times and/or temperatures. This is observed mathematically during the fitting of these peaks, in which the gaussian broadening of the core-level transitions increases from $\sim 0.69$ eV for $t = 0$ to 0.74 eV for the sample annealed

---

[3] The XPS technique is based on the ejection of core-level electrons by an incident X-ray wave. This is based on the Photoelectron effect. The intensity of the signal is proportional to the number of electrons ejected.

[4] The molecule has no Fluorine atom in its structure and no solvent/reagent containing such atom has been used during synthesis and/or purification. We further deducted that, by analyzing the XPS profile of the HSS46 powder on Indium metal, this contamination is issued from the Teflon©filters used before the film deposition.

[5] The determination of the concentration of different species is done considering their specific sensitivity factor and core-hole lifetimes.

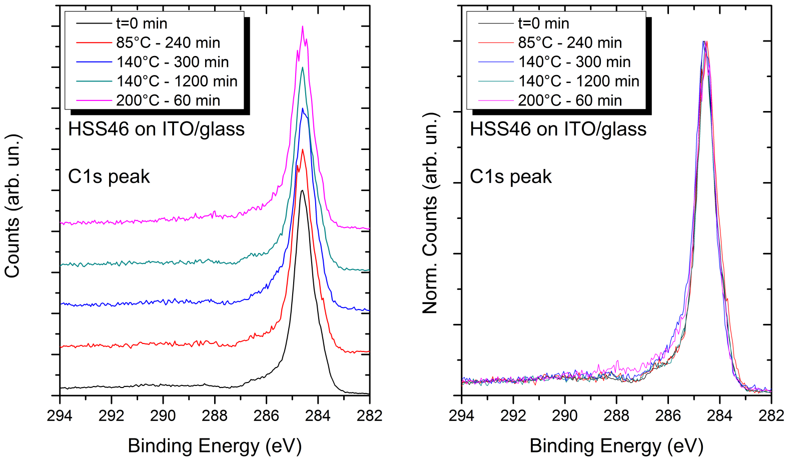

(a) (b)

**Figure 5.12:** Carbon 1*s* XPS peak for HSS46 polymer submitted under different annealing times. In (a), the spectra are stacked and in (b) they are normalized and superimposed.

at 140 °C for 300 min. A slight shift can also be noted for the first carbon shake-up, found at +1.74 eV for $t = 0$ and at +1.86 eV for the sample annealed at 200 °C for 60 min. Together, this may indicate the formation of less homogeneous domains. Even though there are changes, no major trend can be extracted, what indicates no major chemical transformation.

The final last points worth to comment are the oxygen and fluorine atomic concentrations. With increasing annealing times and temperature, the total quantity of these elements decrease within the film. This indicates either that fluorine contaminant is volatile (probably monomers of polytrifluorethylene) and also that oxygen is indeed absorbed.

### 5.1.2 Photochemical degradation

Moreover, it is known that fullerene molecules tend to undergo dimerization with light irradiation under vacuum via a photochemical [2 + 2] cycloaddition reaction and this converts two intramolecular $sp^2$ double bonds in two intermolecular $sp^3$ single-bonds.[171] This process tends to be reversible with temperatures over 100 °C. Distler *et al.* have shown that this may benefit the BHJ-OPVs by creating better percolation paths within fullerene's regime (PC$_{60}$BM, in this case). Whereas these structures only involve two fullerene molecules, their concentration can increase in such way to result in the formation of islands of aggregated material. By its turn, these fullerene-rich regions can also exist where these molecules crystallize.

One should also keep in mind that, in the same way that temperature can break bonds between the comonomer and the fullerene, light can also be a responsible for this type of degradation even under inert atmosphere. This mechanism should be considered alongside the one aforementioned.

To study the stability of the material under light irradiation, films were submitted to illumination under AM1.5 condition in nitrogen atmosphere using a xenon lamp, with emission comprised between 300 and 1100 nm.

#### 5.1.2.1 UV-VIS

The evolution of the morphology was accompanied by UV-VIS optical absorption measured every time on the same spot of the film (in opposite of what was done for the thermal stress, where one needed to apply normalization on the spectra since the parental films were different). Even more, twins samples were also degraded and their irradiation was stopped in a way to have intermediate samples to perform XPS and microscopies analyses further on.

Figure 5.13 presents (a) the time evolution of the UV-VIS spectra recorded for increasing illumination times and (b) the evolution of the $RR$ and $\Phi$ parameters, as described in the previous section.

One can identify an initial phase (t < 12h) when the non-resonant background diminishes and then it increases again, achieving a maximum around 24 h of illumination. This characteristic is kept unchanged until the end of the experiment (120 h illumination time). This may indicate that, firstly, the chains are dynamic and dimerization can occur. After this phase is past, the chains continue to evolve but towards aggregation and formation of bigger clusters.

The polymeric structure of the material and the long alkyl chains should be able to avoid such process to take place. *I.e.*, the long alkyl chains should be able to isolate the fullerene molecules from each other away enough to avoid their aggregation over time without thermal energy being given. If this is not the case, the possibility that comes to

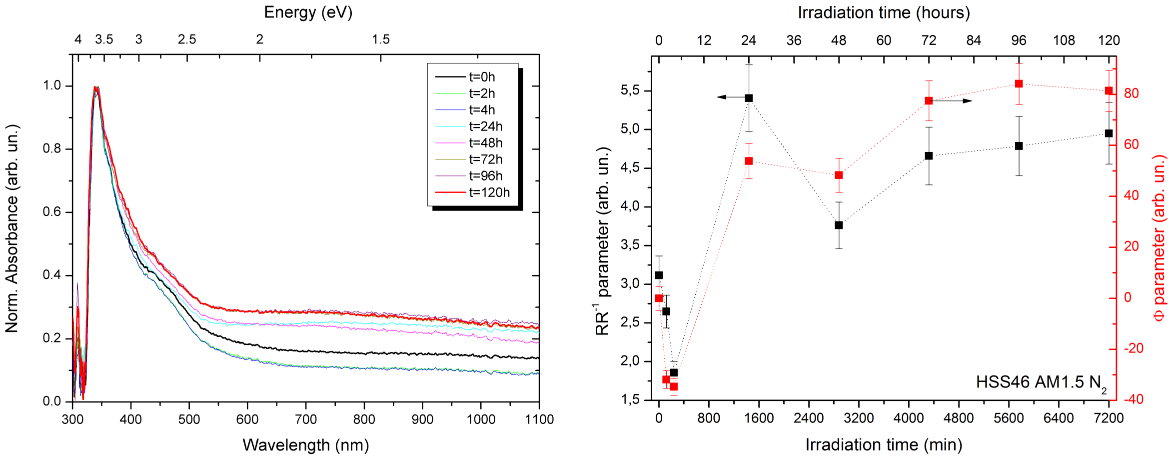

(a) (b)

**Figure 5.13:** Temporal evolution of UV-VIS spectra of HSS46 deposited on ITO/glass illuminated under AM1.5 conditions in inert atmosphere (a) and (b) temporal evolution of $RR$ and $\Phi$ parameters.

mind is the disruption of the polymeric structure based on the depolymerization of the material.

The depolymerization process can also be evoked for the thermal degradation, although the thermal energy may be, by itself, enough to induce reorganization of the chains (and aggregation). In the light-only scenario, it is less likely that the whole polymeric chains can have such mobility over each other up to the point of aggregation. But, if by some light-induced process, the polymeric structure does not exist any longer, fullerene molecules made free can now aggregate and form larger clusters, responsible for scattering light.

This hypothesis will be studied in more details in the next section.

#### 5.1.2.2 XPS

XPS signals were also acquired for this type of degradation. Figure 5.14 presents the $C1s$ peaks for increasing times of irradiation under nitrogen atmosphere.

Here again, the differences that can be noted are the broadening of the peak shape and features that affect the position of the first shake-up. The evolution of these parameters for the increasing exposition times is plotted in Figure 5.15.

Based on this, one can say that the homogeneity of the surface and its electronic structure evolve with irradiation in inert atmosphere, as shown by UV-VIS measurements. Comparing these values to the ones found for evaporated C$_{60}$ (Gaussian width of 0.75 eV; first shake-up energy of 1.80 eV with a total contribution to the curve's components of 8.6%), one could say that the formation of something similar to free fullerene might be in place. This comes from the fact that, if the intensity of the first shake-up is increasing, one

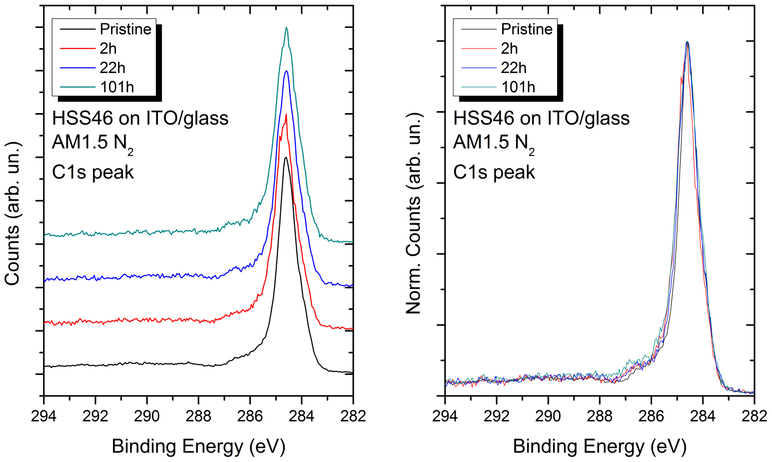

(a) (b)

**Figure 5.14:** Carbon 1$s$ XPS peak for HSS46 polymer submitted under irradiation times. In (a), the spectra are stacked and in (b) they are normalized and superimposed.

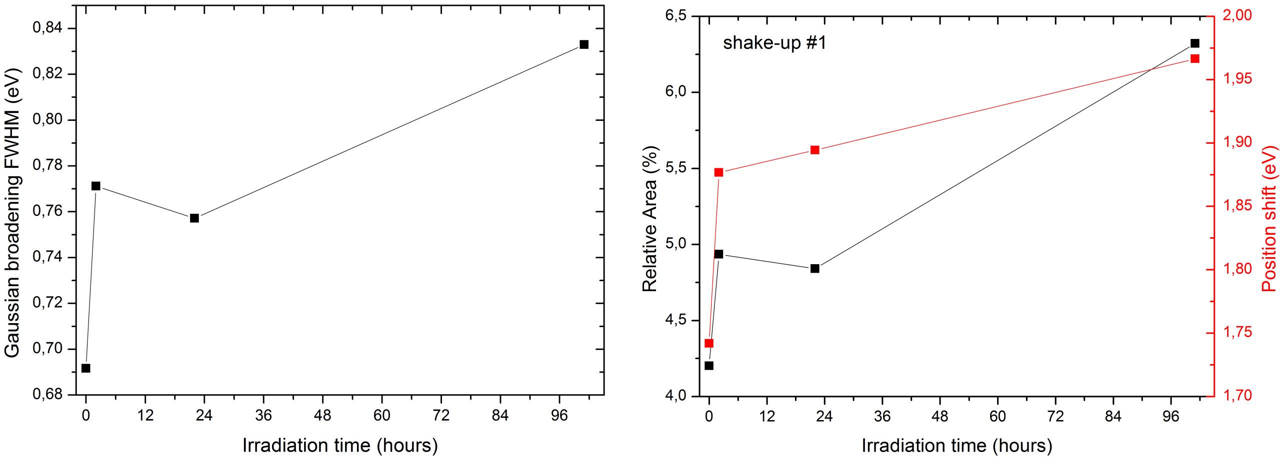

(a) (b)

**Figure 5.15:** Temporal evolution of the gaussian broadening of the core level transition, the first shake-up position and total contribution to the $C1s$ peak for increasing exposition times.

should have an increased quantity of $sp^2$ carbons.[6] On the other hand, this is not capable of affirming, by itself, that dimerization takes place since the shake-up peak intensity increases, instead of decreasing. The reason behind a decrease of the intensity of the shake-up with dimerization is the conversion of $sp^2$ to $sp^3$ bonds during this process.[172] So, the data do not provide evidence for this process to a significant amount.

---

[6] The shake-up peaks originate from core-level → $\pi^*$ transitions.

### 5.1.3 Photo-oxidation

Besides the morphological failures, which have been our focus up to now, it is also interesting to investigate the kinetics of photo-oxidation when the material is exposed to light and atmospheric conditions. A film from the same batch was exposed to controlled AM1.5 irradiation feature under synthetic air (SA) atmosphere, using a Xe lamp.[7] The degradation was accompanied by UV-VIS and sampled later to have XPS measured on it. We also performed the same study in a KBr window and accompanied the kinetics using FTIR microscopy.

#### 5.1.3.1 UV-VIS

The irradiated film had the UV-VIS spectra in function of time at the same spot, therefore there is no need for imposing any normalization. The evolution of the electronic transitions are depicted in Figure 5.16.

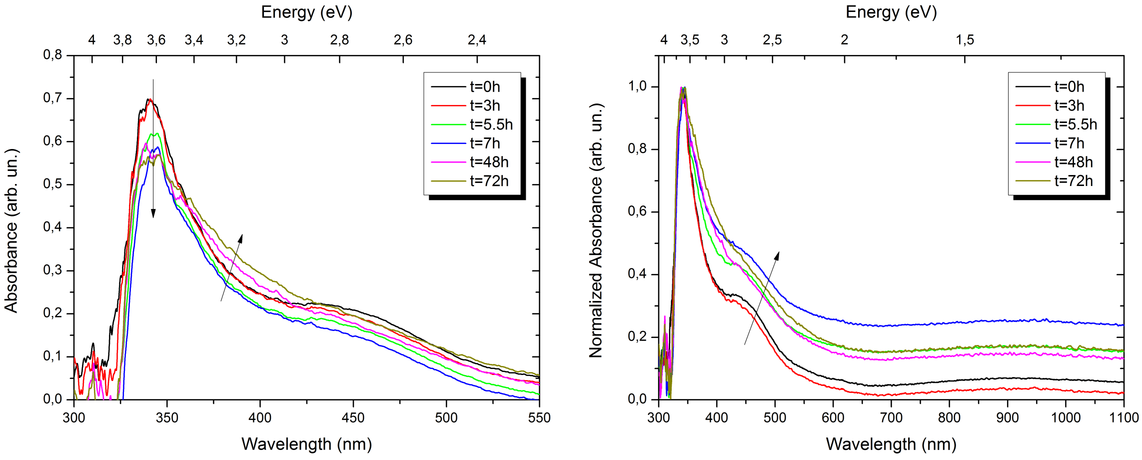

(a) (b)

**Figure 5.16:** Evolution of the UV-VIS spectra under photo-oxidation conditions. In (b), a normalization condition was applied so that the effect of light-only can also be seen.

In these spectra, two representative main bands can be chosen and analyzed during the time evolution and light exposure: one around 340 nm and a second one around 430 nm. These bands can be associated, roughly, to the inner electronic transitions of C$_{60}$ and to the characteristic transitions assigned to the polymerization attack. Although not precise, such assignment allows one to identify at least two different degradation mechanisms taking place at the same time. This is clarified with Figure 5.17.

From this, one can see that, initially, both bands decrease in intensity up to 7h and then, the one centered at 340 nm stabilizes whereas the one centered at 430 nm increase again in time. This may be a result of both: (a) light-only effects, as the one described in last section; and (b) appearance of photo-oxidation products that absorb light in

---

[7] For all these experiments, the reproducibility of the results was tested.

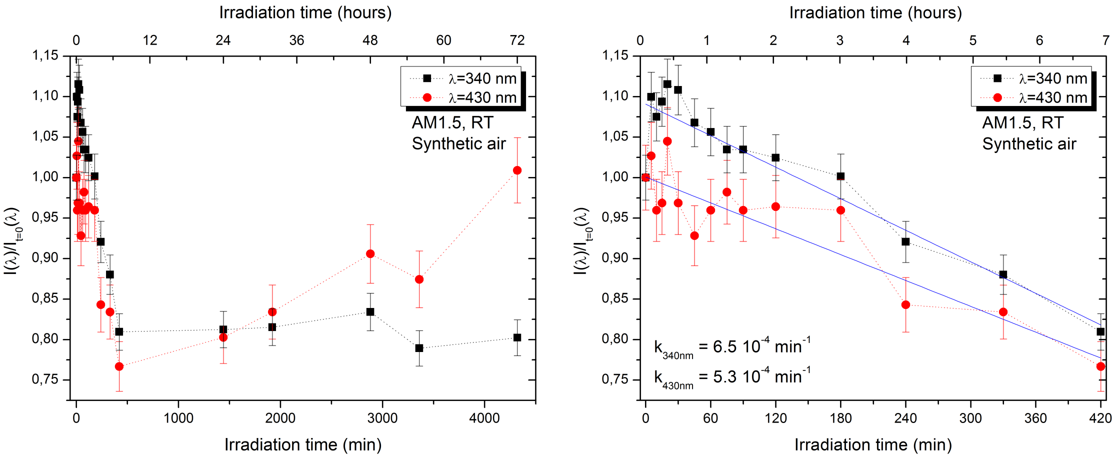

(a) (b)

**Figure 5.17:** Evolution of the UV-VIS spectra under photo-oxidation conditions compared to the pristine sample. In (b), the region inferior to 7 h is zoomed in and the tentative linear fits of each curve is presented in blue, alongside their associate rate constants.

wavelengths higher than 400 nm. Another possible scenario is that for the band centered at 430 nm, there is a period of stabilization under 3h and then the decrease of intensity starts. In both cases, one does not have enough resolution to determine which is the most likely process to taking place.

UV-VIS does not allow to pursue the identification of the mechanism(s) and products of photo-oxidation any further. Then, XPS and FTIR characterizations are done and presented in the next sections.

### 5.1.3.2 XPS

XPS signals were also acquired for this type of degradation. Figure 5.18 presents the $C1s$ peaks for increasing times of irradiation under SA atmosphere. The same can be found for $O1s$ peaks in Figure 5.19.

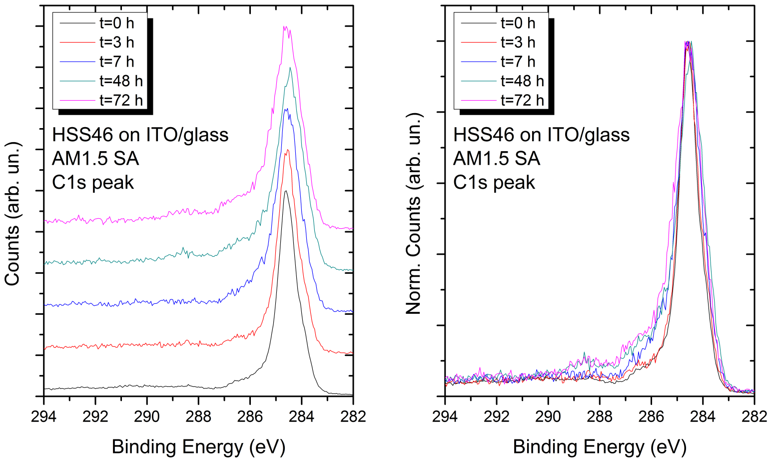

(a) (b)

**Figure 5.18:** Carbon 1$s$ XPS peak for HSS46 polymer submitted under irradiation times in SA atmosphere. In (a), the spectra are stacked and in (b) they are normalized and superimposed.

One should note the increase of the peak intensity centered around 288 eV, associated to oxygenated species. From the $O1s$ plotted in Figure 5.19, one can further see a broadening of the peak associated to the presence of oxygen species others than the initial ones.

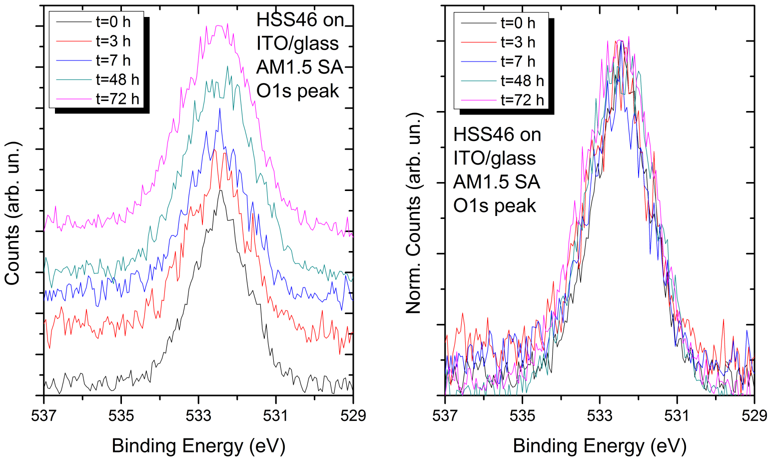

(a) (b)

**Figure 5.19:** Oxygen 1$s$ XPS peak for HSS46 polymer submitted under irradiation times in SA atmosphere. In (a), the spectra are stacked and in (b) they are normalized and superimposed.

In the course of photo-oxidation reaction, photo-oxidation products are created. As already mentioned, these products consists of carboxylic acids, esters, ethers, aldehydes, alcohols and all the sort of oxygenated species. Accordingly to the chemical function being formed, different chemical shifts can be found in the XPS spectra for both $C1s$ and $O1s$ regions. Normally, the more oxidized is a carbon specie, for example, the higher will be the binding energy of the $C1s$ core-level of the photo-oxidation product. This is due to the fact that oxygen is electronegative enough to make carbon electrons more bound, what requires a higher energy to "eject" them. The same analogy is done to $O1s$ core-level.

From this reasoning, one can separate the photo-oxidation products in function of their respective chemical shifts in both $C1s$ and $O1s$ regions, as it can be found in Figure 5.20.

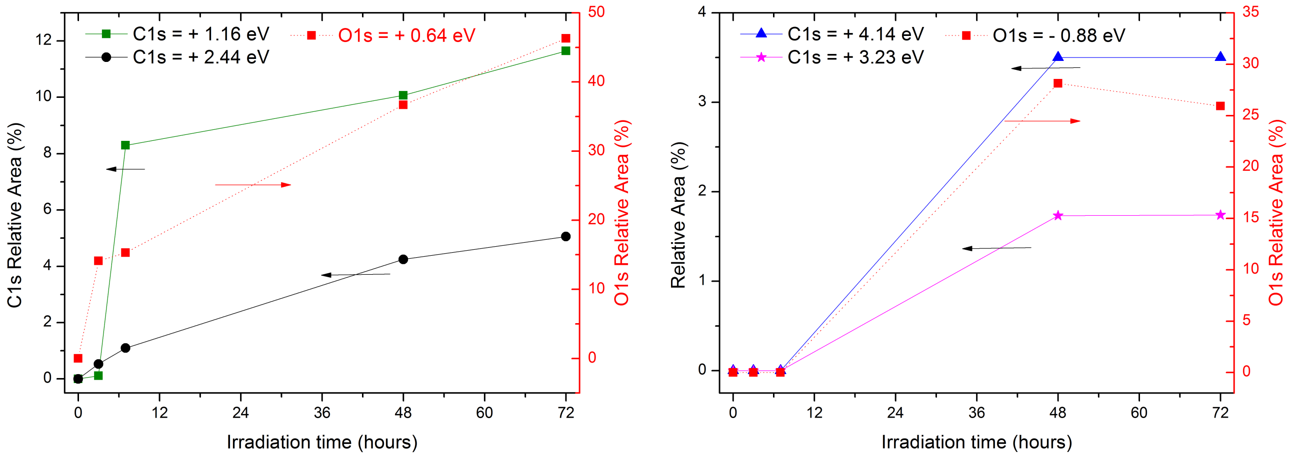

(a) (b)

**Figure 5.20:** Rate of photo-oxidation products formation analyzed by XPS.

These rates were separated based on the time needed by them to appear in XPS spectra. Thus, in (a), the photo-oxidation products that appears since the early stages of exposure to light are characterized by their $C1s$ and $O1s$ signals. The same is done in (b), where these peaks now only appear after longer (>7h) exposure times. Using the sensitivity factors of these two different core-levels, one can estimate that in (a), the peaks represent products in a lower oxidation state than in (b). This is not only seen by the chemical shifts, but also by the $O1s/C1s$ proportions between the two regimes: in (a) this ratio assumes values around 0.7 whilst in (b) they are over 2.6 up to 5. This may indicate that groups like esters and carboxylic acids (high oxygen/carbon ratio and higher oxidation state) are likely to be predominant in the late stages of the photo-oxidation process. The early stages are likely to be dominated by the appearance of alcohols and formation of ether functions (low oxygen/carbon ration and lower oxidation state).

Other explanation to this is the preferential sites for the degradation to start on the molecule. Very likely, the fullerene sphere and the comonomer with its lateral chains should not degrade at the same rates. Moreover, some products can be more likely to form on one compared to the other. To further infer on this, the photo-oxidation was also accompanied by FTIR measurements.

Last but not least, the effects induced only by light can also be extracted from the fitting process and they are exposed in Figure 5.21, considering for this the analysis of the first shake-up.

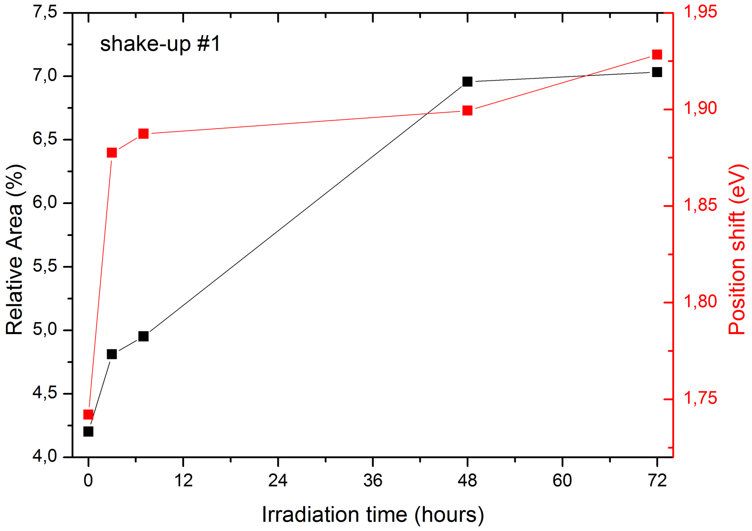

**Figure 5.21:** Temporal evolution of relative area and energy of the first carbon shake-up.

One should note that these effects reproduce those found in the photochemical degradation. *I.e.*, ATRAP-based polymeric derivatives of fullerenes are sensitive to light with or without oxidants. If the latter are present, both effects evolve together for increasing exposure times.

#### 5.1.3.3 Fourier-Transform Infrared Spectroscopy (FTIR)

FTIR measurements were performed on a film drop-cast over a KBr window and irradiated under the same conditions as before up to 96 h. In complement to the analysis already done in Chapter 3, the spectrum of HSS46 film presents the characteristic bands of $C_{60}$ (527, 576, 1182 and 1428 $cm^{-1}$),[157, 36, 173] the $-C-H$ vibrations characteristic of the alkyl chains (2849 and 2920 $cm^{-1}$), benzyl ring vibration (740 $cm^{-1}$) and vibrations associated to the $-CH_2-CH_2$- and ether vibrations (1375-1530 $cm^{-1}$ and 1140-1240 $cm^{-1}$ regions, respectively). Moreover, a wide ensemble of minor bands centered in 1015 $cm^{-1}$ are found and may be associated to the fullere-$CH_2$-comonomer link. Figure 5.22 displays this spectrum (black curve) altogether the time evolution of the FTIR spectra during photo-oxidation experiment measured at the same point on the sample.

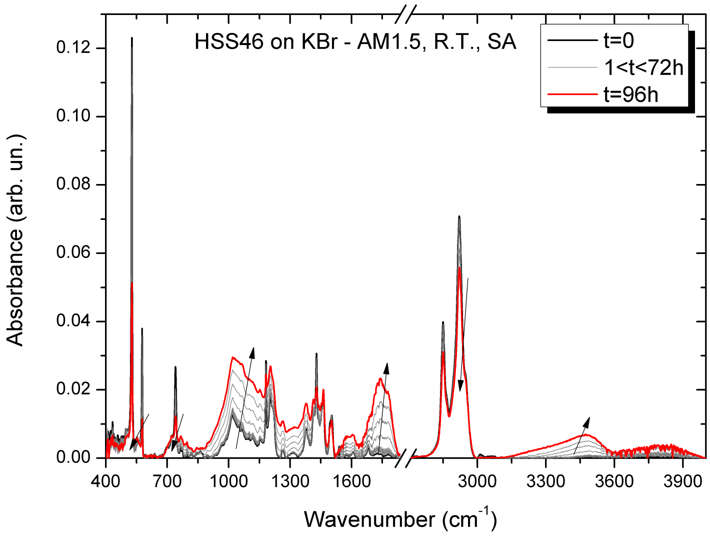

**Figure 5.22:** Time evolution of HSS46 FTIR spectra during photo-oxidation.

The effects of photo-oxidation are sensed in different regions of the spectrum: 1 - in the fullerene inner vibration regions; 2 - in the carbonyl region; 3 - in the hydroxyl region; and in the region around 1000 $cm^{-1}$. To better discriminate the evolution of these bands, the spectrum at each time was subtracted from the initial one ($t = 0$). These differential spectra are presented in Figure 5.23.(a). The whole spectra were fitted with Lorentzian functions for the vanishing bands and with Gaussian functions (as few as possible) for the rising bands. This process, for $t = 96$ h is depicted in Figure 5.23.(b). The rates, in comparison to the initial band intensity, of the (most important) vanishing and rising bands are presented in Figure 5.24.

This figure only presents the bands which increase/decrease are at least superior to 10% from the initial intensity. Meanly for photo-oxidation products bands, there are minor ones at 771, 1060, 1175, 1358 and 1595 $cm^{-1}$ which are not present in this graph.

As mentioned before, three domains of degradation can be separated: the degradation of the $C_{60}$ moiety is observed by the decrease of the bands at 527, 576, 1182 and 1428

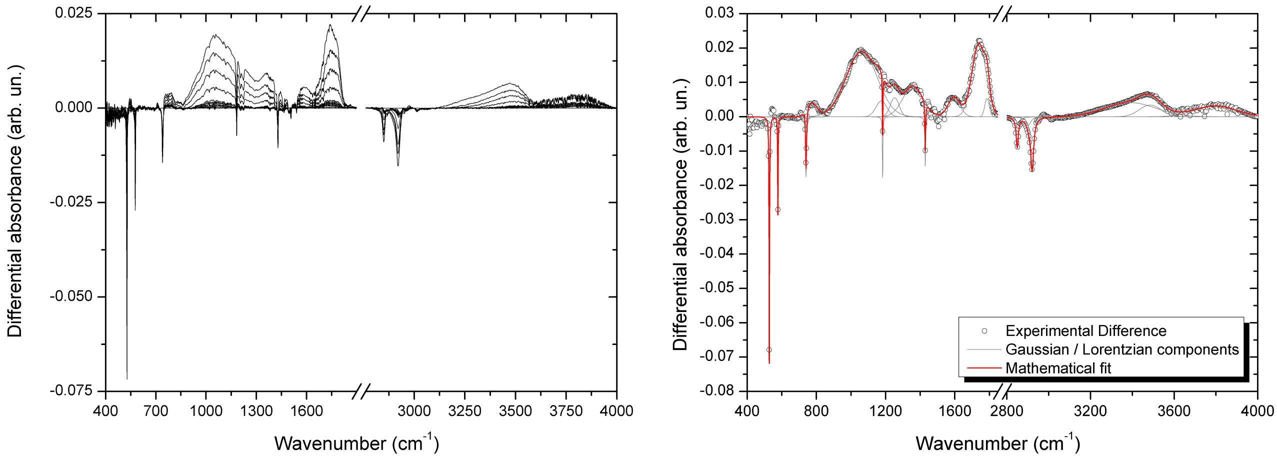

(a) (b)

**Figure 5.23:** Evolution in time of HSS46 FTIR spectra during photo-oxidation. In (a), one can find the superposed spectra during degradation and in (b) the mathematical fit for t=96h is presented. The time steps for (a) is the same used in Figure 5.22.

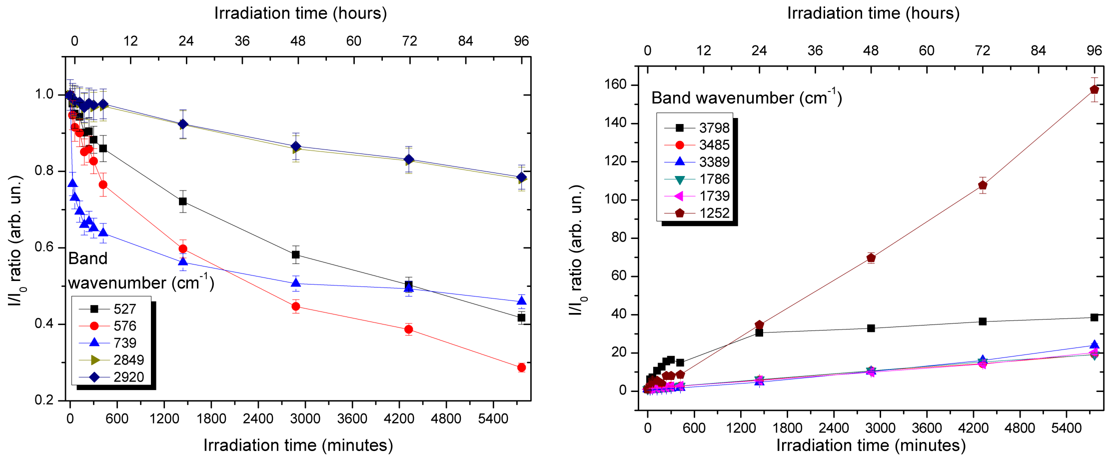

(a) (b)

**Figure 5.24:** Decay and increasing rates for vanishing (a) and photo-oxidation products formation (b).

cm$^{-1}$ (the latter ones are not present for the sake of clarity); the degradation of the monomer (band at 739 cm$^{-1}$); and the degradation of the lateral chain (bands at 2849 and 2920 cm$^{-1}$). Some point should be highlighted:

- 2849 and 2920 cm$^{-1}$ bands have their intensities decreasing in a coupled way. As a matter of fact, they are both bands related to the same vibration;
- For irradiation times below 7 h, the benzene ring band (739 cm$^{-1}$) has its intensity decreased faster than the others. This result may be analyzed under the light of UV-VIS and XPS results;

For the rising bands, we can deduce at least four situations:

1. $C = O$ vibration bands associated to esters, ketones, carboxilic acids anhydrides and aromatic esters appear at 1785 and 1739 cm$^{-1}$.

2. $C - O$ vibration bands associated to alcohols appear at 1175 (tertiary alcohols) and 1060 (primary alcohols) cm$^{-1}$; other bands assigned to $C - O$ bond appear at 1358 and 1251 cm$^{-1}$.

3. $O - H$ vibration bands associated to alcohols and carboxylic acids appear at 3389, 3484 and 3797 cm$^{-1}$;

4. $C - C$ neighbor of $C - O$ or $C = O$ vibration bands appear at 1595 cm$^{-1}$.

Chambon *et al.*[86] studying C$_{60}$ and PC$_{60}$BM photo-oxidation found degradation bands at 1745 and 1782 cm$^{-1}$ which are retrieved herein (1739 and 1785 cm$^{-1}$). Upon chemical derivatization studies in ammonia, they could attribute the one at 1745 cm$^{-1}$ to formation of formates and the one at 1782 to anhydrides. Moreover, using a $SF_4$ treatment, they could also associate these bands to the formation of carboxylic acids. Considering this, the degradation of the C$_{60}$ moiety agrees well with what has already been published[87] and with XPS data.

The degradation of the lateral chains was already well characterized elsewhere[88, 89, 168]. The mechanism behind this degradation is based on radical abstractions of lateral chain's hydrogen atoms (see Chapter 6, section 6.2), which further react within the chain forming low-molecular weight compounds and cross-links.

Finally, it is interesting to note that there is an intense degradation of the comonomer. It is very difficult to separate, by FTIR only, the contributions of photo-oxidation products coming from the attacked fullerene or the aromatic ring of the comonomer. Moreover, the band associated to the comonomer-C$_{60}$ bond vibration (expected between 900-1100 cm$^{-1}$)[86] should be altered if an underlying depolymerization process takes place concomitantely, as it will be discussed further on. Such process could affect the affinity of the molecule to oxygen and explain why the degradation of this moiety is that fast compared to other bands. The effect or not of light on such process will be studied in more details in the last section of this chapter.

## 5.2 P3HT:PC$_{60}$BM:HSS46 blend degradation

As it was discussed before, the phase segregation between the *p*- and *n*-type materials happens basically because of the very different surface energies of the two materials and polymerizing fullerene may be a strategy to increase P3HT:PC$_{60}$BM miscibility, since polyfullerenes can either interact strongly with the other fullerene derivative and be soluble in conjugated polymer matrix based on the polyfullerene comonomer used. Also, PC$_{60}$BM can aggregate around the polyfullerene chains to stop it from moving and over-aggregating.

Two different systems were degraded: (a) BE1, which is a P3HT:PC$_{60}$BM blend and (b) BE2, a P3HT:PC$_{60}$BM:HSS46(10%) composite.[8] For the latter, the total amount of fullerene was kept constant compared to the former. This was done by adjusting the quantity of PC$_{60}$BM in the ternary system.

The films were prepared by Belectric GmbH, as discussed in the previous chapter. HSS46 was employed as an additive in the bulk after the results obtained in the aforementioned chapter.

### 5.2.1 Thermal degradation

BE1 and BE2 films were annealed in a nitrogen atmosphere at 140 °C, using the same procedure as that used for HSS46 alone.

#### 5.2.1.1 UV-VIS

Figure 5.25 presents the evolution of the UV-VIS spectra for both systems for different annealing times. Figure 5.25.c presents the rate of decay of the relation between the band centered at 340 nm compared to the one centered at 514 nm.

The band centered in 340 nm, associated to the fullerene's electronic transitions, has its intensity decreased for increasing annealing times. This is an evidence of the phase segregation and consequent crystallization of PC$_{60}$BM molecules. Although the dimerization effect should also be present in the beginning of the process, its contribution is quickly overwhelmed by the formation of larger clusters.[23]

#### 5.2.1.2 Atomic Force Microscopy - AFM

The initial nanomorphology of the blend does not present big difference when both BE1 and BE2 films are compared. The 3D reconstructions presented in Figure 5.26 are representative of RMS of $\sim 11$ and $\sim 13$ nm, respectively.

---

[8] The justificative why 10% is used can be found in Chapter 4.

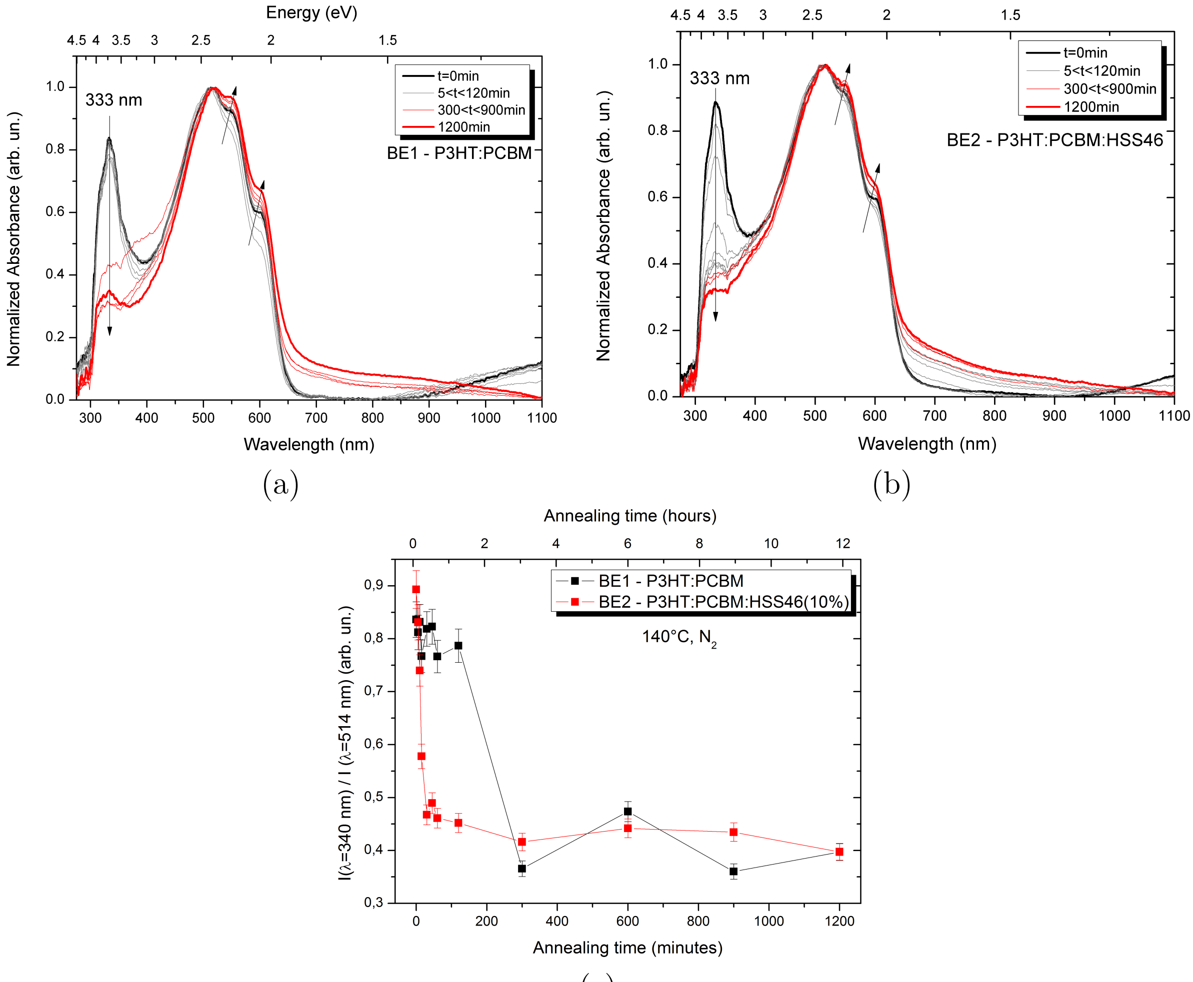

(a) (b)

(c)

**Figure 5.25:** Temporal evolution of the UV-VIS spectra for BE1 and BE2 with increasing annealing time. In (c), the decrease rate of the band centered at 340 nm is plotted.

The similarities of these morphologies are quickly lost with the annealing procedure. The formation of PC$_{60}$BM clusters can be noted for BE2 (blend with HSS46) and becomes more drastic with increasing times, see Figure 5.27.

The evolution of the roughness of these surfaces is plotted and presented in Figure 5.28.

This indicates that although P3HT:PC$_{60}$BM undergoes phase segregation and fullerene molecules crystallize, the effect of HSS46 polymer material is the opposite of what is expected: it speeds up the process of phase separation.

#### 5.2.1.3 XPS

XPS analysis were performed on pristine and temperature-annealed blend films. Accordingly to literature, the surface of P3HT:PC$_{60}$BM films are rich in P3HT molecules and, with annealing, PC$_{60}$BM molecules migrate to the surface. This should be evidenced in XPS analysis by a reduction of the sulfur/carbon ratio. Moreover, oxygen peaks should

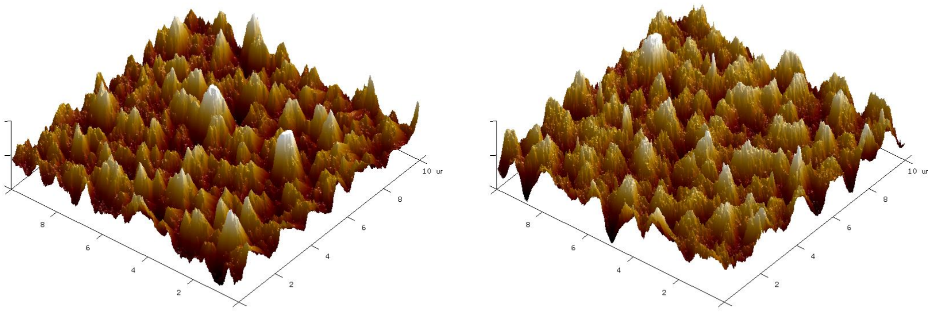

(a) (b)

**Figure 5.26:** 3D reconstruction of the (a) BE1 and (b) BE2 nanomorphologies.

be absent in P3HT-rich surfaces, whereas it should appear when PC$_{60}$BM migrates.

The overview spectra at $t = 0$ are presented for both set of samples in Figure 5.29 These ratios were analyzed and they are summarized in Table 5.1.

| Annealing time (min.) | **BE1** | | | **BE2** | | |
|---|---|---|---|---|---|---|
| | Carbon | Sulfur | Oxygen | Carbon | Sulfur | Oxygen |
| 0 | 100 | 9.60 | 0 | 100 | 7.9 | 0 |
| 120 | 100 | 6.50 | 0.7 | 100 | 8.1 | 1.7 |
| 300 | 100 | 6.70 | 1.8 | 100 | 7.8 | 1.0 |

**Table 5.1:** Relative elementary concentration analyzed for increasing annealing times in BE1 and BE2 films. Sulfur concentration was calculated as an average between $S2s$ and $S2p$ signals.

One can deduct from these data that the concentration of sulfur on the surface decreases compared to the carbon one over time. Added to this, one can also note the increase in the concentration of oxygen, attributed to the PC$_{60}$BM lateral chain. This indicates that PC$_{60}$BM migrates towards the surface for the P3HT:PC$_{60}$BM case. For the sample containing HSS46 as additive, this concentration stays approximately unchanged over time, what, when compared to the initial concentrations of Sulfur, can indicate that the surface is already fullerene-rich and may become richer on the HSS46 derivative (which has a lower Oxygen concentration compared to PC$_{60}$BM).

These results are comforted by the AFM nanomorphologies, which indicate the appearance of island-like structures for BE2 whereas in BE1 samples this is less pronounced. These island structures, as stated before, may be an indicative of the cluster formation of fullerenes and clearly BE2 is more likely to undergo this process than BE1.

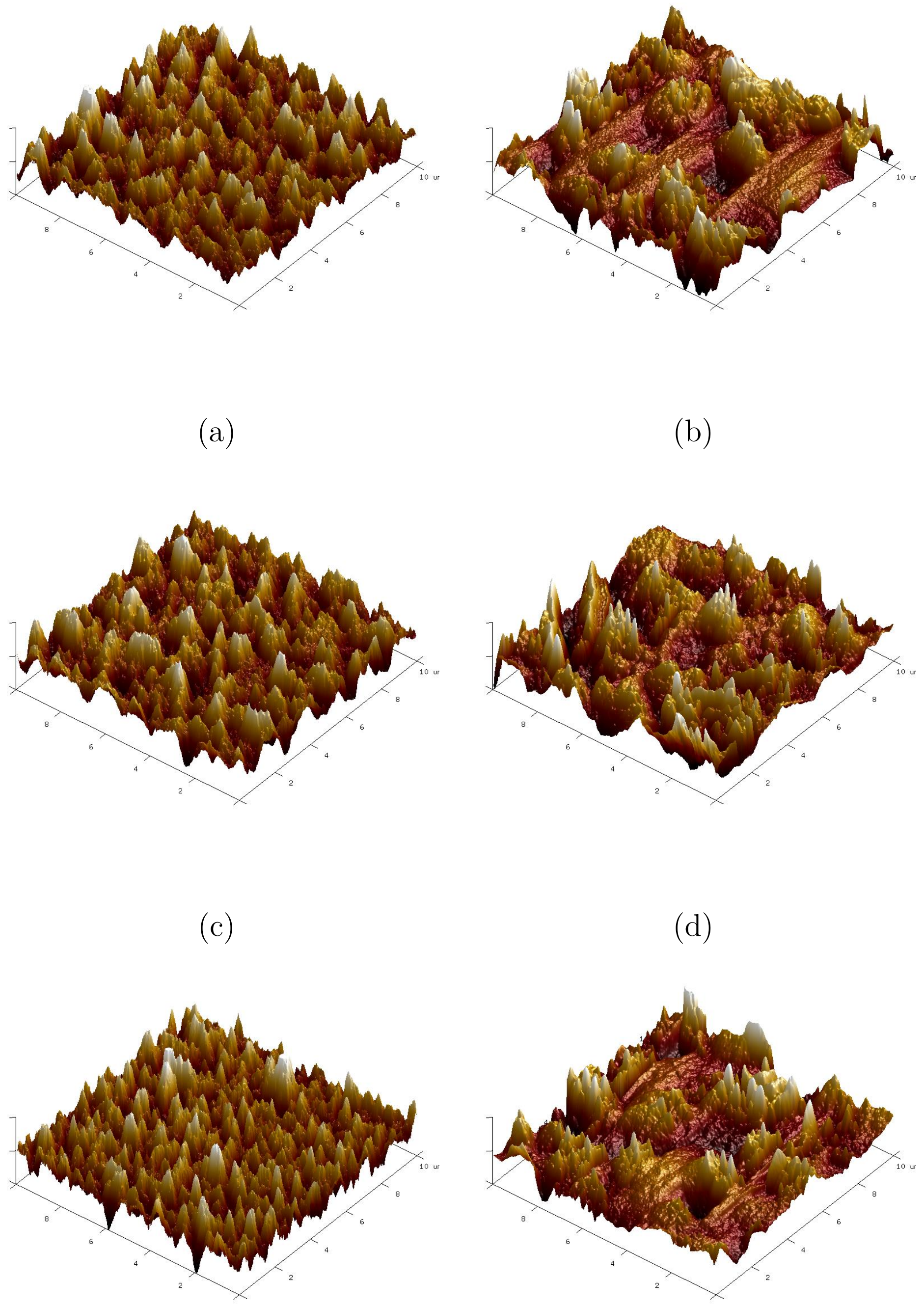

(a) (b)

(c) (d)

(e) (f)

**Figure 5.27:** 3D reconstruction of the (a,c,e) BE1 and (b,d,f) BE2 nanomorphologies annealed at 140 °C for increasing times. These images are from samples annealed for t=30, 120 and 300 min., respectively.

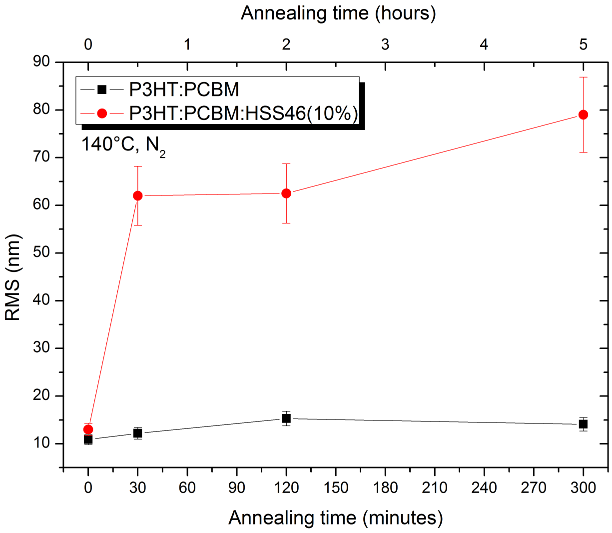

**Figure 5.28:** Temporal evolution of roughness for BE1 and BE2 samples annealed at 140 °C under nitrogen atmosphere.

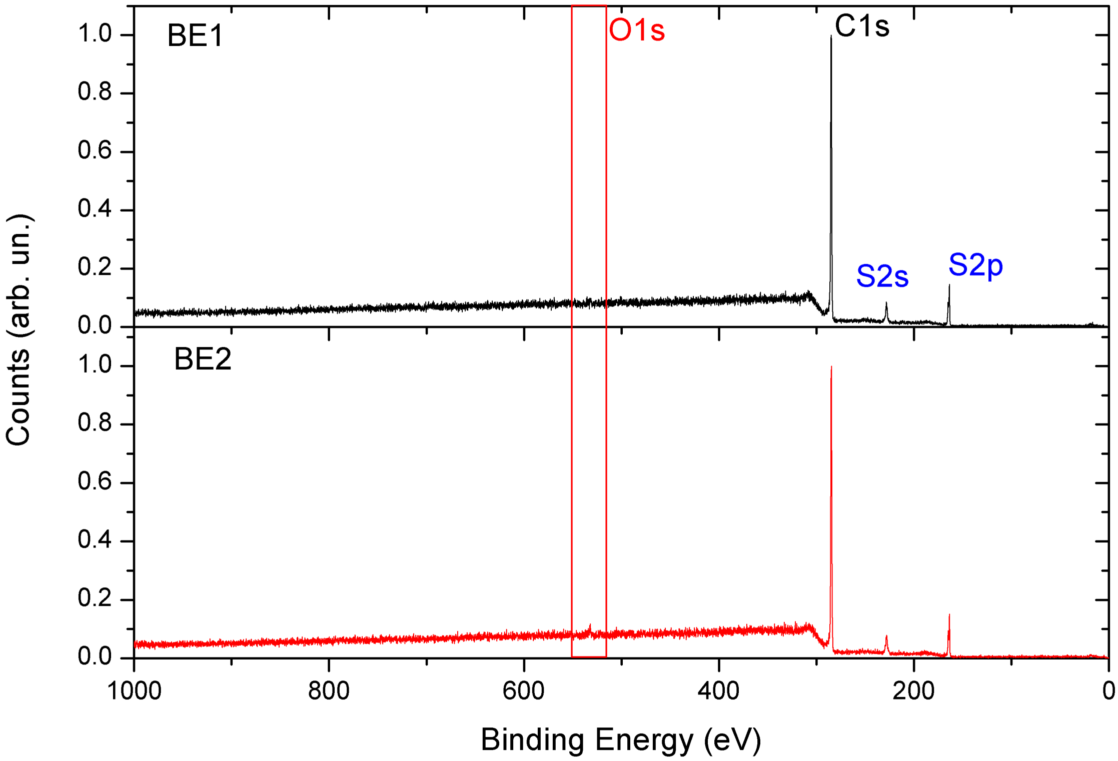

**Figure 5.29:** Overview XPS spectra for BE1 and BE2 samples at $t = 0$.

### 5.2.2 Photochemical degradation

The efficiency of HSS46 polyfullerene material as morphology stabilizer during light illumination in inert atmosphere was studied using UV-VIS, AFM and XPS techniques. As discussed before, the expected role of HSS46 is to avoid the phase segregation and crystallization of PC$_{60}$BM molecules in the P3HT matrix.

Samples were irradiated by a Xe lamp adjusted in AM1.5 conditions in inert (nitrogen) atmosphere.

#### 5.2.2.1 UV-VIS

Figure 5.30 presents the evolution of the UV-VIS spectra for both systems for different exposure times, measured in the very same point of the sample.

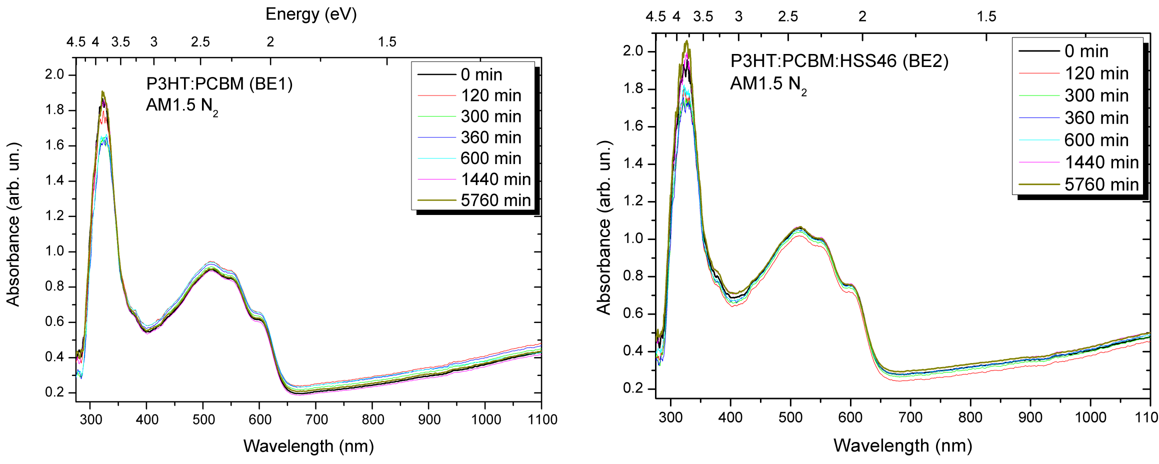

(a) (b)

**Figure 5.30:** Evolution in time of (a) BE1 and (b) BE2 UV-VIS spectra during photochemical degradation.

From these spectra, one can note that the most sensitive region of the spectra is the fullerene absorption band around 340 nm, which has its intensity initially decreased with exposure time, regaining its original position later on. The intensity of this band decreases with illumination exposure time, up to 24h of irradiation. Distler *et al.*[174] identified the increase of the intensity of this band during illumination in inert atmosphere as an indication of the dimerization process between PC$_{60}$BM molecules. The decrease of the same band, on the other hand, is associated to the crystallization of these fullerene-rich domains.[23]

Two parameters can then be plotted to analyze where each process is taking place: (a) the ratio between the fullerene's and P3HT's main absorption bands, and (b) the differential photon flux $\Phi$, as already explained before. This can be found in Figure 5.31.

Both results are coherent in the sense that it seems that a formation of fullerene crystals domains for irradiation up to 24h with a maximum at 6h. This is evidenced by

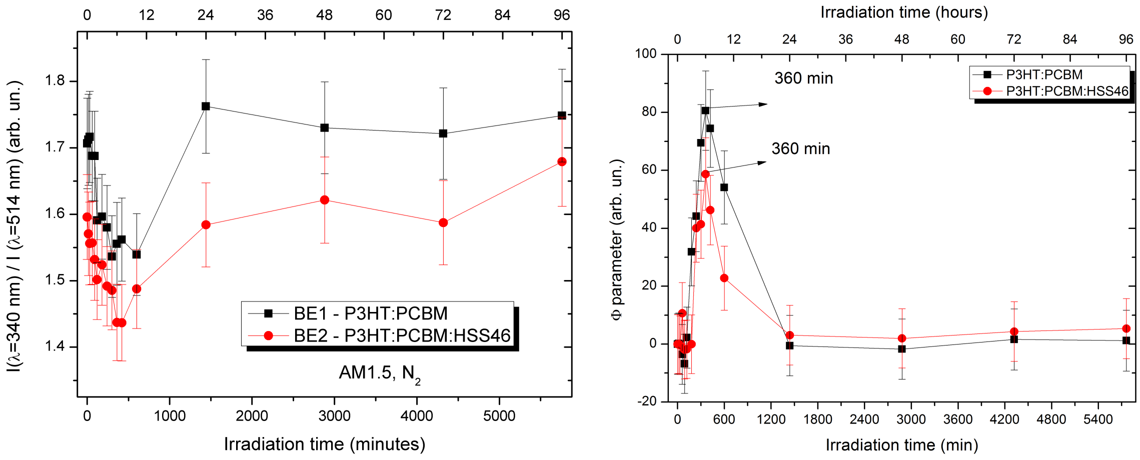

(a) (b)

**Figure 5.31:** Evolution in time of BE1 and BE2 UV-VIS spectra during photochemical degradation.

the decrease of the ratio between fullerene's and P3HT absorption bands and a peak of the Φ parameter.

### 5.2.2.2 Atomic Force Microscopy - AFM

The AFM images of BE1 and BE2 morphologies illuminated under AM1.5 conditions in nitrogen atmosphere are presented in Figure 5.32. The associated RMS are of ∼ 14 and ∼ 23 nm, respectively.

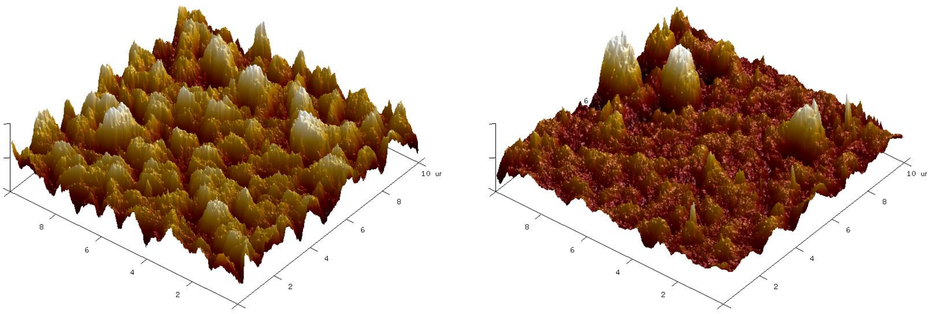

(a) (b)

**Figure 5.32:** 3D reconstruction of the (a) BE1 and (b) BE2 nanomorphologies illuminated in AM1.5 conditions under nitrogen atmosphere.

The RMS of the samples evolve with time of irradiation. Initially, both BE1 and BE2 presents low roughnesses (RMS of 11 and 13 nm, respectively). After 120 hours of exposure, these values evolve to 14 and 23 nm, respectively. This indicates that BE2 (sample containing HSS46) is more sensible to light-only irradiation experiments even though the content of polyfullerene is no higher than 10%. As it is the case for the thermal degradation, light-only conditions induces the formation of PC$_{60}$BM islands in a more pronounced way for BE2 than BE1. This indicates that the photo-instability of HSS46 polymer material should be an issue against its application as previously intended.

### 5.2.2.3 XPS

The same XPS analysis was applied to the films submitted to irradiation under inert conditions. Table 5.2 presents the differences in elementary concentration for $t = 0$ and $t = 96$ h irradiation times.

| Irradiation time (hours) | **BE1** | | | **BE2** | | |
|---|---|---|---|---|---|---|
| | Carbon | Sulfur | Oxygen | Carbon | Sulfur | Oxygen |
| 0 | 100 | 9.6 | 0 | 1 | 7.9 | 0 |
| 96 | 100 | 7.7 | 0.7 | 100 | 7.9 | 1.6 |

**Table 5.2:** Relative elementary concentration analyzed for increasing irradiation times in BE1 and BE2 films. The Sulfur concentration was calculated as an average between $S2s$ and $S2p$ signals.

Here again, one can note that, in BE1 samples, PC$_{60}$BM clearly migrates towards the surface with the irradiation in inert conditions. AFM results goes in the same direction, indicating that the surface has more cluster-like structures likely to be composed of fullerene aggregates. On the other hand, BE2 films, the Sulfur concentration keeps unchanged, probably because the surface can be fullerene rich since the beginning (*c.f.* comparaison between BE1 and BE2 initial Sulfur concentrations). Thus, the irradiation increases the relative concentration of Oxygen, probably influenced by the presence of PC$_{60}$BM molecules.

### 5.2.3 Photo-oxidation

For the photo-oxidation studies of the P3HT:$PC_{60}$BM:HSS46 blend, only UV-VIS technique has been used. This method was chosen so since the identification of photo-oxidation products of both P3HT, P3HT:$PC_{60}$BM and HSS46 have already been done. For the first two, the works of Chambon *et al.*[86], Manceau *et al.*[90], Hintz *et al.*[175, 176] and Sai *et al.*[88], among others, should be extensively referenced.

Photo-oxidation experiments were also performed under AM1.5 light irradiation in synthetic air (SA) atmosphere, following the same procedure as for the HSS46 pristine material.

#### 5.2.3.1 UV-VIS

Figure 5.33 presents the evolution of the UV-VIS spectra for both systems for different exposure times, measured in the very same point of the sample.

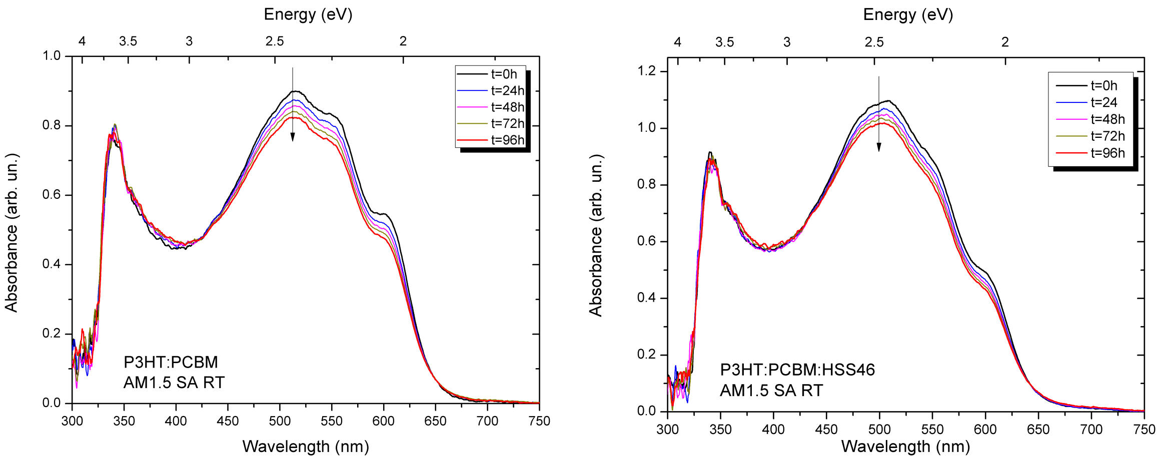

(a) (b)

**Figure 5.33:** Evolution in time of (a) BE1 and (b) BE2 UV-VIS spectra during photo-oxidation.

The rates of degradation of the P3HT main band are depicted in Figure 5.34.

Within the error of the experiment, no significant difference can be observed since the polymer only looses around 10% of its original absorbance after 5 days of irradiation.[9] In any case, what can be said is that there is not big difference between the samples and this may be simply due to the radical scavenger properties of fullerenes that retard the degradation of the polymer, regardless of the form in which the fullerene is incorporated in the matrix. Finally, the fullerene content in the form of polyfullerene is low if compared to the total amount of it, corroborating the absence of deeper differences in the degradation.

---

[9] This delay is the limit that could be reached in the laboratory conditions.

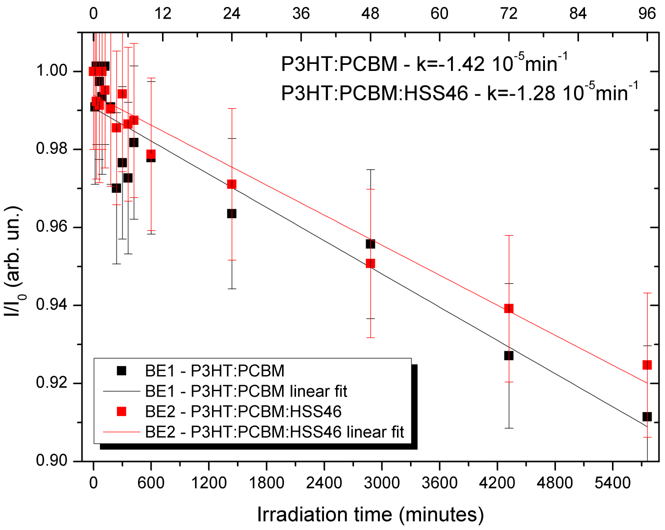

**Figure 5.34:** Evolution in time of BE1 and BE2 UV-VIS spectra during photo-oxidation.

### 5.2.4 Partial Remarks

From these measurements, one can point out:

- Polyfullerene in the form of HSS46 can form films over ITO/glass and these films do not indicate, initially, the presence of large aggregates;
- Thermal annealing of the HSS46 polymer material under nitrogen atmosphere gives rise to aggregation formation of fullerene islands;
- The aggregation occurs for all the tested temperatures under 5 h of annealing time;
- For temperature ranges below 200 °C, the molecular structure is destroyed, what is inferred by the loss of definition of the resonant band associated to the polymerizing attack on the fullerene.
- Light-only irradiation in an inert atmosphere is capable of inducing changes on the HSS46 polymer material morphology;
- Accordingly to literature, photo-oxidation of HSS46 polymer material seems to follow the same mechanism already found to take place in PC$_{60}$BM's case;
- The P3HT:PC$_{60}$BM blend is not beneficially impacted by the presence of HSS46 even as an additive;

  - this can be concluded from the results of the thermal-degradation experiments, where HSS46 induces a faster phase segregation when the opposite would be expected;

  - this can also be noted on the photochemical degradation experiments, where HSS46 also induces the formation of islands of fullerenic material;

- the rate of optical density loss is not changed when HSS46 is added to the bulk.

All that said, one could say that the degradation of HSS46 polymer material may be due to the depolymerization process undergone by the material. To further study this, we perform hereafter a molecular modeling approach to identify up to which point this might be the case.

## 5.3 Revealing the degradation mechanism of ATRAP-based polyfullerenes

During the degradation processes to which the HSS46 polymeric material has been submitted to, one could hypothesize that a depolymerization process takes place. This is so since if the polymeric structure was preserved, the material should have provided at least a slightly better stability against thermal and light treatments.

Two approaches are hereon considered: a light-induced and a thermally-induced depolymerizations. The overview mechanism is proposed in Figure 5.35.

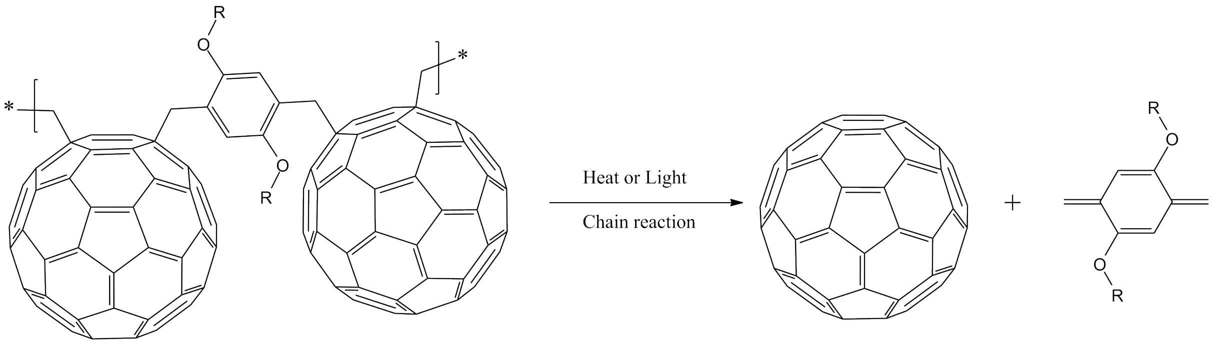

**Figure 5.35:** Proposed depolymerization mechanism of ATRAP polymeric materials.

In this process, a homolytic cleavage between the comonomer and the fullerene would lead to the formation of two radical pairs, one localized on the fullerene sphere and the other one located on the $CH_2$ group of the comonomer. It is common sense that the delocalization of the benzyl-type radicals on the aromatic cycle is straightforward and this would lead to the destabilization of the bond in $\beta$ position to the first cleavage. This having happened, both radicals are now in a closed-shell configuration, gaining stability for both fullerene and the comonomer species.

### 5.3.1 Thermally-induced depolymerization

The stability of the $C_{60}$-comonomer link has first been investigated for the case of $C_{60}$-polymer stars, as it is the case of polystyrene- and polyisoprene-$C_{60}$ compounds.[177] Several reports indicate that the incorporation of pristine $C_{60}$ to polymeric matrices has a beneficial retarding effect on their thermo-oxidative degradations.[178] This is not a surprise since these mechanisms are radical-started processes and as $C_{60}$ is a radical scavenger,[102, 154] they are straightforwardly mitigated.

The situation, however, showed to be different for the covalently-bonded polymer-$C_{60}$ materials, for which thermogravimetric measurements (TGA) indicated that fullerene release could be detected at temperatures around 350 °C, even earlier that the degradation of polystyrene, for example.[49, 52, 150, 166, 179, 180, 181] This strongly indicates that for this type of material, the polymer-$C_{60}$ bond is the weakest bond.[51]

Furthermore, investigation of $(PS)_6C_{60}$ six-arm stars produced from very narrow PSLi living polymerization showed that a continuous release of the lateral arms attached to the fullerene moiety could be detected in solution at temperatures around 100 °C, keeping intact the molecular weight of the polystyrene chain.[51]

The same could be seen for $(PI)_6C_{60}$ stars at room temperature what definitively points toward a low thermal stability of this type of fullerene multiadducts produced by single bond attacks.[177] Pantazis *et al.*[177] deduced that the bond cleavage-formation on the $C_{60}$ sphere is based on a dynamic equilibrium and the presented arguments are that the rate of degradation depends upon the purification/fractionation of the polymers, which is responsible for reducing the quantity of available comonomers, shifting the equilibrium towards the reagents.

In order to further investigate this, we calculated the bond dissociation energies of the fullerene-comonomer link by different ground- and excited-state molecular methodologies. For a B3LYP/6-31G** ground-state molecular geometry, the coordinate reaction of the bond dissociation was scanned and the energy point evaluations along their Morse-like potential fit curve are presented in Figure 5.36.

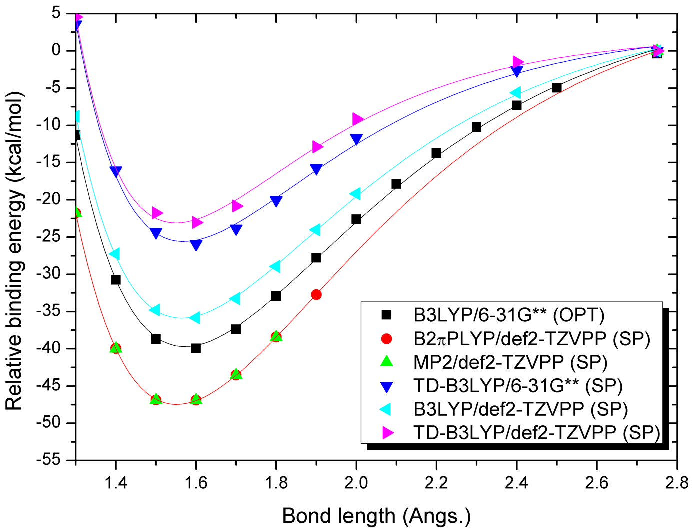

**Figure 5.36:** Bond-dissociation reaction coordinate scan for the ATRAP proposed model material calculated by different level of theories, under fully optimization (OPT) or single-point energy evaluations (SP). They were also calculated on the first excited state (TD label) showing that this bond tends to be photochemically cleaved with moderate energies (20 to 50 kcal/mol). This point will be treated later on.

The theoretical methodologies used for this calculation cover the specific needs of the system, in terms of basis set and level of theory. Both electronic density and wave-function based methods have been used to test if this result might have a methodology-dependent behavior.

This very low bond-dissociation energy range (20 to 50 kcal/mol, average energy of 39.65 kcal/mol) for the fullene-comonomer link is in agreement with the experimental results obtained for 2-, 4- and 6-arms $(PS)_6C_{60}$ materials, measured under TGA conditions (45.45 kcal/mol).[52] This scan on the reaction coordinate corroborates the value found when only the initial (bonded) and final (dissociated) states are calculated (39.65 kcal/mol). This is only possible since no rearrangement reaction can take place during the cleavage. To make sure that this was not a coincidence concerning a high radical stabilization by the monomer molecule, we also studied two other configurations as it is depicted in Figure 5.37, both of them using the same attack route on the fullerene.

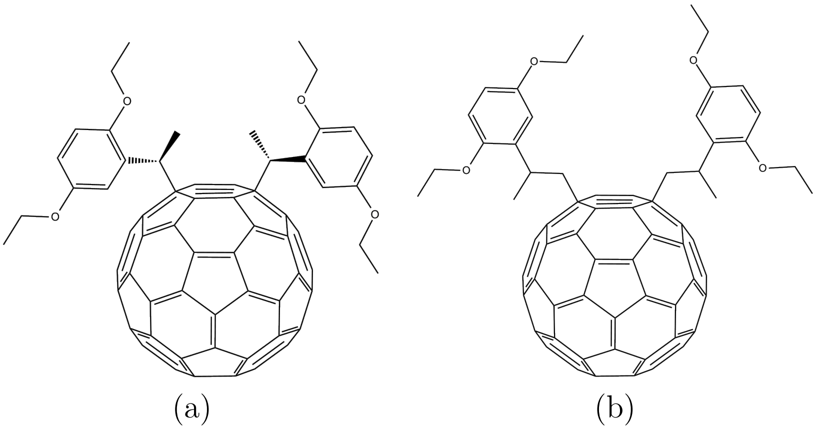

**Figure 5.37:** Modified ATRAP structures used to study the influence on stability of the -$CH_2$-link.

In (a), one hydrogen atom from the $-CH_2-$ linking group has been replaced by a methyl and in (b), one tertiary carbon atom has been added between the $-CH_2-$ and the comonomer. For the former, bond dissociation energies were found to be of the order of $\sim$ 48 kcal/mol and, for the latter of the order of $\sim$ 35 kcal/mol,[10] within B3LYP/6-31G** level of theory. This corroborates the common-sense that tertiary carbons stabilize radicals, leading, in this case, to more unstable monomer-fullerene link.

Mechanistically, the thermal energy induces a breaking of the fullerene-comonomer link leaving behind two radical each one found in one product. Considering the results found by Audouin *et al.*[51], the coupling of two radicals born by the $C_{60}$ is unlikely because of the steric hindrance due to the attached chains and it is also known that $C_{60}$-$C_{60}$ bonds can be easily broken either.[182] These authors proposed that, upon heating, the radicals probably react with impurities.

Once the cleavage of one fullerene-comonomer bond is settled down, one can conclude if there is indeed a chain propagating mechanism of depolymerization. This is so because in our case, for each comonomer, there is one fullerene, what is not the case for the

---

[10] Usual C-C single bonds have a bond dissociation energy comprised between 90 and 100 kcal/mol. Moreover, one should keep in mind that, at room temperature (25 °C), the available thermal energy equals 0.593 kcal/mol.

products found in literature. We then followed this route calculating the bond dissociation energy to cleave the opposite fullerene-comonomer bond once the first is already cleaved, as it is depicted in Figure 5.38.

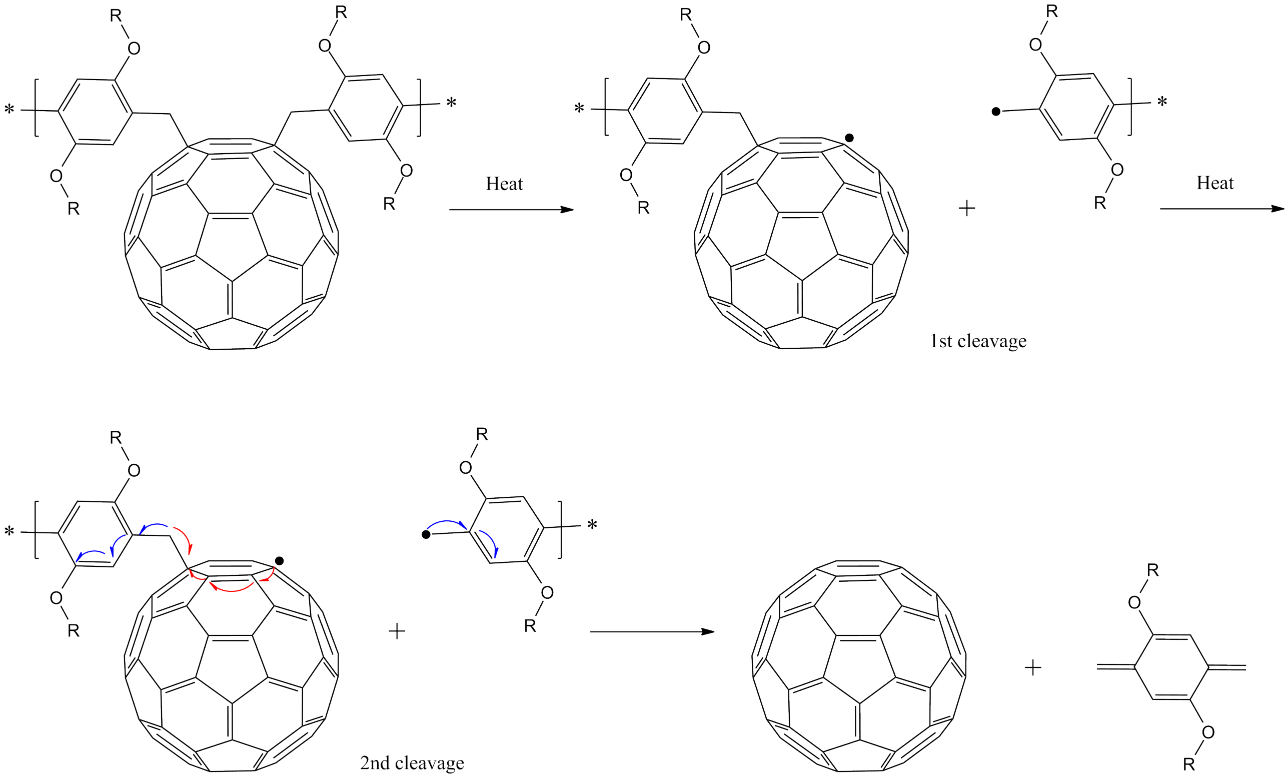

**Figure 5.38:** Chain propagation of the depolymerization reaction.

This mechanism relies on the fact that, once formed, both radicals delocalize in the surroundings, and recombine readily with the next ones formed, what leaves the system to a closed-shell configuration, with an energy gain. One should also pay attention to the formation of vinylic products.

The calculated bond dissociation energy for the 1st cleavage is of the order of ∼ 55 kcal/mol[11] Once it has been cleaved, the 2nd cleavage requires an energy of ∼ 14 kcal/mol. This lower energy required for the second reaction indicates that, once the first bond is cleaved, all the other should follow the same mechanism in a chain reaction, reducing even more the energetic barrier needed to start the degradation.

This explains the set of results obtained from the experimental degradation studies and may also explain why one can not obtain high molecular weights during polymerization: the formation-cleavage of the fullerene-comonomer link should follow an equilibrium that

---

[11] This does not disagree with the results presented just above. The difference here is found on the fact that we now used a bis-attacked fullerene model with terminal bromine atoms on the comonomer, using the 6-311G** basis set. As it was not possible to calculate this reaction using periodic boundary conditions, we assumed, for the sake of simplicity, that the depolymerization process starts at chain ends. Empirically we expect that for middle-chain bonds, these energies should be even lower due to the fact that both $-CH_2-$ groups are free to form vinylic bonds with the cycle, whereas for the case where we have a bromine terminal atom, this cannot be the case.

is easily shifted towards the reagents.

As aforementioned, the formation (or not) of these vinylic products are then studied by $^1$H-NMR spectroscopy. A sample of HSS46 was dissolved in $d_8$-toluene in a nitrogen-sealed glass tube and the thermal behavior of the solution was studied continuously by NMR spectra. The first spectrum is acquired at $t = 0$ at 25 °C, and then it is heated to 100 °C and a spectrum is acquired at intervals of 5 min up to 16h. Then, a last spectrum is acquired at 25 °C again. They are presented in Figure 5.39.

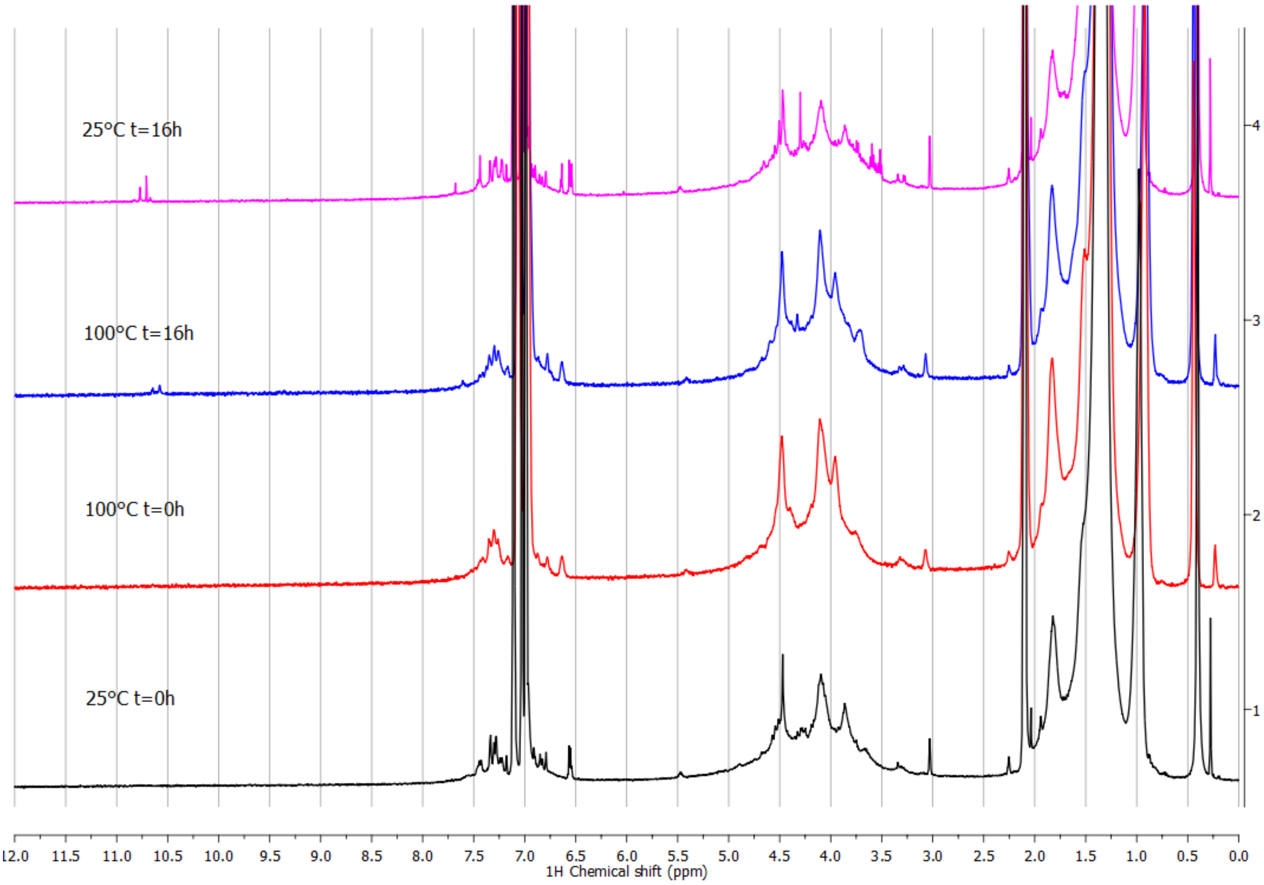

**Figure 5.39:** $^1$H-NMR spectra of HSS46 in $d_8$-toluene solution heated to 100 °C for a 16h period time.

The residual peaks of toluene in $d_8$-toluene are found at 2.08, 6.97, 7.01 and 7.09 ppm. The peaks found at 0.43 and 3.03 ppm correspond to water and methanol, respectively.

Upon heating, straightforwardly, a broadening of the peaks both in the aromatic region as well as in the 3.5-5.0 ppm region is induced, which is associated to the region where the $-CH_2-$ peaks of the monomer-fullerene link are found (see Chapter 3). In this region, the triplets associated to the $-CH_2-$ in alpha position of the oxygen attached to the phenylic group are also found.

From 2 h of heating on, a peak located at 4.3 ppm appears and its intensity increase with time, being maximum when the sample is cooled down again back to 25 °C. Furthermore, a multitude of new peaks can be found in the region around 3.6 ppm. This is more clearly seen in Figure 5.40.

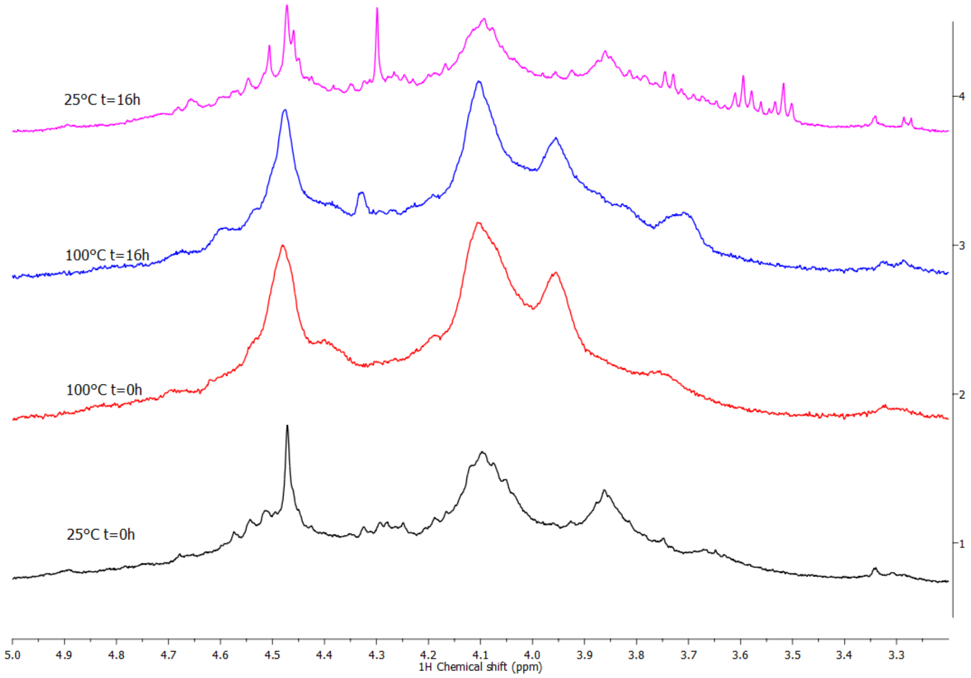

**Figure 5.40:** $^{1}$H-NMR spectra of HSS46 $d_8$-toluene solution heated to 100 °C for a 16h period time - zoom in the 3.5-5.0 ppm regions.

Few changes are also found in the aromatic region. Firstly, the multiplets centered at 6.55 ppm are hindered during heating and are once again detectable when the sample is cooled back down to room temperature. Since the beginning of the heating process, a broad peak centered at 6.55 ppm appears and upon cooling is finally resolved as doublet or a set of two singlets found closely together. This is more clearly seen in Figure 5.41.

The ”bump” centered at 7.45 ppm in the beginning of the experiment is broadening during heating and then, upon cooling, it seems that a new peak is developed in the middle of it. The same can be said for the ”bump” found at 7.25 ppm.

Trying to attribute of these peaks is a very difficult task that may leave it open to controversial conclusions. However, based on the analysis of these spectra, one can say that:

- Apparently the synthetic procedure is consisted of an equilibrium that can either favor the formation of the polymeric material or not; one can think that, during the synthesis, the presence of the catalysts favors the former, whereas after the purification, any heating favor the decomposition of the material.

- From the integration of different regions of the spectra (7.9-6.3, 3.5-5.0 and 1.96-0.7 ppm) acquired at different heating steps, the ratios between them are constant, indicating that there is no complete transformation of the material. It means, no $-CH_3$ group is formed coming from an hydrogen abstraction by a radical from the

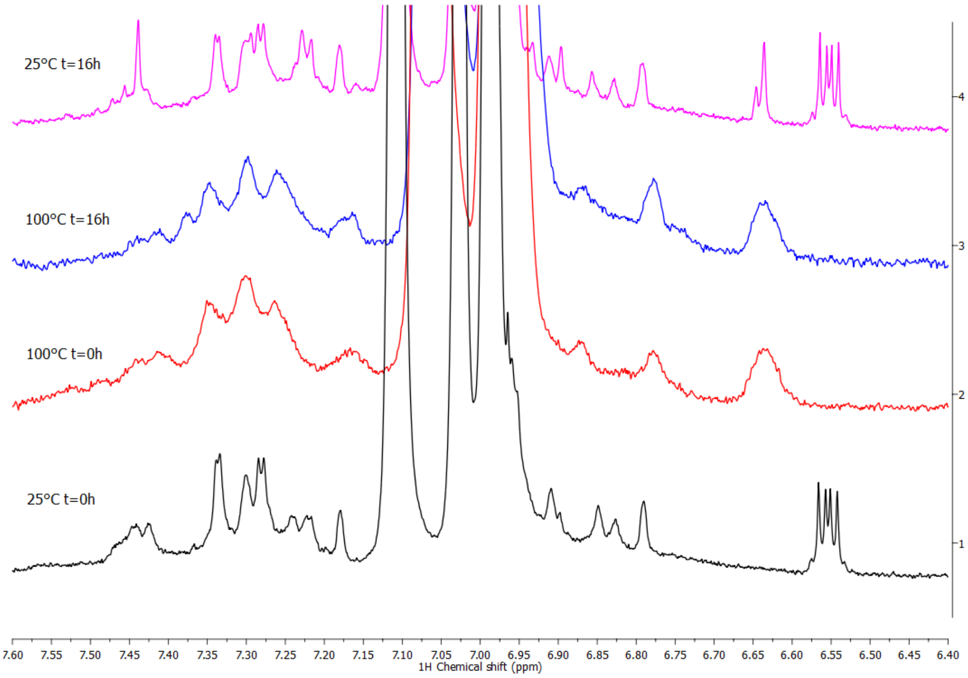

**Figure 5.41:** $^1$H-NMR spectra of HSS46 $d_8$-toluene solution heated to 100 °C for a 16h period time - zoom in the aromatic regions.

solvent, for example. Whatever is going on should have peaks in the same regions of the original product.

- Direct correlation between the new peaks and vinylic peaks could be hypothesized.

One hypothesis is based on the fact that the produced vinylic groups are reactive enough to quickly interact further with fullerene, cross-linking it. Moreover, it can also suffer a $[2+2]$ cycloaddition, forming a $[2,2]$-paracyclophane derivative. Another possibility is the attachment of the two terminal $-CH_2-$ groups to a single fullerene. These possibilities are depicted in Figure 5.42.

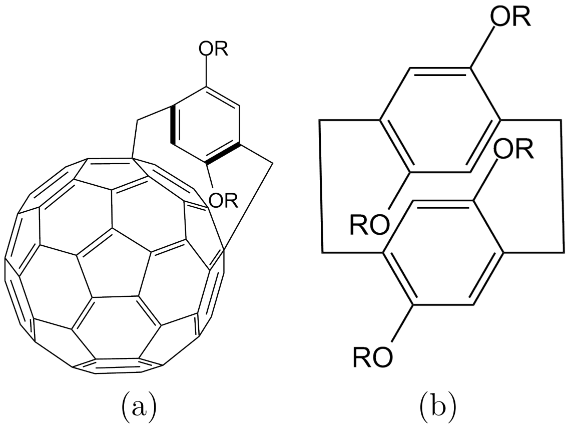

(a) (b)

**Figure 5.42:** Two possible products of degradation being formed during thermal treatment. In (a), the two now free $-CH_2-$ groups attach to a single fullerene, and in (b), they recombine to form a [2, 2]-paracyclophane derivative.

### 5.3.2 Light-induced depolymerization

Besides the thermally-induced bond cleavage of fullerene-comonomer bond, based on the results provided from the photochemical degradation tests, one can also inquire on a light-induced mechanism of bond cleavage.

This hypothesis is also motivated by the dissociation curves presented in Figure 5.36, for which the energy of dissociation on the first excited state is decreased by a factor of at least 2. To go deeper in this hypothesis, we have optimized geometries of hydrogen-passivated comonomers[12] in the ground singlet ($S_0$), first excited singlet ($S_1$) and first excited triplet ($T_1$) states. The calculation was done within the B3LYP/6-31G**/RIJCOSX level of theory using UKS wave-functions.

We found that the geometry of the $T_1$ state is not aromatic and reproduces the vinylic structure hypothesized to be a product of the degradation mechanism. This agrees with the Baird's rule.[183] This said, one can depict the following molecular orbital diagram for the involved electronic transition.

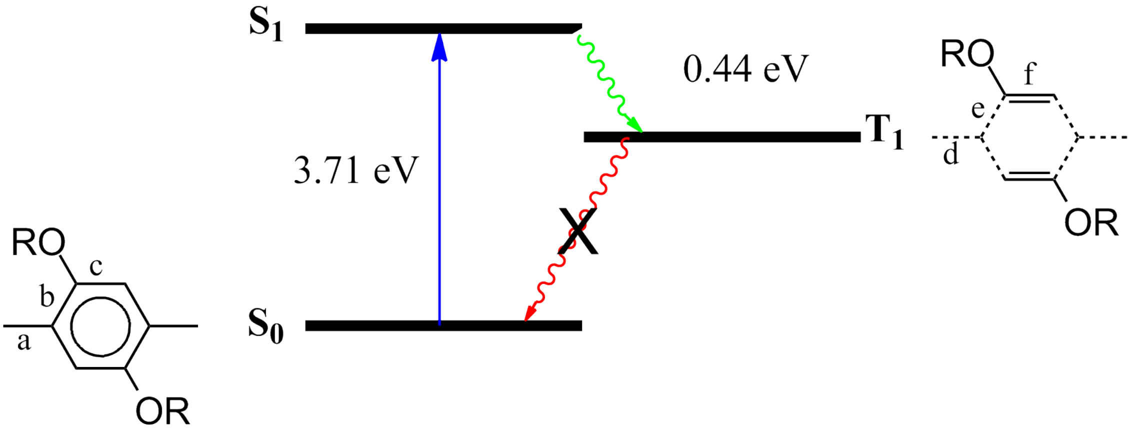

**Figure 5.43:** Molecular orbital diagram for the first photo-excitation of the comonomer depicted in the inset.

One should observe that the comonomer is aromatic in the $S_0$ state and the first photo-excitation takes place with a calculated photon-energy of $\sim$ 3.7 eV ($\sim$ 335 nm). Once in the $S_1$ state, the excited electron can thermally relax and, by successive intersystem crossing (ISC) get to the $T_1$ state, where it has an anti-aromatic structure. This is believed to be the origin of the destabilization of the comonomer-fullerene bond. The bond lengths **a**, **b** and **c** are 1.51, 1.40 and 1.40 Å, respectively, for the molecules in the $S_0$ state, and 1.50, 1.50 and 1.37 Å, for **d**, **e** and **f**, respectively, for the molecules in the $T_1$ state.

These results indicate that the absorption of light by the comonomer leads, in this case, to an anti-bonding-like structure where both fullerene and comonomers are not linked any

---

[12] This means that the monomer has methyl groups grafted in 1,4 positions instead of bromomethyl ones.

longer. Considering the error that may have been induced by TD-DFT calculations in the determination of the $S_1$ state, one should estimate that wavelengths between 330 and 380 nm are enough to break this bond.

## 5.4 Final Remarks

In this chapter, the thermal, photochemical and photo-oxidation degradation of HSS46 polymeric material and the P3HT:PC$_{60}$BM blends containing it as an additive have been addressed.

Several techniques have been used to study these effects, and the bulk material showed to be thermally and photochemically unstable. The photo-oxidation profile, by its turn, is not very different when compared to the C$_{60}$ and PC$_{60}$BM ones.

XPS was particularly useful to distinguish, for thermal and photo-chemical degradation, the formation of compounds that seem to have electronic properties more similar to pristine C$_{60}$ rather than to the pristine polymeric material. These results could be correlated with AFM measurements which show the formation of fullerene clusters on the surface of the film upon light irradiation and thermal treatment, independently, in inert atmosphere. UV-VIS was also a valuable tool to evaluate the dynamics of this system.

XPS/FTIR/UV-VIS coupled results show that there are at least three different mechanisms of degradation and they were attributed to both the degradation of the fullerene, the degradation of the comonomer aromatic cycle and the degradation of the lateral chain.

When applied as a morphology stabilizer in an BHJ blend, this material did not show encouraging results in any domain. Both photochemical and thermal stability were reduced upon its addition when compared to control films. Photo-oxidation profiles are similar and, up to the point where this study was driven, there is no indication for differences during the process.

Molecular modeling was able to propose a depolymerization mechanism under thermal stress or light absorption of the material. For the thermally-induced depolymerization mechanism, abundant literature can be found corroborating these findings for model systems of polystyrene covalently bonded to fullerene. We also proposed a light-induced mechanism of depolymerization based on the light-absorption of the comonomer which, once in its first excited state, can thermally relax and, by intersystem crossing, get to the first long-lived triplet state where it has an anti-aromatic structure. This should induce anti-bonding-like behavior concerning the monomer-fullerene link. The triplet state should be long-lived based on the fact that it cannot readily decay to the ground singlet state based on the spin selection rules that makes this transition forbidden. Moreover, even if the rate of this to happen is low, fullerene is known to have a high quantum yield of $S_1 \rightarrow T_1$ decay rate, being then the driving force of this mechanism. Thus, there is enough time on the molecule referential to a fully geometry optimization on this state, leading to the cleavage of the comonomer-fullerene link.

In the next chapters, we shall discuss strategies and new materials to circumvent this low stability of ATRAP-based polymers.

# Chapter 6

# Models for stabilization of OPV materials

*In this chapter, other interesting degradation routes are studied using molecular modeling. Namely, the stabilization of lateral chains, the development of interlayer materials and the relation between oxygen affinity and geometrical parameters are screened.*

Up to now, degradation pathways such as photochemical, thermal and photo-oxidation have been studied, evidencing the changes in the morphology and chemical structure of a particular polyfullerene. However, it is clear that achieving materials which are completely stable against a wide range of degradation pathways is unlikely. Several mechanisms can take place at the same time and each one of them depends differently on a set of variables.

Within this context, one could, for the sake of simplicity, describe a hypothetical "stability functional" $F$ which depends on several functions of variables in a way of:

$$F = F(X, Y, Z, W...) \tag{6.1}$$

Each of these functions can be associated to a set of intensive and extensive parameters $\{a_i\}$ and $\{A_j\}$, respectively. These functions can be denoted by the bond dissociation energy, ionization potential, molecular packing of the system, solubility of oxygen and light into the bulk, light-absorption in a specific range, etc. The intensive and extensive parameters upon which these functions depend may be denoted by the local electronic structure, total electronic structure, presence of heteroatoms, architectural stability of radicals, geometry parameters, solvents used, etc. In this way, one can see that this "stability functional" $F$ is a complicated function that may be further written as:

$$F(X, Y, Z, W...) = X(\{a_i\}, \{A_j\}) + Y(\{a_i\}, \{A_j\}) + Z(\{a_i\}, \{A_j\}) + W(\{a_i\}, \{A_j\})... \tag{6.2}$$

The functions $X, Y, Z, W...$ can be written in the form of several Puiseux series, which allows the existence of fractional powers for each variable. For instance, for $X$, one has:

$$X = \sum_{i=x}^{\infty} c_i a^{i/n} + \sum_{j=x}^{\infty} d_j A^{j/n} \tag{6.3}$$

Where $X$ may represent the photo-oxidation stability, for example. This expression states that this property would depend on a series of $i$ intensive variables (bulk variables - geometrical arrangement of atoms, ionization potential, etc.) and $j$ extensive variables (film thickness, concentration of drop solution, etc.) and the contribution of each variable power is controlled by the positive integer $n$. $c_i$ and $d_j$ are expansion coefficients of the Puiseux series.

If each material and/or arrangement of materials has a different functional $F$ describing the stability of the system, it is straightforward to see that it is very unlikely to find an ensemble of function coefficients and powers of the several Puiseux series involved that are able to solve these different functionals. This may be due to the fact that, during minimization of an ensemble of parameters for $F$, the found coefficients $c_i$ and $d_j$ and exponents $i$ and $j$ of each function are very probably not the same that also minimize another given functional $G$, which describes another system.

This is a theoretical analysis indicating that what has been treated up to now are projections of these variables on specific directions (one truncates the series). One shall analyze some other variables that can indeed span a little more these series in specific directions but one has to keep in mind that the results obtained can have a big participation in a given system described by $F$ but may not have the same contribution on another system described by another functional $G$.

Hence, in this Chapter, other intensive parameters $a_i$ that might influence the general stability of $n$-type materials are studied. This does not have the intention to be an exhaustive study, but only to span a little more the ”stability functional” that has been worked so far.

## 6.1 Interfacial stabilization

As it was discussed in Chapters 1 and 2, the OPV devices focused in this work are composed of an inverted architecture. It means that the BHJ needs to make contact with an inorganic oxide layer, namely $TiO_x$ or ZnO. Delamination processes are quite common in this interface due to different non-affinities of the organic and inorganic layer.[184, 185] Improving their adhesion is then of paramount importance.

Representative organic compounds which can attach to inorganic layers[1] were studied by a molecular modeling approach with a $(ZnO)_{12}$ cluster in order to study the energy of interaction between an organic and an inorganic layer in an inverted photovoltaic device. With this approach, one can deduct the character of the interaction, whether it is a physisorption or chemisorption and, moreover, to estimate the energetic gain for the system with this (these) new bond(s).

For each molecule chosen, all the possible conformers that could interact with $(ZnO)_{12}$ cluster were studied and the ones presented are only the ones for those the interaction energy is the deepest. In this way, we can depict each ligand by a single parameter.

This $(ZnO)_{12}$ was chosen as representative of an inorganic ZnO layer since it presents Zinc atoms of same valence and it has two distinct faces who could possibly interact with the organic molecule. The literature confirms that for such size of the cluster, most of its energetic parameters have already converged, as HOMO and LUMO energies and they can be representative of interactions of the whole inorganic ZnO layer with specific molecules, as it is the case reported by Zhao, coworkers and many others[186, 187, 188, 189].

Molecular geometries of the ligands were fully optimized within the Density Functional Theory (DFT) methodology, using the B3LYP exchange-correlation functional and an Ahlrichs-type triple-$\zeta$ polarized basis set (TZVP)[190]. Energies and geometries were corrected all over this work for long-range dispersion interactions, delimited by a van der Waals-like potential and semi-empirically parameterized by Stefan Grimme up to the 6th order (vdW06)[191]. All calculations were done using Orca 2.9 software.

For the case of hydrogen migration, the energy of the ligand alone was corrected by an optimization of only the hydrogen atoms.

The ligands were chosen based on polystyrene derivative structure as depicted in Figure 6.1.

In this way, several structures have been proposed and they can be found in Figure 6.2.

The calculated ground-state configuration of $(ZnO)_{12}$ is predicted to be a cage-like structure consisting of six $(ZnO)_2$ and eight $(ZnO)_3$ rings forming a truncated octahedron in which all Zn and O vertices remain equivalent (*cf.* Figure 6.3). These results are

---

[1] The whole work is the subject of Anna Isakova's PhD thesis, from Aston University, in England. The work developed alongside had the full modeling contribution done within this thesis.

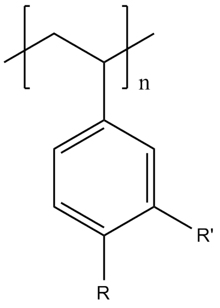

**Figure 6.1:** General structure of polystyrene-based ligands.

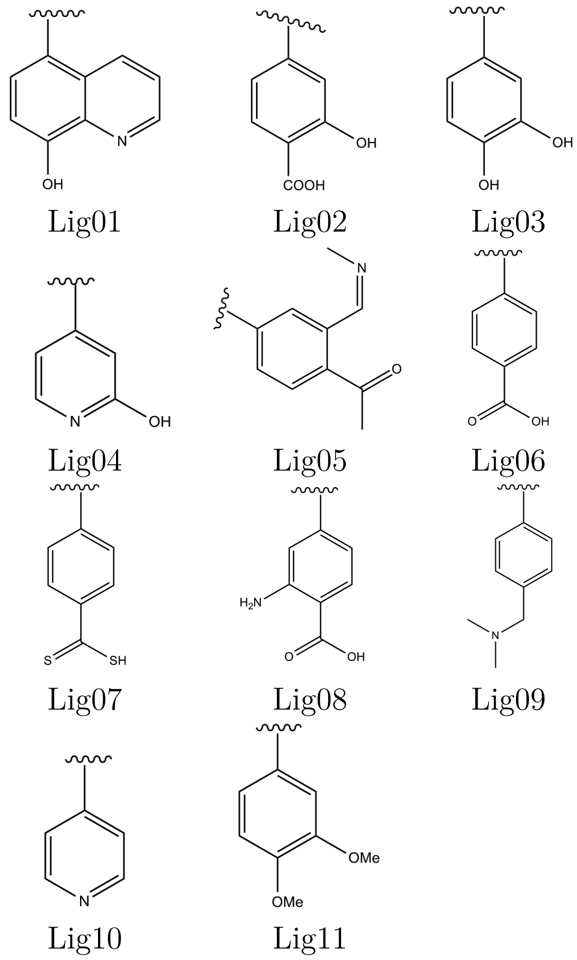

Lig01 Lig02 Lig03

Lig04 Lig05 Lig06

Lig07 Lig08 Lig09

Lig10 Lig11

**Figure 6.2:** Several proposed ligands based on polystyrene.

consistent with other results throughout the literature as well as the structural parameters of such structure.

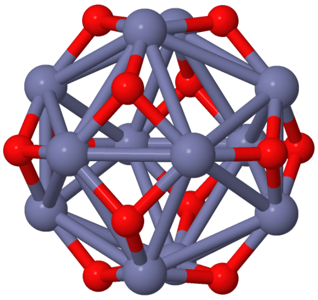

**Figure 6.3:** Optimized structure of $(ZnO)_{12}$ cluster.

Most of the ligands have only one interesting binding site, since no top configuration was studied (the laying down of the molecule directly on the inorganic layer, without a strong site-ion interaction). However, the inorganic cluster has two possible binding sites: the $(ZnO)_2$ or $(ZnO)_3$ rings. They can be preferred for a specific interaction depending on the size of the attaching group in the ligand molecule. If this group needs more tridimensional space in order to bind, it will prefer the Zinc atoms over a $(ZnO)_3$ ring, or the other way round. These interactions are then separated when they exist differently. Moreover, for ligand molecules with more than one binding site, they were studied as possibly interacting with both rings on the inorganic structure.

Table 6.1 summarizes the calculations.

| | Interaction Energy (kcal/mol) | | | | |
|---|---|---|---|---|---|
| | **Conformer 1** | **Conformer 2** | **Conformer 3** | **Conformer 4** | **Conformer 5** |
| **Lig01** | -47.21 | -90.81 | - | - | - |
| **Lig02** | -70.00 | -22.22 | -22.20 | -106.56 | -32.87 |
| **Lig03** | -78.15 | -86.98 | -39.62 | - | - |
| **Lig04** | -34.37 | -33.57 | -84.94 | - | - |
| **Lig05** | -78.62 | -42.98 | - | - | - |
| **Lig06** | -69.16 | -21.12 | -83.60 | - | - |
| **Lig07** | -88.38 | -22.58 | -22.26 | - | - |
| **Lig08** | -65.30 | -30.08 | -30.10 | -34.13 | -35.02 |
| **Lig09** | -37.48 | - | - | - | - |
| **Lig10** | -33.47 | - | - | - | - |
| **Lig11** | -32.48 | -30.37 | -33.15 | - | - |

**Table 6.1:** Calculated Binding Energy (kcal/mol) of the ligand-$(ZnO)_{12}$ complex.

Now, each ligand is depicted individually concerning its interaction with the inorganic cluster. Several binding configurations were tested for each ligand and most of them evolve to the same degenerate structure. Some of them differ from each other by less than 1 kcal/mol and these differences are due to a proper rotation around the binding center. It is worth to note as well that, due to the van der Waals interactions implemented in Orca software, the Hydrogen atoms on the binding structure can indeed determine the energy of interaction based on the Hydrogen bridges with Oxygen atoms in the Zinc structure.

### Lig01

Presented two distinct binding possibilities differentiated apart by approximatively 44 kcal/mol (two degenerated by improper rotation over the N-Zn bond).The first possibility is consisted of the binding of the Nitrogen atom directly to a Zn center. The neighbor alcohol group sets over an Oxygen center and its Hydrogen interacts strongly with this center. The aromatic Hydrogen on the other side of the molecule also interacts with an Oxygen center. The Löwdin charge[2][192] on the Zn center decreases from $0.86e^-$ when it is not bind with the ligand (but conserving the geometry after the binding process) to $0.82e^-$ with the binding process. This characterizes that the bond is mainly due to the delocalization of the lone pair of Nitrogen on this metallic center. This is a non-covalent bond.

The second possibility consists of a direct bond of the Oxygen from the alcohol group with a Zinc center, forming a very tightly bind complex. The Hydrogen is taken by an Oxygen center. Equivalent charges variations are found for this complex, including a charge variation on the other Zinc center which now binds with the alcohol Oxygen. This is a covalent bond.

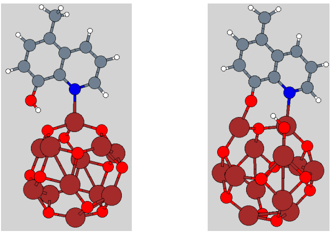

Conformer 1 Conformer 2

**Figure 6.4:** Ligand 1 - $(ZnO)_{12}$ complex.

### Lig02

Present five different binding possibilities, ranging from 20 to 110 kcal/mol. Two of them (1 and 4) are covalent bindings while the other three (2, 3 and 5) are non-covalent bindings. As the molecule has 2 active binding groups, it has a wide range of binding

---

[2] The Löwdin charges differ from the Muliken charges by, among others, considering that the equal partitioning of the electron density between participating atoms is without any foundation. It means that, whereas Muliken charges calculation "only" takes into account the distance between the atomic centers, the Löwdin takes the electronegativity as well within the partition.

possibilities. The one which binds the more tightly is the conformer 4, characterized by an Hydrogen migration to Zinc substrate and the binding of two Oxygen atoms over a Zinc one. This condition is unique for this ligand and has not been observed for no other.

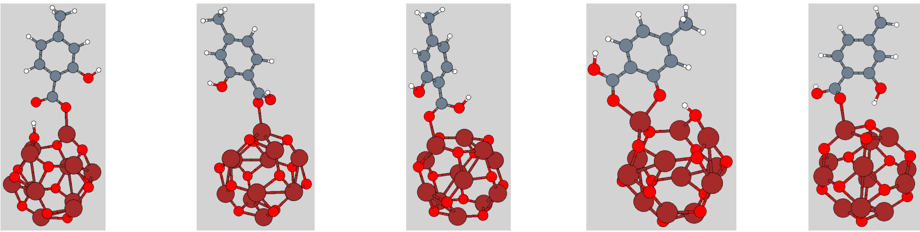

Conformer 1 Conformer 2 Conformer 3 Conformer 4 Conformer 5

**Figure 6.5:** Ligand 2 - $(ZnO)_{12}$ complex.

### Lig03

Presents three binding possibilities which are shown bellow. The first one consists of a Hydrogen migration from one alcohol to an Oxygen site on the Zinc substrate, the second one occurs in a similar way, but with a different complexation among Oxygen atoms and Zinc atom and in the third one no hydrogen migration occurs, but both Oxygen atoms of alcohols functions coordinate with the same Zinc atom. The two first are covalent bindings while the third one is a non-covalent one.

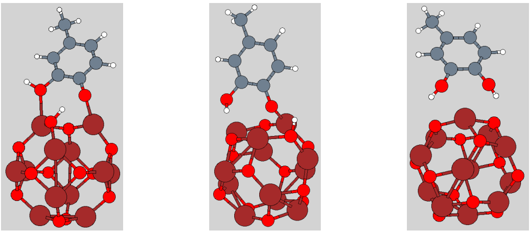

Conformer 1 Conformer 2 Conformer 3

**Figure 6.6:** Ligand 3 - $(ZnO)_{12}$ complex.

### Lig04

Presents three binding possibilities, two of them are equivalent. For these former, both of them are ruled by the interaction of Nitrogen atom with the Zinc one. The difference between them is only due to relative torsion of the alcohol over the substrates' $(ZnO)_2$ or $(ZnO)_3$ rings. This does not change energy of interaction in an appreciative way. However, the latter interaction is based on a covalent bond formed after a migration of Hydrogen atom of the alcohol function to an Oxygen center on Zinc substrate. This was only achieved using "brute force", i.e., Hydrogen does not dissociate spontaneously in calculations to form such complex, indicating a stronger barrier energy. After forcing its migration, a stable structure can be achieved as conformer 3.

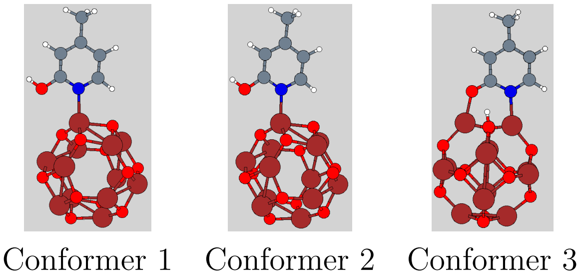
Conformer 1 Conformer 2 Conformer 3

**Figure 6.7:** Ligand 4 - $(ZnO)_{12}$ complex.

### Lig05

All binding possibilities are shown bellow. They are equivalent and the only difference is based on the ring structure to which the molecule is bind to. *I.e.*, depending if it binds over the two Zinc atoms in a $(ZnO)_2$ or $(ZnO)_3$ ring. Surprisingly, conformer 1 seems to be much more stable than conformer 2 and it can be due to the enhanced interactions with Oxygen atoms in Zinc substrate.

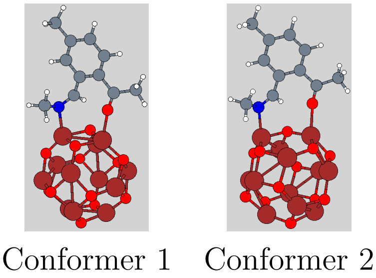
Conformer 1 Conformer 2

**Figure 6.8:** Ligand 5 - $(ZnO)_{12}$ complex.

### Lig06

Binding possibilities can be in a covalent (conformer 1) or non-covalent way (conformer 2). There is a third possibility, similar to conformer 2, in which hydroxyl stands over a hexagon ring in Zinc structure but this not change significantly the energy.

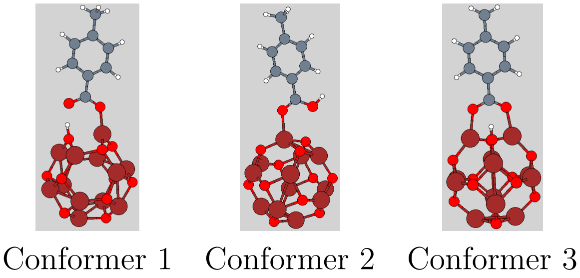
Conformer 1 Conformer 2 Conformer 3

**Figure 6.9:** Ligand 6 - $(ZnO)_{12}$ complex.

### Lig07

Binding possibilities are depicted bellow. As for the case of Lig06, it presents the same possibilities.

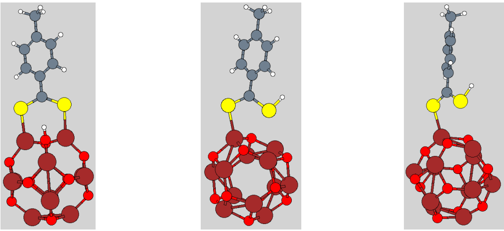

Conformer 1 Conformer 2 Conformer 3

**Figure 6.10:** Ligand 7 - $(ZnO)_{12}$ complex.

### Lig08

With an increased possibility of interactions.

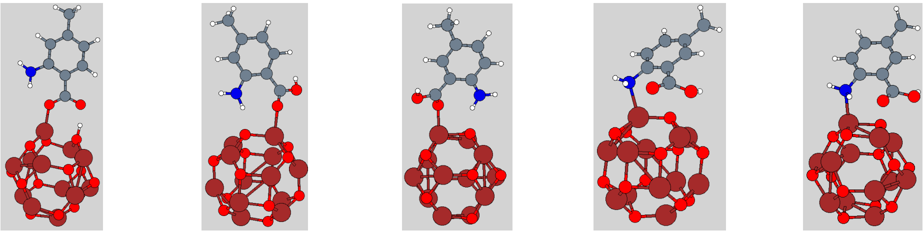

Conformer 1 Conformer 2 Conformer 3 Conformer 4 Conformer 5

**Figure 6.11:** Ligand 8 - $(ZnO)_{12}$ complex.

### Lig09

It presents only one binding position. The charge on the Zinc center decreases from $0.86e^-$ to $0.80e^-$ after the binding. This indicates a delocalization of the Nitrogen's lone pair on the metallic center.

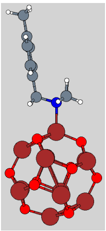

Conformer 1

**Figure 6.12:** Ligand 9 - $(ZnO)_{12}$ complex.

### Lig10

It presents only one binding position, as for the case of Lig09 which is depicted bellow.

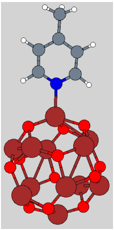

Conformer 1

**Figure 6.13:** Ligand 10 - $(ZnO)_{12}$ complex.

### Lig11

With no possibility of having covalent interactions, the changes in binding possibilities are due to changing the interacting sites over Zinc substrate. For conformer 1, both ether functions interact with only one Zinc atom. For conformer 2, these atoms interact with two distinct Zinc atoms over a $(ZnO)_2$ ring and in conformer 3 they interact with these atoms over a $(ZnO)_3$ ring.

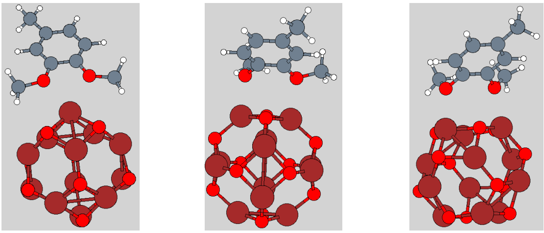

Conformer 1 Conformer 2 Conformer 3

**Figure 6.14:** Ligand 11 - $(ZnO)_{12}$ complex.

As a conclusion, one can verify that ligands which contain carboxylic acid or (thio)-alcohol functions can covalently bind to the inorganic substrate giving energy of interactions higher than the ones that cannot bind in this way. Moreover, binding by a Hydrogen migration is interesting since it passivates atoms in inorganic layer, reducing the probability of them acting as traps in photovoltaic devices.

In a future perspective, these should also be done considering other inorganic layers such as $TiO_x$ and $MoO_x$, since they are also worldwide used in OPVs. These studies have also been performed experimentally by X-ray techniques to prove the binding between the ligands and these inorganic layers and furthers results are found in Anna Isakova's PhD thesis.

## 6.2 Side-chain stabilization

*The following text treating the side-chain stabilization has been published entirely in* ***A universal route to improving conjugated macromolecule photostability****, by H. SANTOS SILVA, A. TOURNEBIZE, D. BÉGUÉ, H. PEISERT, T. CHASSÉ, J.-L. GARDETTE, S. THERIAS, A. RIVATON and R. C. HIORNS, published in RSC Advances in 2014, in the volume 4, pages 54919-54923. This is an open access article. The figures herein are reproduced from this publication.*

Organic materials degrades under light in combination with molecular oxygen.[203, 204] The instability of a material is a constraint to its use. In order to limit the photo-oxidation process, additives such as UV-screeners and antioxidants are thus often used in commercial polymer applications.[205] Unfortunately, these strategies are not available for conjugated polymers in organic electronics and opto-electronics. For example, in OPVs, UV-screeners reduce efficiencies and anti-oxidants can act as charge traps. Therefore, it is necessary to design intrinsically stable materials.

The mechanisms of degradation by which most molecules degrade in air upon exposure to light are well understood.[206, 207, 208, 209, 210] These mechanisms are the same for classic polymer and for modern conjugated polymers. Among these mechanisms, the radical chain oxidation of a polymer (PH) is due to hydrogen abstraction by a free-radical ($r^\bullet$), itself formed from the photonic excitation of a chromophore as in: $PH + r^\bullet \rightarrow P^\bullet + rH$.

During the propagation step, the macroradical ($P^\bullet$) reacts with molecular oxygen to give a peroxy radical ($PO_2^\bullet$) which in turn abstracts another labile hydrogen to yield a hydroperoxide. The latter thermally or photochemically decomposes to furnish macroalkoxy $P^\bullet$ and hydroxyl radicals.[168, 201, 206, 207, 208, 209, 210, 202] Depending on its structure, a macroalkoxy radical $P^\bullet$ decomposes, which variously impact upon the polymer properties.[206] The lability of polymer hydrogens towards abstraction is thus a key point in terms of the durability of material properties.

On the other hand, so that conjugated polymers may be soluble in organic solvents, side-chains are required. However, it has been unambiguously shown that the aforementioned hydrogen abstraction most likely occurs at the side-chains, notably sites alpha to the conjugated backbone.[87, 168, 201, 202] It is therefore crucial to investigate the effect of the structure of the side-chain on the stability of the final material.

The vast majority of conjugated polymers have carbochains, either branched or linear,[211, 212] as side-groups, as shown in Figure 6.15.a. Oxygen has also been used in side-chains, but it has not been for reasons for stability but rather been for solubility, synthetic facility and its ability to act as a charge donor.[62, 213, 214, 215, 216, 217, 218]

Historically, the use of an ether link has been avoided, as in Figure 6.15.b, because it was believed, like in Figure 6.15.c, that it would increase degradation rates. This was because prior work indicated that conjugated aromatic-oxy-alkyl links enhanced photo-oxidation, and this can be seen in Figure 6.16 in simple analogy to the known behaviour of all-aliphatic systems (e.g., polyethylene versus poly(ethylene oxide) (PEO), Figure 6.17).[219]

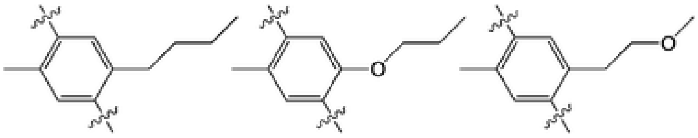

**Figure 6.15:** Chemical groups used in the discussion: (a) aromatic-alkyl; (b) aromatic-oxy-alkyl; and (c) aromatic-alkyl-oxy-alkyl.

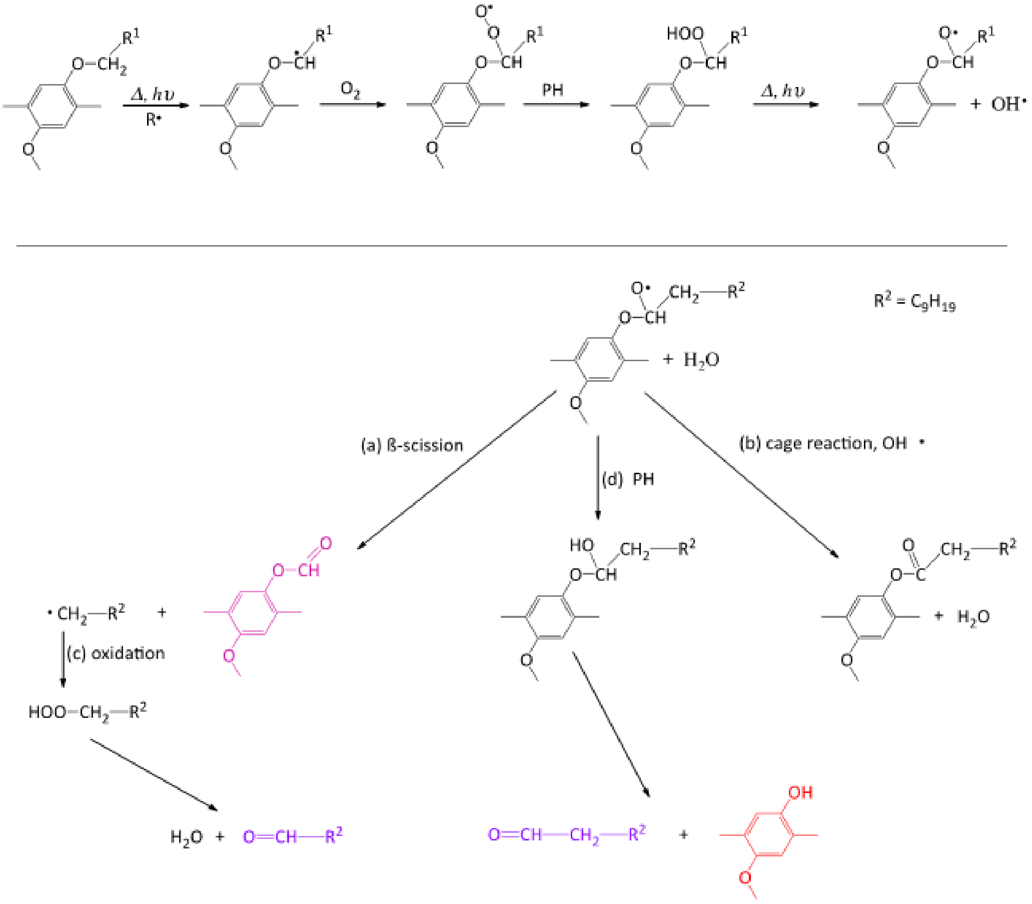

**Figure 6.16:** Proposed chain-radical oxidation of the side-chain of poly[2-methoxy-5-(3',7'-dimethyloctyloxy)-1,4-phenylenevinylene] (MDMO-PPV, also called PH); a possible but no longer considered dominant reaction.

The labile character of several hydrogens within different polymer was studied and it has been found that an oxygen into conjugated and non-conjugated aromatic-alkyl polymers at the position shown in 6.15.b can stabilize polymers against photo-oxidation. In the former case the results were found irrelevant due to the radical (non-polar) nature of the degradation.

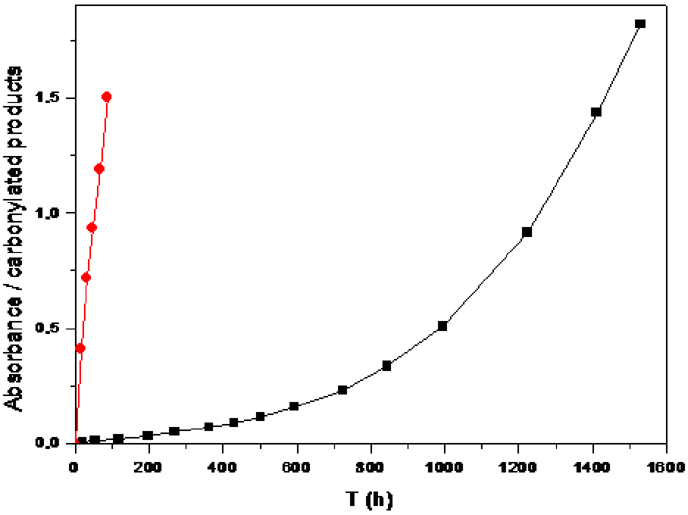

**Figure 6.17:** Comparison of the rates of photo-oxidation of polyethylene (PE, black line) and poly(ethylene oxide) (PEO, red line) as indicated by infra-red measurements of the concentration of carbonylated oxidation products.

Molecular geometries of model compounds were fully optimized within Density Functional Theory (DFT) method, using a double-$\zeta$ polarized basis-set (6-31G**)[225, 227, 228] and the B3LYP exchange-correlation functional.[229] Where required, the open-shell wave function was set to an unrestricted type (UKS). Modeling of hydrogen-abstracted geometries was performed with a *doublet* multiplicity in a neutral state. All calculations were performed using Orca 2.9 software.[93] Spin distribution was extracted from the Löwdin partition.[192, 230]

The model compounds depicted in Figure 6.18 were used since they allow calculations over a variety of typical hydrogen positions.The conclusions drawn from these models were then tested on the range of structures shown in Figure 6.19, which include oligophenylenes, oligothiophenes, oligo-TBT and oligo-BT7.

Molecules 1 to 4 are oligostyrenes, and 5 and 6 are oligo(ethylene)and oligo(oxyethylene), respectively. While molecule 1 provided a standard, 4 was calculated to deduce effects from electronegativity while keeping the chalcogenic character of the heteroatom. $E_{BD}$ values of the $\alpha$-hydrogens to the aromatic group, or nearest neighbor equivalents to the oxygen atom, were calculated along with the thermodynamic stabilities of the final macroradical compound formed after hydrogen abstraction. This was performed on the basis that the mechanism of degradation is initiated by hydrogen abstraction by a photo-generated radical, such that:

$$E_{BD} = (E_T^{MR} + E_T^{HR}) - E_T^{MS} \tag{6.4}$$

where $E_T^{MR}$ is the total energy of the macroradical, the total energy of the hydrogen radical and $E_T^{MS}$ the total energy of the molecule in the singlet state. All geometries

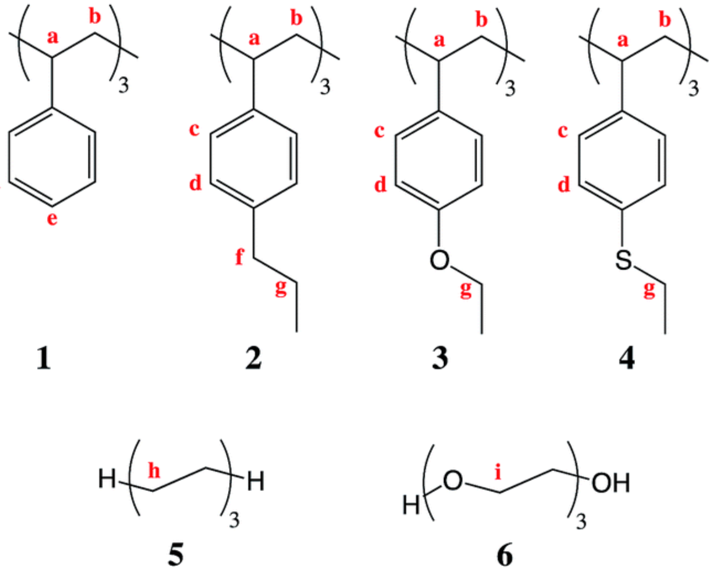

**Figure 6.18:** Basic molecular structures used in this study.

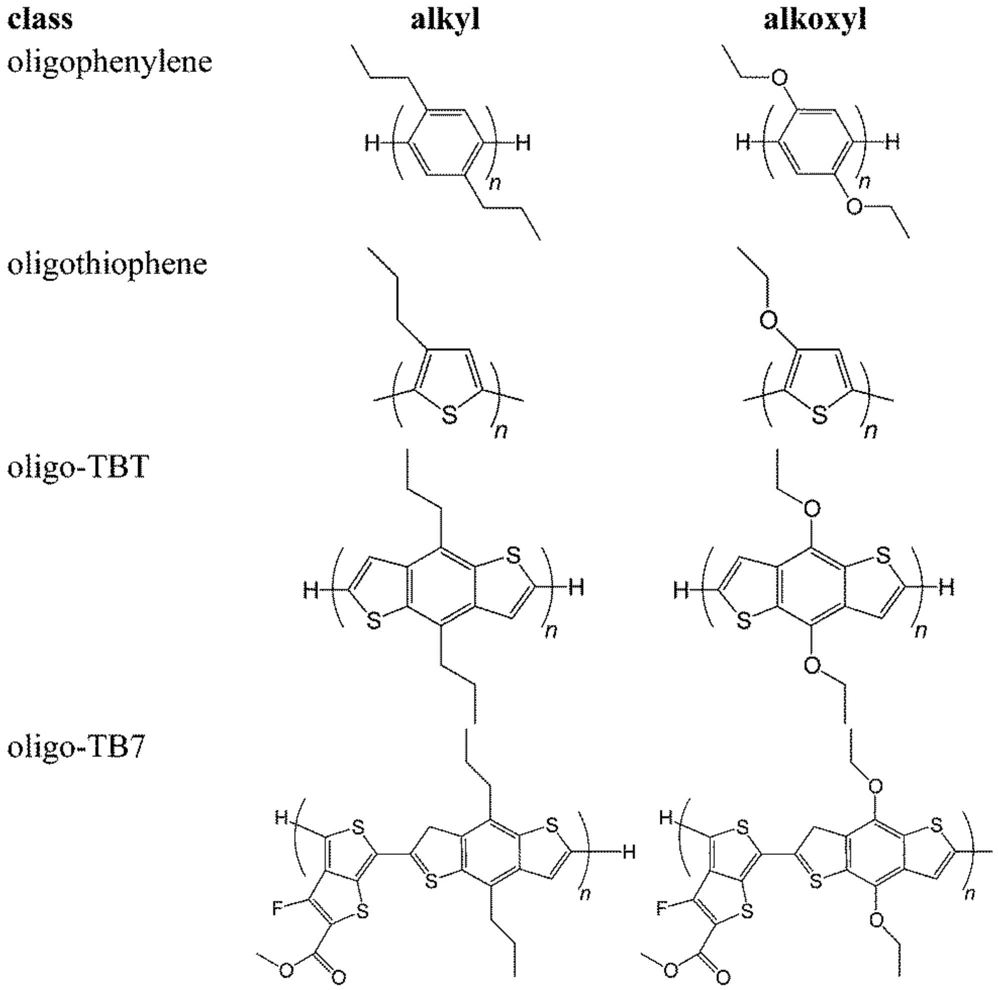

**Figure 6.19:** Additional chemical structures used in this study where n=1 to 4.

were allowed to relax to their minimum configuration. Hydrogens are labeled $a - i$ as indicated in Figure 6.18.

Comparing 5 and 6, one notes that the presence of an oxygen atom makes the attached hydrogen more labile; the energetic difference is around 3 kcal/mol. As expected oxygen favors H-abstraction from adjacent methylene groups in all-aliphatic systems.[231] Comparing molecules 1-4, and excluding the tertiary C-Hs (labeled 'a') as they are expectedly weak, it is found that oxygen has a protecting effect on the nearest hydrogen.The weakest C-H bond is now no longer 92.79 kcal/mol (2f) but 100.45 kcal/mol (3g); a gain in energy of around 8 kcal/mol has been made. Sulfur has a similar impact, raising the lowest energy C-H bond by around 6 kcal/mol. Furthermore the problem has not simply been moved along the alkylated chain. As mentioned above, the $E_{BD}$ values of 1-4a, as expected, are all very low due to the tertiary carbon. Interestingly, oxygen and sulfur slightly stabilize this group. No discernible affect is accorded to hydrogens 2b-4b.

| | Bond Dissociation Energy (kcal/mol) | | | | | |
|---|---|---|---|---|---|---|
| **Hydrogen** | **1** | **2** | **3** | **4** | **5** | **6** |
| **a** | 85.35 | 86.17 | 86.98 | 88.98 | - | - |
| **b** | - | 101.36 | 101.29 | 101.90 | - | - |
| **c** | - | 117.46 | 117.51 | 117.19 | - | - |
| **d** | - | 117.46 | 119.96 | 116.72 | - | - |
| **e** | - | - | - | - | - | - |
| **f** | - | 92.79 | - | - | - | - |
| **g** | - | 104.74 | 100.45 | 98.84 | - | - |
| **h** | - | - | - | - | 104.80 | - |
| **i** | - | - | - | - | - | 101.56 |

**Table 6.2:** Calculated values for EBD for models 1-6 within B3LYP/6-31G** level of theory.

This stabilizing effect of oxygen was tested against the thermodynamic stability of the macroradicals formed after the abstraction of the labile hydrogen (the one in alpha position of each molecule). These energies are differences in the Free Gibbs energy ($\Delta G$) and were calculated after a full frequency calculation of each macroradical. This energy represents the energy gain during for the reaction:

$$RH + OH^{\bullet} \rightarrow R^{\bullet} + H_2O$$

Compound 2 (2f abstraction) gives rise to the most stable structure *i.e.*, the formation of this radical is favored, whereas the one based on aromatic-oxy-alkyl radical of 3 (3g abstraction) is not. For the entirely aliphatic molecules 5 and 6, results confirm the destabilizing effect of oxygen, *i.e.*, the macroradical of 5 is less stable and thus less favored than that of 6 (respectively, -16.74 and -20.63 kcal/mol).

| Thermodynamic stability of $R^\bullet$ (kcal/mol) | | | |
|---|---|---|---|
| **2f** | **3g** | **5h** | **6i** |
| -29.87 | -19.82 | -16.74 | -20.63 |

**Table 6.3:** Calculated thermodynamic stabilities of the macroradicals 2-6 formed following the hydrogen abstraction within B3LYP/6-31G** level of theory.

At this stage, in order to determine why this effect is observed, we payed attention to the spatial delocalization of the unshared electrons in the macroradicals 1-6. In each case, the lowest energy hydrogen (outside of tertiary hydrogens) was removed. In 5 the unpaired electron is highly localized at the carbon from which the hydrogen was abstracted, with a partition coefficient of 0.88. However, in the oxygenated molecule 6, this value is reduced to 0.77; the adjacent oxygen assumes a coefficient of 0.15. This corroborates the above results as the hydrogen is more labile (more unstable) because its radical product is delocalized away from the native carbon. For compounds 2 and 3, the former has a coefficient of 0.63 at the native carbon and 0.35 over the aromatic ring, and in the latter 0.77 on the native carbon, 0.12 on oxygen, and only 0.04 at the ring. In other words, hydrogen abstraction at 2f results in a more stabilized macroradical than that from 3g. In effect, the oxygen in 3 has blocked the unpaired electron from moving towards the aromatic group, with the result that macroradical is less stabilized, and hydrogen abstraction is less favored. In the aliphatic structures, 5 displays a more localized electronic behavior because the oxygen in 6 takes up some of the unpaired electron presence. However, in aromatic structures, this effect gives rise to the opposite result: the oxygen takes part in delocalizing the electron but *blocks* its further delocalization to the aromatic ring; this makes the radical product less stable and less likely to be formed.

To demonstrate that the insertion of oxygen into aromatic-alkyl bonds has a universal effect, we turned to 4 different chemical structures found in Figure 6.19 with variation of the conjugation length. All $E_{BD}$ values were calculated, and the weakest bonds have their energies listed in Table 6.4. In all cases, the introduction of oxygen increases C-H bond strengths. The values, across a range of structures, indicate that the process is based on the local character of the molecule, regardless of the presence of heteroatoms in the conjugated backbone or the conjugation length.

It was than showed that oxygen atom attached to an $sp^3$ carbon decreases the stability of a macromolecule towards oxidative photodegradation, as demonstrated by the known behaviors of PE and PEO. However, an aromatic-oxy-alkyl moiety is more resistant to photo-oxidation than an aromatic-alkyl group and the effect of oxygen is localized. It is its position that determines how stability is impacted: an oxygen atom adjacent to an aromatic group can block electronic communication through its relatively high electronegativity; adjacent to an aliphatic chain, it diminishes stability by spreading unpaired

| | Bond Dissociation Energy (kcal/mol) | | | |
|---|---|---|---|---|
| | **n=1** | **n=2** | **n=3** | **n=4** |
| **oligo(1,4-dialkyl)phenylene** | -92.83 | -92.87 | -94.81 | -95.01 |
| **oligo(1,4-dialkoxy)phenylene** | -100.55 | -100.34 | -100.21 | -100.21 |
| **oligo[(3-akyl)thiophene]** | -92.81 | -90.95 | -90.22 | -86.94 |
| **oligo[(3-akoxy)thiophene]** | -100.67 | -100.61 | -100.90 | -100.97 |
| **oligo(alkyl-TBT)** | -90.39 | -93.19 | -92.55 | -92.51 |
| **oligo(alkoxy-TBT)** | -97.42 | -100.26 | -100.50 | -102.54 |
| **oligo(alkyl-TBT7)** | -87.53 | -92.32 | -91.99 | -92.08 |
| **oligo(alkoxy-TBT7)** | -100.45 | -100.59 | -100.62 | -100.73 |

**Table 6.4:** Calculated bond dissociation energies ($E_{BD}$) within the B3LYP/6-31G** level of theory for chemical structures of Figure 6.19

electrons. This is an important result for designing conjugated materials for which long-term photo-oxidative stability is required.

## 6.3 Correlating geometry of multidimensional carbon allotropes molecules and stability

*The following text treating the relation between geometry of carbonic molecules and their stability has been published entirely in* ***Correlating geometry of multidimensional carbon allotropes molecules and stability****, by H. SANTOS SILVA, J. CRESSON, A. RIVATON, D. BÉGUÉ and R. HIORNS, in press in Organic Electronics in 2015, http://dx.doi.org/10.1016/j.orgel.2015.08.004. The figures herein are reproduced from this publication.*

Among known carbon allotropes, the low-dimensional fullerenes,[233, 234] nanotubes [235, 236, 237] and graphenes[238, 239, 240] are of paramount importance to the development of new nano-based technologies. This is mainly due to their exceptional electron-poor electronic properties, their singular structures and the ease with which they can be obtained.[241, 242] However, the photo-oxidation undergone by these materials is a remaining problem to be solved and understood when picking the most appropriate among this class.

$PC_{60}BM$, for instance, has been proved to enhance the stability of donor polymers by way of its scavenging radicals which might otherwise go on to cause cascading polymer degradation reactions,[260] a result supported by combined spectroscopic and degradation studies.[261] However, given that $PC_{60}BM$ degrades under the combined action of light and oxygen,[208, 258] it is worth considering its own stability with respect to other classes of accepter carbon allotropes materials. This data will become all the more important as donor polymer stabilities increase.

Furthermore, the direct relation between stability of the acceptor material and the photovoltaic device was highlighted by Reese et al.[262] It is clear that oxidized fullerene cages ($PC_{60}BM$) have deeper LUMO levels and act as electron traps in a device, hindering performance and reducing device lifetimes. This is then the motivation to study further this process and the influence of the geometry of the molecule on it.

As the electronic properties of the carbon allotropes arise from $sp^2$-hybridized carbon atoms, the distortion of this character induces pronounced property modifications. For instance, it is a well known that bending the hexagonal planar arrangement that make up graphene into carbon nanotubes (cylindrical bending) or fullerenes (spherical bending) is responsible for determining several properties derived from chemical reactivity.[263, 264] The bending of the carbon bonds over a certain surface defines a curvature of which the radius is known to be decisive for the determination of several properties.[265] Chemical reactions, such as acidic attacks on carbon nanotubes,[266] are understood to be dependent on the $(m, n)$ index of the tube, which defines its radius of curvature. Experience shows that the more bent a carbon surface is, the more easily attacked it becomes.[267] This is generally accepted accordingly to the $\pi$-orbital axis vector analysis (POAV),[268, 269] which provides an appropriate description of the electronic structure on non-planar conjugated molecules. This theory explains how pyramidalization angles are key to the differences in chemical potentials between curved and planar carbon structures. Moreover, carbons residing on curved surfaces should exhibit increased chemical reactivities due to diminished electronic delocalization and higher $\sigma$-bond characters.[270]

Surprisingly though, up to now, no work linking this very intrinsic parameter of carbon curvature to the ease of material degradation caused by oxidation in devices (in particular concerning the well-known routes[6, 167]) could be found in literature. Aside the meaningful work by Hirsch et al.[271] which considers in-depth the influence of the carbon-atom pyramidalization angle on the reactivity of carbon nanotubes and the work done thereafter, we could not find a correlation between structure and device performance over time.

While it is understood that devices architectures that arise from each material type (graphene, fullerene or nanotube) may lend themselves in different ways to providing physical barriers to contaminants, it nevertheless remains a fundamental and important object to systematically study the correlation of the curvature of these carbon structures and their degradation energetics by well-established routes.

To do such correlation, three different attack routes were studied:

1. collision with atomic oxygen;
2. a radical attack;[272]
3. molecular singlet oxygen attack.

These reactions were selected as they model the reactive species playing roles in the degradation process of OPVs.

In the atomic oxygen attack, it is assumed that an epoxide group is formed, rather than a ketone or bridging ether, in accordance with prior studies.[273, 274] Radicals can add on double bonds of the fullerene. In this case, we used a hydroxyl radical as probe since this radical is likely to be present in the degradation mechanism. For the $^1O_2$ attack, a superoxide is formed and the singlet and triplet configurations are studied ($S_0$ and $T_0$, respectively).[272]

The molecules chosen for this study comprise a nanoribbon model molecule which is strained over two parallel edges towards the center of the molecule, allowing one to fully control the radius of curvature, and as a consequence the pyramidalization angle. Where there is no curvature, *i.e.*, the molecule is completely planar, we assume that the radius goes to infinity. The edges are zigzag and hydrogen-passivated and we attribute to this model a graphene-like character. The strain was applied by a controlled constrained distance linking the edge carbons from one side to the other, and the distance along the edge atoms of the same side was not allowed to relax. This defines a chord which was used to calculate the radii of the curvature, as depicted in Figure 6.20.

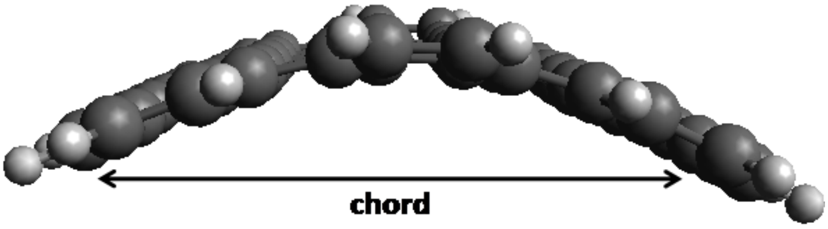

**Figure 6.20:** Definition of the chord caused by the lateral strain.

The chords relates to the radius of curvature by the following formula:

$$R = \frac{c^2 + F^2}{2F} \tag{6.5}$$

Where $c$ stands for the chord, $R$ for the radius of the sphere and $F$ stands for the rise of the sphere.

To study the effect of curvature on fullerene systems, we picked up several medium-size fullerenes, namely $C_{60}$, $C_{70}$, $C_{78}$, $C_{80}$, $C_{82}$ and $C_{84}$ and the attacks were performed, for the asymmetric (accordingly to its axis - all less $C_{60}$ and $C_{80}$), on the equator and on the pole. No symmetry consideration was performed beforehand and this does not influence the final results [*vide infra*]. Although these two attacks were made in different regions of the molecules, one should keep in mind that it is not enough to describe all the chemical environments that arise from this lack of symmetry. This is clearly seen for the case of $C_{70}$: for radical attacks, it has five possible regio-isomeric structures of a $C_{70}^{\bullet}$ radical,[275] where R is generic. Two out of these structures are located in what we call here equatorial region and the other three are nearer to the poles. Each one of these structures has at least 3 iso-energetic carbon sites.

The structures had their ground state geometries completely optimized within B3LYP/6-31G** level of theory[225, 229, 276, 277, 278] using Orca 2.9.1 software.[93]

The quasi-linear behavior of the relation established in the small curvature regime between the pyramidalization angle and the curvature radius for the nanotubes' geometries can be found in Figure 6.21.

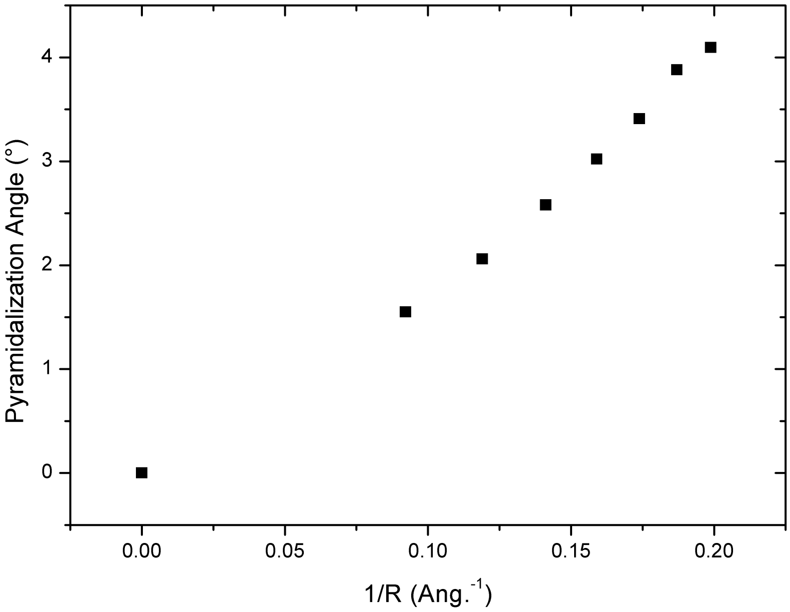

**Figure 6.21:** Relation between Pyramidalization angle and Inverse Radii.

### Atomic oxygen collision

The reaction of the studied materials with an oxygen atom was first studied. The product so-formed is an epoxy group.

In our DFT calculations, ketone formation was not energetically stable and the geometries evolved to an epoxy formation. In Figure 6.22, one can find the binding energies for the curvature-controlled nanoribbons and for the selected fullerenes against the pyramidalization angle. The average over the fullerenes (the center of the cloud of points) is also plotted.

One can see that the binding energy decreases with the increase of the pyramidalization angle. It means that, collisions with atomic oxygen result in more stable products for the case of molecules with accentuated curvature. It is interesting to note that a clear relation between the stability of the so-formed oxidation product against the strain of the carbon atom, regardless of the type of the material (graphene-like, nanotube-like or fullerene) can be seen.

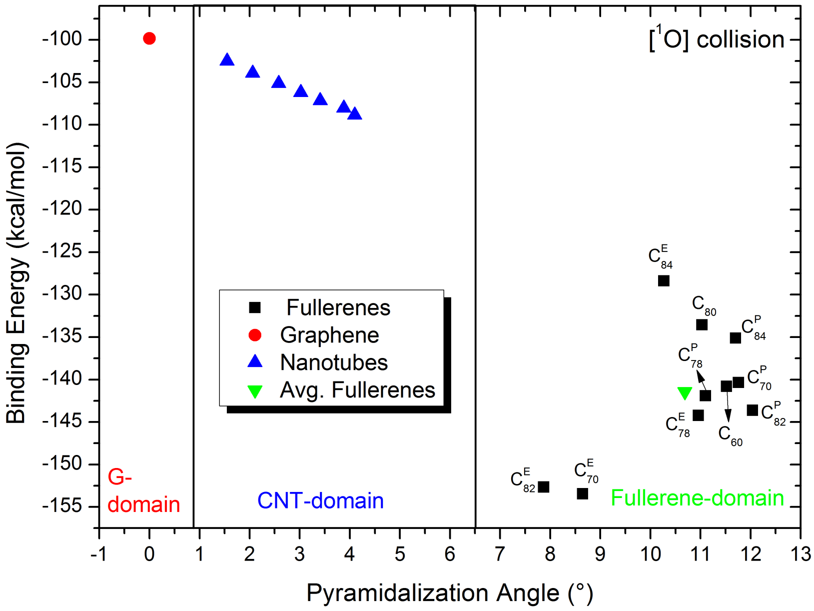

**Figure 6.22:** Relation between Pyramidalization angle and binding energy in epoxy formation.

### Singlet Oxygen molecule attack

Molecular oxygen has a triplet ground state and its first excited state is a singlet state. When excited, the molecule in question transfers its energy to molecular oxygen, making a complex which is responsible for starting the degradation process. In this way, the complex studied is a singlet ground state, which corresponds to the frame after the excitation and the energy transfer. The formation of a superoxide is the first product of the reaction, which can then be dissociated to more stable products such as epoxies. As described *vide supra* one can find the energies for the strained graphene nanoribbon and for the fullerenes, with the inclusion of the average over the fullerene energies within the graphene nanoribbon graphic.

As for the case of the collision with atomic oxygen, singlet molecular oxygen also forms stable complexes with curved molecules. It is interesting to note that, from the theoretical scale of energy, these complexes seems to be more stable the more strained is the molecule. It means that curved molecules like fullerenes seem to have a much higher affinity to molecular oxygen than nanotubes and graphene. One can note that one of the most used fullerenes, $C_{60}$, has a incredibly high affinity with oxygen, what is proved experimentally, if compared to nanotubes, for instance. Moreover, the energy scale also explains the fact that this reaction is reversible for fullerenes in a first moment upon thermal annealing. However, once this complex evolves to form other compounds, such as (endo-)epoxydes, the oxidation is irreversible.

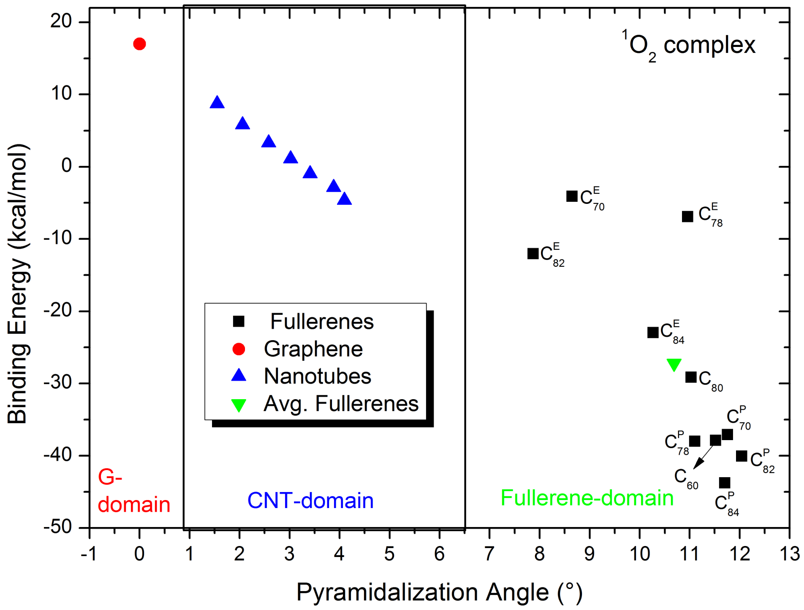

**Figure 6.23:** Relation between Pyramidalization angle and binding energy of a singlet oxygen molecule.

### Hydroxyl radical attack

During the degradation process, radicals can be formed.[207, 279] Due to an extremely high electrophilicity, the double bonds are easily attacked. The graphics of this energetic process are presented in Figure 6.24, using a hydroxyl radical as probe.

Again, a linear relation is found for the graphene and nanotubes regime while it is not coherent for fullerenes, although they present radical scavenger properties.[280] This can be associated to two factors: the curvature in fullerenes is not exactly the same as it is in nanotubes and the $\sigma$-bond character is much more enhanced in these structures compared to the nanotubes.

### Conclusions

The relation between the ease of degradation and molecular curvature has been studied for models of graphenes, nanotubes and fullerenes. Considering only the basic parameter as the geometry of the molecule, one can deduct that it is not possible to avoid degradation of fullerenes, for example, since they have high affinities towards oxidizing species by the simple fact they are round. Spatial protection can be performed, although this may reduce the electronic mobility of the material.

Even though the edges are not treated here, we have conscience that it may play a major role on the degradation pathways of this class of materials. However, we emphasize the *model* character of this study and the trial of generalization of a given microscopic property with the macroscopic degradation mechanisms.

As a conclusion, one should consider using flat carbon materials such as graphene

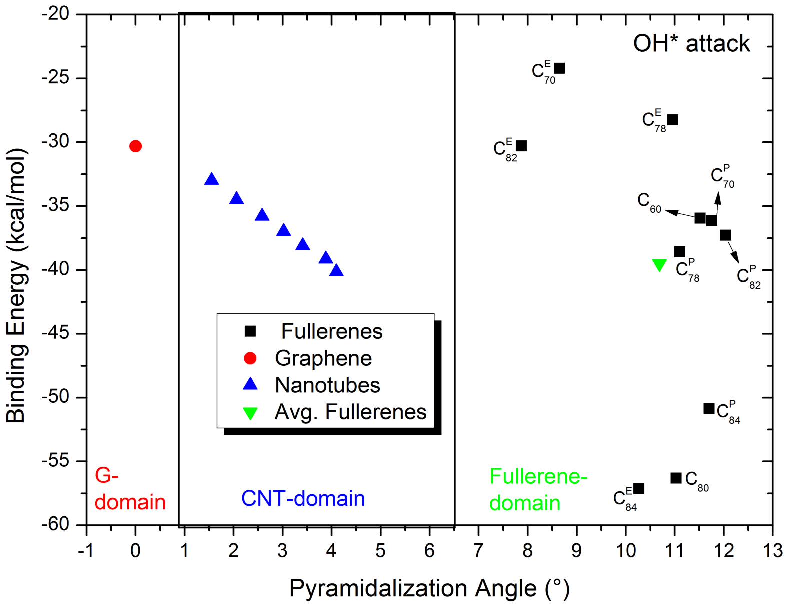

**Figure 6.24:** Relation between Pyramidalization angle and binding energy of a hydroxyl radical.

when designing molecules for use in organic electronics and photovoltaics where stability against oxidative stress over long periods of time is required.

## 6.4 Final Remarks

During this Chapter, three different degradation pathways have been studied altogether and how one could avoid them. This was only possible based on a wide literature review and molecular modeling calculations applied to model systems.

In summary, the following has been shown:

- The general stability of a system can be described as a functional of several functions which depend upon extensive and intensive parameters correlated among themselves. This results in a very unlikely scenario where this functional can be minimized, at the same time, for different systems.

- This means that the stability seems to be intrinsic to each different system and it might be not possible to pick a very definite set of parameters that would design a ”perfectly” stable material.

- Concerning interface delamination problems, when using ligands polymerized to increase adhesion between organic and inorganic layer, carboxylic acids and other functions that can covalently attach to the inorganic metallic sites are of interest.

- Concerning the stability of side-chain of conjugated macromolecules, one should insert an oxygen atom between the aromatic cycle and the $sp^3$-hybridized carbon atoms. This avoids the delocalization of the radical formed upon H abstraction during photo-oxidation process.

- The behavior observed for C$sp^2$-O-C$sp^3$ link is the opposite of what is observed when both carbons are $sp^3$.
- Concerning different carbon allotropes electron acceptor materials, there is a great influence of the pyramidalization angle and the affinity of their surfaces to oxygen attack.
- This is due to the fact that higher pyramidalization angles induce an increased $\sigma$-bond character of the carbon, increasing the affinity with oxygen as well.
- There seems to be a linear relationship between the three domains of carbon allotropes (0D - fullerenes, 1D - carbon nanotubes and 2D - graphene) for what concerns the affinity to oxidizing agents. This seems to be intrinsically related to the Gaussian curvature of their surfaces.

Exploring these last points, the next chapter will introduce new acceptor-donor hybrid materials that try to incorporate all that have presented up to now. Coherently with what has been said in the introduction of this Chapter, the unique stable material does not exist but this does not avoid trying to apply the rules learned until now to new systems.

# Chapter 7

# Alternative Acceptor Materials

*After all that has been discussed along this thesis, this chapter proposes alternative materials for those the stability is predicted to be superior to the ones found for fullerene-derivatives materials based on the results of Chapter 6. This is done by a completely theoretical approach and this is a continuation to what has been already developed by Bégué and co-workers before this thesis. Not only what already has been done is herein presented, but also a new piece of modeling and propositions are discussed to a new class of hybrid stable organic materials for photovoltaics.*

The success of fullerenes in OPVs are due to their unrivaled electron acceptor properties, as described in Chapter 2. These properties depend on the high electron mobility; on the delocalization of the LUMO orbital over the whole surface of the molecules, allowing 3D electron transfer and transport; on the reversible electrochemical reduction profile; and formation of percolation domains from solution when blended with a *p*-type polymer. It has also been shown that this latter property can give rise to morphological failures with thermal stress.[281]

Interest in non-fullerene electron acceptor materials is a growing field of research in Organic Electronics but only very few systems can exceed efficiency if compared to fullerenes.[282, 283, 284, 285] It is worthy noting that all of these are derived of perylene diimide motifs.

Not only on the efficiency point of view, but also from that of stability, Głowacki *et al.*[286] presented low price electron acceptors based on small molecules that are nature-inspired and air-stable over long periods of operation in field-effect transistors. They attribute the stability of the molecules proposed by them to the strong intermolecular hydrogen-bonding interactions, that block the structure of the bulk and avoid contaminants to absorb in. They also report good electron and hole mobilities even though the $\pi$-delocalization of the molecules are low enough to be discarded from the library of acceptors during the design of new molecules. This is an encouraging piece of work because they associate on the same simple systems, air stability, efficiency and low price.[1]

Many stable pigments and dyes of natural origin are exactly based on hydrogen-bonded $\pi$-stacked organic compounds. A remarkable example of this family is indigo-based compounds,[287] which display both ambipolar charge transport and air-stability.

On the other hand, based on the results obtained in the previous chapter, one can deduct that plane-shaped electron acceptors such as graphene-like molecules are expected to be more stable against several chemical attacks taking place during the degradation process. Moreover, these molecules are known to efficiently $\pi$-stack as it is the case of graphite, compound based only on the stacking of graphene sheets.

The work herein presented intends to be a proof of concept based on the work done by Bégué *et al.* on stable planar hybrid acceptor-donor conjugated materials and that is one of the motivations why the modeling done by this team is slightly different from the one herein presented.

## 7.1 Graphene-like systems and columnar H-bond-linked architecture

Hexabenzocoronenes (HBC) are symmetric synthetic molecules that mime a graphene sheet under specific and controlled conditions. In Figure 7.1, one can find it depicted.

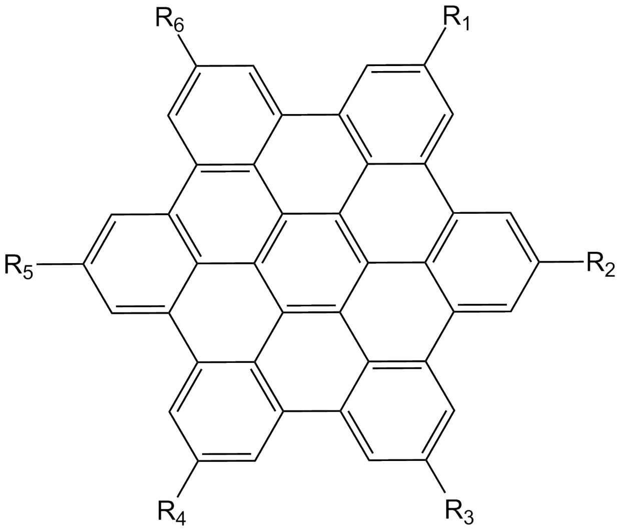

**Figure 7.1:** General structure of circular hexabenzocoronenes.

The positions $R_i$, $i = 1$ to 6, can be fully functionalized with different chemical functions. By appropriate functionalization, acceptor structures can be obtained with optimal electronic properties to match to the donor material. In order to create self-ordered acceptor-donor molecules with optimal spatial arrangement for photovoltaic application,

---

[1] The reader in invited to see comment in the introduction of Chapter 1.

such as the ones described in Figure 1.3, one should envisage functionalizing one of these $R$ positions with a $p-$type material. This methodology is explored in more details in a paper by Bégué *et al.*, in preparation.[2]

This work has shown that using $-COOH$ functions to functionalize positions $R_1$, $R_3$, $R_4$, $R_6$ is a good approach to efficiently match the electronic levels between the conjugated acceptor core and the lateral donor branches. This is presented in Figure 7.2.

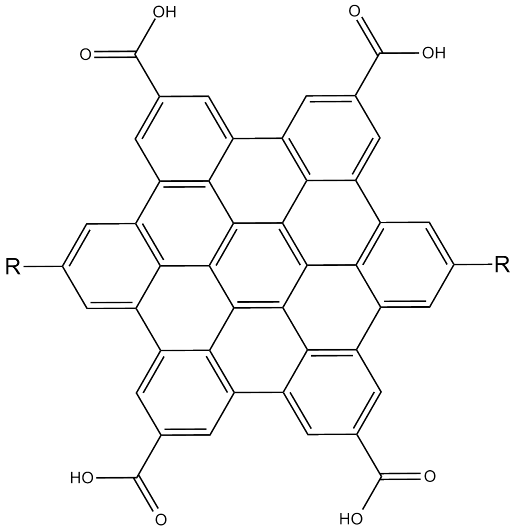

**Figure 7.2:** Functionalized structure of circular hexabenzocoronenes.

The missing functions can be functionalized by insertion of $\pi-$conjugated polymers segments, as it was performed by Bégué *et al.*, using oligo-alkoxy-thiophene units and described in the next section. Particularly, these molecules induce a $\pi$-stacking in the $z$ direction based on the $\pi - \pi$ interactions of the aromatic core and on the hydrogen bonds between $-COOH$ groups of adjacent molecules. As described by Jackson *et al.*,[288] $CH - N$ and $CH - O$ pair interactions are strong enough (2.20 and 1.86 kcal/mol, respectively) to lock conformations in $\pi-$conjugated polymers, and that is why such columnar structure stays in place, as presented in Figure 7.3, where a quick overview of the supramolecular structure of HBC-P3AOT system (see next section) can also be found.

---

[2] Graphene-based acceptor molecules for organic photovoltaic cells: a predictive study identifying high modularity and morphological stability, Didier Bégué, Emilie Guille, Sebastian Metz, Marc Alexandre Arnaud, Hugo Santos-Silva, Mamadou Seck, Pierre Fayon, Christine Dagron-Lartigau, Pierre Iratçabal, Roger C. Hiorns, *in preparation.*

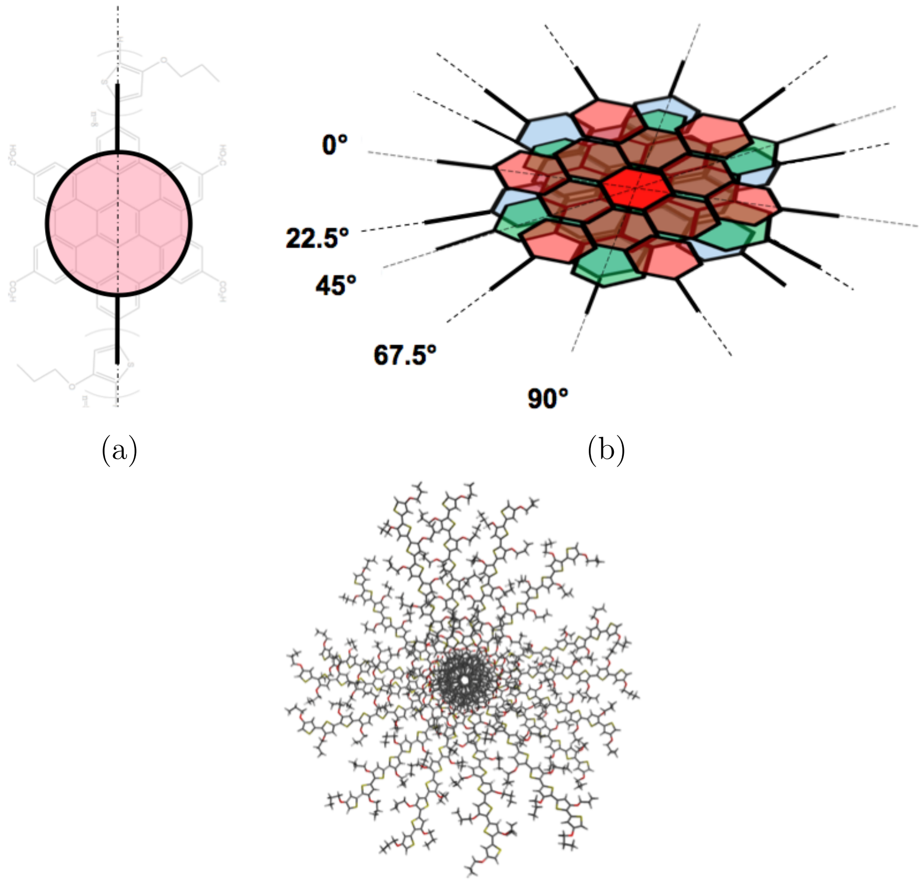

(a)

(b)

(c)

**Figure 7.3:** Supramolecular columnar organization of HBC-COOH-based molecules with a discotic liquid crystal behavior. In (c), the system depicted is the one treated in the next section.

## 7.2 HBC-P3AOT system

Idé *et al.*[289] proposed that acceptor materials with discotic liquid crystals properties can exhibit enhanced charge separation in photovoltaic arrangements. In the work done by this group, they have proposed that contiguous columns of donor and acceptor materials are detrimental to the solar cell efficiency.

Modern polymers rarely display discotic liquid crystal properties, whereas HBC-like molecules do. In this way, linking both of them together, one might obtain columnar structures of hybrid $p-n-$ type materials with appropriate charge separation in the excited state.

Considering the case where $R_2$ and $R_5$ in Figure 7.2 are both an oligo-3-propyloxy-thiophene with ten segments each (Figure 7.4), the ground state geometries of the oligomer segments were fully optimized within the HF-3C method followed by single point calculations performed by B3LYP/6-31G** methodology, using RIJCOSX approximation[3]. Figure 7.5 presents the evolution of the HOMO and LUMO energy values for these segments.

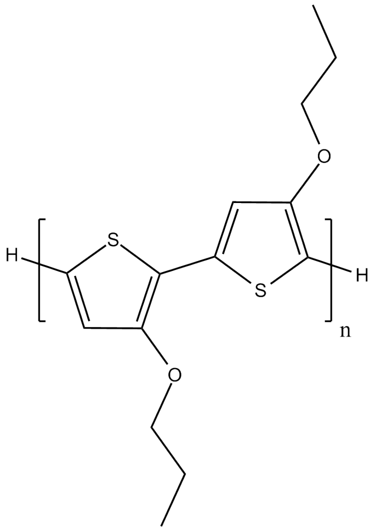

**Figure 7.4:** Oligo-3-propyloxy-thiophene (P3AOT) with $n$ ranging from 1 to 10 units grafted to the HBC core.

The UV-VIS absorption spectra of this series were calculated within both TDDFT/B3LYP/6-31G** and CIS-ZINDO/S methodologies. This double approach was employed since the former cannot be used for the case where the oligomers of P3AOT (with $n > 4$) are grafted to the HBC core. Figure 7.6 presents the evolution of the calculated spectra enveloped with Gaussian functions having a FWHM of 35 nm in the real space as well

---

[3] Originally, these geometries were obtained at the $\omega$B97X-D/6-31G* level of theory. However, for the sake of coherence with the next section, we re-optimized them at a lighter yet accurate HF-3C method. This procedure was employed since the level of theory orignally used is prohibitive for the systems presented in section 7.3.

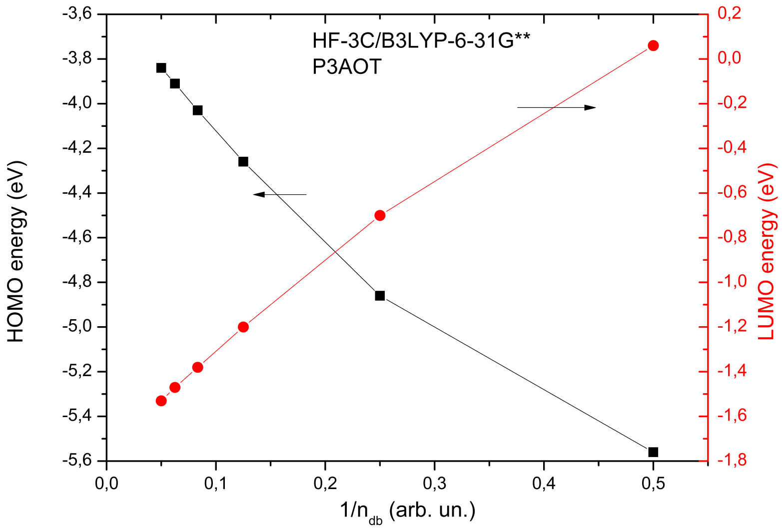

**Figure 7.5:** Evolution of the HOMO and LUMO energies of P3AOT with the increase of the chain length. $n_{db}$ stands for the number of double bonds in the chain.

as the evolution of the energy gap measured by the excited state approach and by the ground state single points.

From these spectra, one can note that the prevision of the lowest energy transition is kept almost unchanged at the $n = 8$ or 10 limit. This can also be seen by the HOMO-LUMO evolutions, indicating that segments longer than this do not represent any improvement in the electronic transitions properties of the chains. Moreover, it is worthy noting the energy difference of the lowest energy electronic transition for both methods: 39 nm (0.15 eV) which is a value to keep in mind to better estimate the cases where the TD-DFT method can not be used.

In this way, the molecules having these chains grafted to HBC core were also fully optimized and the evolution of the HOMO and LUMO energies are presented in Figure 7.8.

It is interesting to note that only a slight increase on the wavelength takes place for the maximum of absorption of the grafted molecule compared to the pristine P3AOT segment, as it can be noted in Figure 7.8.(a). In Figure 7.8.(b), one can see the effect on the electronic structure of grafting the P3AOT chains on HBC conjugated core. Clearly, a "camel back" characteristic[290] is developed, indicating the electron-donor hybrid properties of the molecule. In Figure 7.8.(c) the differences between the calculated spectra of HBC-COOH core by both methods is presented and it is again worthy noting that ZINDO/S underestimates the absorption maximum by 18 nm (0.19 eV), what is comparable with the previous calculated difference.

Using a Natural Transition Orbitals analysis[291], the first low-lying electronic transitions are composed of two main individual transitions each and these have an equal ($\sim$ 30%) participation on the intensity of each excited state . Considering only these two states, one has $|HOMO\rangle \rightarrow |LUMO\rangle$ and $|HOMO-1\rangle \rightarrow |LUMO+1\rangle$ participating

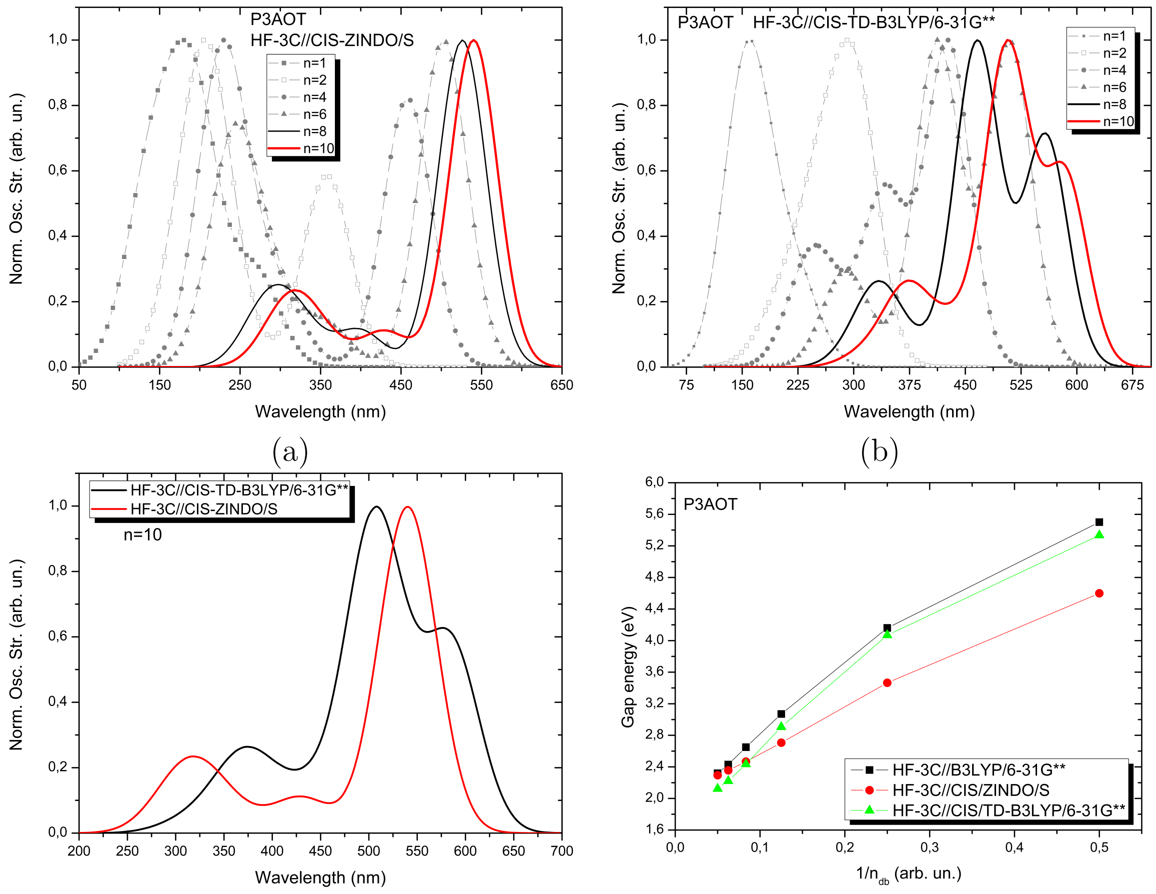

(a) (b)

(c) (d)

**Figure 7.6:** (a) Evolution of HF-3C//CIS-ZINDOS/S calculated UV-VIS absorption spectra of P3AOT with increasing chain length; (b) the same, calculated within HF-3C//TD-B3LYP/6-31G** level of theory; (c) comparison between the two approaches for $n = 10$; and (d) evolution of the electronic gap calculated by the HOMO-LUMO difference in the ground state (see Figure 7.5) and the optical gap calculated by the two different levels of theory for increasing chain length.

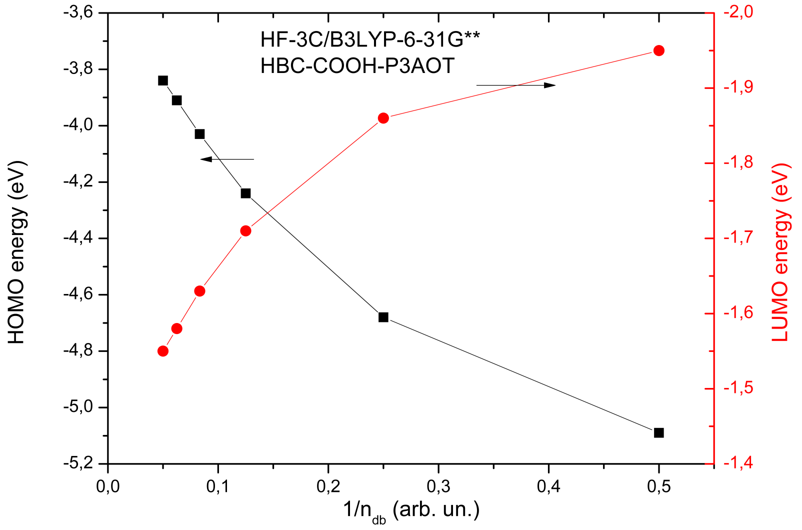

**Figure 7.7:** Evolution of the HOMO and LUMO energies of P3AOT with the increase of the chain length. $n_{db}$ stands for the number of double bonds in the chain.

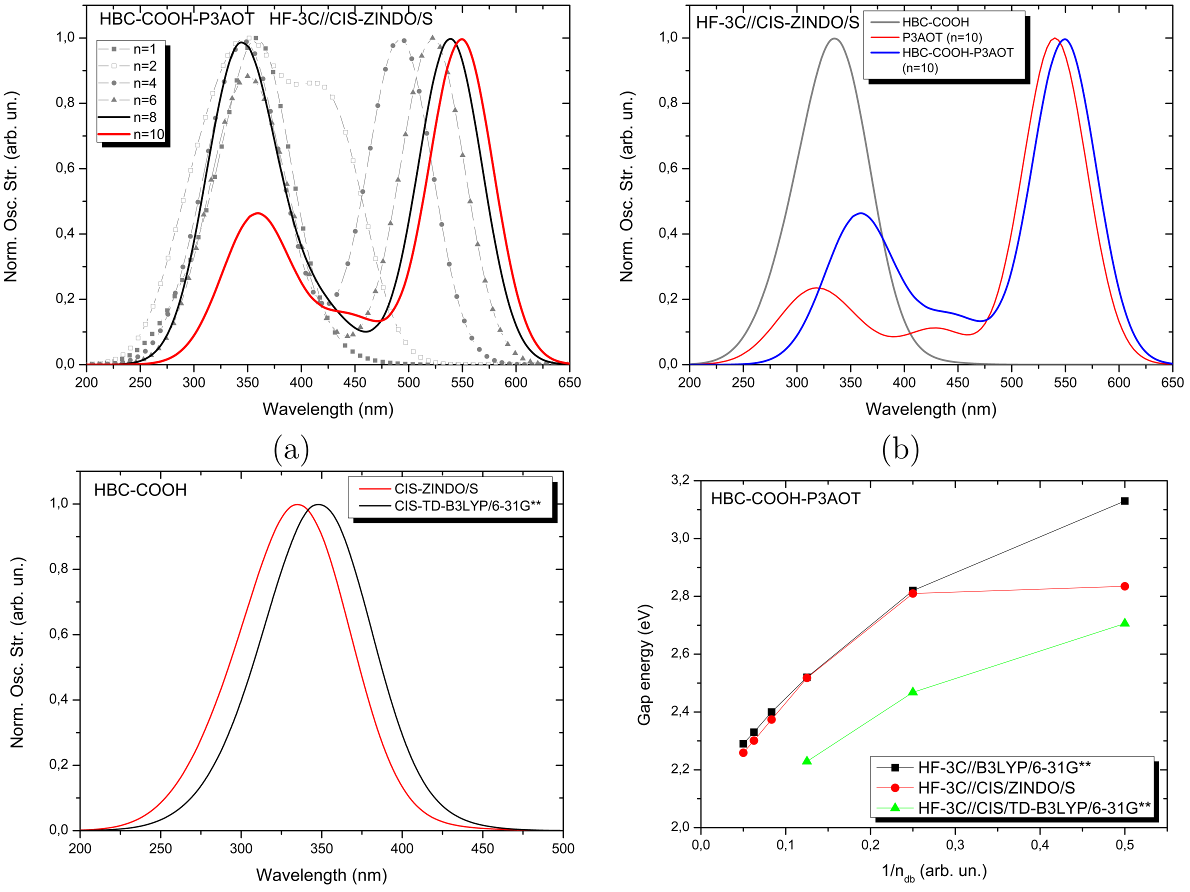

(a) (b)

(c) (d)

**Figure 7.8:** (a) Comparison between HF-3C//CIS-ZINDOS/S calculated UV-VIS absorption spectra with increasing chain length; (b) HF-3C//CIS-ZINDOS/S calculated UV-VIS absorption spectra for HBC-COOH, P3AOT ($n = 10$) and HBC-COOH-P3AOT ($n = 10$); (c) comparison between the two approaches for HBC-COOH; and (d) evolution of the electronic gap calculated by the HOMO-LUMO difference in the ground state (see (a)) and the optical gap calculated by the two different levels of theory for increasing chain length.

equally. In Figure 7.9 one can visualize the traces of these orbitals.

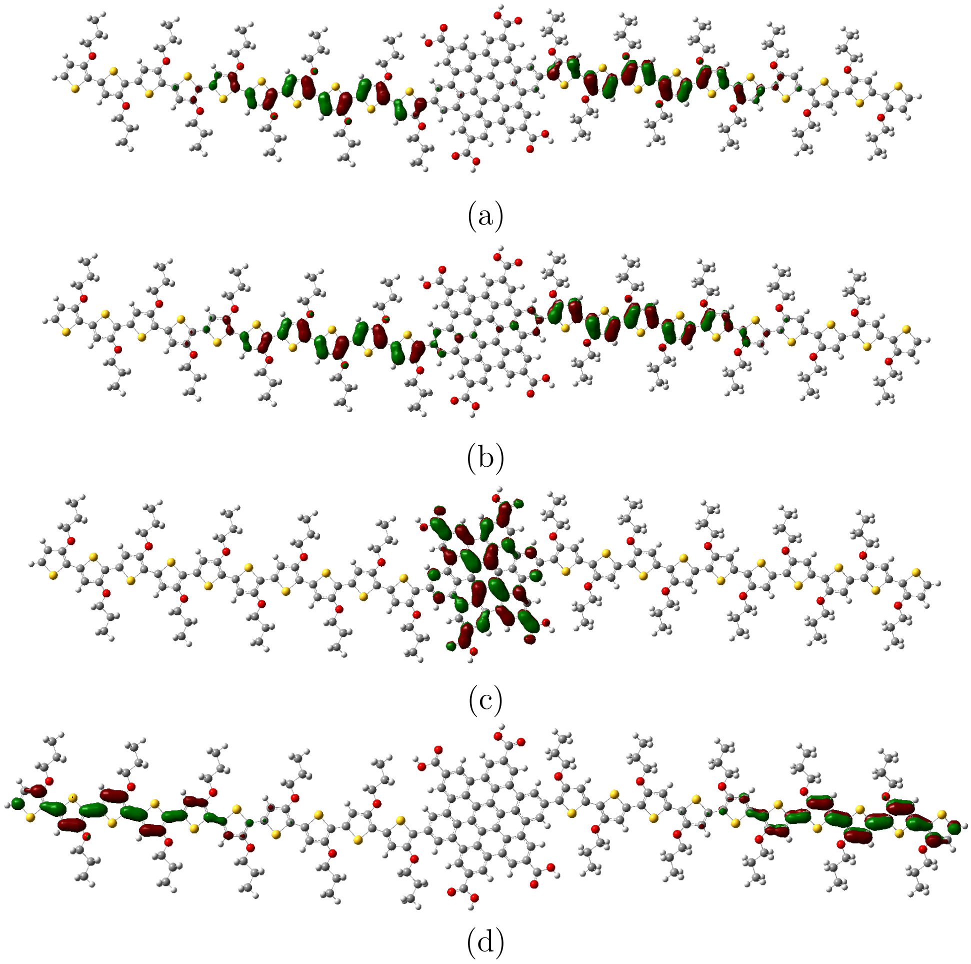

**Figure 7.9:** (a) $|HOMO - 1\rangle$, (b) $|HOMO\rangle$, (c) $|LUMO\rangle$, and (d) $|LUMO + 1\rangle$ molecular orbitals traces of the HBC-COOH-P3AOT ($n = 10$) molecule.

Clearly, there is a charge dissociation upon light excitation with a transition arising from the $|HOMO\rangle$ of the P3AOT chains towards the $|LUMO\rangle$ of the HBC-COOH conjugated core. But, there is also a transition between the same $|HOMO\rangle$ (actually $|HOMO - 1\rangle$) towards the $|LUMO\rangle$ (actually $|LUMO + 1\rangle$) of the P3AOT segment as well.

Although the interesting electronic properties of this compound, an increased morphological and photo-oxidation stability can arise from its planar structure and use of oxygen atoms on the alkyl chain (see Chapter 6) but also from the $\pi$-stacking of the HBC-COOH cores, and this can avoid the insertion of oxidants in-between planes. So that, the global stability can be pushed further, we propose in the next section the use of another conjugated oligomer attached to the HBC-COOH core so that the stability of this segment can also be improved, yielding globally stable materials.

## 7.3 HBC-ZP46 system

Recently, a copolymer based on alternating benzo[1,2-*b*;3,4-*b*]dithiophene and thieno[3,4-*c*]pyrrole-4,6-dione has been indicated as a material with remarkable resistance against photo-oxidation based on its molecular and supramolecular arrangement,[292] besides its optimized electronic properties and device yields.[212, 293, 294, 295] This material, also known as ZP46, is presented in Figure 7.10.

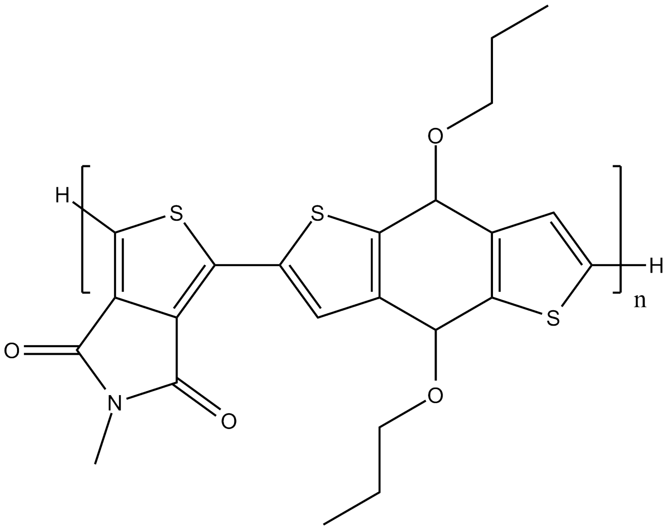

**Figure 7.10:** ZP46's molecular structure.

The supramolecular structure of this material is determined by the non-bonding hydrogen and sulfur interactions within the two comonomers, being able to lock the chain in a planar configuration[288] and can induce a mimetic discotic liquid crystal characteristic with adjacent chains based on the same interactions.

The ground state geometries of oligomers of this material were fully optimized within the HF-3C method followed by B3LYP/6-31G** single points whenever possible (each monomer increases considerably the quantity of atoms being treated).

In Figure 7.11, one can find the evolution of the HOMO and LUMO energies for an increasing chain length.

Apparently, the convergence of the energies is almost reached for $n$ =4 or 5. The same can be noted for their calculated electronic transitions, presented in Figure 7.12.

In this way, the molecules having these chains grafted to HBC core were also fully optimized and the evolution of the HOMO and LUMO energies are presented in Figure 7.13.

Although the energy of the absorption maximum is kept almost unchanged going from $n = 3$ to $n = 5$, the "camel back" characteristic is continuously lost, what is seen by the decreasing ratio between the two main bands. One should also note that, because of the increased localization of the orbitals in the Hartree-Fock treatment in ZINDO/S

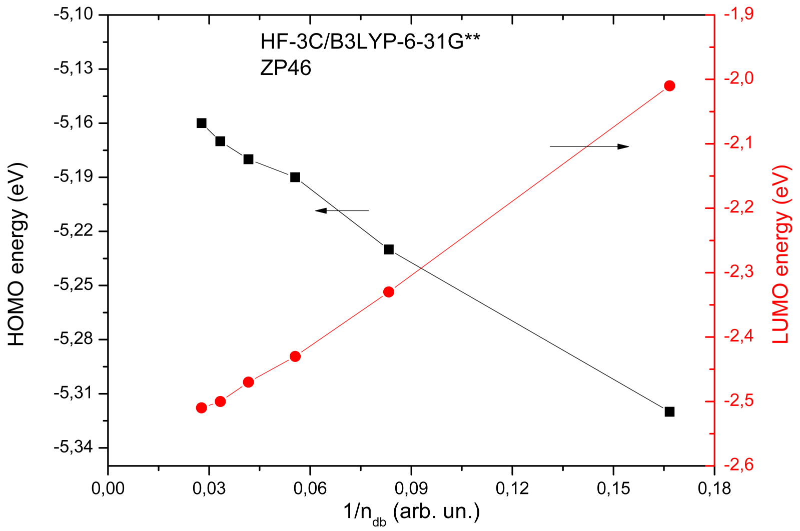

**Figure 7.11:** Evolution of the HOMO and LUMO energies with the increase of the chain length for ZP46. $n_{db}$ stands for the number of double bonds in the chain.

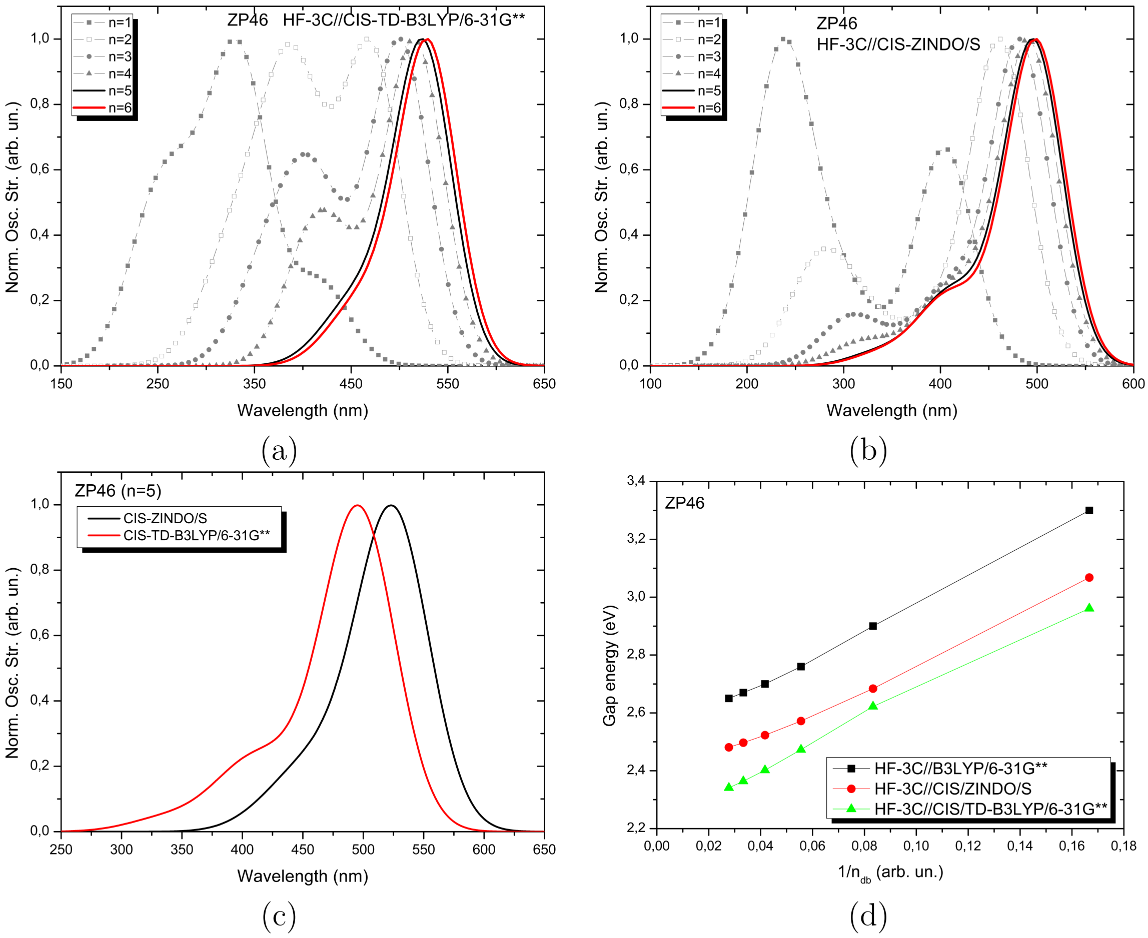

(a)

(b)

(c)

(d)

**Figure 7.12:** (a) Evolution of HF-3C//CIS-ZINDOS/S calculated UV-VIS absorption spectra with increasing chain length; (b) the same, calculated within HF-3C//TD-B3LYP/6-31G** level of theory; (c) comparison between the two approaches for $n = 10$; and (d) evolution of the electronic gap calculated by the HOMO-LUMO difference in the ground state (see Figure 7.11) and the optical gap calculated by the two different levels of theory for increasing chain length.

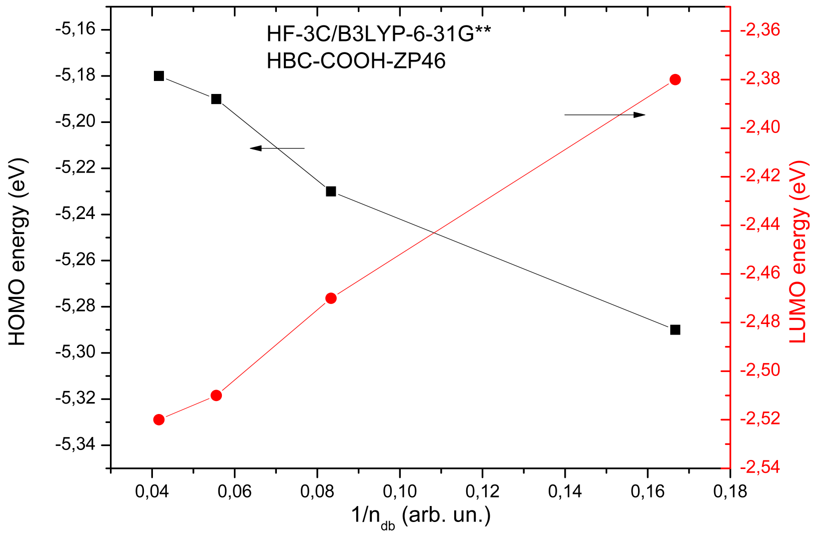

**Figure 7.13:** Evolution of the HOMO and LUMO energies with the increase of the chain length for HBC-COOH-ZP46. $n_{db}$ stands for the number of double bonds in the chain.

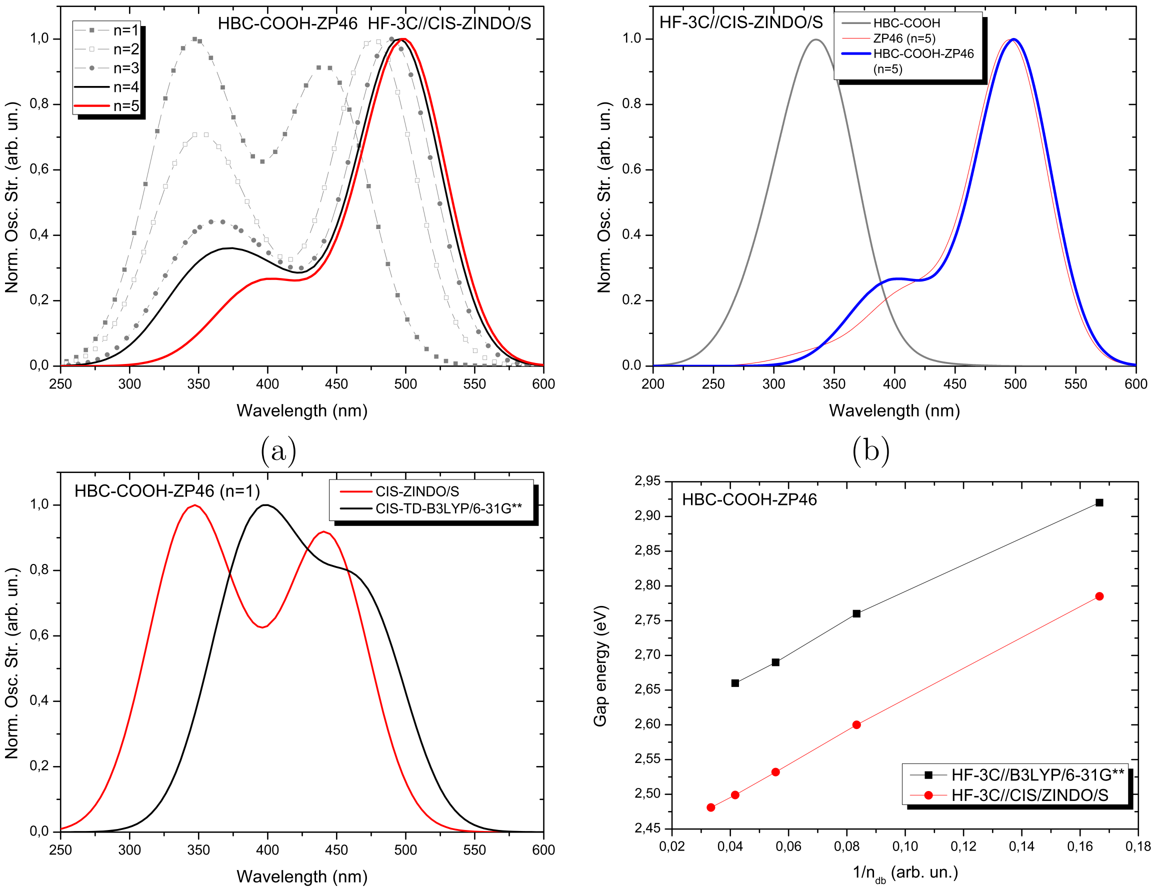

(a) (b)

(c) (d)

**Figure 7.14:** (a) Evolution of HF-3C//CIS-ZINDOS/S calculated UV-VIS absorption spectra with increasing chain length; (b) the same, calculated within HF-3C//TD-B3LYP/6-31G** level of theory; (c) comparison between the two approaches for $n = 1$; and (d) evolution of the electronic gap calculated by the HOMO-LUMO difference in the ground state (see Figure 7.13) and the optical gap calculated by the semi-empirical approach for increasing chain length.

method, this feature of the absorption spectra is late compared to the TD-B3LYP/6-31G** prevision. In the limit of the infinite molecule, the optical gap would be $\sim$ 2,3 eV, considering only the error induced by ZINDO/S energies compared to TD-B3LYP/6-31G** ones.

Similarly to the previous case, the low-lying electronic transitions are composed of several individual ones and the most important contributions ($\sim$ 21% each) come from $|HOMO\rangle \rightarrow |LUMO\rangle$ and $|HOMO{-}1\rangle \rightarrow |LUMO{+}1\rangle$ and the corresponding molecular orbitals traces are presented in Figure 7.15.

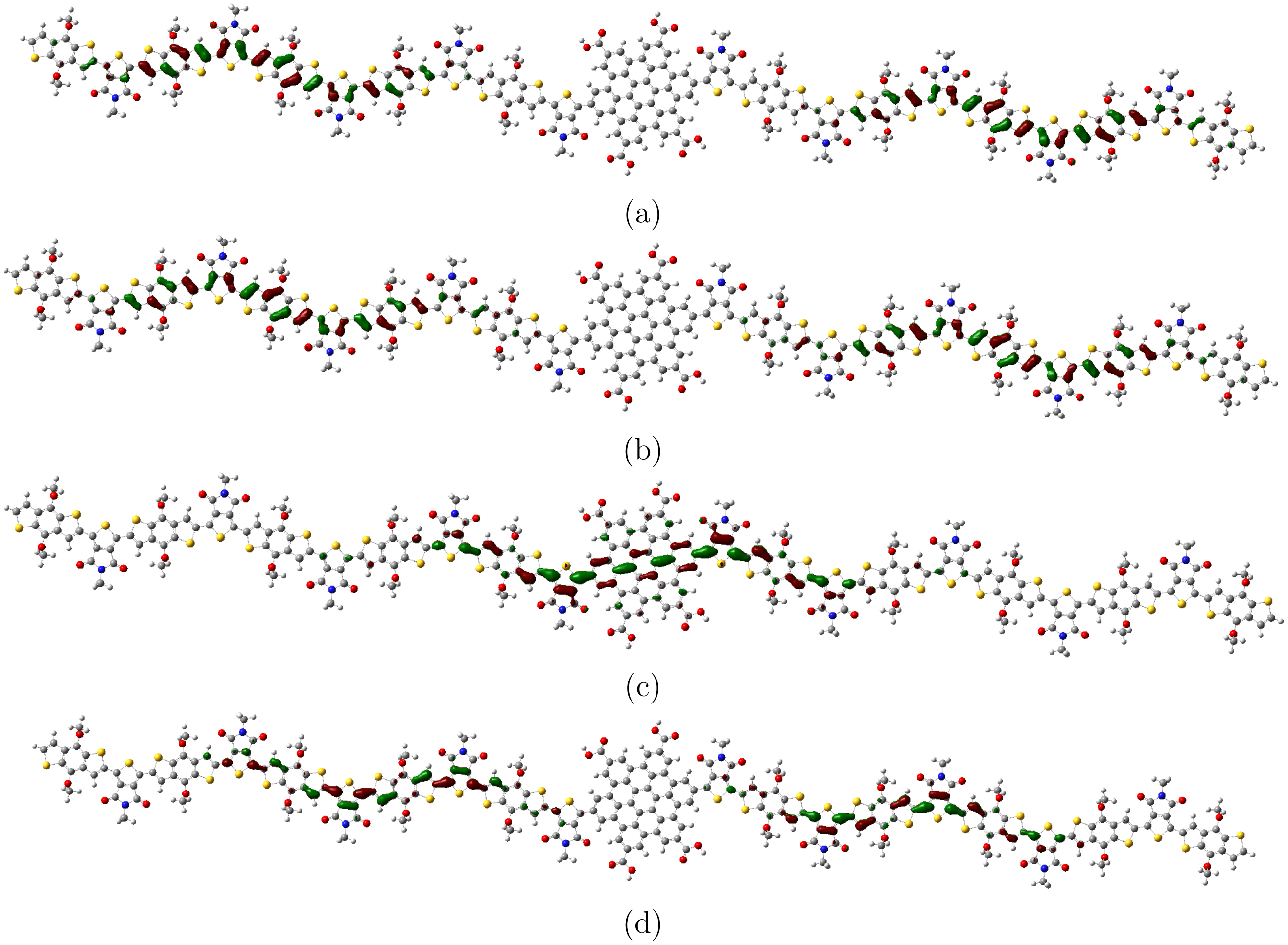
(a)

(b)

(c)

(d)

**Figure 7.15:** (a) $|HOMO-1\rangle$, (b) $|HOMO\rangle$, (c) $|LUMO\rangle$, and (d) $|LUMO+1\rangle$ molecular orbitals traces of the HBC-COOH-ZP46 ($n = 5$) molecule.

Visibly, the charge separation upon light excitation is not spatially as efficient as it can be for the HBC-COOH-P3AOT case, as it can be seen in Figure 7.15.(c): the $|LUMO\rangle$ orbital is not localized only on the HBC-COOH conjugated core and delocalizes over the ZP46 segment itself, being able to hinder the charge dissociation and transfer in the $\pi$-stacking direction. This may be due to the acceptor properties of the comonomer that is directly linked to the HBC-COOH core, which may compete during the delocalization of the electronic cloud of the LUMO level (poor electron character in the ground state).

However, grafting the ZP46 chain in the other sense, *i.e.*, linking directly the donor moiety first is not desirable because of the lack of non-bond interactions between the segment and the HBC-COOH core by hydrogen bonding. In this way, the planar arrangement between these two molecules would be lost.

A way of contouring this would be the insertion of a bridge atom between HBC-COOH core and the conjugated polymer segment in a way of isolating the electronic densities of the two species. Using an adaptation of the knowledge gained in Chapter 6, this could be a simple oxygen atom and this possibility will be investigated in the future. Besides this possibility, using another functional group in the place of $-COOH$ would make the conjugated core more electron deficient, increasing the electronic density of the LUMO orbital.

## 7.4 Final Remarks

A series of two new hybrid donor-acceptor materials has been proposed based on a recent work by Bégué *et al.* This work consists on the use of tetra-COOH-functionalized Hexabenzocoronenes to which a conjugated polymer segment has been attached directly on the conjugated core. This arrangement would induce a supramolecular arrangement in columns following a discotic liquid crystal feature, favoring the charge dissociation and transfer in the $\pi$-stacking direction.

Two different molecules have been proposed to be used as grafting agents on the HBC molecule: P3AOT and ZP46, from which one can preliminarily state:

- Although the convergence of the electronic properties is reached for $n \sim 8$ segments of P3AOT and $n \sim 4$ of ZP46, the charge dissociation feature calculated by the absorption spectra is dependent on the number of molecules of the chain.
- Planar structures can be proposed making use of non-bonding interactions within the conjugated chain and in-between the chain and the HBC core. The use of planar structure is crucial for the supramolecular $\pi$-stacking.
- The use of P3AOT, although electronically efficient, may induce a fragility on the photo-oxidation robustness of the chain. Because of this, the ZP46 fragment has been proposed based on its recent remarkable results under photo-degradation conditions.
- When grafted to the HBC core, this molecule remains planar and is capable of locking the planarity in-between the chain and the core.
- The electronic transitions calculations show that the low-lying states are consisted of transitions that do not represent an efficient spatial charge-dissociation and this may hinder the application of this material in devices.

Finally, this chapter was proposed as a logical sequence after what has been discussed about the need of developing efficient and stable $n-$type materials for OPVs. It takes into account the difficulties of synthesizing well-controlled fullerene-derivative structures that may be thermally and photo stable and with supramolecular architectures that favor the electron transport and diffusion. It also takes into account the dependence of oxygen molecule affinities with flat molecules and the use of oxygen atoms in lateral chains, protecting the labile protons during the photo-oxidation process. Last, but not least, it takes into account the need of developing ”ideal” interdigitated-like structures (*c.f* Chapter 1) for ideal light absorption, charge dissociation and migration towards the electrodes in devices.

# Conclusions

This thesis has addressed the design, synthesis and molecular modeling of polyfullerenes to be applied in Organic Photovoltaic Devices as electron acceptor materials or morphology stabilizer agents.

The use of fullerene as electron acceptors is based on the fact that they can easily accept up to 6 electrons, making of it one of the strongest organic $n$-type materials known. This is due to the fact that fullerene is, at the ground state, non-aromatic, and to be so, based on the three-dimensional generalization of the Hückel's rule, it would need $2(N+1)^2$ $\pi$-electrons, where $N$ is the number of atoms in the conjugated network. To this, one can add the following remarkable properties of fullerenes:

1. high electron mobility;
2. delocalized LUMO over the whole molecule surface, allowing the 3D electron transfer and transport;
3. LUMO energy level compared to the $p$-type material, allowing an efficient electron transfer;
4. reversible electrochemical reduction that allows the formation of stable reduced charged species;
5. formation of domains from solution deposition, allowing charge separation when an appropriate length-scale is obtained.

Even with all this, fullerene $C_{60}$ presents non-optimal morphological properties, suffering from phase segregation under even mild thermal stress. This is due to the very different surface energies between fullerenes and the $p$-type polymers, hindering the photovoltaic properties of this composite.

The functionalization of fullerenes with lateral chains and indene groups, as explored in Chapter 2, has been used in literature to circumvent this problem but a final success is still to be presented.

The use of fullerene polymers appeared as a way to have, at the same time, the excellent electronic properties of fullerenes and the mechanical properties of polymers.

In this way, the composites so-made with $p-$type materials do not phase segregate since the ”like likes like” character of the system has been improved. Chapter 2 also proposed six different routes to achieve polymers and their electronic properties and position of bis-adduct formation was studied by means of molecular modeling techniques.

Considering the interest in ATRAP route, their easiness to yield polymeric materials and the fact that the fullerene keeps $58\pi$ electrons, as it is the case of the benchmark $PC_{60}BM$, motivated us to explore it during the synthetic work. This was done so during Chapter 3 and a series of polymers with varying lateral chains were synthesized so that their solubility and miscibility within the $p-$type matrix could be tuned as needed.

Chapter 4 presented the application of these materials in OPV devices following three possible ways of employing them: as the sole electron acceptor, as an interfacial layer between the active matrix and the hole extraction layer based on an inorganic oxide and as an additive to the active matrix. The latter was retained as the work pathway since loads of up to 10% of ATRAP-based polyfullerene do not induce hazardous photovoltaic properties loss in the devices.

Annealing of these devices showed that the use of these polymers did not improve the stability of the active layers against thermal stress when compared to the control cells. Then, the degradation pathways to which the polyfullerenes can be submitted to were studied by several physical-chemical characterization techniques in Chapter 5.

These experiments have identified that thermal and light-only stresses are able to induce morphological changes on the polyfullerene bulk that are compatible with a depolymerization process. Studying this further process, one could indicate that this depolymerization arises from the low energy required to homolytically cleave the monomer-fullerene bond. One could also state that the chemical route used to achieve these materials is consisted of a dynamic equilibrium that, under reaction conditions, points towards the formation of the polymer, however after isolated, temperature and light-only treatments favor the equilibrium to opposite sense, towards the starting materials, as it has been suggested already by literature.

Chapter 6 then explores other possible stabilization pathways, treating the incorporation of oxygen as bridge atoms in alkyl chains of conjugated polymers to decrease the lability of the alpha hydrogens; the determination optimal zinc oxide ligands to be polymerized and used as interfacial layers; and the relation between the affinities with oxidants of carbon allotrope molecules based on their dimensionality and on the curvature parameter.

Finally, taking into account all the knowledge acquired throughout the thesis, new hybrid $p-n$ materials have been proposed based on the discotic liquid crystal properties of hexabenzocoronenes. These conjugated electron-deficient cores have their electronic properties determined by molecular modeling techniques when grafted with two different conjugated polymer segments, namely poly(3-alkoxy-thiophene) and a copolymer based on alternating benzo[1,2-*b*;3,4-*b*]dithiophene and thieno[3,4-*c*]pyrrole-4,6-dione, named ZP46. The former showed interesting robustness against photo-oxidation based on its supramolecular arrangement that avoids the inclusion of oxidants in-between the chains. Ideally, the association of both materials (HBC: planar, discotic liquid crystal, non-polymeric, well-defined electronic properties, etc.; and ZP46: robust against photo-oxidation, low band-gap material, soluble, supramolecular arrangement, etc.) would lead to efficient and stable OPV devices. However, in the first tests, the charge dissociation in the excited state is not optimal and future work is going to be performed in order to optimize this at the same time as assuring the supramolecular architecture.

# Appendices

# Appendix A

# Synthetic Routes

Here can be found the synthetic routes and procedures used to obtain the comonomers used in Chapter 3.

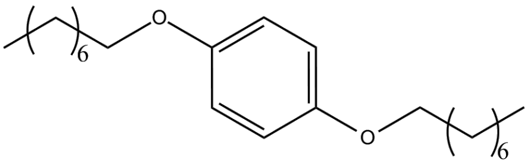

**1,4-bis(octyloxy)benzene (1)**: Hydroquinone (90.8 mmol, 10.0 g) and $K_2CO_3$ (272.0 mmol, 37.7 g) were added to acetone (200 mL) in a single-necked flask and heated to reflux. After some minutes, the suspension became dark yellow, at which point *n*-octylbromide (272.0 mmol, 52.6 g) was added in one shot. It was then refluxed for 48 h under air. The mother liquor was poured onto cold water to quench the reaction, and the product recovered by filtration. Repeated solubilization in the minimum of hot chloroform and precipitation in cold methanol purified the product. After drying under reduced pressure, a beige solid was recovered with a yield of 75%. $^1$H NMR (400 MHz, $CDCl_3$) $\delta$ 6.82 (s, 4H), 3.90 (t, $J$= 6.6 Hz, 4H), 1.80 - 1.71 (m, 4H), 1.43 (dd, $J$= 15.0, 7.0 Hz, 4H), 1.39 - 1.22 (m, 16H), 0.89 (t, $J$= 6.9 Hz, 6H). $^{13}$C NMR (101 MHz, $CDCl_3$) $\delta$ 153.36 (s), 115.55 (s), 68.83 (s), 31.97 (s), 29.66 - 29.30 (m), 26.22 (s), 22.81 (s), 14.24 (s).

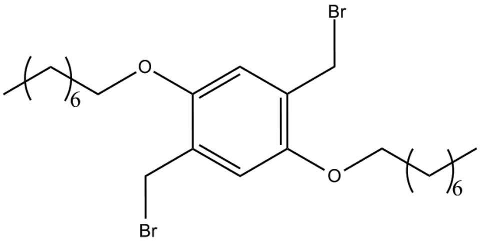

**1,4-bis(bromomethyl)-2,5-bis(octyloxy) benzene (2)**: **1** (15.0 mmol, 5.0 g) and paraformaldehyde (31.0 mmol, 0.9 g) were added to acetic acid (100 mL) in a single-necked flask and heated to 60 °C. After dissolution, HBr (33 % - 5 mL) in acetic acid is added in one shot. It was then sealed and left to react for 2 h. The mother liquor was poured onto cold water to quench the reaction, and the product recovered by filtration. Repeated solubilization in the minimum of hot chloroform and precipitation in cold methanol purified the product.

The product was left to rest overnight in methanol to remove residual HBr and then it was recovered by filtration. After drying under reduced pressure, a white fluffy product was recovered with a yield of 42%. $^1$H NMR (400 MHz, $CDCl_3$) $\delta$ 6.85 (s, 2H), 4.52 (s, 2H), 3.98 (t, $J$= 6.4 Hz, 4H), 1.86 - 1.75 (m, 4H), 1.60 - 1.20 (m, 20H), 0.89 (t, $J$= 6.7 Hz, 6H). $^{13}$C NMR (101 MHz, $CDCl_3$) $\delta$ 150.82 (s), 127.67 (s), 114.81 (s), 69.18 (s), 31.98 (s), 29.45 (d, $J$= 8.3 Hz), 29.45 (d, $J$= 8.3 Hz), 28.90 (s), 26.24 (s), 22.82 (s), 14.27 (s).

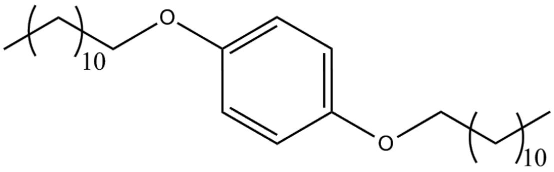

**1,4-bis(dodecyloxy)benzene (3)**: Hydroquinone (27.2 mmol, 3.0 g) and $K_2CO_3$ (82.4 mmol, 11.4 g) were added to acetone (120 mL) in a single-necked flask and heated to reflux. After some minutes, the suspension became dark yellow, at which point $n$-dodecylbromide (68.1 mmol, 17.0 g) was added in one shot. It was then refluxed for 48 h under air. The mother liquor was poured onto cold water to quench the reaction, and the product recovered by filtration. Repeated solubilization in the minimum of hot chloroform and precipitation in cold methanol purified the product. After drying under reduced pressure, a beige solid was recovered with a yield of 60%. $^1$H NMR (400 MHz, $CDCl_3$) $\delta$ 6.82 (s, 4H), 3.90 (t, $J$= 6.6 Hz, 4H), 1.80 - 1.70 (m, 4H), 1.52 - 1.01 (m, 36H), 0.88 (t, $J$= 6.7 Hz, 6H). $^{13}$C NMR (101 MHz, $CDCl_3$) $\delta$ 153.35 (s), 115.54 (s), 68.82 (s), 32.07 (s), 29.96 - 29.36 (m), 26.22 (s), 22.84 (s), 14.27 (s).

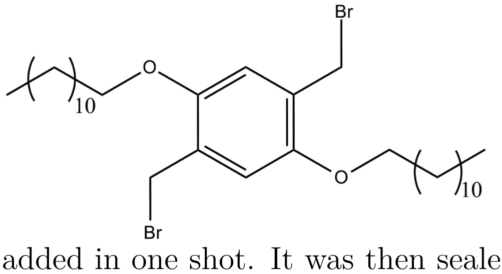

**1,4-bis(bromomethyl)-2,5-bis(dodecyloxy) benzene (4)**: **3** (11.2 mmol, 5.0 g) and paraformaldehyde (67.2 mmol, 2.0 g) were added to a acetic acid / $CH_2Br_2$ (1:1) mixture (80 mL) in a single-necked flask and heated to 70 °C. After dissolution, HBr (33 % - 8 mL) in acetic acid was added in one shot. It was then sealed and left to react for 48 h. The mother liquor was poured onto cold methanol to quench the reaction, and the product recovered by filtration. Repeated solubilization in the minimum of hot chloroform and precipitation in cold methanol purified the product. The product was left to rest overnight in methanol to remove residual HBr and then it was recovered by filtration. After drying under reduced pressure, a white powder was recovered with a yield of 75%. $^1$H NMR (400 MHz, $CDCl_3$) $\delta$ 6.85 (s, 2H), 4.52 (s, 4H), 3.98 (t, $J$= 6.4 Hz, 4H), 1.85 - 1.76 (m, 8H), 1.41 - 1.21 (m, 32H), 0.88 (t, $J$= 6.8 Hz, 6H). $^{13}$C NMR (101 MHz, $CDCl_3$) $\delta$ 150.82 (s), 127.68 (s), 114.81 (s), 69.18 (s), 32.08 (s), 29.93 - 29.65 (m), 29.50 (d, $J$= 2.1 Hz), 28.90 (s), 26.23 (s), 22.85 (s), 14.27 (s).

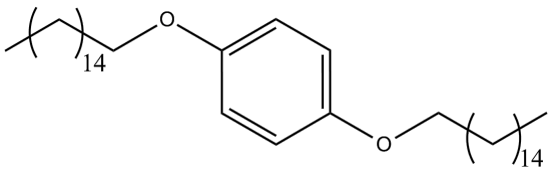

**1,4-bis(hexadecaloxy)benzene (5)**: Hydroquinone (45.5 mmol, 5.0 g) and $K_2CO_3$ (137.0 mmol, 19.0 g) were added to acetonitrile (200 mL) in a single-necked flask and heated to reflux. After some minutes, the suspension became dark yellow, at which point *n*-hexadecylbromide (137.0 mmol, 41.8 g) was added in one shot. It was then refluxed for 48 h under air. The mother liquor was poured onto cold water to quench the reaction, and the product recovered by filtration. Repeated solubilization in the minimum of hot chloroform and precipitation in cold methanol purified the product. After drying under reduced pressure, a beige solid was recovered with a yield of 67%. $^1$H NMR (400 MHz, $CDCl_3$) $\delta$ 6.82 (s, 4H), 3.89 (t, $J$= 6.6 Hz, 4H), 1.80 - 1.69 (m, 2H), 1.49 - 1.18 (m, 54H), 0.88 (t, $J$= 6.8 Hz, 6H). $^{13}$C NMR (101 MHz, $CDCl_3$) $\delta$ 153.35 (s), 115.55 (s), 68.84 (s), 32.09 (s), 30.09 - 29.42 (m), 26.22 (s), 22.85 (s), 14.28 (s).

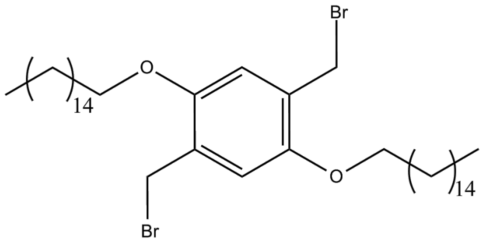

**1,4-bis(bromomethyl)-2,5-bis(hexadecaloxy)benzene (6)**: **5** (2.0 mmol, 1.1 g) and paraformaldehyde (11.8 mmol, 0.4 g) were added to $CH_2Br_2$ (50 mL) in a single-necked flask and heated to 80 °C. After dissolution, HBr (33 % - 5 mL) in acetic acid was added in one shot. It was then sealed and left to react for 48 h. The mother liquor was poured onto cold methanol to quench the reaction, and the product recovered by filtration. Repeated solubilization in the minimum of hot chloroform and precipitation in cold methanol purified the product. The product was left to rest overnight in methanol to remove residual HBr and then it was recovered by filtration. After drying under reduced pressure, a white powder was recovered with a yield of 54%. $^1$H NMR (400 MHz, $CDCl_3$) $\delta$ 6.85 (s, 2H), 4.52 (s, 4H), 3.98 (t, $J$= 6.4 Hz, 4H), 1.91 - 1.70 (m, 4H), 1.63 - 1.43 (m, 6H), 1.40 - 1.20 (m, 46H), 0.88 (t, $J$= 6.8 Hz, 6H). $^{13}$C NMR (101 MHz, $CDCl_3$) $\delta$ 150.83 (s), 127.69 (s), 114.83 (s), 69.19 (s), 32.09 (s), 29.86 (s), 29.76 (s), 29.51 (d, $J$= 2.6 Hz), 28.91 (s), 26.24 (s), 22.85 (s), 14.28 (s).

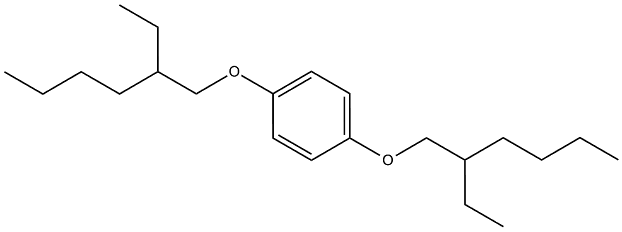

**1,4-bis[(2-ethyl)-hexyloxy]benzene (7)**: Hydroquinone (30.9 mmol, 3.4 g) and KOH (71.0 mmol, 4.0 g) were added to DMSO (50 mL) in a single-necked flask and heated to 90 °C. After some minutes, the suspension became dark yellow, at which point (2-ehtyl)hexylbromide (71.0 mmol, 13.7 g) was added in one shot. It was left to react for 48 h under air. The mother liquor was poured onto cold methanol to quench the reaction, and the product recovered by filtration. Repeated solubilization in the minimum of hot chloroform and precipitation in cold methanol purified the product. After drying under reduced pressure, a beige solid was recovered with a yield of 77%. $^1$H NMR (400 MHz, $CDCl_3$) $\delta$ 6.86 (s, 4H), 3.91 - 3.84 (m, 4H), 1.75 (dt, $J$= 12.0, 6.0 Hz, 2H), 1.62 - 1.40 (m, 8H), 1.34 (dd, $J$= 7.3, 3.5 Hz, 8H), 1.02 - 0.82 (m, 12H). $^{13}$C NMR (101 MHz, $CDCl_3$) $\delta$ 153.56 (s), 115.48 (s), 71.30 (s), 39.59 (s), 30.66 (s), 29.21 (s), 23.98 (s), 23.18 (s), 14.18 (s), 11.19 (s).

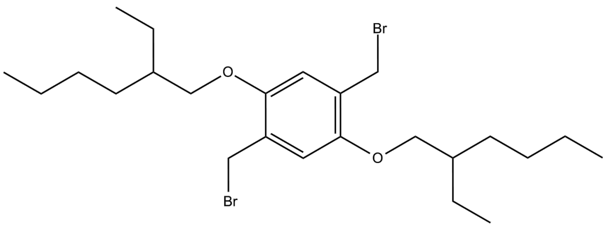

**1,4-bis(bromomethyl)-2,5-bis[(2-ethyl)-hexyloxy]benzene (8)**: **7** (4.5 mmol, 1.5 g) and paraformaldehyde (27.0 mmol, 0.8 g) were added to acetic acid (50 mL) in a single-necked flask and heated to 70 °C. After dissolution, HBr (33 % - 4 mL) in acetic acid was added in one shot. It was then sealed and left to react for 8 h. The mother liquor was poured onto cold methanol to quench the reaction, and the product recovered by filtration. Repeated solubilization in the minimum of hot chloroform and precipitation in cold methanol purified the product. The product was left to rest overnight in methanol to remove residual HBr and then it was recovered by filtration. After drying under reduced pressure, a white solid was recovered with a yield of 60%. $^1$H NMR (400 MHz, $CDCl_3$) $\delta$ 6.85 (s, 2H), 4.52 (s, 4H), 3.91 - 3.84 (m, 4H), 1.75 (dt, $J$= 12.0, 6.0 Hz, 2H), 1.62 - 1.40 (m, 8H), 1.34 (dd, $J$= 7.3, 3.5 Hz, 8H), 1.02 - 0.82 (m, 12H). $^{13}$C NMR (101 MHz, $CDCl_3$) $\delta$ 150.87 (s), 127.54 (s), 114.39 (s), 71.09 (s), 39.76 (s), 30.79 (s), 29.27 (s), 28.90 (s), 24.18 (s), 23.21 (s), 14.25 (s), 11.40 (s).

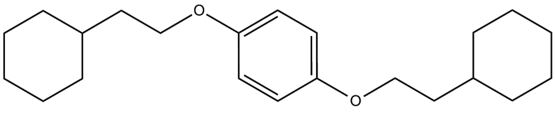

**1,4-bis[(cyclohexane)-ethyloxy] benzene (9)**: Hydroquinone (12.2 mmol, 1.4 g) and $K_2CO_3$ (36.6 mmol, 5.0 g) were added to acetone (75 mL) in a single-necked flask and heated to reflux. After some minutes, the suspension became dark yellow, at which point (cyclohexane)ethylbromide (25.6 mmol, 5.0 g) was added in one shot. It was then refluxed for 48 h under air. The mother liquor was poured onto cold water to quench the reaction, and the product recovered by filtration. Repeated solubilization in the minimum of hot chloroform and precipitation in cold methanol purified the product. After drying under reduced pressure, a beige solid was recovered with a yield of 40%. $^1$H NMR (400 MHz, $CDCl_3$) $\delta$ 6.82 (s, 4H), 3.94 (t, $J$= 6.7 Hz, 4H), 1.81 - 1.41 (m, 26H). 13C NMR (101 MHz, $CDCl_3$) $\delta$ 153.34 (s), 115.53 (s), 66.75 (s), 36.93 (s), 34.70 (s), 33.48 (s), 26.71 (s), 26.42 (s).

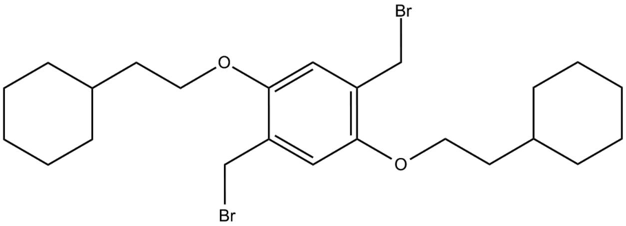

**1,4-bis(bromomethyl)-2,5-bis[(cyclohexane)-ethyloxy]benzene (10)**: **9** (4.5 mmol, 1.5 g) and paraformaldehyde (27.0 mmol, 0.8 g) were added to a acetic acid / $CH_2Br_2$ (1:1) mixture (80 mL) in a single-necked flask and heated to 70 °C. After dissolution, HBr (33 % - 4 mL) in acetic acid was added in one shot. It was then sealed and left to react for 8 h. The mother liquor was poured onto cold methanol to quench the reaction, and the product recovered by filtration. Repeated solubilization in the minimum of hot chloroform and precipitation in cold methanol purified the product. The product was left to rest overnight in methanol to remove residual HBr and then it was recovered by filtration. After drying under reduced pressure, a white solid was recovered with a yield of 50%. $^1$H NMR (400 MHz, $CDCl_3$) $\delta$ 6.91 (s, 2H), 4.49 (s, 4H), 3.98 (t, $J$= 6.6 Hz, 4H), 1.81 - 1.41 (m, 26H). $^{13}$C NMR (101 MHz, $CDCl_3$) $\delta$ 150.57 (s), 126.71 (s), 112.48 (s), 67.08 (s), 58.52 (s), 36.97 (s), 34.87 (s), 33.47 (s), 26.70 (s), 26.45 (s).

# Appendix B

# Experimental Conditions

In this appendix, the experimental protocols, conditions and equipment used for experiments are listed.

### UV-VIS spectroscopy

UV-VIS spectra were recorded in transmission mode using a homemade set up containing an optic fiber spectrometer from Ocean Optics (Maya2000 Pro). An UV-VIS-NIR Deuterium-Halogen DH-2000-BAL (Mikropack) light source was used as excitation.

### FTIR spectroscopy

FTIR spectra were recorded using a standard Bruker Vertex 70v spectrometer in transmission mode with a resolution of 1 $\mathrm{cm}^{-1}$. The sample was placed and measured in vacuum with pressure of 1 mbar.

### XPS spectroscopy

XPS measurements were performed using a multi-chamber UHV-system (base pressure $10^{-10}$ mbar) equipped with a Phoibos 150 cylindrical hemispherical analyzer (SPECS). The employed excitation X-rays have a monochromatic energy of 1486.7 eV, from an Al K$\alpha$ source.

### Atomic Force Microscopy

AFM measurements were performed using a Multi Mode$^{\mathrm{TM}}$ Scanning Probe Microscope (MM-SPM) by Digital Instrument in tapping mode. Images were recorded using NanoScope software.

### Nuclear Magnetic Ressonance

NMR measurements were performed in a Bruker 400 UltraShield$^{TM}$ equipment using 400 MHz as excitation for $^1H$ signals and 100 MHz for $^{13}C$.

### Thermogravimetric Analysis

TGA measurements were performed in a TA Instruments DSC Q100 piece of equipment.

### Differential Scanning Calorimetry

DSC measurements were performed in a TA Instruments TGA Q50 piece of equipment.

### Size-exlusion Chromatography in THF

SEC-THF measurements were performed in a Viscotek set equipped with a VE 5200 GPC auto-sampler and a VE 3580 RI detector. The elution was performed at 1 mL/min rate with 30 °C HPLC grade tetrahydrofuran (VWR) through a Viscotek styrene-divinyl benzene (300x8.0 mm) SEC column.

### Size-exlusion Chromatography in CB

SEC-CB measurements were performed in a Agilent Technologies 1260 Infinity equipment eluted at 1 mL/min with 50 °C HPLC grade chlorobenzene (Aldrich) through a PLgel 10 micrometer Mixed-B (300x7.5 mm) SEC column.

### Solvents

All solvents were acquired and used as received from VWR International. Toluene was distilled in a column using metallic Sodium as water trap. *o*-xylene was acquired from Merck.

### Chemicals

All chemicals were acquired and used without further purification from Aldrich International. $C_{60}$ was cleaned by Soxhlet extraction in THF overnight, dried under vacuum and stored in a $N_2$-filled glove-box.

# Appendix C

# Molecular Modeling based on DFT calculations and the RIJCOSX approximation

In this appendix, the basics of the theory behind *ab initio* molecular modeling is presented, focusing on the development of Density Functional Theory (DFT). The approximation RIJCOSX is also briefly described as it was used throughout this thesis. The description made here is qualitatively and does not claim to be complete.

## C.1 Description of electronic structure of molecules

When one wants to determine electronic properties of atoms and molecules by the point of view of molecular modeling, one has to remember that in the "quantum world" the Schrödinger Equation is the master equation that describes the behavior of all the bodies in submicroscopic scale. Based on the De Broglie's observations on the wave-particle behavior of the matter, the Schrödinger equation is based on the fact that all bodies behave as waves with a certain wavelength.

This equation has some special characteristics:

1. it is best solved as an algebraic partial differential equation, not as an analytical one;
2. it is an equation of eigenvalues, as the ones in algebraic mathematics and, for this, it needs linear operators and functions that describes vector in an algebraic space;
3. it needs the function to give the same function back, *i.e.*, it needs a "guess" function to find this same function itself after a cycle of calculation.

The item number 3 states the basis of what is called the *self-consistent field*. The guess function is used to solve Schrödinger Equation, yielding eigenvalues and a function in a “better shape”.

In a realistic world, solving this equation is not possible for a system with more than two electrons. It is in this point that “quantum chemistry” started to be developed more strongly with the introduction of approximations that allow one to solve the electronic structure of multi-electronic atoms and molecules. These approximations can be divided into physical-mathematical approximations and physical approximations. The first physical approximation is the Born-Oppenheimer, that states that as the nuclei of the atoms are much heavier than the electrons, they are much slower, so, they can be considered as statistic while the electrons move. This results in the decoupling of partial equations that would have needed to be calculated on both spatial coordinates (nuclei and electrons) before, and now, with such approximation, they need to be calculated only on the nuclei coordinates OR on the electron coordinates.

By the third decade of XXth century, novel approaches have been proposed to determine the electronic structure of molecular systems and solids. The first one was proposed by D. R. Hartree and Vladimir A. Fock. The so-called **Hartree-Fock** method consists in treating the electrons and their wave-function as a determinant called Slater’s determinant. This mathematics allowed the calculation to take place considering that the multi-electronic problem could be resolved as “multi” problems of one electron. This was introduced by an effective potential operator (Fock operator) which states a general field of electrons. This means that one electron is sensible to the electromagnetic field of the nuclei and the other N-1 electrons. This also does not take into account any relativistic effect that may happen.

This one-electron picture could then be implemented in a computational code to be solved iteratively (based on the *self-consistent field* scheme). The electrons could be translated into mathematical functions called *basis set*. These electrons could then be associated to specific orbitals (wave-functions) respecting the Pauli’s exclusion theorem. The composition of the molecular orbitals was performed on the basis of a linear combination of atomic orbitals (LCAO method). The basis set can then be decorticated and designed to accommodate the needs of the physical problem being studied (number of core functions, polarization effects, flexibility to accommodate ionic clouds, etc.).

Because of the one-electron picture, the Hartree-Fock method lacks of description of the electronic correlation in a many-body system. In this way, metallic systems and systems where electrons can delocalize over a region of the space are poorly-described by this method. Many others, called **post-Hartree-Fock methods** have tried, with different degrees of success, to incorporate these effects on the Hartree-Fock scheme. This has been accomplished by Perturbation Theory, as it is the case of nth order Møller-Plesset Perturbation theory (MPn), coupled-cluster, configuration of interactions, multi-configuration methods, and semi-empirical ones.

A common point between these methods, exception made for the semi-empirical ones, is the limitation on the number of basis functions. These methods, although quite efficient on the description of the electronic structure of molecules, mainly, scale quickly with the number of atoms and, in this way, are not practical for every system being studied, even though they would be very appropriate because the description of both exchange and correlation would be the appropriate in many cases. The semi-empirical methods, by their turn, can be employed for large systems, with a very low accuracy though. This is due to the fact that multi-center integrals are not calculated on-the-fly but are replaced by experimentally-obtained (or calculated with a higher level of theory method for model systems) values.

This has been circumvented in parts by the introduction of Density Functional Theory and this is discussed in the next section.

### C.1.1 Semi-empirical methods

Herein a closer look on the semi-empirical methods is presented. The approximations introduced into the HF equation so that the *ab initio* result can be reproduced using a small number of basis set and having a low-computational cost are commonly called semi-empirical methods. This methods are part of the post-Hartree-Fock methodologies as already discussed.

Several parameterizations have been proposed. The most striking introduced approximations are:

1. integrals involving different basis functions are not taken into account;
2. instead of treating the positive core and the core electrons, an effective core charge is considered;
3. two-centered integrals equal a parameter dependent on atom A, on atom B and the distance in-between.

The obtaining of values for multi-centered integrals and overlapping orbitals may be done based on experiments. The most part of these methods focus on the determination of ground-state geometries. Several methods exist, such as AM1, the PMn series (n=3, 5, 6, 7), the RM1 method, among others. They level of accuracy is variable and depends on the type of molecules that are modeled. The most interesting among them are still AM1 and the new PM7 method,[296] developed by J. Stewart and implemented in MOPAC code.[297]

To describe the excited state, some semi-empirical methodologies have also been developed. M. C. Zerner[298] reparameterized the INDO method[299] (Intermediate Neglect of Differential Overlap) with spectroscopic parameters (S) using configuration of interactions (of single electrons) (CI(S)). This method, called ZINDO/S-CI(S) has been used for the las three decades as a simple way of calculating excited-states of systems for which higher-level methods are not available.

This method considers the two-centered integrals equal a parameter dependent on atom A, on atom B and the distance between both of them. This parameter, $\gamma_{AB}$ is given by the Mataga-Nishimoto relation:[300].

$$\gamma_{AB} = \frac{f_y}{\frac{2f_y}{y_{AA}+y_{BB}} + R_{AB}} \tag{C.1}$$

Where $y_{AA}$ is proportional to the difference between the ionization potential and the electron affinity of atom A, $f_y$ is obtained by adjust of experimental data and it is currently assumed to be equal to 1.2, and $R_{AB}$ is the distance separating atoms A and B.

The biggest advantage of using this method to calculate excited states is the fact that it can be readily employed for large systems without compromising qualitatively the accuracy of the results.

## C.2 Density Functional Theory (DFT)

The use of Density Functional Theory (DFT) became a common-place in the molecular modeling of materials in the nanometric scale. In this method, the energy of a system is described as a functional of the electronic density, skipping the direct wave-function calculation in the process. Whilst wave-function-based methods, such as Hartree-Fock (HF), solve a Schröredinger-like equation (the Fock equation)[1], DFT is based on the assumption that there is a relationship between the total electronic energy and the overall electronic density.

The first basis of this idea was already present in the Thomas-Fermi model, however the breakthrough came by the Hohenberg-Kohn theorem in 1964, showing that the ground-state energy and other properties of a system were uniquely defined by the electron density. In other words, the energy $E$ is hence a *functional* of the density $\rho(\vec{r})$ at the point $\vec{r}$. Based on the definition of the electric potential, one can write this as:

$$E[\rho(\vec{r})] = \int V_{ext}(\vec{r})\rho(\vec{r})d\vec{r} + F[\rho(\vec{r})] \tag{C.2}$$

The first term $V_{ext}(\vec{r})$ arises from the interaction of the electrons with the external potential produced by the Coulomb interaction with the nuclei. On the other hand, $F[\rho(\vec{r})]$ is the sum of the kinetic energy of the electrons and the contribution from inter-

---

[1] The same is valid for Perturbation Theory based methods, such as MP2, and Coupled-Cluster ones.

electronic interactions.

The variational method can be applied in the solving of this equation, in which the minimum value of $E[\rho(\vec{r})]$ represent the energy of the electron density of the ground-state. From this, it is a common-sense that DFT is intrinsically incapable of describing excited-states without further physical-mathematical considerations.

Then, in 1965, with the Kohn-Sham (KS) theorem, the term $F[\rho(\vec{r})]$ is suggested to be approximated as the sum of three terms in the form:

$$F[\rho(\vec{r})] = E_{KE}[\rho(\vec{r})] + E_H[\rho(\vec{r})] + E_{XC}[\rho(\vec{r})] \tag{C.3}$$

Where $E_{KE}[\rho(\vec{r})]$ is the kinetic energy, $E_H[\rho(\vec{r})]$ the electron-electron Coulombic energy (also known as Hartree electrostatic energy), and $E_{XC}[\rho(\vec{r})]$ a term responsible for describing the exchange and correlation contributions.

The first term is further defined as the kinetic energy of a system of *non-interacting* electrons with the same density $\rho(\vec{r})$ as the real system. The second term associates the electrostatic energy as the classical interaction between two charged densities over all possible pairwise interactions. It is interesting to note that this terms is classical and do not take into account the quantum *many-body* behavior of the electrons, *i.e.*, as they are correlated to each other and the Heisenberg uncertainty principle, for instance.

Finally, the last term is then responsible for accounting for this quantum behavior of electrons and it is one of the master pieces of DFT, known as the exchange-correlation functional. As no analytical form of this functional is known, several approximations are proposed to treat this quantum mechanical problem and based on this, DFT cannot be considered always as an *ab initio* method, since the definition of this functional can take into account empirical parameters. However, even simple approximations to it can give favorable results and this is the key success of DFT.

Numerically, the electronic structure of the system is solved in a self-consistent way, in which a guess of a initial electronic density is fed into the above equations. The application of the variational approach allows one to reach the ground-state electronic density and, consequently, energy by a so-called *self-consistent field.*

Calculating these specific energies for a multi-electronic system takes the form of multi-centered multi-index integrals, what is responsible for a ready increase in the computation time (often in the order of $O(N^4)$, where $N$ is the number of atoms). In this way, treating large molecular systems becomes almost non-practical.

Moreover, the combination of these two equations bears a striking resemblance to those of Hartree-Fock theory. The difference between them is found on the fact that the HF has no correlation being calculated whereas KS is a correlated method. To go from the former to the latter, one only needs to replace the exchange energy by the exchange-correlation one.

### C.2.1 The exchange-correlation functionals

The fact that the exchange-correlation functional is not known gives rise to the appearance of several different ready to be employed by the user. Choosing the most appropriate demands testing it against the class of materials being studied and the nature of the physical-chemical problem.

The first functionals are based on two different approximations: the Local Density Approximation (LDA) and Generalized Gradient Approximation (GGA). For the former, the electron density varies locally whereas for the latter it also depends on gradient of it. In well-behaviored systems, the electron density is smooth, almost constant, so, it does not depend on its gradient, justifying the use of LDA for these cases. For heteroatomic systems, this may not be true and GGA may become needed.

To refine even more the quality of the results, mainly the atomization energies, bond lengths and vibrational frequencies, functionals called *hybrid* have been developed over the three last decades. These functionals incorporate a portion of the exact exchange in HF theory with exchange and correlation from other sources such as LDA and GGA.

These functionals are constructed by a linear combination of the HF exact exchange functional and any other exchange-correlation functional. The weight of participation of each component is typically found by fitting the predictions done by these functionals to experimental results.

The most used hybrid functionals are B3LYP,[301, 302] PBE0,[303, 304] HSE[305] and meta-hybrid GGA (as the Minnesota functionals)[306, 307]. Specifically, the B3LYP functional which has been used throughout this thesis, is written in the form of:

$$E_{XC}^{B3LYP} = E_X^{LDA} + a_0(E_X^{HF} - E_X^{LDA}) + a_x(E_X^{GGA} - E_X^{LDA}) + E_C^{LDA} + a_c(E_C^{GGA} - E_C^{LDA}) \quad (C.4)$$

Where $E_{XC}^{B3LYP}$ stands for the exchange-correlation energy in the B3LYP scheme, $E_X^{LDA}$ the exchange energy in the LDA scheme, $E_X^{HF}$ the exchange energy of HF, $E_X^{GGA}$ the exchange energy in GGA scheme, $E_C^{LDA}$ the correlation energy in LDA scheme, and $E_C^{GGA}$ the correlation energy in GGA scheme. The parameters $a_0$, $a_x$ and $a_c$ are the weight of participation of each component and assume the values of 0.20, 0.72 and 0.81, respectively. These parameters were determined beforehand by A. Becke by fitting the analogous B3PW91 functional to a set of molecular parameters.[308]

This functional has been widely used for description of ground state properties of molecular systems. However, a serious low accuracy appears when trying to describe excited state properties and where the self-interaction problem becomes pathological.[2] This drawback has limited the use of B3LYP functional for charge-transfer systems and

---

[2] The self-interaction problem consists on the fact that a electron can interact with itself. This leads to problem of over-delocalization of the electron cloud since this electron tends to repulse itself.

problems evolving the energies of the excited states of $\pi$-conjugated materials (specially long oligomers), for example.

This is not incompatible with its use in this thesis. The use of this functional to determine ground state properties (such the geometry) is not questionable. To determine excitation energies in the time-dependent domain, as it was performed in Chapter 7, it is more problematic. However, it was used only as a support to the ZINDO/S method, to estimate the discrepancy of this method with a high-level one. For the previsions done in Chapter 2 concerning the calculation of excited state of fullerenes, this is less problematic. The low-lying excitations which were calculated concern the electron cloud of fullerene molecule only and this is not the case of charge-transfer states, as it is in Chapter 7.

## C.3 The ”RIJCOSX” approximation

In order to treat bigger molecules within DFT approach, several physical-mathematical approximations have been proposed throughout the years since early 1980s.

Within wave-function-based methods, such HF and MP2, the Resolution of Identity (RI) method is remarkable for its speedups in machine time. This approximation takes into consideration that these wave-function methods have their key quantities expressible in terms of products of basis functions of single particles, which are then expanded in a set of auxiliary basis functions. This technique facilitates an efficient treatment of the two-electron Coulomb repulsion integrals, needed to the Fock matrix.[309].

By extension, this technique can also be applied to hybrid DFT (for which the exchange-correlation function has a contribution of the exact HF exchange energy) in the formation of the Coulomb part of the Fock matrix. [310] Using this approximation only is able to present speedups in the order of 20% compared to no approximative treatment. All this, at a very low accuracy price.

However, to harmonize these savings in a global speedup method, the exchange matrix calculation also needed to be improved. This would lead to an efficient Fock-matrix formation algorithm. Recently, Neese *et al.*[311] proposed an algorithm based on a semi-numeric exchange matrix approximation that is called *chain of spheres exchange* (COSX). The main idea behind the concept consists of constructing chains of shells of basis functions that, for a given cutoff range, give non-negligible contribution to the exchange matrix. An extensive explanation and details of implementation of this method is found in the original publications of F. Neese's group, for both ground[311] and excited [312] states calculations.

Thus, the use of this combined methodology, RIJCOSX, allows one to, at a fairly low accuracy price, compute properties of large molecules using accurate (double-, triple-,...$\zeta$) basis set functions. The gain in machine time can reach up to 60 times the one where no numerical approximation is used.

This method is fully implemented in ORCA package[93] and it was quite appropriate to work with these conditions in this thesis, based on the size of the molecular systems being treated here.

# Appendix D

# Résumé Général

Le présent travail de thèse est axé sur les problématiques de stabilité des matériaux accepteurs d'électrons employés au sein des couches minces des dispositifs de type photovoltaïque organique. Ces questions ont été traitées à la lumière d'un couplage expérience-théorie, en comparant quelques voies de polymérisation des molécules de type C60 (*c.f.* Figure E.1.(b)), conduisant aux polyfullerènes.

Largement utilisées au sein des dispositifs organiques, les molécules dérivées du $C_{60}$, tels le $PC_{60}BM$ et les dérivés d'indène-$C_{60}$, se révèlent particulièrement sensibles aux effets thermiques lorsqu'elles se trouvent mélangées à la matrice du polymère donneur (majoritairement du poly(3-hexylthiophène), *c.f.* Figure E.1.(a)). Du fait de la différence d'énergie de surface entre ces deux composés, la ségrégation de phases du dérivé de fullerène devient inévitable, engendrant une réduction de l'aire d'interface et, de fait, une dissociation des charges dans l'état excité.

Afin de pallier ce problème, plusieurs stratégies ont été proposées dans la littérature, qui consistent principalement i) en l'utilisation d'additifs au sein de la couche mince, ii) au greffage direct du fullerène sur le polymère donneur ou iii) en la polymérisation du fullerène.C'est cette dernière hypothèse de travail que nous avons retenue pour étude tout au long de cette thèse.

Six voies de synthèse de ces polymères ont été étudiées et les propriétés électroniques (énergie de l'orbitale LUMO, électroaffinité, électrophilicité, énergie de réorganisation, intégrale de transfert et mobilité électronique) qui en résultent ont été déterminées au moyen de la modélisation numérique. Parmi ces voies de synthèse, le chemin dit «ATRAP» («Atom Transfer Radical Addition Polymerization», ou polymérisation par addition et transfert radicalaire d'atomes), a été privilégié pour la synthèse de nouveaux matériaux, greffés de différentes chaînes latérales susceptibles d'entraîner un réglage fin des propriétés de miscibilité au sein du polymère donneur. La Figure E.2 présente le schéma général des molécules obtenues par cette voie de synthèse.

Les propriétés physico-chimiques des composés synthétisés, greffés de différentes chaînes

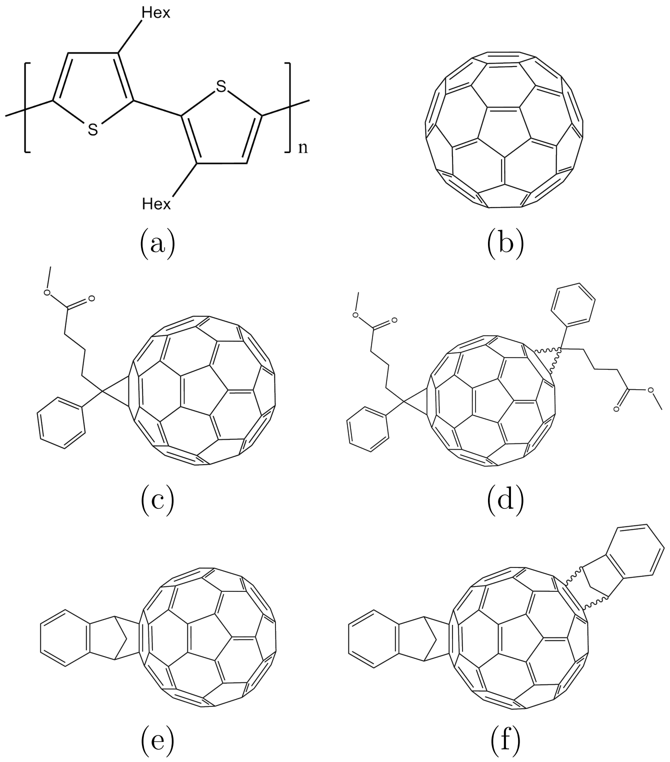

(a) (b) (c) (d) (e) (f)

**Figure D.1:** Structures moléculaires du (a) Poly(3-hexylthiophène) régio-régulaire, (b) $C_{60}$, (c) $PC_{60}BM$, (d) bis-$PC_{60}BM$, (e) $IC_{60}MA$ et (f) $IC_{60}BA$.

latérales, ont été déterminées au moyen de diverses techniques de caractérisation et leur application dans des couches minces, au sein de dispositifs photovoltaïques, a été mise en œuvre. Utilisés en tant qu'additifs, ces matériaux révèlent un potentiel de stabilisation de la couche de P3HT/$PC_{60}BM$, cette propriété n'affectant pas, pour autant, les performances de la cellule. Le comportement de ces couches après soumission à un traitement thermique a montré, à l'inverse, un phénomène de déstabilisation dont le mécanisme a été, lui aussi, étudié par diverses techniques expérimentales.

Finalement, un mécanisme de dépolymérisation, induit par la lumière et/ou par la chaleur, a été proposé. Dans ce processus, la rupture de la liaison chimique entre le monomère et le fullerène est responsable de la création des défauts, comme de la dépolymérisation, des phénomènes de *cross-linking* ou du réarrangement irréversible de la couche mince. Cette rupture peut être soit thermiquement activée, soit induite par l'état triplet du monomère, qui déstabilise la liaison.

Outre l'étude de ces composés, le présent travail s'est également intéressé i) à la stabilisation de l'interface organique-inorganique au sein des dispositifs photovoltaïques, ii) à la stabilisation de la chaîne latérale des polymères conjugués, ainsi que iii) à la relation entre la géométrie de la molécule et sa réactivité avec l'oxygène moléculaire. Ces études, menées en parallèle, nous ont conduit à proposer de nouveaux matériaux hybrides du type donneur-accepteur, dérivés de l'hexabenzocoronène et capables de s'empiler pour former des structures similaires à des cristaux liquides discotiques. Partant de l'ensemble

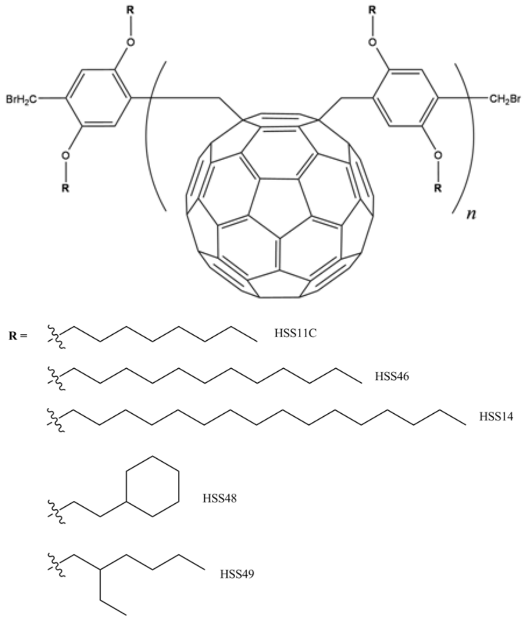

**Figure D.2:** Structure générale des molécules synthétisées par la voie ATRAP.

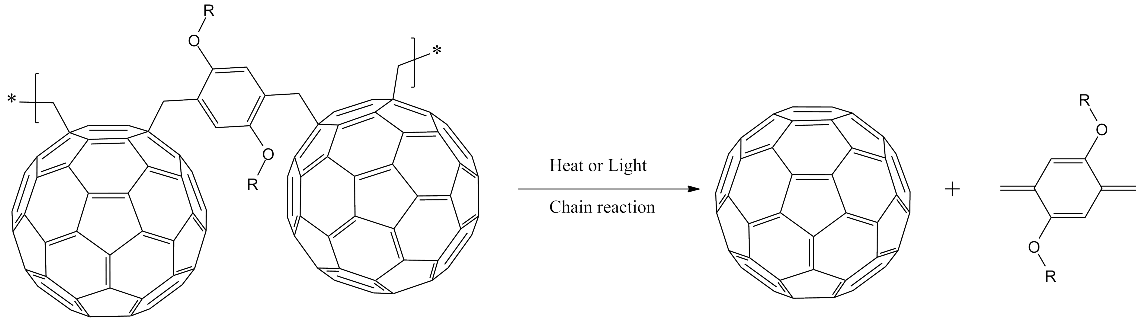

**Figure D.3:** Réaction de dépolymérisation avec propagation en chaîne.

des conclusions tirées de ces travaux de thèse, deux composés ont été proposés, dont les propriétés électroniques révèlent qu'il est possible de dessiner des matériaux à la fois stables et efficaces pour une utilisation dans le domaine du photovoltaïque organique.

Ce travail de thèse s'est toutefois initialement intéressé à l'utilisation des molécules dérivées du fullerène, à l'heure actuelle couramment employés au sein des couches minces, et a étudié la possibilité de faire face aux problèmes que posent ces composés en envisageant leur polymérisation par une voie radicalaire encore peu étudiée. Les matériaux obtenus par cette méthode se sont montrés trop sensibles à la température et non appropriés à une utilisation en tant qu'accepteur d'électrons ou de stabilisateur morphologique de la couche mince.

Les concepts physico-chimiques sous-tendant ce phénomène ont été étudiés et ont abouti à la proposition, déjà émise par notre groupe de recherche, consistant à utiliser des matériaux bidimensionnels en tant qu'accepteurs, de sorte à les rendre plus résistants à la photo-oxydation et aux problématiques de stabilité morphologique.

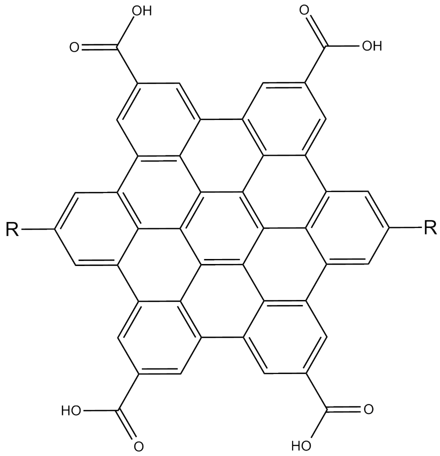

**Figure D.4:** Proposition de composés dérivés de l'hexabenzocoronène. Dans le cadre de ce travail, les substituants *R* envisagés correspondent soit à une chaîne dérivée du poly(3-isopropoxythiophène), soit à une chaîne dérivée de benzo[1,2-*b*;3,4-*b*]dithiophene - *co* - thieno[3,4-*c*]pyrrole-4,6-dione.

# Appendix E

# Zusammenfassung

Diese Arbeit konzentriert sich auf die Probleme der Stabilität der Elektronenakzeptormaterialien in dünnen Schichten, welche in organischen Solarzellen Anwendung finden. Vielversprechende Materialien in diesem Zusammenhang sind Polyfullerene. Für die Untersuchung verschiedener Polymerisationsrouten für $C_{60}$ Moleküle, dargestellt in Abb. E.1.(b), wurden sowohl experimentelle, als auch theoretische Arbeiten wurden durchgeführt.

Gegenwärtig werden als Akzeptormaterialien in organischen Bauelementen vor allem Moleküle basierend auf $C_{60}$ verwendet, wie beispielsweise $PC_{60}BM$ und indene$C_{60}$-Derivate. Diese liegen in sogenannten bulk-heterojunction Solarzellen in einer Mischung mit mit den Donor-Polymeren vor (z.B. Poly (3-hexylthiophen), siehe Abb. 1 E.1.(a)) und sind insbesondere sensibel auf eine thermische Behandlung. Aufgrund der unterschiedlichen Oberflächenenergien dieser Verbindungen, führt eine thermische Behandlung zu einer Phasentrennung zwischen Donor und Akzeptormaterialien, wodurch die Grenzflächen verringert werden und somit die Dissoziation von Exzitonen an diesen Grenzflächen verringert wird.

Um dies zu umgehen, sind verschiedene Strategien aus der Literatur bekannt, diese beinhalten im Wesentlichen i) die Verwendung von Additiven in der dünnen Schicht, ii) die Ankopplung des Fullerens direkt an das Donor-Polymer und iii) die Polymerisation der Fulleren-Moleküle. Letztere Strategie wurde in dieser Diplomarbeit verfolgt.

Sechs verschiedene Synthesewege wurden angewandt und die elektronischen Eigenschaften (LUMO Orbitalenergie, Elektroaffinität, Elektrophilie, Reorganisationsenergie, Transferintegral und Elektronenbeweglichkeit) wurden durch Molecular Modelling untersucht. Unter diesen Synthesewegen wurde erwies sich schließlich die sogenannte " ATRAP " Route als erfolgreich ("Atom Transfer Radical Addition Polymerization"), welche bisher wenig in der Literatur untersuchtwurde. Es wurden Polymere mit unterschiedlichen Seitenketten synthetisiert, die die Verbesserung der Löslichkeit in organischen SOLVANTS und die Mischbarkeit im Donor Polymermaterial zeigen. Abbildung E.2 zeigt das allge-

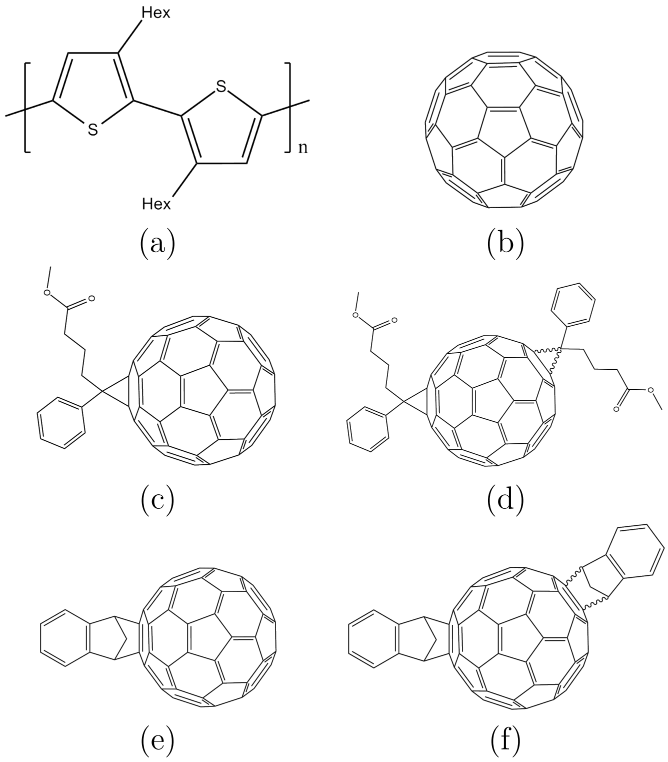

(a) (b) (c) (d) (e) (f)

**Figure E.1:** Molekülstrukturen von (a) Poly (3-hexylthiophen), (b) $C_{60}$, (c) $PC_{60}BM$, (d) bis-$PC_{60}BM$, (e) $IC_{60}MA$ und (f) $IC_{60}BA$.

meine Schema der auf diesem Weg gewonnenen Moleküle.

Die physikalisch-chemischen Eigenschaften der so synthetisierten Materialien mit verschiedenen Seitenketten, wurden mit verschiedenen Charakterisierungstechniken untersucht und ihre Anwendung in dünnen Filmen für Organische Photovoltaik getestet. Wenn sie als Additive verwendet werden, können diese Materialien ein die Morphologie von P3HT / $PC_{60}BM$ Schichten stabilisieren, während die Performance der Bauelemente nahezu unverändert bleibt. Eine Nach einer thermischen Behandlung führte überraschenderweise zu einer Destabilisierung der aktiven Schicht. Dieser Mechanismus auch wurde mit mehreren experimentellen Techniken studiert.

Schließlich Depolymerisation Mechanismus durch Licht und / oder Wärme induzierter vorgeschlagen. In diesem Prozess ist die Spaltung des Monomeren-Fulleren-Bindung zum Erzeugen Defekte, wie Depolymerisation, Vernetzungen oder irreversible Neuanordnung der dünnen Schicht verantwortlich. Diese Spaltung kann entweder thermisch aktivierte oder vom Triplettzustand des Monomers, das ebenfalls destabilisiert diese Bindung induziert werden.

Darüber hinaus beschäftigt sich diese Arbeit mit i) der Stabilisierung der organisch-anorganischen Grenzflächen inphotovolaischen Bauelementen ii) der Stabilisierung der Seitenketten von konjugierten Polymeren, sowie mit iii) dem Zusammenhang zwischen der Struktur von Kohlenstoff-basierten Molekülen und der Reaktivität gegenüber molekularem Sauerstoff.

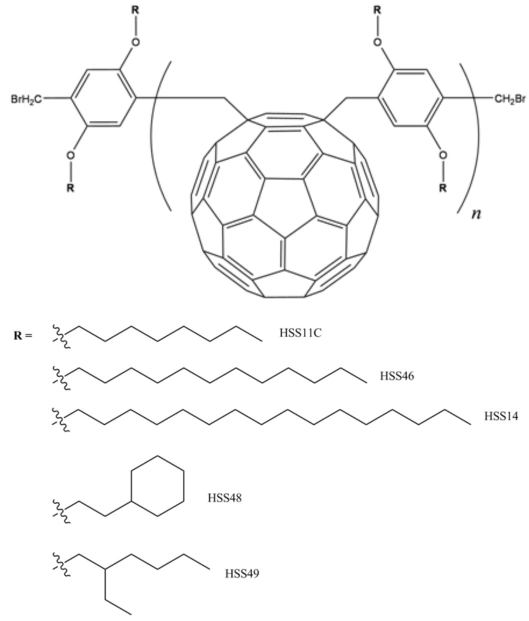

**Figure E.2:** Allgemeine Struktur der Moleküle, die durch die ATRAP Route synthetisiert

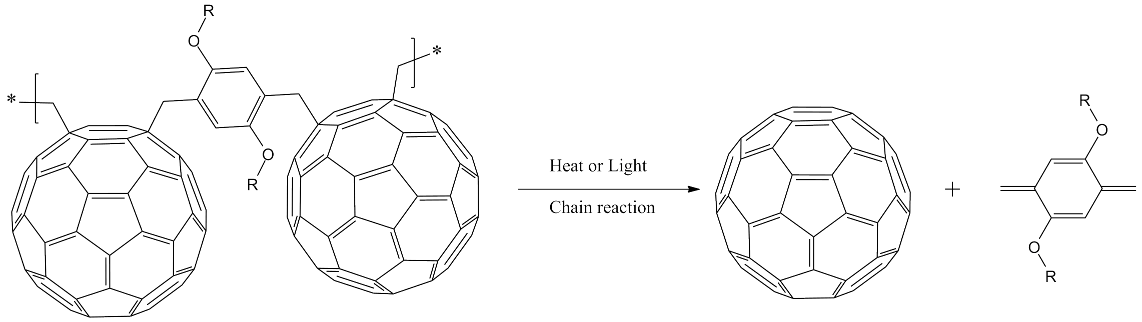

**Figure E.3:** Depolymerisation Mechanismus durch Licht und / oder Wärme induzierter vorgeschlagen.

Diese Studien, parallel durchgeführt, fuhr zu dem Satz neuer Donor-Akzeptor-Hybridmaterialien auf Basis von Hexabenzocoronen, die in der Lage Stapeln über sich selbst zu supramolekularen ähnlich diskotische Flüssigkristalle Strukturen zu bilden. Aus den Schlussfolgerungen dieses Dokuments wurden zwei Produkte vorgeschlagen, die elektronischen Eigenschaften zeigen, dass es möglich ist, neue Materialien, die zur gleichen Zeit für den Einsatz in der organischen Photovoltaik stabil und effizient sein kann, zu entwerfen.

Diese Arbeit hat sich auf die Untersuchung der elektronischen Eigenschaften von Molekülen basierend auf $C_{60}$ und wie ihre Polymerisation könnte eine Alternative zu den bekannten morphologischen Stabilitätsprobleme geben konzentriert. Dann wurde ein kürzlich radikalischer Polymerisation Route verwendet, um polymere Derivate der Fullerene zu synthetisieren. Die so erhaltenen Materialien wurden geringe Beständigkeit gegenüber Wärmebehandlung und damit angezeigt, nicht gebundenen Elektronenakzeptorfähigkeiten oder morphologische Stabilisatoren innerhalb dünnen Schicht einer photovoltaischen Substanz eingesetzt werden.

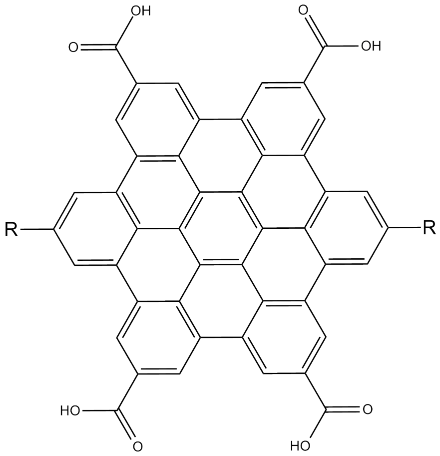

**Figure E.4:** Neuer Donor-Akzeptor-Hybridmaterialien auf Basis von Hexabenzocoronen vorgeschlagen. Aus den Schlussfolgerungen dieses Dokuments wurden zwei Produkte vorgeschlagen: $R$ = Poly (3-isopropoxy-thiophen) oder benzo[1,2-*b*;3,4-*b*]dithiophene - *co* - thieno[3,4-*c*]pyrrole-4,6-dione.

Die physikalisch-chemischen Konzepte hinter diesen Phänomenen wurden untersucht und mit dem Vorschlag, bereits vor dem von unserer Arbeitsgruppe durchgeführt, unter Verwendung von zweidimensionalen Materialien als Elektronenakzeptoren, so dass sowohl die Beständigkeit gegen Photooxidation und morphologischen Ausfall könnte zu verbessern geführt gleichzeitig.

# Bibliography

[1] Bas van der Wiel, Hans-Joachim Egelhaaf, Hermann Issa, Maria Roos, and Norbert Henze. Market readiness of organic photovoltaics for building integration. In *Symposium Y - Physics of Organic and Hybrid Organic-Inorganic Solar Cells*, volume 1639 of *MRS Proceedings*, 2014.

[2] Terje A Skotheim and John Reynolds. *Conjugated polymers: theory, synthesis, properties, and characterization.* CRC press, 2006.

[3] Dionys Baeriswyl, David K Campbell, and Sumit Mazumdar. *An overview of the theory of $\pi$-conjugated polymers.* Springer, 1992.

[4] B. Kraabel, D. McBranch, N. S. Sariciftci, D. Moses, and A. J. Heeger. Ultrafast spectroscopic studies of photoinduced electron transfer from semiconducting polymers to $c_{60}$. *Phys. Rev. B*, 50:18543–18552, Dec 1994.

[5] Sabrina Kirner, Michael Sekita, and Dirk M Guldi. 25th anniversary article: 25 years of fullerene research in electron transfer chemistry. *Advanced Materials*, 26(10):1482–1493, 2014.

[6] Alan J Heeger. 25th anniversary article: bulk heterojunction solar cells: understanding the mechanism of operation. *Advanced Materials*, 26(1):10–28, 2014.

[7] Seth B Darling and Fengqi You. The case for organic photovoltaics. *Rsc Advances*, 3(39):17633–17648, 2013.

[8] Santosh Shrestha. Photovoltaics literature survey (no. 112). *Progress in Photovoltaics: Research and Applications*, 22(8):933–936, 2014.

[9] Martin A Green, Keith Emery, Yoshihiro Hishikawa, Wilhelm Warta, and Ewan D Dunlop. Solar cell efficiency tables (version 45). *Progress in photovoltaics: research and applications*, 23(1):1–9, 2015.

[10] Markus C Scharber, David Mühlbacher, Markus Koppe, Patrick Denk, Christoph Waldauf, Alan J Heeger, and Christoph J Brabec. Design rules for donors in bulk-heterojunction solar cells?towards 10% energy-conversion efficiency. *Advanced Materials*, 18(6):789–794, 2006.

[11] Bernard Kippelen and Jean-Luc Brédas. Organic photovoltaics. *Energy & Environmental Science*, 2(3):251–261, 2009.

[12] Richard R Lunt, Noel C Giebink, Anna A Belak, Jay B Benziger, and Stephen R Forrest. Exciton diffusion lengths of organic semiconductor thin films measured

by spectrally resolved photoluminescence quenching. *Journal of Applied Physics*, 105(5):053711, 2009.

[13] Wade A Luhman and Russell J Holmes. Investigation of energy transfer in organic photovoltaic cells and impact on exciton diffusion length measurements. *Advanced Functional Materials*, 21(4):764–771, 2011.

[14] Harald Hoppe and Niyazi Serdar Sariciftci. Morphology of polymer/fullerene bulk heterojunction solar cells. *Journal of Materials Chemistry*, 16(1):45–61, 2006.

[15] Serap Günes, Helmut Neugebauer, and Niyazi Serdar Sariciftci. Conjugated polymer-based organic solar cells. *Chemical reviews*, 107(4):1324–1338, 2007.

[16] Wonyong Koh, Dominique Dubois, Wlodzimierz Kutner, M. Thomas Jones, and Karl M. Kadish. Simultaneous cyclic voltammetry and electrochemical quartz crystal microbalance studies of buckminsterfullerene (c60) film electrodeposition and tetra-n-butylammonium electrodoping in acetonitrile. *The Journal of Physical Chemistry*, 96(11):4163–4165, 1992.

[17] Erich Hückel. Quantentheoretische beiträge zum problem der aromatischen und ungesättigten verbindungen. iii. *Zeitschrift für Physik*, 76(9-10):628–648, 1932.

[18] Ivan Gutman. Proof of the hückel rule. *Chemical Physics Letters*, 46(1):169–171, 1977.

[19] PW Fowler and Arnout Ceulemans. Electron deficiency of the fullerenes. *The Journal of Physical Chemistry*, 99(2):508–510, 1995.

[20] Nathan S Lewis and Daniel G Nocera. Powering the planet: Chemical challenges in solar energy utilization. *Proceedings of the National Academy of Sciences*, 103(43):15729–15735, 2006.

[21] Jakaria Ahmad, Kateryna Bazaka, Liam J Anderson, Ronald D White, and Mohan V Jacob. Materials and methods for encapsulation of opv: A review. *Renewable and Sustainable Energy Reviews*, 27:104–117, 2013.

[22] Mikkel Jørgensen, Kion Norrman, and Frederik C Krebs. Stability/degradation of polymer solar cells. *Solar Energy Materials and Solar Cells*, 92(7):686–714, 2008.

[23] Lionel Derue, Olivier Dautel, Aurélien Tournebize, Martin Drees, Hualong Pan, Sébastien Berthumeyrie, Bertrand Pavageau, Eric Cloutet, Sylvain Chambon, Lionel Hirsch, et al. Thermal stabilisation of polymer–fullerene bulk heterojunction morphology for efficient photovoltaic solar cells. *Advanced Materials*, 26(33):5831–5838, 2014.

[24] René AJ Janssen, Jan C Hummelen, and N Serdar Sariciftci. Polymer–fullerene bulk heterojunction solar cells. *MRS bulletin*, 30(01):33–36, 2005.

[25] Joshua A Moore, Shariq Ali, and Brian C Berry. Stabilization of pcbm domains in bulk heterojunctions using polystyrene-tethered fullerene. *Solar Energy Materials and Solar Cells*, 118:96–101, 2013.

[26] Xiaoniu Yang, Joachim Loos, Sjoerd C Veenstra, Wiljan JH Verhees, Martijn M Wienk, Jan M Kroon, Matthias AJ Michels, and René AJ Janssen. Nanoscale morphology of high-performance polymer solar cells. *Nano letters*, 5(4):579–583, 2005.

[27] Jeffery Peet, JY Kim, Nelson E Coates, Wang Li Ma, Daniel Moses, Alan J Heeger, and Guillermo C Bazan. Efficiency enhancement in low-bandgap polymer solar cells by processing with alkane dithiols. *Nature materials*, 6(7):497–500, 2007.

[28] Jae Kwan Lee, Wan Li Ma, Christoph J Brabec, Jonathan Yuen, Ji Sun Moon, Jin Young Kim, Kwanghee Lee, Guillermo C Bazan, and Alan J Heeger. Processing additives for improved efficiency from bulk heterojunction solar cells. *Journal of the American Chemical Society*, 130(11):3619–3623, 2008.

[29] Eszter Voroshazi, Bregt Verreet, Andrea Buri, Robert Müller, Daniele Di Nuzzo, and Paul Heremans. Influence of cathode oxidation via the hole extraction layer in polymer: fullerene solar cells. *Organic Electronics*, 12(5):736–744, 2011.

[30] Priscilla G Taylor, Jin-Kyun Lee, Alexander A Zakhidov, Margarita Chatzichristidi, Hon Hang Fong, John A DeFranco, George G Malliaras, and Christopher K Ober. Orthogonal patterning of pedot: Pss for organic electronics using hydrofluoroether solvents. *Advanced Materials*, 21(22):2314–2317, 2009.

[31] Ayse Turak. Degradation at interfaces: Oleds and opvs. *Journal of Photonic Science and Technology*, 3(1):1–10, 2013.

[32] Matthew T Lloyd, Craig H Peters, Andres Garcia, Isaac V Kauvar, Joseph J Berry, Matthew O Reese, Michael D McGehee, David S Ginley, and Dana C Olson. Influence of the hole-transport layer on the initial behavior and lifetime of inverted organic photovoltaics. *Solar Energy Materials and Solar Cells*, 95(5):1382–1388, 2011.

[33] Jenny Nelson. Polymer: fullerene bulk heterojunction solar cells. *Materials today*, 14(10):462–470, 2011.

[34] Gilles Dennler, Markus C Scharber, and Christoph J Brabec. Polymer-fullerene bulk-heterojunction solar cells. *Advanced Materials*, 21(13):1323–1338, 2009.

[35] Harold W Kroto, James R Heath, Sean C O'Brien, Robert F Curl, and Richard E Smalley. C 60: buckminsterfullerene. *Nature*, 318(6042):162–163, 1985.

[36] Wolfgang Krätschmer, Lowell D Lamb, K Fostiropoulos, and Donald R Huffman. C60: a new form of carbon. *Nature*, 347(6291):354–358, 1990.

[37] Jack B Howard, J Thomas McKinnon, Yakov Makarovsky, Arthur L Lafleur, and M Elaine Johnson. Fullerenes c60 and c70 in flames. *Nature*, 352(6331):139–141, 1991.

[38] Ken-ichi Yoshie, Shigeaki Kasuya, Keisuke Eguchi, and Toyonobu Yoshida. Novel method for c60 synthesis: a thermal plasma at atmospheric pressure. *Applied physics letters*, 61(23):2782–2783, 1992.

[39] VV Brazhkin, AG Lyapin, SV Popova, Yu A Klyuev, and AM Naletov. Mechanical properties of the 3d polymerized, sp2–sp3 amorphous, and diamond-plus-graphite nanocomposite carbon phases prepared from c60 under high pressure. *Journal of applied physics*, 84(1):219–226, 1998.

[40] Robert D Bolskar, Angelo F Benedetto, Lars O Husebo, Roger E Price, Edward F Jackson, Sidney Wallace, Lon J Wilson, and J Michael Alford. First soluble m@ c60 derivatives provide enhanced access to metallofullerenes and permit in vivo evaluation of gd@ c60 [c (cooh) 2] 10 as a mri contrast agent. *Journal of the American Chemical Society*, 125(18):5471–5478, 2003.

[41] M_ J Rosseinsky, AP Ramirez, SH Glarum, DW Murphy, RC Haddon, AF Hebard, TTM Palstra, AR Kortan, SM Zahurak, and AV Makhija. Superconductivity at 28 k in rb x c 60. *Physical review letters*, 66(21):2830, 1991.

[42] Derya Baran, Abidin Balan, Selin Celebi, Beatriz Meana Esteban, Helmut Neugebauer, N Serdar Sariciftci, and Levent Toppare. Processable multipurpose conjugated polymer for electrochromic and photovoltaic applications. *Chemistry of Materials*, 22(9):2978–2987, 2010.

[43] James W Arbogast, Aleksander P Darmanyan, Christopher S Foote, FN Diederich, RL Whetten, Y Rubin, Marcos M Alvarez, and Samir J Anz. Photophysical properties of sixty atom carbon molecule (c60). *The Journal of Physical Chemistry*, 95(1):11–12, 1991.

[44] Luis Martín-Gomis, Kei Ohkubo, Fernando Fernández-Lázaro, Shunichi Fukuzumi, and Ángela Sastre-Santos. Synthesis and photophysical studies of a new nonaggregated c60-silicon phthalocyanine-c60 triad. *Organic letters*, 9(17):3441–3444, 2007.

[45] George A Olah, Imre Bucsi, Christian Lambert, Robert Aniszfeld, Nirupam J Trivedi, Dilip K Sensharma, and GK Surya Prakash. Chlorination and bromination of fullerenes. nucleophilic methoxylation of polychlorofullerenes and their aluminum trichloride catalyzed friedel-crafts reaction with aromatics to polyarylfullerenes. *Journal of the American Chemical Society*, 113(24):9385–9387, 1991.

[46] Maurizio Prato, Nazario Martín, and Francesco Giacalone. *Fullerene polymers: synthesis, properties and applications.* John Wiley & Sons, 2009.

[47] Uwe Reuther, Torsten Brandmueller, Wolfgang Donaubauer, Frank Hampel, and Andreas Hirsch. A highly regioselective approach to multiple adducts of c60 governed by strain minimization of macrocyclic malonate addends. *Chemistry-A European Journal*, 8(10):2261–2273, 2002.

[48] Shashadhar Samal, Bum-Jin Choi, and Kurt E Geckeler. The first water-soluble main-chain polyfullerene. *Chem. Commun.*, (15):1373–1374, 2000.

[49] C Mathis, S Nunige, F Audouin, and R Nuffer. Thermal stability of a c60-polystyrene bond. *Synthetic metals*, 121(1-3):1153–1154, 2001.

[50] F Audouin, S Nunige, R Nuffer, and C Mathis. Grafting polymers onto c60 via an atom transfer reaction. *Synthetic metals*, 121(1-3):1149–1150, 2001.

[51] Fabrice Audouin, Richard Nuffer, and Claude Mathis. Thermal stability of the fullerene-chain link in 6-arm ps stars with a c60 core. *Journal of Polymer Science Part A: Polymer Chemistry*, 42(19):4820–4829, 2004.

[52] Claude Mathis, Bruno Schmaltz, and Martin Brinkmann. Controlled grafting of polymer chains onto c 60 and thermal stability of the obtained materials. *Comptes Rendus Chimie*, 9(7):1075–1084, 2006.

[53] Yuanqin Liu, Zhaoling Yao, and Alex Adronov. Functionalization of single-walled carbon nanotubes with well-defined polymers by radical coupling. *Macromolecules*, 38(4):1172–1179, 2005.

[54] H Yu, LH Gan, X Hu, and YY Gan. A ph-sensitive double [60] fullerene-end-capped polymers via atrp: Synthesis and aggregation behavior. *Polymer*, 48(8):2312–2321, 2007.

[55] Haruyuki Okamura, Nobuhiro Ide, Masahiko Minoda, Koichi Komatsu, and Takeshi Fukuda. Solubility and micellization behavior of c60 fullerenes with two well-defined polymer arms. *Macromolecules*, 31(6):1859–1865, 1998.

[56] Haruyuki Okamura, Takashi Takemura, Masahiro Tsunooka, and Masamitsu Shirai. Synthesis of novel c60-containing polymers based on poly (vinyl phenol) and their photo-transformation properties. *Polymer Bulletin*, 52(6):381–391, 2004.

[57] Haruyuki Okamura, Masahiko Minoda, Takeshi Fukuda, Takeaki Miyamoto, and Koichi Komatsu. Solubility characteristics of c60 fullerenes with two well-defined polystyrene arms in a polystyrene matrix. *Macromolecular rapid communications*, 20(2):37–40, 1999.

[58] Peng Zhou, Guang-Qiang Chen, Han Hong, Fu-Sheng Du, Zi-Chen Li, and Fu-Mian Li. Synthesis of c60-end-bonded polymers with designed molecular weights and narrow molecular weight distributions via atom transfer radical polymerization. *Macromolecules*, 33(6):1948–1954, 2000.

[59] Fabrice Audouin, Richard Nuffer, and Claude Mathis. Synthesis of di-and tetra-adducts by addition of polystyrene macroradicals onto fullerene c60. *Journal of Polymer Science Part A: Polymer Chemistry*, 42(14):3456–3463, 2004.

[60] Haruyuki Okamura, Tomoya Terauchi, Masahiko Minoda, Takeshi Fukuda, and Koichi Komatsu. Synthesis of 1, 4-dipolystyryldihydro [60] fullerenes by using 2, 2, 6, 6-tetramethyl-1-polystyroxypiperidine as a radical source. *Macromolecules*, 30(18):5279–5284, 1997.

[61] Roger C. Hiorns, Eric Cloutet, Emmanuel Ibarboure, Laurence Vignau, Noëlla Lemaitre, Stéphane Guillerez, Christelle Absalon, and Henri Cramail. Main-chain fullerene polymers for photovoltaic devices. *Macromolecules*, 42(10):3549–3558, 2009.

[62] Roger C. Hiorns, Eric Cloutet, Emmanuel Ibarboure, Abdel Khoukh, Habiba Bejbouji, Laurence Vignau, and Henri Cramail. Synthesis of donor-acceptor multiblock copolymers incorporating fullerene backbone repeat units. *Macromolecules*, 43(14):6033–6044, 2010.

[63] Antonio Cravino and Niyazi Serdar Sariciftci. Double-cable polymers for fullerene based organic optoelectronic applications. *Journal of Materials Chemistry*, 12(7):1931–1943, 2002.

[64] A Yassar, M Hmyene, DC Loveday, and JP Ferraris. Synthesis and characterization of polythiophenes functionalized by buckminsterfullerene. *Synthetic metals*, 84(1):231–232, 1997.

[65] John P Ferraris, Abderrahim Yassar, David C Loveday, and Mohamed Hmyene. Grafting of buckminsterfullerene onto polythiophene: novel intramolecular donor-acceptor polymers. *Optical Materials*, 9(1):34–42, 1998.

[66] Ching W Tang. Two-layer organic photovoltaic cell. *Applied Physics Letters*, 48(2):183–185, 1986.

[67] Brian A Gregg. Excitonic solar cells. *The Journal of Physical Chemistry B*, 107(20):4688–4698, 2003.

[68] Stephan Kirchmeyer and Knud Reuter. Scientific importance, properties and growing applications of poly (3, 4-ethylenedioxythiophene). *Journal of Materials Chemistry*, 15(21):2077–2088, 2005.

[69] Wei-Ru Wu, U-Ser Jeng, Chun-Jen Su, Kung-Hwa Wei, Ming-Shin Su, Mao-Yuan Chiu, Chun-Yu Chen, Wen-Bin Su, Chiu-Hun Su, and An-Chung Su. Competition between fullerene aggregation and poly (3-hexylthiophene) crystallization upon annealing of bulk heterojunction solar cells. *Acs Nano*, 5(8):6233–6243, 2011.

[70] Dian Chen, Atsuhiro Nakahara, Dongguang Wei, Dennis Nordlund, and Thomas P Russell. P3ht/pcbm bulk heterojunction organic photovoltaics: correlating efficiency and morphology. *Nano letters*, 11(2):561–567, 2010.

[71] Yu Xie, Yong Li, Lixin Xiao, Qiquan Qiao, Rabin Dhakal, Zhiling Zhang, Qihuang Gong, David Galipeau, and Xingzhong Yan. Femtosecond time-resolved fluorescence study of p3ht/pcbm blend films. *The Journal of Physical Chemistry C*, 114(34):14590–14600, 2010.

[72] Wanli Ma, Cuiying Yang, Xiong Gong, Kwanghee Lee, and Alan J Heeger. Thermally stable, efficient polymer solar cells with nanoscale control of the interpenetrating network morphology. *Advanced Functional Materials*, 15(10):1617–1622, 2005.

[73] Jan C Hummelen, Brian W Knight, F LePeq, Fred Wudl, Jie Yao, and Charles L Wilkins. Preparation and characterization of fulleroid and methanofullerene derivatives. *The Journal of Organic Chemistry*, 60(3):532–538, 1995.

[74] Cecilia M Björström, Andrzej Bernasik, Jakub Rysz, Andrzej Budkowski, Svante Nilsson, Mattias Svensson, Mats R Andersson, Kjell O Magnusson, and Ellen Moons. Multilayer formation in spin-coated thin films of low-bandgap polyfluorene: Pcbm blends. *Journal of Physics: Condensed Matter*, 17(50):L529, 2005.

[75] Long Ye, Shaoqing Zhang, Deping Qian, Qi Wang, and Jianhui Hou. Application of bis-pcbm in polymer solar cells with improved voltage. *The Journal of Physical Chemistry C*, 117(48):25360–25366, 2013.

[76] Yongfang Li. Molecular design of photovoltaic materials for polymer solar cells: toward suitable electronic energy levels and broad absorption. *Accounts of chemical research*, 45(5):723–733, 2012.

[77] Youjun He and Yongfang Li. Fullerene derivative acceptors for high performance polymer solar cells. *Phys. Chem. Chem. Phys.*, 13:1970–1983, 2011.

[78] Youjun He, Hsiang-Yu Chen, Jianhui Hou, and Yongfang Li. Indene-c60 bisadduct: A new acceptor for high-performance polymer solar cells. *Journal of the American Chemical Society*, 132(4):1377–1382, 2010. PMID: 20055460.

[79] Guangjin Zhao, Youjun He, and Yongfang Li. 6.5poly(3-hexylthiophene) and indene-c60 bisadduct by device optimization. *Advanced Materials*, 22(39):4355–4358, 2010.

[80] Günter Schopf and Gerhard Koßmehl. *Polythiophenes-electrically conductive polymers*, volume 129. Springer Berlin, 1997.

[81] Diana K. Susarova, Andrey E. Goryachev, Dmitry V. Novikov, Nadezhda N. Dremova, Svetlana M. Peregudova, Vladimir F. Razumov, and Pavel A. Troshin. Material solubility effects in bulk heterojunction solar cells based on the biscyclopropane fullerene adducts and {P3HT}. *Solar Energy Materials and Solar Cells*, 120, Part A(0):30 – 36, 2014.

[82] Myoung Hee Yun, Gi-Hwan Kim, Changduk Yang, and Jin Young Kim. Towards optimization of p3ht: bispcbm composites for highly efficient polymer solar cells. *Journal of Materials Chemistry*, 20(36):7710–7714, 2010.

[83] Ala'a F. Eftaiha, Jon-Paul Sun, Ian G. Hill, and Gregory C. Welch. Recent advances of non-fullerene, small molecular acceptors for solution processed bulk heterojunction solar cells. *J. Mater. Chem. A*, 2:1201–1213, 2014.

[84] Sarah Holliday, Raja Shahid Ashraf, Christian B. Nielsen, Mindaugas Kirkus, Jason A. Röhr, Ching-Hong Tan, Elisa Collado-Fregoso, Astrid-Caroline Knall, James R. Durrant, Jenny Nelson, and Iain McCulloch. A rhodanine flanked nonfullerene acceptor for solution-processed organic photovoltaics. *Journal of the American Chemical Society*, 137(2):898–904, 2015. PMID: 25545017.

[85] Pabitra K Nayak, Ron Rosenberg, Lee Barnea-Nehoshtan, and David Cahen. O 2 and organic semiconductors: Electronic effects. *Organic Electronics*, 14(3):966–972, 2013.

[86] Sylvain Chambon, Agnès Rivaton, Jean-Luc Gardette, and Muriel Firon. Photo- and thermal degradation of mdmo-ppv: Pcbm blends. *Solar energy materials and solar cells*, 91(5):394–398, 2007.

[87] Agnès Rivaton, Sylvain Chambon, Matthieu Manceau, Jean-Luc Gardette, Noëlla Lemaître, and Stéphane Guillerez. Light-induced degradation of the active layer of polymer-based solar cells. *Polymer Degradation and Stability*, 95(3):278–284, 2010.

[88] Na Sai, Kevin Leung, Judit Zádor, and Graeme Henkelman. First principles study of photo-oxidation degradation mechanisms in p3ht for organic solar cells. *Physical Chemistry Chemical Physics*, 16(17):8092–8099, 2014.

[89] H Hintz, C Sessler, H Peisert, H-J Egelhaaf, and T Chassé. Wavelength-dependent pathways of poly-3-hexylthiophene photo-oxidation. *Chemistry of Materials*, 24(14):2739–2743, 2012.

[90] Matthieu Manceau, Agnès Rivaton, Jean-Luc Gardette, Stephane Guillerez, and Noëlla Lemaître. Light-induced degradation of the p3ht-based solar cells active layer. *Solar Energy Materials and Solar Cells*, 95(5):1315–1325, 2011.

[91] Axel D Becke. Perspective: Fifty years of density-functional theory in chemical physics. *The Journal of chemical physics*, 140(18):18A301, 2014.

[92] Richard Phillips Feynman. Forces in molecules. *Physical Review*, 56(4):340, 1939.

[93] Frank Neese. The orca program system. *Wiley Interdisciplinary Reviews: Computational Molecular Science*, 2(1):73–78, 2012.

[94] Roger Taylor and David RM Walton. The chemistry of fullerenes. 1993.

[95] Maurizio Prato. [60] fullerene chemistry for materials science applications. *Journal of Materials Chemistry*, 7(7):1097–1109, 1997.

[96] Stephen R Wilson, David I Schuster, Berthold Nuber, Mark S Meier, Michele Maggini, Maurizio Prato, and Roger Taylor. *Organic chemistry of fullerenes*. John Wiley and Sons: New York, 2000.

[97] Andreas Hirsch and Michael Brettreich. *Fullerenes: chemistry and reactions*. John Wiley & Sons, 2006.

[98] Andreas Hirsch, Qiaoying Li, and Fred Wudl. Globe-trotting hydrogens on the surface of the fullerene compound c60h6 (n (ch2ch2) 2o) 6. *Angewandte Chemie International Edition in English*, 30(10):1309–1310, 1991.

[99] Klaus-Dieter Kampe, Norbert Egger, and Martin Vogel. Diamino and tetraamino derivatives of buckminsterfullerene c60. *Angewandte Chemie International Edition in English*, 32(8):1174–1176, 1993.

[100] Ram Seshadri, A Govindaraj, R Nagarajan, T Pradeep, and CNR Rao. Addition of amines and halogens to fullerenes c 60 and c 70. *Tetrahedron letters*, 33(15):2069–2070, 1992.

[101] Andreas Skiebe, Andreas Hirsch, Holger Klos, and Bernd Gotschy. [dbu] c 60. spin pairing in a fullerene salt. *Chemical physics letters*, 220(1):138–140, 1994.

[102] Manolis D. Tzirakis and Michael Orfanopoulos. Radical reactions of fullerenes: From synthetic organic chemistry to materials science and biology. *Chemical Reviews*, 113(7):5262–5321, 2013. PMID: 23570603.

[103] Konstantinos Kordatos and Maurizio Prato. Fullerene-based materials. In *Functionalized Fullerenes: Proceedings of the International Symposium*, volume 9, page 45. The Electrochemical Society, 2000.

[104] Kosmas Prassides and Henri Alloul. *Fullerene-based materials: structures and properties*, volume 109. Springer Science & Business Media, 2004.

[105] Carsten Bingel. Cyclopropanierung von fullerenen. *Chemische Berichte*, 126(8):1957–1959, 1993.

[106] Xavier Camps and Andreas Hirsch. Efficient cyclopropanation of c 60 starting from malonates. *Journal of the Chemical Society, Perkin Transactions 1*, (11):1595–1596, 1997.

[107] Ming-Hung Liao, Yin-Yu Lai, Yu-Ying Lai, Yen-Ting Chen, Che-En Tsai, Wei-Wei Liang, and Yen-Ju Cheng. Reducing regioisomers of fullerene-bisadducts by tether-directed remote functionalization: Investigation of electronically and sterically isomeric effects on bulk-heterojunction solar cells. *ACS Applied Materials & Interfaces*, 6(2):996–1004, 2014. PMID: 24344911.

[108] Koichi Mikami, Shoji Matsumoto, Yasutaka Okubo, Mamoru Fujitsuka, Osamu Ito, Tomoyoshi Suenobu, and Shunichi Fukuzumi. Stepwise bond formation in photochemical and thermal diels-alder reactions of c60 with danishefsky's dienes. *Journal of the American Chemical Society*, 122(10):2236–2243, 2000.

[109] Yves Rubin, Saeed Khan, Daron I Freedberg, and Chahan Yeretzian. Synthesis and x-ray structure of a diels-alder adduct of fullerene c60. *Journal of the American Chemical Society*, 115(1):344–345, 1993.

[110] Andreas Hirsch, Iris Lamparth, and Heinrich R Karfunkel. Fullerene chemistry in three dimensions: Isolation of seven regioisomeric bisadducts and chiral trisadducts of c60 and di (ethoxycarbonyl) methylene. *Angewandte Chemie International Edition in English*, 33(4):437–438, 1994.

[111] REINER Sustmann. Orbital energy control of cycloaddition reactivity. *Pure and Applied Chemistry*, 40(4):569–593, 1974.

[112] Qing Lu, David I Schuster, and Stephen R Wilson. Preparation and characterization of six bis (n-methylpyrrolidine)-c60 isomers: magnetic deshielding in isomeric bisadducts of c60. *The Journal of organic chemistry*, 61(14):4764–4768, 1996.

[113] Junia Melin, Paul W Ayers, and Joseph Vincent Ortiz. Removing electrons can increase the electron density: a computational study of negative fukui functions. *The Journal of Physical Chemistry A*, 111(40):10017–10019, 2007.

[114] Patrick Bultinck, Ramon Carbó-Dorca, and Wilfried Langenaeker. Negative fukui functions: New insights based on electronegativity equalization. *The Journal of chemical physics*, 118(10):4349–4356, 2003.

[115] H Santos Silva, SL Nogueira, JE Manzoli, NM Barbosa Neto, A Marletta, F Serein-Spirau, J-P Lere-Porte, Sandrine Lois, and RA Silva. Controlling bandgap energy and multivibronic modes of a poly (2, 5-thiophene-1, 4-dialkoxyphenylene) derivative by gamma photons. *The Journal of Physical Chemistry A*, 115(29):8288–8294, 2011.

[116] Mauricio Foschini, Hugo Santos Silva, Raigna A Silva, Alexandre Marletta, and Débora Gonçalves. Theoretical and experimental studies on the electronic, optical, and structural properties of poly-pyrrole-2-carboxylic acid films. *Chemical Physics*, 425:91–95, 2013.

[117] Christoph J Brabec, Antonio Cravino, Dieter Meissner, N Serdar Sariciftci, Thomas Fromherz, Minze T Rispens, Luis Sanchez, and Jan C Hummelen. Origin of the open circuit voltage of plastic solar cells. *Advanced Functional Materials*, 11(5):374–380, 2001.

[118] Antonio Facchetti, Myung-Han Yoon, Charlotte L Stern, Howard E Katz, and Tobin J Marks. Building blocks for n-type organic electronics: Regiochemically modulated inversion of majority carrier sign in perfluoroarene-modified polythiophene semiconductors. *Angewandte Chemie International Edition*, 42(33):3900–3903, 2003.

[119] Maxwell J Robb, Sung-Yu Ku, Fulvio G Brunetti, and Craig J Hawker. A renaissance of color: New structures and building blocks for organic electronics. *Journal of Polymer Science Part A: Polymer Chemistry*, 51(6):1263–1271, 2013.

[120] Kazuo Takimiya, Itaru Osaka, and Masahiro Nakano. $\pi$-building blocks for organic electronics: revaluation of inductive and resonance effects of $\pi$-electron deficient units. *Chemistry of Materials*, 26(1):587–593, 2013.

[121] Ralf Stowasser and Roald Hoffmann. What do the kohn-sham orbitals and eigenvalues mean? *Journal of the American Chemical Society*, 121(14):3414–3420, 1999.

[122] E. J. Baerends and O. V. Gritsenko. A quantum chemical view of density functional theory. *The Journal of Physical Chemistry A*, 101(30):5383–5403, 1997.

[123] Alexandre M Nardes, Andrew J Ferguson, James B Whitaker, Bryon W Larson, Ross E Larsen, Klára Maturová, Peter A Graf, Olga V Boltalina, Steven H Strauss, and Nikos Kopidakis. Beyond pcbm: Understanding the photovoltaic performance of blends of indene-c60 multiadducts with poly (3-hexylthiophene). *Advanced Functional Materials*, 22(19):4115–4127, 2012.

[124] Martijn Lenes, Gert-Jan AH Wetzelaer, Floris B Kooistra, Sjoerd C Veenstra, Jan C Hummelen, and Paul WM Blom. Fullerene bisadducts for enhanced open-circuit voltages and efficiencies in polymer solar cells. *Advanced Materials*, 20(11):2116–2119, 2008.

[125] Noach Treitel, Roy Shenhar, Ivan Aprahamian, Tuvia Sheradsky, and Mordecai Rabinovitz. Calculations of pah anions: When are diffuse functions necessary? *Physical Chemistry Chemical Physics*, 6(6):1113–1121, 2004.

[126] Maryam Anafcheh, Reza Ghafouri, and Nasser L Hadipour. A computational proof toward correlation between the theoretical chemical concept of electrophilicity index for the acceptors of c60 and c70 fullerene derivatives with the open-circuit voltage of polymer-fullerene solar cells. *Solar Energy Materials and Solar Cells*, 105:125–131, 2012.

[127] Robert G. Parr, László v. Szentpály, and Shubin Liu. Electrophilicity index. *Journal of the American Chemical Society*, 121(9):1922–1924, 1999.

[128] Rudolph A Marcus. On the theory of oxidation-reduction reactions involving electron transfer. i. *The Journal of Chemical Physics*, 24(5):966–978, 1956.

[129] Yi-Kang Lan, Cheng Han Yang, and Hsiao-Ching Yang. Theoretical investigations of electronic structure and charge transport properties in polythiophene-based organic field-effect transistors. *Polymer International*, 59(1):16–21, 2010.

[130] Jean-Luc Brédas, David Beljonne, Veaceslav Coropceanu, and Jérôme Cornil. Charge-transfer and energy-transfer processes in $\pi$-conjugated oligomers and polymers: a molecular picture. *Chemical Reviews*, 104(11):4971–5004, 2004.

[131] Roel S Sánchez-Carrera. *Theoretical characterization of charge transport in organic molecular crystals*. ProQuest, 2008.

[132] Andreas Gügel, Pavel Belik, Michael Walter, Alexander Kraus, Eva Harth, Manfred Wagner, Jochen Spickermann, and Klaus Müllen. The repetitive diels-alder reaction: A new approach to [60] fullerene maindashchain polymers. *Tetrahedron*, 52(14):5007–5014, 1996.

[133] Rebecca Sure and Stefan Grimme. Corrected small basis set hartree-fock method for large systems. *Journal of computational chemistry*, 34(19):1672–1685, 2013.

[134] Yosei Shibata, Takahiro Kono, Nagatoshi Komura, and Yuji Yoshida. Structural control of bulk heterojunction films based on oligothiophene with sterically-bulky groups. *Organic Electronics*, 14(4):1073–1080, 2013.

[135] Masayuki Chikamatsu, Shuichi Nagamatsu, Yuji Yoshida, Kazuhiro Saito, Kiyoshi Yase, and Koichi Kikuchi. Solution-processed n-type organic thin-film transistors with high field-effect mobility. *Applied Physics Letters*, 87(20):203504–203504, 2005.

[136] Xiangyue Meng, Qi Xu, Wenqing Zhang, Zhan?ao Tan, Yongfang Li, Zhuxia Zhang, Li Jiang, Chunying Shu, and Chunru Wang. Effects of alkoxy chain length in alkoxy-substituted dihydronaphthyl-based [60] fullerene bisadduct acceptors on their photovoltaic properties. *ACS applied materials & interfaces*, 4(11):5966–5973, 2012.

[137] Takashi Nakanishi, Yanfei Shen, Jiaobing Wang, Shiki Yagai, Masahiro Funahashi, Takashi Kato, Paulo Fernandes, Helmuth Mo?hwald, and Dirk G Kurth. Electron transport and electrochemistry of mesomorphic fullerenes with long-range ordered lamellae. *Journal of the American Chemical Society*, 130(29):9236–9237, 2008.

[138] Lukas Schmidt-Mende, Andreas Fechtenkötter, Klaus Müllen, Ellen Moons, Richard H Friend, and JD MacKenzie. Self-organized discotic liquid crystals for high-efficiency organic photovoltaics. *Science*, 293(5532):1119–1122, 2001.

[139] Sandeep Kumar, Ellen J Wachtel, and Ehud Keinan. Hexaalkoxytricycloquinazolines: new discotic liquid crystals. *The Journal of Organic Chemistry*, 58(15):3821–3827, 1993.

[140] Sergey Sergeyev, Wojciech Pisula, and Yves Henri Geerts. Discotic liquid crystals: a new generation of organic semiconductors. *Chemical Society Reviews*, 36(12):1902–1929, 2007.

[141] Li-Yin Chen, Fei-Hsiung Chien, Yen-Wei Liu, Wenjun Zheng, Cheng-Yan Chiang, Chia-Yi Hwang, Chi-Wi Ong, Yi-Kang Lan, and Hsiao Ching Yang. Ambipolar carrier transport properties in a built-in donor–acceptor discogen. *Organic Electronics*, 14(8):2065–2070, 2013.

[142] AW Van der Made and RH Van der Made. A convenient procedure for bromomethylation of aromatic compounds. selective mono-, bis-, or trisbromomethylation. *The Journal of Organic Chemistry*, 58(5):1262–1263, 1993.

[143] Guan-Wu Wang, Koichi Komatsu, Yasujiro Murata, and Motoo Shiro. Synthesis and x-ray structure of dumb-bell-shaped c120. *Nature*, 387(6633):583–586, 1997.

[144] G Blanc. *Bull. Soc. Chim. France*, 33:313, 1923.

[145] Reynold C Fuson and CH McKeever. Chloromethylation of aromatic compounds. *Organic reactions*, 1942.

[146] Wallace FrankáShort et al. Liv.?the introduction of the chloromethyl group into the aromatic nucleus. *Journal of the Chemical Society, Transactions*, 117:510–527, 1920.

[147] Reginald H Mitchell and Vivekanantan S Iyer. An improved procedure for bromomethylation of aromatics using phase-transfer catalysis. rapid bis-haloalkylation. *Synlett*, 1989(01):55–57, 1989.

[148] Leonid I Belen'kii, Yu B Vol'kenshtein, and IB Karmanova. New data on the chloromethylation of aromatic and heteroaromatic compounds. *Russian Chemical Reviews*, 46(9):891, 1977.

[149] Zhengping Fang, Pingan Song, Lifang Tong, and Zhenghong Guo. Thermal degradation and flame retardancy of polypropylene/c 60 nanocomposites. *Thermochimica Acta*, 473(1):106–108, 2008.

[150] OF Pozdnyakov, BP Redkov, GK Lebedeva, LS Litvinova, VN Ivanova, AO Pozdnyakov, and VV Kudryavtsev. Effect of the film thickness on the thermal stability of submicron polymer layers containing fullerene c60. *Technical Physics Letters*, 28(3):188–190, 2002.

[151] Jin-Shan Wang and Krzysztof Matyjaszewski. Controlled/" living" radical polymerization. halogen atom transfer radical polymerization promoted by a cu (i)/cu (ii) redox process. *Macromolecules*, 28(23):7901–7910, 1995.

[152] Richard G Jones, Edward S Wilks, W Val Metanomski, Jaroslav Kahovec, Michael Hess, Robert Stepto, and Tatsuki Kitayama. *Compendium of Polymer Terminology and Nomenclature: IUPAC Recommendations, 2008.* Royal Society of Chemistry Cambridge, 2009.

[153] Krzysztof Matyjaszewski. Ranking living systems. *Macromolecules*, 26(7):1787–1788, 1993.

[154] Eldar B Zeynalov and Joerg F Friedrich. Anti-radical activity of fullerenes and carbon nanotubes in reactions of radical polymerization and polymer thermal/thermo-oxidative degradation: A review. *Materials Testing*, 49(5):265–270, 2007.

[155] RS Ruoff, Doris S Tse, Ripudaman Malhotra, and Donald C Lorents. Solubility of fullerene (c60) in a variety of solvents. *The Journal of Physical Chemistry*, 97(13):3379–3383, 1993.

[156] Changduk Yang, Jae Kwan Lee, Alan J Heeger, and Fred Wudl. Well-defined donor–acceptor rod–coil diblock copolymers based on p3ht containing c 60: the morphology and role as a surfactant in bulk-heterojunction solar cells. *Journal of Materials Chemistry*, 19(30):5416–5423, 2009.

[157] AM Rao, Ping Zhou, Kai-An Wang, GT Hager, JM Holden, Ying Wang, W-T Lee, Xiang-Xin Bi, PC Ecklund, and DS Cornett. Photoinduced polymerization of solid c60 films. *Science*, 259:955–957, 1993.

[158] Shende Jiang and Gurdial Singh. Chemical synthesis of shikimic acid and its analogues. *Tetrahedron*, 54(19):4697–4753, 1998.

[159] Haruyuki Okamura, Yasujiro Murata, Masahiko Minoda, Koichi Komatsu, Takeaki Miyamoto, and Terence SM Wan. Synthesis of disubstituted 1, 2-dihydro [60] fullerenes with well-defined structure by addition of 1-alkoxy-1-chloroethanes to 2-(1-octynyl)-1, 2-dihydro [60] fulleren-1-ide ion. *The Journal of Organic Chemistry*, 61(24):8500–8502, 1996.

[160] Shunichi Fukuzumi, Hisahiro Mori, Tomoyoshi Suenobu, Hiroshi Imahori, Xiang Gao, and Karl M Kadish. Effects of lowering symmetry on the esr spectra of radical anions of fullerene derivatives and the reduction potentials. *The Journal of Physical Chemistry A*, 104(46):10688–10694, 2000.

[161] Shunichi Fukuzumi, Tomoyoshi Suenobu, Xiang Gao, and Karl M Kadish. Splitting of degenerate orbitals of dibenzyl and tetrabenzyl adducts of c60: Esr of the radical anions and the rotation barriers of benzyl groups. *The Journal of Physical Chemistry A*, 104(13):2908–2913, 2000.

[162] Karl M Kadish, Xiang Gao, Eric Van Caemelbecke, Tomoyoshi Suenobu, and Shunichi Fukuzumi. Electrosynthesis and structural characterization of two (c6h5ch2) 4c60 isomers. *Journal of the American Chemical Society*, 122(4):563–570, 2000.

[163] Karl M Kadish, Xiang Gao, Eric Van Caemelbecke, Takeomi Hirasaka, Tomoyoshi Suenobu, and Shunichi Fukuzumi. Synthesis and spectroscopic and electrochemical characterization of di-and tetrasubstituted c60 derivatives. *The Journal of Physical Chemistry A*, 102(22):3898–3906, 1998.

[164] Tsuyoshi Michinobu, Takashi Nakanishi, Jonathan P Hill, Masahiro Funahashi, and Katsuhiko Ariga. Room temperature liquid fullerenes: an uncommon morphology of c60 derivatives. *Journal of the American Chemical Society*, 128(32):10384–10385, 2006.

[165] Karl M Kadish, Xiang Gao, Eric Van Caemelbecke, Tomoyoshi Suenobu, and Shunichi Fukuzumi. Effect of addition pattern on the electrochemical and spectroscopic properties of neutral and reduced 1, 2-and 1, 4-(c6h5ch2) 2c60 isomers. *The Journal of Physical Chemistry A*, 104(17):3878–3883, 2000.

[166] OF Pozdnyakov, AO Pozdnyakov, B Schmaltz, and C Mathis. Thermal degradation in bulk and thin films of 2-, 4-, and 6-arm polystyrene stars with a c 60 core. *Polymer*, 47(4):1028–1035, 2006.

[167] Nadia Grossiord, Jan M Kroon, Ronn Andriessen, and Paul WM Blom. Degradation mechanisms in organic photovoltaic devices. *Organic Electronics*, 13(3):432–456, 2012.

[168] Aurélien Tournebize, Pierre-Olivier Bussière, Pascal Wong-Wah-Chung, Sandrine Thérias, Agnès Rivaton, Jean-Luc Gardette, Serge Beaupré, and Mario Leclerc. Impact of uv-visible light on the morphological and photochemical behavior of a low-bandgap poly (2, 7-carbazole) derivative for use in high-performance solar cells. *Advanced Energy Materials*, 3(4):478–487, 2013.

[169] Roger Taylor, Jonathan P Parsons, Anthony G Avent, Steven P Rannard, T John Dennis, Jonathan P Hare, Harold W Kroto, and David RM Walton. Degradation of c60 by light. *Nature*, 351:277, 1991.

[170] Yongqiang Tan and Daniel E Resasco. Dispersion of single-walled carbon nanotubes of narrow diameter distribution. *The Journal of Physical Chemistry B*, 109(30):14454–14460, 2005.

[171] Fortunato Piersimoni, Giedrius Degutis, Sabine Bertho, Koen Vandewal, Donato Spoltore, Tim Vangerven, Jeroen Drijkoningen, Marlies K Van Bael, An Hardy, Jan D'Haen, et al. Influence of fullerene photodimerization on the pcbm crystallization in polymer: Fullerene bulk heterojunctions under thermal stress. *Journal of Polymer Science Part B: Polymer Physics*, 51(16):1209–1214, 2013.

[172] Amit Kumar, F Singh, SM Shivaprasad, DK Avasthi, JC Pivin, et al. X-ray photoelectron and x-ray auger electron spectroscopy studies of heavy ion irradiated c 60 films. *Applied Surface Science*, 254(22):7280–7284, 2008.

[173] H Yamawaki, M Yoshida, Y Kakudate, S Usuba, H Yokoi, S Fujiwara, K Aoki, R Ruoff, R Malhotra, and D Lorents. Infrared study of vibrational property and polymerization of fullerene c60 and c70 under pressure. *The Journal of Physical Chemistry*, 97(43):11161–11163, 1993.

[174] Andreas Distler, Tobias Sauermann, Hans-Joachim Egelhaaf, Sheila Rodman, Dave Waller, Kap-Soo Cheon, Mike Lee, and Dirk M Guldi. The effect of pcbm dimerization on the performance of bulk heterojunction solar cells. *Advanced Energy Materials*, 4(1), 2014.

[175] Holger Hintz, H-J Egelhaaf, Larry Lu?er, Jens Hauch, Heiko Peisert, and Thomas Chassé. Photodegradation of p3ht- a systematic study of environmental factors. *Chemistry of Materials*, 23(2):145–154, 2010.

[176] H Hintz, H Peisert, H-J Egelhaaf, and T Chassé. Reversible and irreversible light-induced p-doping of p3ht by oxygen studied by photoelectron spectroscopy (xps/ups). *The Journal of Physical Chemistry C*, 115(27):13373–13376, 2011.

[177] Dimitris Pantazis, Stergios Pispas, and Nikos Hadjichristidis. Synthesis and stability of linear and star polymers containing [c60] fullerene. *Journal of Polymer Science Part A: Polymer Chemistry*, 39(14):2494–2507, 2001.

[178] Ping?an Song, Yan Zhu, Lifang Tong, and Zhengping Fang. C60 reduces the flammability of polypropylene nanocomposites by in situ forming a gelled-ball network. *Nanotechnology*, 19(22):225707, 2008.

[179] BM Ginzburg, AO Pozdnyakov, VN Zgonnik, OF Podzdnyakov, BP Redkov, E Yu Melenevskaya, and LV Vinogradova. Influence of fullerene on the thermal stability of free and grafted polystyrene. *Technical Physics Letters*, 22:166–167, 1996.

[180] AO Pozdnyakov, OF Pozdnyakov, BP Redkov, VN Zgonnik, LV Vinogradova, E Yu Melenevskaya, and BM Ginzburg. The effect of polystyrene on the thermal behavior of c60 fullerene. *Technical Physics Letters*, 22:759–760, 1996.

[181] BM Ginzburg, AO Pozdnyakov, OF Pozdnyakov, and BP Redkov. Mechanism for thermal destruction of polystyrene grafted to fullerene c 60. *Technical Physics Letters*, 25(10):812–814, 1999.

[182] Ting-Hu Zhang, Ping Lu, Fan Wang, and Guan-Wu Wang. Reaction of [60] fullerene with free radicals generated from active methylene compounds by manganese (iii) acetate dihydrate. *Organic & biomolecular chemistry*, 1(24):4403–4407, 2003.

[183] N Colin Baird. Quantum organic photochemistry. ii. resonance and aromaticity in the lowest 3. pi.. pi.* state of cyclic hydrocarbons. *Journal of the American Chemical Society*, 94(14):4941–4948, 1972.

[184] Eleni Pavlopoulou, Guillaume Fleury, Dargie Deribew, Fabrice Cousin, Mark Geoghegan, and Georges Hadziioannou. Phase separation-driven stratification in conventional and inverted p3ht: Pcbm organic solar cells. *Organic Electronics*, 14(5):1249–1254, 2013.

[185] Hyosung Choi, Junghoon Lee, Wonho Lee, Seo-Jin Ko, Renqiang Yang, Jeong Chul Lee, Han Young Woo, Changduk Yang, and Jin Young Kim. Acid-functionalized fullerenes used as interfacial layer materials in inverted polymer solar cells. *Organic Electronics*, 14(11):3138–3145, 2013.

[186] Xueli Cheng, Feng Li, and Yanyun Zhao. A dft investigation on zno clusters and nanostructures. *Journal of Molecular Structure: THEOCHEM*, 894(1):121–127, 2009.

[187] Yongliang Yong, Bin Song, and Pimo He. Growth pattern and electronic properties of cluster-assembled material based on zn12o12: A density-functional study. *The Journal of Physical Chemistry C*, 115(14):6455–6461, 2011.

[188] Mingwen Zhao, Yueyuan Xia, Zhenyu Tan, Xiangdong Liu, and Liangmo Mei. Design and energetic characterization of zno clusters from first-principles calculations. *Physics Letters A*, 372(1):39–43, 2007.

[189] Baolin Wang, Shigeru Nagase, Jijun Zhao, and Guanghou Wang. Structural growth sequences and electronic properties of zinc oxide clusters (zno) n (n= 2-18). *The Journal of Physical Chemistry C*, 111(13):4956–4963, 2007.

[190] Ansgar Schäfer, Hans Horn, and Reinhart Ahlrichs. Fully optimized contracted gaussian basis sets for atoms li to kr. *The Journal of Chemical Physics*, 97(4):2571–2577, 1992.

[191] Stefan Grimme. Semiempirical gga-type density functional constructed with a long-range dispersion correction. *Journal of computational chemistry*, 27(15):1787–1799, 2006.

[192] Per-Olov Löwdin. On the non-orthogonality problem connected with the use of atomic wave functions in the theory of molecules and crystals. *The Journal of Chemical Physics*, 18(3):365–375, 1950.

[193] Xin Guo, Martin Baumgarten, and Klaus Müllen. Designing $\pi$-conjugated polymers for organic electronics. *Progress in Polymer Science*, 38(12):1832–1908, 2013.

[194] Adam Pron, Pawel Gawrys, Malgorzata Zagorska, David Djurado, and Renaud Demadrille. Electroactive materials for organic electronics: preparation strategies, structural aspects and characterization techniques. *Chemical Society Reviews*, 39(7):2577–2632, 2010.

[195] Delwin L Elder, Stephanie J Benight, Jinsheng Song, Bruce H Robinson, and Larry R Dalton. Matrix-assisted poling of monolithic bridge-disubstituted organic nlo chromophores. *Chemistry of Materials*, 26(2):872–874, 2014.

[196] Jonathan Rivnay, Róisín M Owens, and George G Malliaras. The rise of organic bioelectronics. *Chemistry of Materials*, 26(1):679–685, 2013.

[197] Quan Li. *Intelligent Stimuli-Responsive Materials: From Well-Defined Nanostructures to Applications.* John Wiley & Sons, 2013.

[198] Pierre M Beaujuge, Hoi Nok Tsao, Michael Ryan Hansen, Chad M Amb, Chad Risko, Jegadesan Subbiah, Kaushik Roy Choudhury, Alexei Mavrinskiy, Wojciech Pisula, Jean-Luc Bre?das, et al. Synthetic principles directing charge transport in low-band-gap dithienosilole–benzothiadiazole copolymers. *Journal of the American Chemical Society*, 134(21):8944–8957, 2012.

[199] Xumeng Wu, Xuanrong Sun, Zhiqian Guo, Jianbin Tang, Youqing Shen, Tony D James, He Tian, and Weihong Zhu. In vivo and in situ tracking cancer chemotherapy by highly photostable nir fluorescent theranostic prodrug. *Journal of the American Chemical Society*, 136(9):3579–3588, 2014.

[200] Sebastiano Bellani, Daniele Fazzi, Paola Bruno, Ester Giussani, Eleonora Valeria Canesi, Guglielmo Lanzani, and Maria Rosa Antognazza. Reversible p3ht/oxygen charge transfer complex identification in thin films exposed to direct contact with water. *The Journal of Physical Chemistry C*, 118(12):6291–6299, 2014.

[201] Aurélien Tournebize, Agnès Rivaton, Jean-Luc Gardette, Christian Lombard, Brigitte Pépin-Donat, Serge Beaupré, and Mario Leclerc. How photoinduced crosslinking under operating conditions can reduce pcdtbt-based solar cell efficiency and then stabilize it. *Advanced Energy Materials*, 4(10), 2014.

[202] Agnès Rivaton, Aurélien Tournebize, Julien Gaume, Pierre-Olivier Bussière, Jean-Luc Gardette, and Sandrine Therias. Photostability of organic materials used in polymer solar cells. *Polymer International*, 63(8):1335–1345, 2014.

[203] MR Kamal, B Huang, SH Hamid, MB Amin, and AG Maadhah. Handbook of polymer degradation. *ed. By SH Hamid, MB Amin, and AG Maadhah*, pages 127–168, 1992.

[204] Jan F Rabek and Jan F Rabek. *Photodegradation of polymers.* Springer Berlin, 1996.

[205] J-L Gardette. Fundamental and technical aspects of the photooxidation of polymers. *ENVIRONMENTAL SCIENCE AND POLLUTION CONTROL SERIES*, pages 671–698, 2000.

[206] Mélanie Gardette, Anthony Perthue, Jean-Luc Gardette, Tünde Janecska, Enikő Földes, Béla Pukánszky, and Sandrine Therias. Photo-and thermal-oxidation of polyethylene: Comparison of mechanisms and influence of unsaturation content. *Polymer Degradation and Stability*, 98(11):2383–2390, 2013.

[207] Matthieu Manceau, Agnès Rivaton, Jean-Luc Gardette, Stéphane Guillerez, and Noëlla Lemaître. The mechanism of photo-and thermooxidation of poly (3-hexylthiophene)(p3ht) reconsidered. *Polymer Degradation and Stability*, 94(6):898–907, 2009.

[208] Aurélien Tournebize, Pierre-Olivier Bussière, Agnes Rivaton, Jean-Luc Gardette, Hussein Medlej, Roger C Hiorns, Christine Dagron-Lartigau, Frederik C Krebs, and Kion Norrman. New insights into the mechanisms of photodegradation/stabilization of p3ht: Pcbm active layers using poly (3-hexyl-d 13-thiophene). *Chemistry of Materials*, 25(22):4522–4528, 2013.

[209] JL Bolland and Geoffrey Gee. Kinetic studies in the chemistry of rubber and related materials. ii. the kinetics of oxidation of unconjugated olefins. *Transactions of the Faraday Society*, 42:236–243, 1946.

[210] L Audouin, V Langlois, J Verdu, and JCM De Bruijn. Role of oxygen diffusion in polymer ageing: kinetic and mechanical aspects. *Journal of Materials science*, 29(3):569–583, 1994.

[211] Nicolas Blouin, Alexandre Michaud, David Gendron, Salem Wakim, Emily Blair, Rodica Neagu-Plesu, Michel Belletete, Gilles Durocher, Ye Tao, and Mario Leclerc. Toward a rational design of poly (2, 7-carbazole) derivatives for solar cells. *Journal of the American Chemical Society*, 130(2):732–742, 2008.

[212] Pierre-Luc T Boudreault, Ahmed Najari, and Mario Leclerc. Processable low-bandgap polymers for photovoltaic applications? *Chemistry of Materials*, 23(3):456–469, 2010.

[213] Brett VanVeller, Derek J Schipper, and Timothy M Swager. Polycyclic aromatic triptycenes: Oxygen substitution cyclization strategies. *Journal of the American Chemical Society*, 134(17):7282–7285, 2012.

[214] Andrew C Grimsdale, Khai Leok Chan, Rainer E Martin, Pawel G Jokisz, and Andrew B Holmes. Synthesis of light-emitting conjugated polymers for applications in electroluminescent devices. *Chemical reviews*, 109(3):897–1091, 2009.

[215] J Roncali. Molecular engineering of the band gap of $\pi$-conjugated systems: Facing technological applications. *Macromolecular Rapid Communications*, 28(17):1761–1775, 2007.

[216] Guy Koeckelberghs, Marnix Vangheluwe, Celest Samyn, André Persoons, and Thierry Verbiest. Regioregular poly (3-alkoxythiophene) s: toward soluble, chiral conjugated polymers with a stable oxidized state. *Macromolecules*, 38(13):5554–5559, 2005.

[217] Yongye Liang, Zheng Xu, Jiangbin Xia, Szu-Ting Tsai, Yue Wu, Gang Li, Claire Ray, and Luping Yu. For the bright future?bulk heterojunction polymer solar cells with power conversion efficiency of 7.4%. *Advanced Materials*, 22(20):E135–E138, 2010.

[218] Farid Ouhib, Ahmed Dkhissi, Pierre Iratçabal, Roger C Hiorns, Abdel Khoukh, Jacques Desbrières, Claude Pouchan, and Christine Dagron-Lartigau. Electronic structure and optical properties of poly [3-(4-octylphenoxy) thiophene]: Experimental and theoretical studies. *Journal of Polymer Science Part A: Polymer Chemistry*, 46(22):7505–7516, 2008.

[219] Sylvain Chambon, Agnès Rivaton, Jean-Luc Gardette, and Muriel Firon. Photo- and thermal degradation of mdmo-ppv: Pcbm blends. *Solar energy materials and solar cells*, 91(5):394–398, 2007.

[220] Stephen J Blanksby and G Barney Ellison. Bond dissociation energies of organic molecules. *Accounts of Chemical Research*, 36(4):255–263, 2003.

[221] F Posada, P Malfreyt, and J-L Gardette. Hydrogen abstraction from poly (propylene) and poly (propylene oxide) by hydroxyl radicals: a computational quantum semi-empirical study. *Computational and Theoretical Polymer Science*, 11(2):95–104, 2001.

[222] Fabrice Posada, Jean-Louis Philippart, Patrick Kappler, and Jean-Luc Gardette. Photooxidation of cured fluorinated polymers?i. photooxidation of copolymers of fluorinated olefins and allyl or vinyl ethers. *Polymer degradation and stability*, 50(2):141–158, 1995.

[223] Ganna Gryn?ova, KU Ingold, and Michelle L Coote. New insights into the mechanism of amine/nitroxide cycling during the hindered amine light stabilizer inhibited oxidative degradation of polymers. *Journal of the American Chemical Society*, 134(31):12979–12988, 2012.

[224] Ivan Rossi, Alessandro Venturini, and Alessandro Zedda. Modeling hindered-amine light stabilizer-promoted polymer stabilization: computational insight into the mechanism for nitroxyl radical regeneration from aminoethers. *Journal of the American Chemical Society*, 121(34):7914–7917, 1999.

[225] Warren J Hehre, Robert Ditchfield, and John A Pople. Self?consistent molecular orbital methods. xii. further extensions of gaussian?type basis sets for use in molecular orbital studies of organic molecules. *The Journal of Chemical Physics*, 56(5):2257–2261, 1972.

[226] Didier Bégué, Greg GuangHua Qiao, and Curt Wentrup. Nitrile imines: matrix isolation, ir spectra, structures, and rearrangement to carbodiimides. *Journal of the American Chemical Society*, 134(11):5339–5350, 2012.

[227] James D Dill and John A Pople. Self-consistent molecular orbital methods. xv. extended gaussian-type basis sets for lithium, beryllium, and boron. *The Journal of Chemical Physics*, 62(7):2921–2923, 1975.

[228] Michelle M Francl, William J Pietro, Warren J Hehre, J Stephen Binkley, Mark S Gordon, Douglas J DeFrees, and John A Pople. Self-consistent molecular orbital methods. xxiii. a polarization-type basis set for second-row elements. *The Journal of Chemical Physics*, 77(7):3654–3665, 1982.

[229] Axel D Becke. Density-functional thermochemistry. iii. the role of exact exchange. *The Journal of Chemical Physics*, 98(7):5648–5652, 1993.

[230] Per-Olov Löwdin. On the nonorthogonality problem. *Advances in quantum chemistry*, 5:185–199, 1970.

[231] Sandrine Morlat and Jean-Luc Gardette. Phototransformation of water-soluble polymers. i: photo-and thermooxidation of poly (ethylene oxide) in solid state. *Polymer*, 42(14):6071–6079, 2001.

[232] Ying W Soon, Hoduk Cho, Jonathan Low, Hugo Bronstein, Iain McCulloch, and James R Durrant. Correlating triplet yield, singlet oxygen generation and photochemical stability in polymer/fullerene blend films. *Chemical Communications*, 49(13):1291–1293, 2013.

[233] Chris Rutherglen, Dheeraj Jain, and Peter Burke. Nanotube electronics for radiofrequency applications. *Nature Nanotechnology*, 4(12):811–819, 2009.

[234] Frank Schwierz. Graphene transistors. *Nature nanotechnology*, 5(7):487–496, 2010.

[235] Michael FL De Volder, Sameh H Tawfick, Ray H Baughman, and A John Hart. Carbon nanotubes: present and future commercial applications. *Science*, 339(6119):535–539, 2013.

[236] E Kymakis, I Alexandrou, and GAJ Amaratunga. High open-circuit voltage photovoltaic devices from carbon-nanotube-polymer composites. *Journal of applied physics*, 93(3):1764–1768, 2003.

[237] Brian J Landi, Ryne P Raffaelle, Stephanie L Castro, and Sheila G Bailey. Single-wall carbon nanotube–polymer solar cells. *Progress in photovoltaics: research and applications*, 13(2):165–172, 2005.

[238] Rahul Mukherjee, Abhay Varghese Thomas, Ajay Krishnamurthy, and Nikhil Koratkar. Photothermally reduced graphene as high-power anodes for lithium-ion batteries. *Acs Nano*, 6(9):7867–7878, 2012.

[239] Tarun Bhardwaj, Aleks Antic, Barbara Pavan, Veronica Barone, and Bradley D Fahlman. Enhanced electrochemical lithium storage by graphene nanoribbons. *Journal of the American Chemical Society*, 132(36):12556–12558, 2010.

[240] Freddie Withers, Thomas Hardisty Bointon, Monica Felicia Craciun, and Saverio Russo. All-graphene photodetectors. *ACS nano*, 7(6):5052–5057, 2013.

[241] Andrew J Ferguson, Jeffrey L Blackburn, and Nikos Kopidakis. Fullerenes and carbon nanotubes as acceptor materials in organic photovoltaics. *Materials Letters*, 90:115–125, 2013.

[242] Massimo Marcaccio and Francesco Paolucci. *Making and exploiting fullerenes, graphene, and carbon nanotubes*. Springer, 2014.

[243] B Kraabel, CH Lee, D McBranch, D Moses, NS Sariciftci, and AJ Heeger. Ultrafast photoinduced electron transfer in conducting polymer?buckminsterfullerene composites. *Chemical physics letters*, 213(3):389–394, 1993.

[244] Hongjie Dai. Carbon nanotubes: synthesis, integration, and properties. *Accounts of chemical research*, 35(12):1035–1044, 2002.

[245] P Byszewski and Z Klusek. Some properties of fullerenes and carbon nanotubes. *Optoelectronics Review*, (2):203–210, 2001.

[246] Gang Li, Vishal Shrotriya, Jinsong Huang, Yan Yao, Tom Moriarty, Keith Emery, and Yang Yang. High-efficiency solution processable polymer photovoltaic cells by self-organization of polymer blends. *Nature materials*, 4(11):864–868, 2005.

[247] Yanming Sun, Gregory C Welch, Wei Lin Leong, Christopher J Takacs, Guillermo C Bazan, and Alan J Heeger. Solution-processed small-molecule solar cells with 6.7% efficiency. *Nature materials*, 11(1):44–48, 2012.

[248] B Paci, A Generosi, V Rossi Albertini, R Generosi, P Perfetti, R de Bettignies, and C Sentein. Time-resolved morphological study of bulk heterojunction films for efficient organic solar devices. *The Journal of Physical Chemistry C*, 112(26):9931–9936, 2008.

[249] Minh Trung Dang, Lionel Hirsch, Guillaume Wantz, and James D Wuest. Controlling the morphology and performance of bulk heterojunctions in solar cells. lessons learned from the benchmark poly (3-hexylthiophene):[6, 6]-phenyl-c61-butyric acid methyl ester system. *Chemical reviews*, 113(5):3734–3765, 2013.

[250] H Santos Silva, A Tournebize, D Bégué, H Peisert, T Chassé, J-L Gardette, S Therias, A Rivaton, and RC Hiorns. A universal route to improving conjugated macromolecule photostability. *RSC Advances*, 4(97):54919–54923, 2014.

[251] Kion Norrman, Morten V Madsen, Suren A Gevorgyan, and Frederik C Krebs. Degradation patterns in water and oxygen of an inverted polymer solar cell. *Journal of the American Chemical Society*, 132(47):16883–16892, 2010.

[252] Chao-Hsiang Hsieh, Yen-Ju Cheng, Pei-Jung Li, Chiu-Hsiang Chen, Martin Dubosc, Ru-Meng Liang, and Chain-Shu Hsu. Highly efficient and stable inverted polymer solar cells integrated with a cross-linked fullerene material as an interlayer. *Journal of the American Chemical Society*, 132(13):4887–4893, 2010.

[253] Martin Drees, Harald Hoppe, Christoph Winder, Helmut Neugebauer, Niyazi S Sariciftci, Wolfgang Schwinger, Friedrich Schäffler, Christoph Topf, Markus C Scharber, Zhengguo Zhu, et al. Stabilization of the nanomorphology of polymer–fullerene ?bulk heterojunction? blends using a novel polymerizable fullerene derivative. *Journal of Materials Chemistry*, 15(48):5158–5163, 2005.

[254] Bumjoon J Kim, Yoshikazu Miyamoto, Biwu Ma, and Jean MJ Frechet. Photocrosslinkable polythiophenes for efficient, thermally stable, organic photovoltaics. *Advanced functional materials*, 19(14):2273–2281, 2009.

[255] Steven K Hau, Hin-Lap Yip, Nam Seob Baek, Jingyu Zou, Kevin O?Malley, and Alex K-Y Jen. Air-stable inverted flexible polymer solar cells using zinc oxide nanoparticles as an electron selective layer. *Applied Physics Letters*, 92(25):253301, 2008.

[256] Li-Min Chen, Ziruo Hong, Gang Li, and Yang Yang. Recent progress in polymer solar cells: manipulation of polymer: fullerene morphology and the formation of efficient inverted polymer solar cells. *Advanced Materials*, 21(14-15):1434–1449, 2009.

[257] Patrick Heinstein, Christophe Ballif, and Laure-Emmanuelle Perret-Aebi. Building integrated photovoltaics (bipv): review, potentials, barriers and myths. *Green*, 3(2):125–156, 2013.

[258] Thomas Tromholt, Morten Vesterager Madsen, Jon E Carlé, Martin Helgesen, and Frederik C Krebs. Photochemical stability of conjugated polymers, electron acceptors and blends for polymer solar cells resolved in terms of film thickness and absorbance. *Journal of Materials Chemistry*, 22(15):7592–7601, 2012.

[259] S Ravaine, F Le Pecq, C Mingotaud, P Delhaes, JC Hummelen, F Wudl, and LK Patterson. Synthesis, physical characterizations, and langmuir films of new methanofullerenes. *The Journal of Physical Chemistry*, 99(23):9551–9557, 1995.

[260] Matthieu Manceau, Sylvain Chambon, Agnès Rivaton, Jean-Luc Gardette, Stephane Guillerez, and Noëlla Lemaître. Effects of long-term uv–visible light irradiation in the absence of oxygen on p3ht and p3ht: Pcbm blend. *Solar Energy Materials and Solar Cells*, 94(10):1572–1577, 2010.

[261] Andreas Distler, Peter Kutka, Tobias Sauermann, Hans-Joachim Egelhaaf, Dirk M Guldi, Daniele Di Nuzzo, Stefan CJ Meskers, and Rene? AJ Janssen. Effect of pcbm on the photodegradation kinetics of polymers for organic photovoltaics. *Chemistry of Materials*, 24(22):4397–4405, 2012.

[262] Matthew O Reese, Alexandre M Nardes, Benjamin L Rupert, Ross E Larsen, Dana C Olson, Matthew T Lloyd, Sean E Shaheen, David S Ginley, Garry Rumbles, and Nikos Kopidakis. Photoinduced degradation of polymer and polymer–fullerene active layers: experiment and theory. *Advanced Functional Materials*, 20(20):3476–3483, 2010.

[263] Carlo Thilgen and François Diederich. The higher fullerenes: covalent chemistry and chirality. In *Fullerenes and Related Structures*, pages 135–171. Springer, 1999.

[264] Michael Bühl and Andreas Hirsch. Spherical aromaticity of fullerenes. *Chemical reviews*, 101(5):1153–1184, 2001.

[265] H Kataura, Y Kumazawa, Y Maniwa, I Umezu, S Suzuki, Yo Ohtsuka, and Y Achiba. Optical properties of single-wall carbon nanotubes. *Synthetic metals*, 103(1):2555–2558, 1999.

[266] Kimberly A Worsley, Irina Kalinina, Elena Bekyarova, and Robert C Haddon. Functionalization and dissolution of nitric acid treated single-walled carbon nanotubes. *Journal of the American Chemical Society*, 131(50):18153–18158, 2009.

[267] O Gülseren, T Yildirim, and S Ciraci. Tunable adsorption on carbon nanotubes. *Physical review letters*, 87(11):116802, 2001.

[268] RC Haddon. Chemistry of the fullerenes: The manifestation of strain in a class of continuous aromatic molecules. *Science*, 261(5128):1545–1550, 1993.

[269] RC Haddon. C60: Sphere or polyhedron? *Journal of the American Chemical Society*, 119(7):1797–1798, 1997.

[270] RC Haddon. Comment on the relationship of the pyramidalization angle at a conjugated carbon atom to the $\sigma$ bond angles. *The Journal of Physical Chemistry A*, 105(16):4164–4165, 2001.

[271] Zhongfang Chen, Walter Thiel, and Andreas Hirsch. Reactivity of the convex and concave surfaces of single-walled carbon nanotubes (swcnts) towards addition reactions: Dependence on the carbon-atom pyramidalization. *ChemPhysChem*, 4(1):93–97, 2003.

[272] Sylvain Chambon, Matthieu Manceau, Muriel Firon, Stéphane Cros, Agnès Rivaton, and Jean-Luc Gardette. Photo-oxidation in an $^{18}o_2$ atmosphere: A powerful tool to elucidate the mechanism of uv–visible light oxidation of polymers–application to the photodegradation of mdmo-ppv. *Polymer*, 49(15):3288–3294, 2008.

[273] S Dag, O Gülseren, T Yildirim, and S Ciraci. Oxygenation of carbon nanotubes: Atomic structure, energetics, and electronic structure. *Physical Review B*, 67(16):165424, 2003.

[274] Seung Mi Lee, Young Hee Lee, Yong Gyoo Hwang, JR Hahn, and H Kang. Defect-induced oxidation of graphite. *Physical review letters*, 82(1):217, 1999.

[275] Roberta Borghi, Lodovico Lunazzi, Giuseppe Placucci, Paul J Krusic, David A Dixon, and Lon B Knight Jr. Regiochemistry of radical addition to c70. *The Journal of Physical Chemistry*, 98(21):5395–5398, 1994.

[276] Chengteh Lee, Weitao Yang, and Robert G Parr. Development of the colle-salvetti correlation-energy formula into a functional of the electron density. *Physical review B*, 37(2):785, 1988.

[277] SH Vosko, Ll Wilk, and M Nusair. Accurate spin-dependent electron liquid correlation energies for local spin density calculations: a critical analysis. *Canadian Journal of physics*, 58(8):1200–1211, 1980.

[278] PJ Stephens, FJ Devlin, CF Chabalowski, and Michael J Frisch. Ab initio calculation of vibrational absorption and circular dichroism spectra using density functional force fields. *The Journal of Physical Chemistry*, 98(45):11623–11627, 1994.

[279] Aurélien Tournebize, Jean-Luc Gardette, Christine Taviot-Guého, Didier Bégué, Marc Alexandre Arnaud, Christine Dagron-Lartigau, Hussein Medlej, Roger C Hiorns, Serge Beaupré, Mario Leclerc, et al. Is there a photostable conjugated polymer for efficient solar cells? *Polymer Degradation and Stability*, 2014.

[280] Yun Chen and Kou-Cheng Lin. Radical polymerization of styrene in the presence of c60. *Journal of Polymer Science Part A: Polymer Chemistry*, 37(15):2969–2975, 1999.

[281] Sarah Holliday. A rhodanine flanked non-fullerene acceptor for solution-processed organic photovoltaics. *Journal of the American Chemical Society*, 2014.

[282] Xin Zhang, Zhenhuan Lu, Long Ye, Chuanlang Zhan, Jianhui Hou, Shaoqing Zhang, Bo Jiang, Yan Zhao, Jianhua Huang, Shanlin Zhang, et al. A potential perylene diimide dimer-based acceptor material for highly efficient solution-processed non-fullerene organic solar cells with 4.03% efficiency. *Advanced Materials*, 25(40):5791–5797, 2013.

[283] Yuze Lin, Yifan Wang, Jiayu Wang, Jianhui Hou, Yongfang Li, Daoben Zhu, and Xiaowei Zhan. A star-shaped perylene diimide electron acceptor for high-performance organic solar cells. *Advanced Materials*, 26(30):5137–5142, 2014.

[284] Yue Zang, Chang-Zhi Li, Chu-Chen Chueh, Spencer T Williams, Wei Jiang, Zhao-Hui Wang, Jun-Sheng Yu, and Alex K-Y Jen. Integrated molecular, interfacial, and device engineering towards high-performance non-fullerene based organic solar cells. *Advanced Materials*, 26(32):5708–5714, 2014.

[285] Yuhang Liu, Cheng Mu, Kui Jiang, Jingbo Zhao, Yunke Li, Lu Zhang, Zhengke Li, Joshua Yuk Lin Lai, Huawei Hu, Tingxuan Ma, et al. A tetraphenylethylene core-based 3d structure small molecular acceptor enabling efficient non-fullerene organic solar cells. *Advanced Materials*, 2014.

[286] Eric Daniel Głowacki, Mihai Irimia-Vladu, Martin Kaltenbrunner, Jacek Gsiorowski, Matthew S White, Uwe Monkowius, Giuseppe Romanazzi, Gian Paolo Suranna, Piero Mastrorilli, Tsuyoshi Sekitani, et al. Hydrogen-bonded semiconducting pigments for air-stable field-effect transistors. *Advanced Materials*, 25(11):1563–1569, 2013.

[287] Thomas Lazar. Color chemistry: synthesis, properties, and applications of organic dyes and pigments, 2005.

[288] Nicholas E Jackson, Brett M Savoie, Kevin L Kohlstedt, Monica Olvera de la Cruz, George C Schatz, Lin X Chen, and Mark A Ratner. Controlling conformations of conjugated polymers and small molecules: The role of nonbonding interactions. *Journal of the American Chemical Society*, 135(28):10475–10483, 2013.

[289] Julien Ide?, Raphae?l Me?reau, Laurent Ducasse, Fre?de?ric Castet, Harald Bock, Yoann Olivier, Je?ro?me Cornil, David Beljonne, Gabriele D?Avino, Otello Maria Roscioni, et al. Charge dissociation at interfaces between discotic liquid crystals: The surprising role of column mismatch. *Journal of the American Chemical Society*, 136(7):2911–2920, 2014.

[290] Carla D Canestraro, Paula C Rodrigues, Cleber FN Marchiori, Camila B Schneider, Leni Akcelrud, Marlus Koehler, and Lucimara S Roman. The role of the double peaked absorption spectrum in the efficiency of solar cells based on donor–acceptor–donor copolymers. *Solar Energy Materials and Solar Cells*, 95(8):2287–2294, 2011.

[291] Richard L Martin. Natural transition orbitals. *The Journal of chemical physics*, 118(11):4775–4777, 2003.

[292] Aurélien Tournebize, Jean-Luc Gardette, Christine Taviot-Guého, Didier Bégué, Marc Alexandre Arnaud, Christine Dagron-Lartigau, Hussein Medlej, Roger C Hiorns, Serge Beaupré, Mario Leclerc, et al. Is there a photostable conjugated polymer for efficient solar cells? *Polymer Degradation and Stability*, 2014.

[293] Claudia Piliego, Thomas W Holcombe, Jessica D Douglas, Claire H Woo, Pierre M Beaujuge, and Jean MJ Fréchet. Synthetic control of structural order in n-alkylthieno [3, 4-c] pyrrole-4, 6-dione-based polymers for efficient solar cells. *Journal of the American Chemical Society*, 132(22):7595–7597, 2010.

[294] Yingping Zou, Ahmed Najari, Philippe Berrouard, Serge Beaupré, Badrou Re?da Ai?ch, Ye Tao, and Mario Leclerc. A thieno [3, 4-c] pyrrole-4, 6-dione-based copolymer for efficient solar cells. *Journal of the American Chemical Society*, 132(15):5330–5331, 2010.

[295] Badrou Réda Aïch, Jianping Lu, Serge Beaupré, Mario Leclerc, and Ye Tao. Control of the active layer nanomorphology by using co-additives towards high-performance bulk heterojunction solar cells. *Organic Electronics*, 13(9):1736–1741, 2012.

[296] James JP Stewart. Optimization of parameters for semiempirical methods vi: more modifications to the nddo approximations and re-optimization of parameters. *Journal of molecular modeling*, 19(1):1–32, 2013.

[297] James JP Stewart. Mopac: a semiempirical molecular orbital program. *Journal of computer-aided molecular design*, 4(1):1–103, 1990.

[298] MC Zerner. Zindo/s-ci a comprehensive semi-empirical scf/ci package. *Quantum Theory Project*, 1987.

[299] Rudolph Pariser and Robert G Parr. A semi-empirical theory of the electronic spectra and electronic structure of complex unsaturated molecules. i. *The Journal of Chemical Physics*, 21(3):466–471, 1953.

[300] Leszek Z Stolarczyk, Hendrik J Monkhorst, et al. Exact hartree-fock exchange in one-dimensional metals. *Physical Review B*, 37(18):10646, 1988.

[301] Ks Kim and KD Jordan. Comparison of density functional and mp2 calculations on the water monomer and dimer. *The Journal of Physical Chemistry*, 98(40):10089–10094, 1994.

[302] PJ Stephens, FJ Devlin, CF Chabalowski, and Michael J Frisch. Ab initio calculation of vibrational absorption and circular dichroism spectra using density functional force fields. *The Journal of Physical Chemistry*, 98(45):11623–11627, 1994.

[303] John P Perdew, Matthias Ernzerhof, and Kieron Burke. Rationale for mixing exact exchange with density functional approximations. *The Journal of Chemical Physics*, 105(22):9982–9985, 1996.

[304] Carlo Adamo and Vincenzo Barone. Toward reliable density functional methods without adjustable parameters: The pbe0 model. *The Journal of chemical physics*, 110(13):6158–6170, 1999.

[305] Jochen Heyd, Gustavo E Scuseria, and Matthias Ernzerhof. Hybrid functionals based on a screened coulomb potential. *The Journal of Chemical Physics*, 118(18):8207–8215, 2003.

[306] Yan Zhao and Donald G Truhlar. The m06 suite of density functionals for main group thermochemistry, thermochemical kinetics, noncovalent interactions, excited states, and transition elements: two new functionals and systematic testing of four m06-class functionals and 12 other functionals. *Theoretical Chemistry Accounts*, 120(1-3):215–241, 2008.

[307] Yan Zhao and Donald G Truhlar. Density functional for spectroscopy: no long-range self-interaction error, good performance for rydberg and charge-transfer states, and better performance on average than b3lyp for ground states. *The Journal of Physical Chemistry A*, 110(49):13126–13130, 2006.

[308] Axel D Becke. Density-functional thermochemistry. iii. the role of exact exchange. *The Journal of chemical physics*, 98(7):5648–5652, 1993.

[309] Xinguo Ren, Patrick Rinke, Volker Blum, Jürgen Wieferink, Alexandre Tkatchenko, Andrea Sanfilippo, Karsten Reuter, and Matthias Scheffler. Resolution-of-identity approach to hartree–fock, hybrid density functionals, rpa, mp2 and gw with numeric atom-centered orbital basis functions. *New Journal of Physics*, 14(5):053020, 2012.

[310] Frank Neese. An improvement of the resolution of the identity approximation for the formation of the coulomb matrix. *Journal of computational chemistry*, 24(14):1740–1747, 2003.

[311] Frank Neese, Frank Wennmohs, Andreas Hansen, and Ute Becker. Efficient, approximate and parallel hartree–fock and hybrid dft calculations. a ?chain-of-spheres? algorithm for the hartree–fock exchange. *Chemical Physics*, 356(1):98–109, 2009.

[312] Taras Petrenko, Simone Kossmann, and Frank Neese. Efficient time-dependent density functional theory approximations for hybrid density functionals: Analytical gradients and parallelization. *The Journal of chemical physics*, 134(5):054116, 2011.